İSTANBUL UNIVERSITY PRESS

EISSN 2619-9831

ELECTRICA

dergipark.gov.tr/iujeee

Official journal of İstanbul University Faculty of Engineering

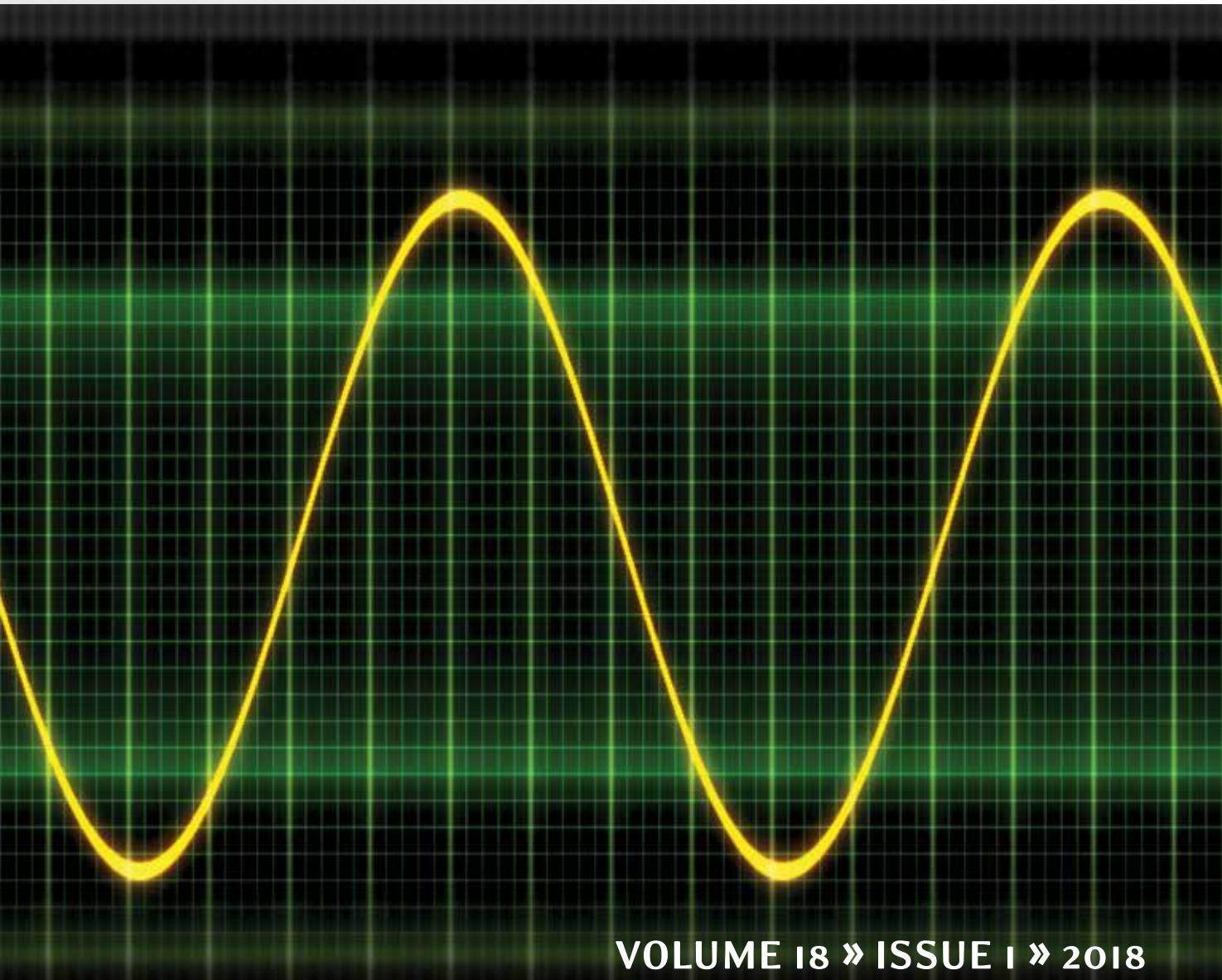

VOLUME 18 » ISSUE 1 » 2018

Editorial Board

Advisory Board

Publisher
İbrahim KARA

Publication Director
Ali ŞAHİN

Deputy Publication Director
Gökhan ÇİMEN

Publication Coordinators
Betül ÇİMEN
Zeynep YAKIŞIRER
Gizem KAYAN

Melike Buse ŞENAY
Özlem ÇAKMAK
Okan AYDOĞAN
Melek Ceren ALĞIN
Merve SAĞLAMER
Hanife Aylin ÖZATA
İrem DELİÇAY

Project Assistants
Cansu ERDOĞAN
Büşra PARMAKSIZ
Ecenur ASLIM

Graphics Department
Ünal ÖZER
Neslihan YAMAN
Deniz DURAN

Contact
Address: Buyukdere Street
No: 105/9 34394
Mecidiyekoy, Sisli, Istanbul, TURKEY
Phone: +90 212 217 17 00
Fax : +90 212 217 22 92
E-mail : info@avesyayincilik.com

Aims and Scope

Electrica is an international, scientific, open access periodical published in accordance with indepen¬dent, unbiased, and double-blinded peer-review principles. The journal is the official publication of İstanbul University Faculty of Engineering and it is published biannually on January and July. The publication language of the journal is English.

Electrica aims to contribute to the literature by publishing manuscripts at the highest scientific level on all fields of electrical and electronics engineering. The journal publishes original research and review articles that are prepared in accordance with ethical guidelines.

The scope of the journal includes but not limited to; electronics, microwave, transmission, control sytems, electrical machines, energy transmission and high voltage.

The target audience of the journal includes specialists and professionals working and interested in all disciplines of electrical and electronics engineering.

The editorial and publication processes of the journal are shaped in accordance with the guidelines of the Institute of Electrical and Electronics Engineers (IEEE), the World Commission on the Ethics of Scientific Knowledge and Technology (COMEST), Council of Science Editors (CSE), Committee on Publication Ethics (COPE), European Association of Science Editors (EASE), and National Information Standards Organization (NISO). The journal is in conformity with the Principles of Transparency and Best Practice in Scholarly Publishing (doaj.org/bestpractice).

The journal is currently indexed in Web of Science-Emerging Sources Citation Index, Scopus, Compendex, Gale and TUBITAK ULAKBIM TR Index.

All expenses of the journal are covered by İstanbul University. Processing and publication are free of charge with the journal. No fees are requested from the authors at any point throughout the evaluation and publication process. All manuscripts must be submitted via the online submission system, which is available at dergipark.gov.tr/iujeee. The journal guidelines, technical information, and the required forms are available on the journal's web page.

Statements or opinions expressed in the manuscripts published in the journal reflect the views of the author(s) and not the opinions of the Electrica editors, editorial board, and/or publisher; the editors, editorial board, and publisher disclaim any responsibility or liability for such materials.

All published content is available online, free of charge at dergipark.gov.tr/iujeee. Printed copies of the journal are distributed free of charge.

OPEN ACCESS

Editor in Chief : Sıddık YARMAN
Address : İstanbul Üniversitesi Mühendislik Fakültesi Elektrik-Elektronik Mühendisliği Bölüm Başkanlığı Avcılar Kampüsü, Avcılar, İstanbul, Turkey
Phone : +90 212 4737070
Fax : +90 212 4737064
E-mail : sbyarman@gmail.com

Publisher : AVES
Address : Büyükdere Cad. 105/9 34394 Mecidiyeköy, Şişli, İstanbul, Turkey
Phone : +90 212 217 17 00
Fax : +90 212 217 22 92
E-mail : info@avesyayincilik.com
Web page : www.avesyayincilik.com

Instructions for Authors

Instructions for Authors

Electrica is an international, scientific, open access periodical published in accordance with indepen¬dent, unbiased, and double-blinded peer-review principles. The journal is the official publication of İstanbul University Faculty of Engineering and it is published biannually on January and July. The publication language of the journal is English.

Electrica aims to contribute to the literature by publishing manuscripts at the highest scientific level on all fields of electricity. The journal publishes original research and review articles that are prepared in accordance with ethical guidelines.

The scope of the journal includes but not limited to; electronics, microwave, transmission, control sytems, electrical machines, energy transmission and high voltage.

The target audience of the journal includes specialists and professionals working and interested in all disciplines of electrical and electronics engineering.

The editorial and publication processes of the journal are shaped in accordance with the guidelines of the Institute of Electrical and Electronics Engineers (IEEE), the World Commission on the Ethics of Scientific Knowledge and Technology (COMEST), Council of Science Editors (CSE), the Committee on Publication Ethics (COPE), the European Association of Science Editors (EASE), and National Information Standards Organization (NISO). The journal conforms to the Principles of Transparency and Best Practice in Scholarly Publishing (doaj.org/bestpractice).

Originality, high scientific quality, and citation potential are the most important criteria for a manuscript to be accepted for publication. Manuscripts submitted for evaluation should not have been previously presented or already published in an electronic or printed medium. The journal should be informed of manuscripts that have been submitted to another journal for evaluation and rejected for publication. The submission of previous reviewer reports will expedite the evaluation process. Manuscripts that have been presented in a meeting should be submitted with detailed information on the organization, including the name, date, and location of the organization.

Manuscripts submitted to Electrica will go through a double-blind peer-review process. Each submission will be reviewed by at least two external, independent peer reviewers who are experts in their fields in order to ensure an unbiased evaluation process. The editorial board will invite an external and independent editor to manage the evaluation processes of manuscripts submitted by editors or by the editorial board members of the journal. The Editor in Chief is the final authority in the decision-making process for all submissions.

The authors are expected to submit researches that comply with the general ethical principles which include; scientific integrity, collegiality, data integrity, institutional integrity and social responsibility.

All submissions are screened by a similarity detection software (iThenticate by CrossCheck).

In the event of alleged or suspected research misconduct, e.g., plagiarism, citation manipulation, and data falsification/fabrication, the Editorial Board will follow and act in accordance with COPE guidelines.

Authorship

Being an author of a scientific article mainly indicates a person who has a significant contribution to the article and shares the responsibility and accountability of that article. To be defined as an author of a scientific article, researchers should fulfil below criteria:

- Making a significant contribution to the work in all or some of the following phases: Research conception or design, acquisition of data, analysis and interpretation.
- Drafting, writing or revising the manuscript
- Agreeing on the final version of the manuscript and the journal which it will be submitted
- Taking responsibility and accountability of the content of the article

Outside the above mentioned authorship criteria, any other form of specific contribution should be stated in the Acknowledgement section.

In addition to being accountable for the parts of the work he/she has done, an author should be able to identify which co-authors are responsible for specific other parts of the work. In addition, authors should have confidence in the integrity of the contributions of their co-authors.

If an article is written by more than one person, one of the co-authors should be chosen as the corresponding author for handling all the correspondences regarding the article. Before submission, all authors should agree on the order of the authors and provide their current affiliations and contact details. Corresponding author is responsible for ensuring the correctness of these information.

Electrica requires corresponding authors to submit a signed and scanned version of the authorship contribution form (available for download through http://dergipark.gov.tr/iujeee) during the initial submission process in order to act appropriately on authorship rights and to prevent ghost or honorary authorship. If the editorial board suspects a case of "gift authorship," the submission will be rejected without further review. As part of the submission of the manuscript, the corresponding author should also send a short statement declaring that he/she accepts to undertake all the responsibility for authorship during the submission and review stages of the manuscript.

Electrica requires and encourages the authors and the individuals involved in the evaluation process of submitted manuscripts to disclose any existing or potential conflicts of interests, including financial, consultant, and institutional, that might lead to potential bias or a conflict of interest. Any financial grants or other support received for a submitted study from individuals or institutions should be disclosed to the Editorial Board. Cases of a potential conflict of interest of the editors, authors, or reviewers are resolved by the journal's Editorial Board within the scope of COPE guidelines.

The Editorial Board of the journal handles all appeal and complaint cases within the scope of COPE guidelines. In such cases, authors should get in direct contact with the editorial office regarding their appeals and complaints. When needed, an ombudsperson may be assigned to resolve cases that cannot be resolved internally. The Editor in Chief is the final authority in the decision-making process for all appeals and complaints.

When submitting a manuscript to Electrica authors accept to assign the copyright of their manuscript to İstanbul University Faculty of Engineering. If rejected for publication, the copyright of the manuscript will be assigned back to the authors. Electrica requires each submission to be accompanied by a Copyright Transfer Form (available for download at http://dergipark.gov.tr/iujeee). When using previously published content, including figures, tables, or any other material in both print and electronic formats, authors must obtain permission from the copyright holder. Legal, financial and criminal liabilities in this regard belong to the author(s).

Statements or opinions expressed in the manuscripts published in Electrica reflect the views of the author(s) and not the opinions of the editors, the editorial board, or the publisher; the editors, the editorial board, and the publisher disclaim any responsibility or liability for such materials. The final responsibility in regard to the published content rests with the authors.

MANUSCRIPT PREPARATION

Manuscripts can only be submitted through the journal's online manuscript submission and evaluation system, available at http://dergipark.gov.tr/iujeee. Manuscripts submitted via any other medium will not be evaluated.

Manuscripts submitted to the journal will first go through a technical evaluation process where the editorial office staff will ensure that the manuscript has been prepared and submitted in accordance with the journal's guidelines. Submissions that do not conform to the journal's guidelines will be returned to the submitting author with technical correction requests.

Authors are required to submit the following:

- Copyright Transfer Form,
- Author Contributions Form, and

during the initial submission. These forms are available for download at http://dergipark.gov.tr/iujeee.

Preparation of the Manuscript
Title page: A separate title page should be submitted with all submissions and this page should include:

- The full title of the manuscript as well as a short title (running head) of no more than 50 characters,
- Name(s), affiliations highest academic degree(s) and ORCID iD's of the author(s),
- Grant information and detailed information on the other sources of support,
- Name, address, telephone (including the mobile phone number) and fax numbers, and email address of the corresponding author,
- Acknowledgment of the individuals who contributed to the preparation of the manuscript but who do not fulfill the authorship criteria.

Biography page: A separate page should be submitted providing short biographies of the contributing authors with their photographs included.

Abstract: An abstract should be submitted with all submissions except for Letters to the Editor. The abstract of articles should be structured without subheadings. Please check Table 1 below for word count specifications.

Keywords: Each submission must be accompanied by a minimum of three to a maximum of six keywords for subject indexing at the end of the abstract. The keywords should be listed in full without abbreviations.

Manuscript Types
Original Articles: This is the most important type of article since it provides new information based on original research. The main text of original articles should be begun with an Introduction section and finalized with a Conclusion section. The remaining parts can be named relevantly to the essence of the research. Please check Table 1 for the limitations for Original Articles.

Review Articles: Reviews prepared by authors who have extensive knowledge on a particular field and whose scientific background has been translated into a high volume of publications with a high citation potential are welcomed. These authors may even be invited by the journal. Reviews should describe, discuss, and evaluate the current level of knowledge of a topic in the field and should guide future studies. sections Please check Table 1 for the limitations for Review Articles.

Letters to the Editor: This type of manuscript discusses important parts, overlooked aspects, or lacking parts of a previously published article. Articles on subjects within the scope of the journal that might attract the readers' attention, may also be submitted in the form of a "Letter to the Editor." Readers can also present their comments on the published manuscripts in the form of a "Letter to the Editor." Abstract, Keywords, and Tables, Figures, Images, and other media should not be included. The text should be unstructured. The manuscript that is being commented on must be properly cited within this manuscript.

Table 1. Limitations for each manuscript type

Type of manuscript	Word limit	Abstract word limit	Reference limit	Table limit	Figure limit
Original Article	3500	250 (Structured)	30	6	7 or total of 15 images
Review Article	5000	250	50	6	10 or total of 20 images
Letter to the Editor	500	No abstract	5	No tables	No media

Tables
Tables should be included in the main document, presented after the reference list, and they should be numbered consecutively in the order they are referred to within the main text. A descriptive title must be placed above the tables. Abbreviations used in the tables should be defined below the tables by footnotes (even if they are defined within the main text). Tables should be created using the "insert table" command of the word processing software and they should be arranged clearly to provide easy reading. Data presented in the tables should not be a repetition of the data presented within the main text but should be supporting the main text.

Figures and Figure Legends
Figures, graphics, and photographs should be submitted as separate files (in TIFF or JPEG format) through the submission system. The files should not be embedded in a Word document or the main document. When there are figure subunits, the subunits should not be merged to form a single image. Each subunit should be submitted separately through the submission system. Images should not be labeled (a, b, c, etc.) to indicate figure subunits. Thick and thin arrows, arrowheads, stars, asterisks, and similar marks can be used on the images to support figure legends. Like the rest of the submission, the figures too should be blind. Any information within the images that may indicate an individual or institution should be blinded. The minimum resolution of each submitted figure should be 300 DPI. To prevent delays in the evaluation process, all submitted figures should be clear in resolution and large in size (minimum dimensions: 100 × 100 mm). Figure legends should be listed at the end of the main document.

Equations
The equations must be stated separated from the text by a blank line. They should be numbered consecutively in parenthesis at the right side of the equation. Symbols and variables as well as in the main text should be written in italics while vectors and matrices should be written in bold type.

All acronyms and abbreviations used in the manuscript should be defined at first use, both in the abstract and in the main text. The abbreviation should be provided in parentheses following the definition.

When a product, hardware, or software program is mentioned within the main text, product information, including the name of the product, the producer of the product, and city and the country of the company (including the state if in USA), should be provided in parentheses in the following format: "Discovery St PET/CT scanner (General Electric, Milwaukee, WI, USA)"

All references, tables, and figures should be referred to within the main text, and they should be numbered consecutively in the order they are referred to within the main text.

References

While citing publications, preference should be given to the latest, most up-to-date publications. If an ahead-of-print publication is cited, the DOI number should be provided. Authors are responsible for the accuracy of references. In the main text of the manuscript, references should be cited using Arabic numbers in square brackets. The reference styles for different types of publications are presented in the following examples.

Journal Article: J.K. Author, "Name of the article", Abbrev. Title of Periodical, vol. x, no. x, pp. xxx-xxx, Abbrev. Month, year.

Book Section: J. K. Author, "Title of chapter in the book," in Title of His Published Book, xth ed. City of Publisher, Country: Abbrev. of Publisher, year, ch. x, sec. x, pp. xxx–xxx.

Books with a Single Author: J.K. Author, "Title of the Book", Abbrev. Of Publisher, City of Publisher, Country, Year.

Conference Proceedings: J. K. Author, "Title of paper," in Unabbreviated Name of Conf., City of Conf., Abbrev. St ate (if given), year, pp. xxx-xxx.

Report: J. K. Author, "Title of report," Abbrev. Name of Co., City of Co., Abbrev. State, Rep. xxx, year.

Thesis: J. K. Author, "Title of thesis," M.S. thesis, Abbrev. Dept., Abbrev. Univ., City of Univ., Abbrev. State, year.

Standards: Title of Standard, Standard number, date.

Manuscripts Accepted for Publication, Not Published Yet: J. K. Author, "Title of paper," unpublished.

Manuscripts Published in Electronic Format: J. K. Au thor. (year, month). Title. Journal [Ty pe of medium]. volume(issue), pag ing i f g iven. A vailable: site/path/file

REVISIONS

When submitting a revised version of a paper, the author must submit a detailed "Response to the reviewers" that states point by point how each issue raised by the reviewers has been covered and where it can be found (each reviewer's comment, followed by the author's reply and line numbers where the changes have been made) as well as an annotated copy of the main document. Revised manuscripts must be submitted within 30 days from the date of the decision letter. If the revised version of the manuscript is not submitted within the allocated time, the revision option may be cancelled. If the submitting author(s) believe that additional time is required, they should request this extension before the initial 30-day period is over.

Accepted manuscripts are copy-edited for grammar, punctuation, and format. Once the publication process of a manuscript is completed, it is published online on the journal's webpage as an ahead-of-print publication before it is included in its scheduled issue. A PDF proof of the accepted manuscript is sent to the corresponding author and their publication approval is requested within 2 days of their receipt of the proof.

Editor in Chief : Sıddık YARMAN
Address : İstanbul Üniversitesi Mühendislik Fakültesi Elektrik-Elektronik Mühendisliği Bölüm Başkanlığı Avcılar Kampüsü, Avcılar, İstanbul, Turkey
Phone : +90 212 4737070
Fax : +90 212 4737064
E-mail : sbyarman@gmail.com

Publisher : AVES
Address : Büyükdere Cad. 105/9 34394 Mecidiyeköy, Şişli, İstanbul, Turkey
Phone : +90 212 217 17 00
Fax : +90 212 217 22 92
E-mail : info@avesyayincilik.com
www.avesyayincilik.com

Contents

İSTANBUL UNIVERSITY PRESS

RESEARCH ARTICLE

Electrica 2018; 18(1): 1-5

An Analysis of the Effects of SVM Parameters on the Dead-Time System Modeling

Nihat Kabaoğlu[1], Rana Ortaç Kabaoğlu[2]

[1]Department of Electrical and Electronics Engineering, İstanbul Medeniyet University School of Engineering and Natural Science, İstanbul, Turkey
[2]Department of Electrical and Electronics Engineering, İstanbul University School of Engineering, İstanbul, Turkey

Cite this article as: N. Kabaoğlu, R. Ortaç Kabaoğlu. "An Analysis of the Effects of SVM Parameters on the Dead-Time System Modeling". *Electrica*, vol. 18, no. 1, pp. 1-5, 2018.

ABSTRACT

Modeling a dead-time system is a common issue in engineering applications. To address this issue, existing research has employed neural networks and fuzzy logic-based intelligent systems. Herein, a dead-time system modeled with the aid of support vector machine regression, which has a good generalization feature, was investigated. The performance of the method proposed herein was examined with different parameters in linear and nonlinear dead-time systems.

Keywords: Modeling, support vector machine, regression

Address for Correspondence:
Nihat Kabaoğlu

E-mail:
nihat.kabaoglu@medeniyet.edu.tr

Received: 12.07.2017

Accepted: 04.01.2018

Available online at
http://dergipark.gov.tr/iujeee

DOI: 10.5152/iujeee.2018.1801

Introduction

Optimal generalization success can be achieved for a learning task with a finite number of training cases, if the machine capacity is correctly balanced, which means that the result is a definitive conclusion on a given training group and the learning ability every single training set excellently. The classic neural network attitude has faced several challenges, especially in applications with few data, in generalizing and generating data-compatible models. The Support Vector Machines (SVM) presented by Vapnik in the 1970s is a combination of statistics, machine learning, Neural Networks (NN) [1, 2]. The formulation includes the Structural Risk Minimization rule. SVM can also carry out a well generalising of classifying and regressing even on little sized data using the kernel function mapping tecnique [3, 4]. In addition, SVM are becoming increasingly popular due to their many attractive features in theoretical and engineering applications. Unlike NN, SVM can overcome the problem of classifying and regressing via being transformed to the problem of quadratic programming without being deterred by any regional minimum. One other adverse side of NN is not to know exactly to choose the hidden cells numbers. SVM that can be utilized at the nonlinear system modelling, is utilized at many fields of model identification, identification of hidden handwriting, identification of objects, determination of sound, search and characterization of a face, regression, estimation of a function and optimal control areas [5, 6].

The purpose of this work is to present the regression method according to SVM by applying it in order to model of the system with dead-time. The proposed article is arranged as below:

A general information about SVM is given in Chapter 2. The proposed support vector machine regression method and its structure are expressed in Chapter 3, the examples are in Chapter 4. They are followed by conclusion and references sections.

Support Vector Regression

Vapnik found in 1997 that support vector techniques were successfully applied to solve regression problems [1]. Contrary to pattern recognition problems, there are real-value func-

tions. Support vector machine is an effective way to model linear and nonlinear systems.

The training data set to be used to learn the function f(x) with input-output relation is as follows:

$$(x_1,y_1),(x_2,y_2).....(x_n,y_n),\quad x\in R^N,\quad y\in R \tag{1}$$

Here, input data, *X*, stand for N-size vectors and generally system responds, *Y*, stand for scalar values. The function to be estimated in the support vector machines is processed as follows. The input/output connection may be modeled as follows at the feature space by the linear regressing model:

$$f(\mathrm{x},\mathrm{w})=\mathrm{w}^{\mathrm{T}}\mathrm{x}+b \tag{2}$$

Several loss functions are used in regression operations. The ε-tolerance loss function used here is given as follows:

$$Y_\varepsilon=\begin{cases}0\ if\quad \left|y-f(x,w)\right|<\varepsilon\\ \left|y-f(x,w)\right|-\varepsilon\ \ otherwise\end{cases} \tag{3}$$

It is the objective to minimize the observational and also the experimental risk that symbolizes the whole of errors at SVM algorithm formula and $\|w\|^2$ at once. As a result, a regressing hyper-plane $f(x,w)$ can be detected in x and x* slack variables via minimization as follow:

$$R(w,\xi,\xi^*)=\frac{1}{2}\left\|\mathrm{w}\right\|^2+\mathrm{C}\sum_{\mathrm{i}=1}^{\mathrm{n}}(\xi+\xi^*) \tag{4}$$

The trade-off parameter between error and $\|w\|$ weight vector form is C and it is chosen by the user. ε value, another parameter, which will be chosen by the user, like C, and defines the size of the ε-tube. This optimization problem with restriction is resolved via installing a secondary Lagrangian as follows:

$$\begin{aligned}\max_{\alpha,\alpha^*}\ \mathrm{W}(\alpha,\alpha^*)=&-\varepsilon.\sum_{i=1}^{n}(\alpha_i^*+\alpha_i)+\sum_{i=1}^{n}(\alpha_i^*-\alpha_i)y_i\\ &-\frac{1}{2}\sum_{i=1,j=1}^{n}(\alpha_i^*-\alpha_i)(\alpha_j^*-\alpha_j)x_i^{\mathrm{T}}x_j\end{aligned} \tag{5}$$

The restrictions are as the following.

$$\begin{aligned}&\sum_{i=1}^{n}\alpha_i^*=\sum_{i=1}^{n}\alpha_i\\ &0\le\alpha_i^*\le C\quad i=1,..,n\\ &0\le\alpha_i\le C\quad i=1,..,n\end{aligned} \tag{6}$$

By combining the results of optimal regression hyper-plane, it is rewritten as:

$$z=f(\mathrm{x},\mathrm{w})=\mathrm{w}^{\mathrm{T}}\mathrm{x}+b=\sum_{i=1}^{n}(\alpha_i^*-\alpha_i)<x_ix>+b \tag{7}$$

In non-linear SVM regression, it is passed through from nonlinear input space to a linear features space using "kernel functions", which meet Mercer conditions and are symmetric final positive. Any kernel function, which corresponds to any internal multiplication to be done, in this space having high-degree size has been defined in the present space [7].

$$K(x_i,x_j)=<\varphi(x_i),\varphi(x_j)> \tag{8}$$

Using kernel function, need for making multiplications in (7) is eliminated. In the feature space, which is linear, the algorithm for linear regression by SVM is applied. Thus, $f(x,w)$ hyperplane of regression, which is linear in the features space, will create nonlinear regressing hyper-plane in the specific input space. The formulation for non-linear regression is rewritten as follows:

$$f(\mathrm{x},\mathrm{w})=\sum_{i=1}^{n}(\alpha_i^*-\alpha_i)K(x_ix)+b \tag{9}$$

The most popular kernel functions, the polynom kernel function, Radial Base kernel Function (RBF) have been used and tested in this study.

Polynomial kernel function: $K(\mathbf{x},\mathbf{x}')=(\langle\mathbf{x},\mathbf{x}'\rangle+1)^p$

RBF : $K(\mathbf{x},\mathbf{x}')=\exp\left(-\left\|\mathbf{x}-\mathbf{x}'\right\|^2/2\sigma^2\right)$

Modeling with SVM-Regression

The proposed form of the modelling of the dynamic system using the SVM-Regression (SVM-R) is shown in Figure 1.

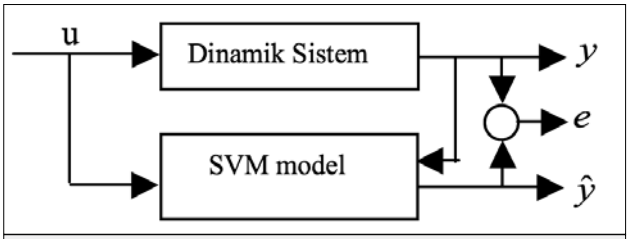

Figure 1. Propsed modelling using SVM-R

where u and *y's* refer sytem input and outputs. y is the actual one belonging to system given. $\hat{y}$ is the one of the SVM-R modeling, *e* refers the error inbetween outputs of the actual and the modelled systems. This is a modeling error and also depends on the approximate ability.

It is presumed that the structure of the actual system or its mathematical model is not known. SVM modeling data set is planned as to input - output values batch of the system. Usually, the outputs of each systems at the k+1 time, can be stated as a function with former output specimens, and-with former input specimens.

$$\begin{aligned}y(k+1)=f(&y(k),....,y(k-n+1),u(k-d),...,\\ &u(k-d-m+1),\eta(k),....,\eta(k-l))=f(x(k))\end{aligned} \tag{10}$$

where, $\eta(k)$ is uncertainness (including some noises, unmodeled dynamics… etc), *d* is the time lag being in samples (when T_s is the sampling period, the system dead time is d.T_s) *n, m, l*

is the maximum delay of the output, input and noise respectively, and $f(.)$ is a nonlinear function. To enter the SVM, the vector is as follows:

$$x(k)=[y(k),....,y(k-n+1),u(k-d),....,u(k-d-m+1), \eta(k),....,\eta(k-l)]^T \quad (11)$$

where $x \in R^{n+m+l}$, k = d+1, ... ,d+N. $y(k+1)$ is output. $\hat{y}(k+1)$ refers predicted output value at time (k+1). As a result, this nonlinear system model is rewritten as folows:

$$\hat{y}(k+1)=\sum_{i=1}^{SVs}(\alpha_i^* - \alpha_i).K(x_i x(k))+b \quad (12)$$

Modeling algorithm with SVM-R

Stage 1: Create training data set $\{(\vec{x}_i, y_i), i=1,...,N\}$. The number of training data pairs in the group is N.

Stage 2: Parameter and kernel function selections depending on user are done. (C and ε)

Stage 3: SVM is trained with training data.

Stage 4: Various test and input data are used for testing of the performance of the SVM based model.

Examples

Linear system modeling example

A first order dead system is seen as below [8].

$$y(k+1)=0.9512.y(k)+0.07316.u(k-d) \quad (13)$$

- Sample period is 0.1s., delay step is *d=5* . The design parameters are selected and applied as follows.
- $u(t)=1+\sin(10.t+5)+\sin(2.t+1)$ is the selected sign as input. The system is run for a period of time to collect input - output training data.
- $X(k)=[y(k.)\ y(k-1)\ u(k.)\ u(k-1)]^T$, $Y(k)=y(k+1)$ are the selected input and output of the SVM.
- User defined parameters are selected like C: 200, also ε: 0.01. Every training set involves 150 components.
- This method is applied for both RBF and also polynomial kernel function. RBF is tested for $\sigma=0.5,2,3,4$ and polynomial kernel parameter *p* is selected as *p*=1, 2, 3, 4. In addition, 3 different test inputs are applied for comparison (Table 1). The outputs for different inputs are shown in Figure 2, 3.

Nonlinear system modeling example

The method was applied to a nonlinear dead time system after it was applied to a linear system. Here a nonlinear second order dead time system is considered.

The system considered with 3 varied dead times T=0.25sec., 1sec., 2sec., are given like follows [9].

$$\ddot{y}(t)+\dot{y}(t.)+y(t.)+y^3(t)=u(t-T) \quad (14)$$

The design parameters are selected and applied as follows.

- $u(t)=1+\sin(10.t+5)+\sin(2.t+1)$ is the selected sign as input. the system is run for a period of time to collect input - output training data.
- $X(k)=[y(k.)\ y(k-1)\ u(k.)\ u(k-1)]^T$, $Y(k)=y(k+1)$ are the selected input and output of the SVM.
- User defined parameters are selected like C: 200, ε : 0.001. Every training set involves 200 components.
- This method is applied for both RBF and also polynomial kernel function. RBF is tested for $\sigma=9,10$ and polynomial kernel parameter p is selected as *p*=1, 2. In addition, 3 different test inputs are applied for comparison (Table 2). The outputs for different inputs are shown in Figure 4, 5.

Conclusion

In this work, a method based on modeling of dead time systems using SVM regression algorithm is presented. In the proposed method, any mathematical or theoretical forms of the system do not need to be known. The system is modeled by the SVM-R method constituted via a loss function. The SVM regression has high generalization potency and gives very good results even with a small number of training data. As it guarantees a global minimum it is also a very dependable approach. The method has been applied on linear time and

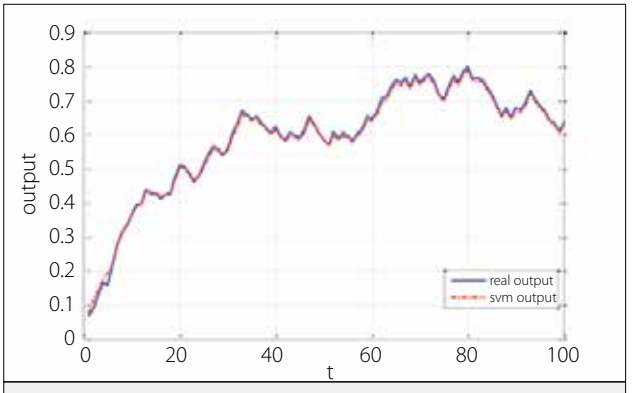

Figure 2. Polinomial kernel (p=3), u=random

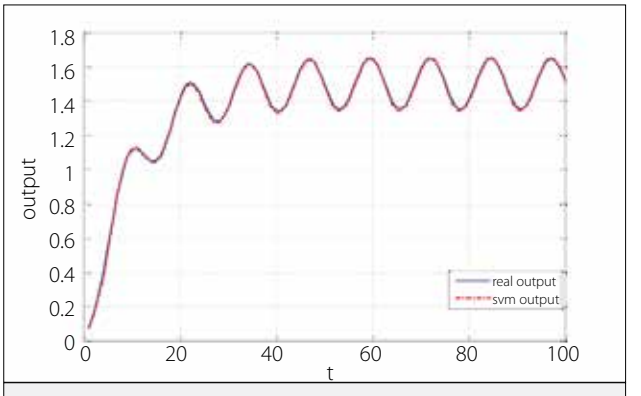

Figure 3. RBF kernel (σ=0.5), u=exp(-t)+1+sin(5t+5)

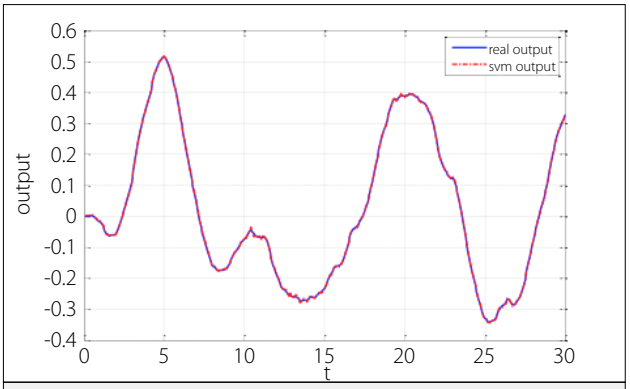

Figure 4. Polinomial kernel (p=3), u=random

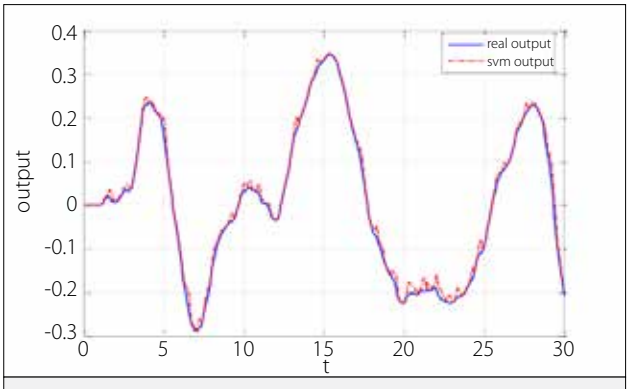

Figure 5. RBF kernel (σ=9), u=random

Table 1. Training and testing errors for different kernel parameters and different inputs (for linear system)

Kernel function	Kernel parameter	Training error	Testing error	Step error	Error of u=exp (-t)+1+sin(5t+5)	Error of random signal
Polinomial	p=1	0.0047	0.0057	0.0047	0.0052	0.0035
	p=2	0.0070	0.0065	0.0073	0.0064	0.0053
	p=3	0.0059	0.0062	0.0065	0.0059	0.0084
	p=4	0.0057	0.0053	0.0087	0.0080	0.0089
RBF	σ=0.5	0.0065	0.0069	0.0109	0.0087	0.0136
	σ=2	0.0058	0.0060	0.0081	0.0084	0.0081
	σ=3	0.0059	0.0064	0.0083	0.0082	0.0062
	σ=4	0.0052	0.0057	0.0088	0.0073	0.0072

Table 2. Training and testing errors for different kernel parameters and different inputs (for nonlinear system)

Kernel function	Kernel parameter	Dead time (second)	Training error	Testing error	Step error	Error of u= exp(-t) +1+sin(5t+5)	Error of 1. random signal	Error of 2. random signal	Error of 3. random signal	Error of 4. random signal
Polinomial	p=1	0.25	0.0047	0.0046	0.0018	0.0028	0.0091	0.0098	0.0085	0.0095
		1	0.0049	0.0046	0.0022	0.0031	0.0091	0.0097	0.0080	0.0095
		2	0.0051	0.0048	0.0027	0.0036	0.0094	0.0093	0.0081	0.0099
	p=2	0.25	0.0037	0.0035	0.0025	0.0037	0.0093	0.0102	0.0097	0.0099
		1	0.0049	0.0045	0.0028	0.0043	0.0099	0.0108	0.0100	0.0096
		2	0.0052	0.0048	0.0033	0.0038	0.0101	0.0109	0.0101	0.0099
RBF	σ=9	0.25	0.0062	0.0061	0.0025	0.0035	0.0145	0.0166	0.0122	0.0162
		1	0.0064	0.0062	0.0028	0.0038	0.0140	0.0157	0.0112	0.0155
		2	0.0065	0.0064	0.0032	0.0043	0.0152	0.0145	0.0112	0.0160
	σ=10	0.25	0.0063	0.0062	0.0027	0.0036	0.0128	0.0149	0.0112	0.0145
		1	0.0066	0.0065	0.0029	0.0040	0.0130	0.0144	0.0106	0.0143
		2	0.0067	0.0066	0.0033	0.0045	0.0140	0.0135	0.0106	0.0148

nonlinear dead time systems, and a very high modeling and generalization success has been observed even at various inputs. These results are evident from the small size of the modeling errors. Also, it has been found that as the dead time increased, there was a small increase in modeling errors and the modeling performance was not adversely effected by the change of the system's dead time. This is very important in terms of modeling performance. As Table 2 shows, the error grows as the polynomial level grows for the polynomial kernel, and the error decreases as the variance for the rbf kernel grows. On the other hand, selecting kernel and its parameters is a very important question of the SVM. This can be seen on the tables. the choice of parameters depends on the user, there are still studies focusing on making the right choice [9]. increasing the training data provides a better performance, but this can lead time problems in some complex systems. Various studies have also been done on this topic [10-12].

References

1. V. N. Vapnik. "Statistical Learning Theory", John Wiley and Sons, New York, 1998.
2. V. N. Vapnik. "The Nature of Statistical Learning Theory", Springer-Verlag. New York, 1995. [CrossRef]
3. C. Junli, J. Licheng, "Classification Mechanism of Support Vector Machines", *IEEE Proceedings of ICSP* p. 1556-1559, 2000.
4. A. Smola, B. Scholkopf, "A Tutorial on Support Vector Regression", *NeuroCOLT2 Technical Report NC-TR* pp. 98-30, 1998.
5. L. Guohai, Z. Dawei, X. Haixia, M. Congli "Soft sensor modeling using SVM in fermentation process", *Chinese Journal of Scientific Instrument,* vol. 6, 2009.
6. V. Kecman, "Learning and Soft Computing: Support Vector Machines, Neural Networks, and Fuzzy Logic Models", Cambridge, Mass.: MIT Press, 2001.
7. C. Campbell, "Kernel Methods: A Survey of Current Techniques", *Neurocomputing* vol. 48, pp. 63-84, 2002. [CrossRef]
8. Z. Hongdong, S. Huihe, "A Novel Method of Process Dead-Time Identification: Support Vector Machine Approach", *Proceeding of American Control Conference,* pp. 880- 884, 2004.
9. G. Yan, C. Li, G. Ma, "Parameter selection for support vector machines based on hybrid genetic algorithms", *Journal of Harbin Institute of Technology,* vol.5, 2008.
10. H. Zhang, X. Wang, C. Zhang, X. Xu, "Modeling Nonlinear Dynamical Systems Using Support Vector Machine", Proceeding of 4. International Conf. *On Machine Learning and Cybernetics*, pp. 3204-3209, 2005.
11. J. Ma, J. Theiler, S. Perkins, "Accurate on-line support vector regression", Neural Computation, vol.15, pp. 2683-2703, 2003. [CrossRef]
12. http://www.sciencedirect.com/science/article/pii/S1226086X13003742 - !A. M. Ghaedi, M. Hossainpour, A. Ansari, M.H. Habibi, A.R. Asghari "Least square-support vector (LS-SVM) method for modeling of methylene blue dye adsorption using copper oxide loaded on activated carbon"Journal of Industrial and Engineering Chemistry, Volume 20, Issue 4, 25 July 2014, pp. 1641-1649.

Nihat Kabaoğlu received the B.S. and M.S. degrees in electronics engineering from İstanbul University, and the Ph.D. degree in electronics and telecommunication engineering from İstanbul Technical University, İstanbul, Turkey, in 1997, 2000, 2005 respectively. After working in different positions at İstanbul University, The Scientific and Technological Research Council of Turkey, Kadir Has University and Maltepe University, he joined to İstanbul Medeniyet University as an associate professor in 2015. His general research interests cover estimation theory, statistical signal processing, communication theory, wireless sensor networks and array processing. His current research areas are focused on wireless communication concepts with specific attention to channel estimation for spread-spectrum and multicarrier systems, on beamforming design for next generation systems and on optimal power allocation in wireless sensor networks.

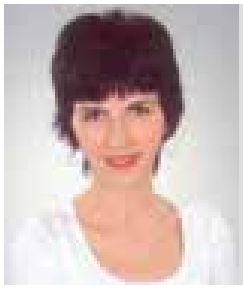

Rana Ortaç Kabaoğlu received the B.S. and M.S. degrees in electrical and electronics engineering from İstanbul University, and the Ph.D. degree in control engineering from İstanbul Technical University, İstanbul, Turkey, in 1997, 2001, 2010 respectively. At 1998, she joined to İstanbul University, electrical and electronics engineering department as a reseach assistant. She has been working as an assosiated professor at the same department since 2015. Her research areas are control systems, modelling, intelligent systems, fault dedection and control.

İSTANBUL UNIVERSITY PRESS

RESEARCH ARTICLE

Electrica 2018; 18(1): 6-12

Current and Voltage Mode Quadrature Oscillator Based on Voltage Differencing Buffered Amplifier

Abdullah Yeşil[1], Fırat Kaçar[2]

[1]Department of Naval Architecture and Marine Engineering, Bandırma Onyedi Eylül University Maritime Faculty, Balıkesir, Turkey
[2]Department of Electrical and Electronics Engineering, İstanbul University School of Engineering, İstanbul, Turkey

Cite this article as: A. Yeşil, F. Kaçar. "Current and Voltage Mode Quadrature Oscillator Based on Voltage Differencing Buffered Amplifier". *Electrica*, vol. 18, no. 1, pp. 6-12, 2018.

ABSTRACT

In this work, we present a current-mode and voltage-mode quadrature oscillator circuit using a voltage differencing buffered amplifier (VDBA), two grounded capacitors, and a grounded resistor. The oscillation condition and frequency are orthogonally (or independently) controllable. The current-mode and voltage-mode quadrature signals can be simultaneously obtained from the proposed circuit. The use of only grounded capacitors and resistors makes the proposed circuits ideal for integrated circuit implementation. The quadrature oscillator is simulated with SPICE simulation program using 0.35-μm technology parameters.

Keywords: Quadrature oscillator, CMOS active elements, non-ideal analysis, voltage mode

Introduction

In the design of electronic systems, the need often arises both single periodic waveform and two periodic waveforms with 90° phase difference called a quadrature oscillator. Application areas of quadrature oscillator are in the communication system for quadrature mixers, in test and measurement system for testing characterizing electronic devices and circuits, in single-sideband generators or selective voltmeters [1, 2]. Different kinds of active elements have been used in quadrature oscillators up to now. Designers of quadrature oscillators utilize various active elements such as the positive, negative and inverting second generation current conveyor (ICCII-, CCII+, CCII-) [3-5], current differencing transconductance amplifier (CDTA) [6-8], current differencing buffered amplifier (CDBA) [9-10], operational amplifier [11], current feedback operational amplifier (CFOA) [12-14], differential difference current conveyor (DDCC) [15], fully balanced voltage differencing buffered amplifier (FB-VDBA) [16], also known as current backward transconductance amplifier (CBTA) [17], differential difference dual-X second generation current conveyor (DD-DXCCII) [18] and four terminal floating nullor (FTFN) [19-21].

A summary of the performance parameters of compared oscillators and the proposed oscillator are shown in Table 1. It can be observed from Table 1 that the proposed oscillator possesses superior features according to recently reported oscillators.

In this paper, voltage differencing buffered amplifier (VDBA) which is attractive active element contains two basic blocks like voltage buffer and transconductance stage which can be tuned electronically biasing current. Therefore, in this paper, the VDBA is chosen to be used in the design of an electronically tunable quadrature oscillator having two voltage outputs and three current outputs. Its main advantages are the minimum number of active and passive elements and independent setting of frequency and condition of oscillations. Besides, all passive elements are grounded and the required oscillator frequency could be easily adjusted by varying the external DC bias currents of the VDBAs.

Address for Correspondence:
Fırat Kaçar

E-mail:
fkacar@istanbul.edu.tr

Received: 08.03.2017

Accepted: 05.12.2017

DOI: 10.5152/iujeee.2018.1802

Table 1. Comparison of the proposed oscillator with those of previous circuits

	Number of active elements	Number of passive elements	Electronically adjusting oscillation condition independently of oscillation frequency	Types of passive elements' tie	Type (VM/CM) and number of outputs	Frequency of oscillation
Sobhy and Soliman (2007) [3]a	3 ICCII-	4R/2C	No	Grounded	2 VM	3.98 MHz
Khateb et al. (2012) [4]	2 CCII	3R/2C	No	Grounded	2 CM	10 kHz
Yucel and Yuce (2015)[5]	2 CCII-	4R/2C	No	Floating	3 VM	4.54 MHz
Horng et al. (2010) [6]b	3 CDTA	3C	Yes	Grounded	2 VM / 2 CM	410 kHz
Jin & Wang (2014) [7]	2 CDTA	1R/2C	Yes	Floating	4 CM	240 MHz
Jin and Wang (2012) [8]	1 CDTA	1R/2C	No	Floating	2 CM	1.87 MHz
Tangsrirat et al. (2008) [9]	2 CDBA	3R/2C	No	Floating	2 VM	15.91 kHz
Keskin (2005) [10]	1 CDBA	2R/2C	No	Floating	1 VM	795.8 Hz
Horng (2011) [11]c	3 OP-AMP	5R/3C	No	Floating	2 VM	15.91 kHz*
Tangsrirat & Surakamponton (2009) [12]	2 CFOA	3R/2C	No	Floating	2 VM	15.8 kHz
Lahiri et al. (2013) [13]d	3 CFOA	4R/2C	No	Floating	1 VM/2 CM	128.9 kHz
Soliman (2000) [14]e	1 CFOA	2R/2C	No	Floating	1 VM	160.9 kHz
Soliman (2000) [14]f	2 CFOA	2R/2C	No	Grounded	2 VM	153.43 kHz
Kumngern & Dejhan (2009) [15]	2 DDCC	3R/2C	No	Grounded	2 VM	640 kHz
Yesil et al. (2016) [16]	1 FB-VDBA	1R/2C	No	Floating	2VM	1.33 MHz
Ayten et al. (2012) [17]g	1 CBTA	1R/2C	No	Grounded	2 VM/1CM	18.9 MHz
Chaturvedi, & Mohan (2015) [18]	1 DD-DXCCII	3R/2C	No	Grounded	3VM/2CM	15.78 MHz
Bhaskar and Senani (2005) [19]	2 PFTFN	4R/2C	No	Floating	1 CM	17.36 kHz*
Kumar and Senani (2007) [20]	1 PFTFN	5R/2C	No	Floating	1 VM	4.98 kHz
Cam et al. (2000) [21]i	1 FTFN	5R/2C	No	Floating	1 CM	28 kHz
The proposed oscillator	2 VDBA	1R/2C	Yes	Grounded	2 VM/3 CM	1.14 MHz

[a]Figure 8a in [3], [b]Third order QO, [c]Figure 1 in [11], [d]Figure 1a in [13], [e]Figure 1 in [14], [f]Figure 2 in [14], [g]Figure 3 in [17], [i] 2. circuit in Table-1 in [21], *theoretical result of FO; VM: voltage-mode; CM: current-mode; ICCII: inverting second generation current conveyor; CCII: second generation current conveyor; CDTA: current differencing transconductance amplifier; CDBA: current differencing buffered amplifier; OPAMP: operational amplifier; CFOA: current feedback operational amplifier; DDCC: differential difference current conveyor; FB-VDBA: fully balanced voltage differencing buffered amplifier; CBTA: current backward transconductance amplifier; DD-DXCCII: differential difference dual-X second generation current conveyor; FTFN: four terminal floating nullor; VDBA: voltage differencing buffered amplifier

Voltage Differencing Buffered Amplifier

In the paper [22], the schematic symbol of the VDBA is added ZC- terminals, which is negative of the Z terminal. Its modified schematic symbol of the VDBA is given in Figure 1.

Using standard notation, the relationship between port currents and voltages of the VDBA can be defined by the following hybrid matrix:

$$\begin{pmatrix} I_P \\ I_N \\ I_Z \\ I_{ZC-} \\ V_W \end{pmatrix} = \begin{pmatrix} 0 & 0 & 0 \\ 0 & 0 & 0 \\ g_m & -g_m & 0 \\ -g_m & g_m & 0 \\ 0 & 0 & \alpha \end{pmatrix} \begin{pmatrix} V_P \\ V_N \\ V_Z \end{pmatrix} \quad (1)$$

where g_m and α represent transconductance and the non-ideal voltage gain of the VDBA, respectively. The value of α in an ideal VDBA is equal to unity. It should be noted from the above

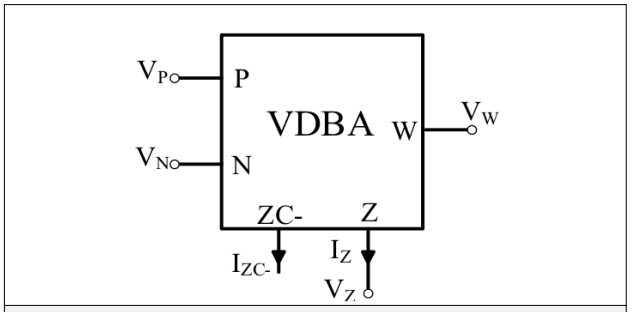

Figure 1. The circuit symbol of the VDBA

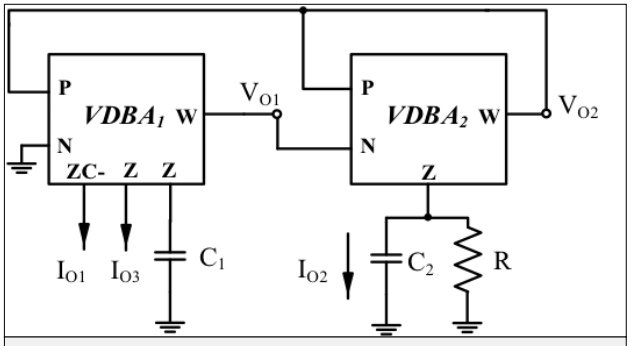

Figure 2. Proposed quadrature oscillator circuit

that it possesses W terminal of low impedance and other terminals of high impedance. The CMOS implementation of the VDBA consists of an operational transconductance amplifier and a voltage buffer. The current of P and N are approximated to zero. The terminal W is the output of voltage buffer; thus the voltage of W is approximated to Z.

Proposed Quadrature Oscillator Circuit

The proposed quadrature oscillator which is shown in Figure 2 offers two voltage outputs and three current outputs. It is made up of two VDBAs and three passive elements such as two grounded capacitors and a resistor.

The circuit analysis yields the following second order characteristic equation.

$$s^2C_1C_2 + sC_1\left(\frac{1}{R} - g_{m2}\right) + g_{m1}g_{m2} = 0 \tag{2}$$

The frequency of oscillation (FO) and the condition of oscillation (CO) are found as

$$FO: f_0 = \frac{1}{2\pi}\sqrt{\frac{g_{m1}g_{m2}}{C_1C_2}} \tag{3a}$$

$$CO: \quad R.g_{m2} = 1 \tag{3b}$$

It is apparent that FO and CO can be set independently. The relation between the two output voltages at the oscillation frequency is

$$V_{O1} = e^{-j90^\circ}V_{O2}k_{VM}; \qquad k_{VM} = \sqrt{\frac{g_{m1}C_2}{g_{m2}C_1}} \tag{4}$$

This confirms that the output voltages are in quadrature and indicates that if the output voltage amplitudes are to be equal, we must choose k_{VM}=1. At the oscillation frequency it holds for the three output currents;

$$I_{O1} = e^{j90^\circ}I_{O2}k_{CM} = e^{j180^\circ}I_{O3}; \qquad k_{CM} = \sqrt{\frac{g_{m1}C_1}{g_{m2}C_2}} \tag{5}$$

The currents are not only shifted by 90º but also shifted by 180º and they have the same amplitude if k_{CM}=1 abstract

Non-Ideal and Parasitic Effects Analyses

Considering the non-ideal voltage gain α of the VDBA, the second order characteristic equation in Equation (2) convert to:

$$s^2C_1C_2 + sC_1\left(\frac{1}{R} - g_{m2}\alpha_2\right) + g_{m1}g_{m2}\alpha_1\alpha_2 = 0 \tag{6}$$

and non-ideal FO and the CO are given as:

$$FO: f_0 = \frac{1}{2\pi}\sqrt{\frac{g_{m1}g_{m2}\alpha_1\alpha_2}{C_1C_2}} \tag{7a}$$

$$CO: \quad R.g_{m2} = \alpha_2 \tag{7b}$$

From Equations (7a) and (7b), the tracking errors slightly change the FO and CO. However, the FO and CO still can be adjusted. Also, the non-ideal relation between the two output voltages at the oscillation frequency is

$$V_{O1} = e^{-j90}k_1V_{O2}; \quad k_1 = \sqrt{\frac{g_{m1}C_2\alpha_1}{g_{m2}C_1\alpha_2}} \tag{8}$$

It is clear from equation (8) that the phase difference between V_{O1} and V_{O2} is -90º under the sinusoidal steady state. In other words, its output voltages are in quadrature. It is seen from Equation (8) that the output voltages have to equal to amplitude for k_1=1. The non-ideal relationships among the current outputs are also given below at Equation (9);

$$I_{O1} = e^{j90}k_2I_{O2} = e^{j180}I_{O3}; \quad k_2 = \sqrt{\frac{g_{m1}C_1\alpha_2}{g_{m2}C_2\alpha_1}} \tag{9}$$

Similarly, It is obvious from Equation (9) that not only the outputs of current have to equal to amplitude for k_2=1 but also phase difference among the current outputs are 90º. Note that, in order to obtain the I_{O2} current output through the capacitor, CCII- can be easily preferred by grounding Y terminal and using X and Z as input and output, respectively. By taking into account the parasitic effects of the VDBA, Figure 3 depicts parasitic effects of the proposed quadrature oscillator circuit.

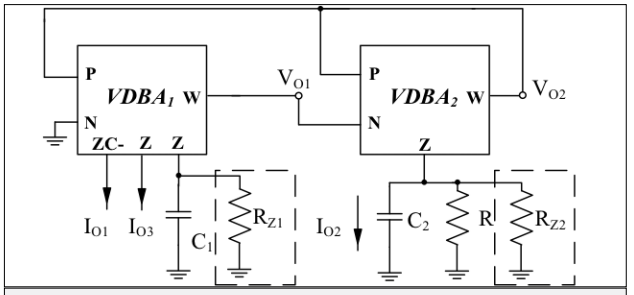

Figure 3. Parasitic impedances of VDBA affecting oscillator circuit

R_{Z1} and R_{Z2} are the parasitic resistance of Z terminal of VDBA which belongs i[th] the VDBA. R_{Z1} and R_{Z2} are the mainly parasitic elements for the proposed oscillator circuit. Reanalyzing the oscillator circuit shown in Figure3 yields the following modified second order characteristic equation;

$$s^2C_1C_2 + s\left(\frac{C_1}{R//R_{Z2}} + \frac{C_2}{R_{Z1}} - C_1g_{m2}\right)\ldots$$

$$+g_{m1}g_{m2} + \frac{1}{R_{Z1}R_{Z2}//R} - \frac{g_{m2}}{R_{Z1}} = 0 \qquad (10)$$

The parameter of the modified FO and the modified CO can be expressed as follows;

$$FO: f_0 = \frac{1}{2\pi}\sqrt{\frac{g_{m1}g_{m2}}{C_1C_2} + \frac{1}{C_1C_2R_{Z1}R_{Z2}//R} - \frac{g_{m2}}{C_1C_2R_{Z1}}} \qquad (11a)$$

$$CO: \quad C_1g_{m2} = \frac{C_1}{R//R_{Z2}} + \frac{C_2}{R_{Z1}} \qquad (11b)$$

The value of the modified FO and CO may be altered slightly by parasitic effects of VDBA. To minimize the deviation of the FO, output resistance of Z terminal of the VDBA should be increased by using cascode current mirror for the first stage of VDBA.

Simulation Results

So as to confirm the theoretical results of the proposed quadrature oscillator circuit, Figure 2 has been simulated using SPICE simulation program. According to previous version [22], the modified CMOS implementation of VDBA is depicted in Figure 4. The aspect ratios of the CMOS transistors used in the modified VDBA are given in Table 2.The supply voltages, biasing voltage and current are chosen as V_{DD}=-V_{SS}=1.5V, V_B=-0.9V, and I_B=100μA.

Table 2. Transistors aspect ratios for the modified VDBA

Transistors	W(μm)	L(μm)
M_1-M_4, M_{18}-M_{21}	7	0.35
M_5- M_8	21	0.7
M_9-M_{12}	7	0.7
M_{13}-M_{14}	3.5	0.7
M_{15}-M_{17}	14	0.35

VDBA: voltage differencing buffered amplifier

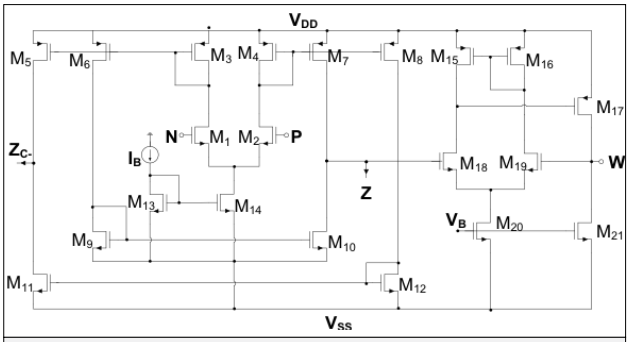

Figure 4. The modified CMOS structure for the VDBA

The quadrature oscillator has been built with C_1=C_2=100pF, g_{m1}=g_{m2}=735μA/V and R=1.4kΩ which is slightly bigger than the value 1.36kΩ calculated from CO. This is to ensure that oscillations would start. The theoretical FO is calculated as f_0=1.17MHz. The simulated FO obtained from the simulation results is measured as 1.14MHz. the slightly discrepancy between simulation and theoretical resutls stems from limited frequency bandwidth of the transconductance and voltage transfer gain error, and parasitic effects. The simulated output waveforms of the quadrature voltages are demostrated in Figure 5, whereas Figure 6 depicts the spectrum of the oscillator output voltages. As it is seen from Figure 6, voltage outputs, V_{O1} and V_{O2}, of the proposed oscillator provide 52.2dB and 48.1dB of rejection at the second harmonic, respectively.

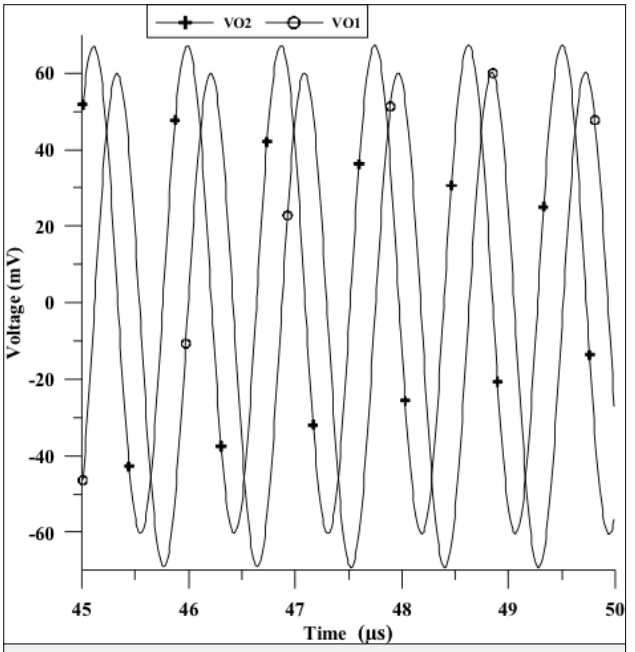

Figure 5. The steady-state waveforms for the quadrature voltages V_{O1} and V_{O2}

The waveforms of the oscillator output currents are illustrated in Figure 7, whereas Figure 8 depicts the spectrum of the

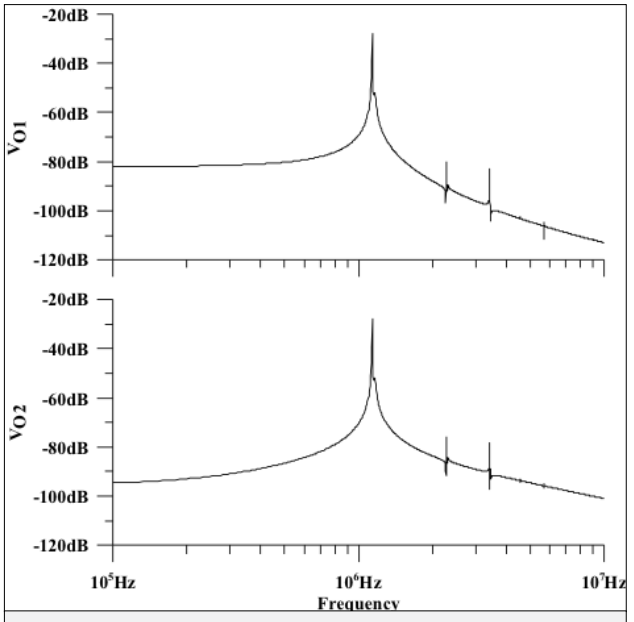

Figure 6. Frequency spectrums of outputs V_{O1} and V_{O2}

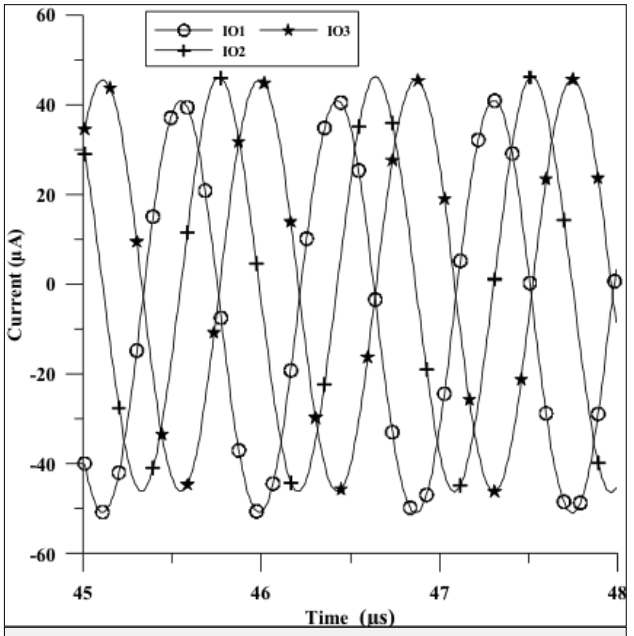

Figure 7. The steady-state waveforms for the quadrature currents I_{O1}, I_{O2}, and I_{O3}

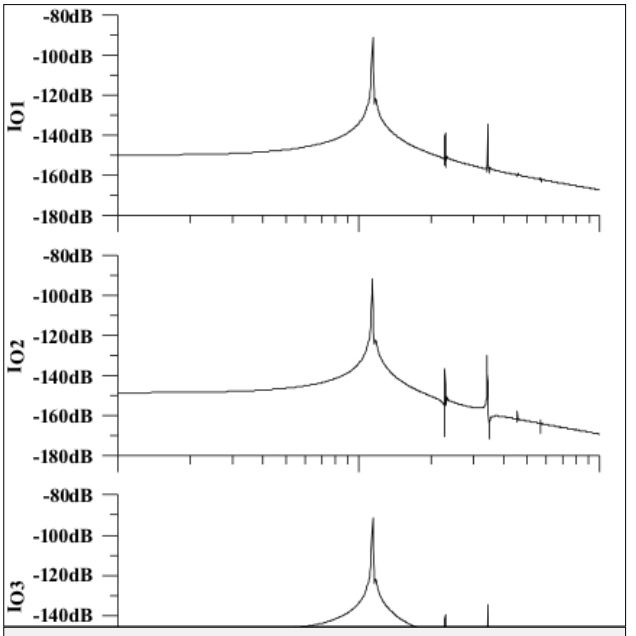

Figure 8. Frequency spectrums of outputs I_{O1}, I_{O2}, and I_{O3}

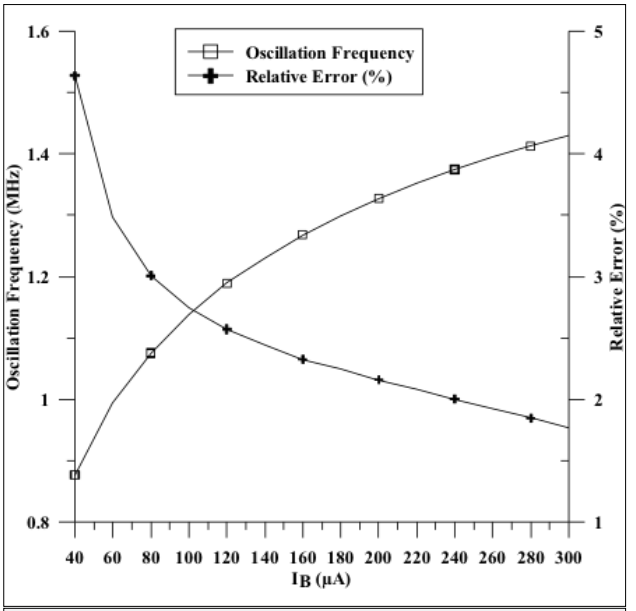

Figure 9. Variations of oscillation frequency and relative error via IB biasing current

oscillator output currents. As it is seen from Figure 8, second harmonic rejection ratios of current outputs, I_{O1}, $I_{O2,}$ and I_{O3} are around 47.4dB, 45dB, and 48.5dB, respectively. The total harmonic distortion (THD) is 0.33% for voltage output V_{O1}, 0.52% for voltage output V_{O2}, 0.87% for current output I_{O1}, 1.4% for current output I_{O2} and 0.84% for current output I_{O3}.

In order to change electronically oscillation frequency, transconductance value (g_{m1}) of first VDBA element is tuned by the means of I_B biasing current. Variation of between oscillation frequency and I_B biasing current is given in Figure9. Moreover, the definition of percentage relative error can be described by the following equation;

$$\%\,Relative\ Error = 100\frac{f_{Theoretical} - f_{Simulation}}{f_{Theoretial}} \quad (12)$$

Variation of between I_B biasing current and percentage relative error value is also depicted in Figure9. It can be observed from Figure 9 that percentage relative error is decreased with increasing biasing current (I_B).

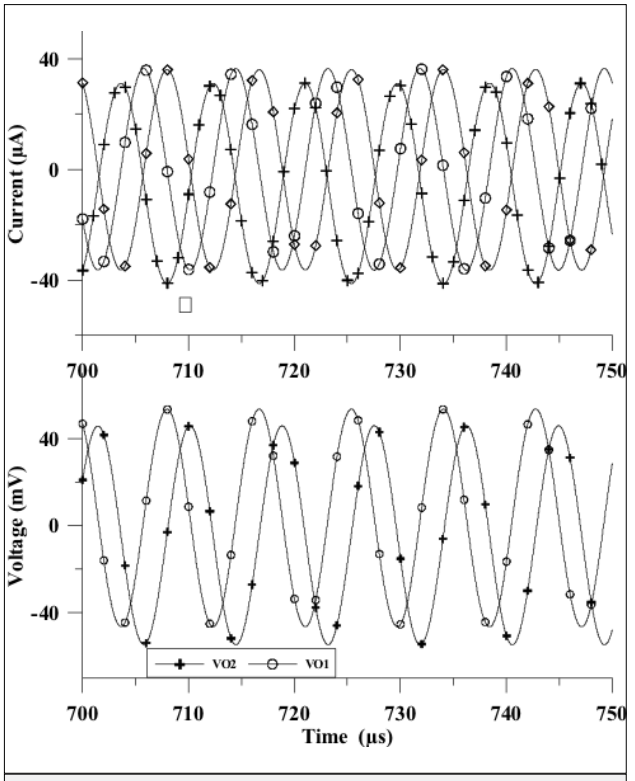

Figure 10. The steady-state waveforms for voltage and current outputs

So as to survey the performance of the proposed quadrature oscillator at low frequencies, external capacitances values are chosen as 1nF to obtain frequency oscillation of f_0=114 kHz. The steady-state waveforms for voltage and current outputs are depicted in Figure 10. THDs of voltage outputs (V_{O1} and V_{O2}) are calculated as 0.23% and 0.35%, respectively, whereas THDs of current outputs (I_{O1}, I_{O2}, and I_{O3}) are calculated as 0.58%, 0.89%, and 0.56%, respectively.

The behaviors of the CMOS implementation of VDBA in Figure 4 with respect to capacitors and resistor have been appreciated with the help of statistical analysis results by using the well-known Monte Carlo analysis. Monte Carlo simulation is carried out one hundred times for proposed oscillator circuit in Figure 2. The Monte Carlo analyses having 5% Gauss deviation of capacitors and 1% Gauss deviation of the resistor are obtained as in Figure 11 where FO and THD of V_{O1} variations of the proposed oscillator circuit in Figure 2 are given.

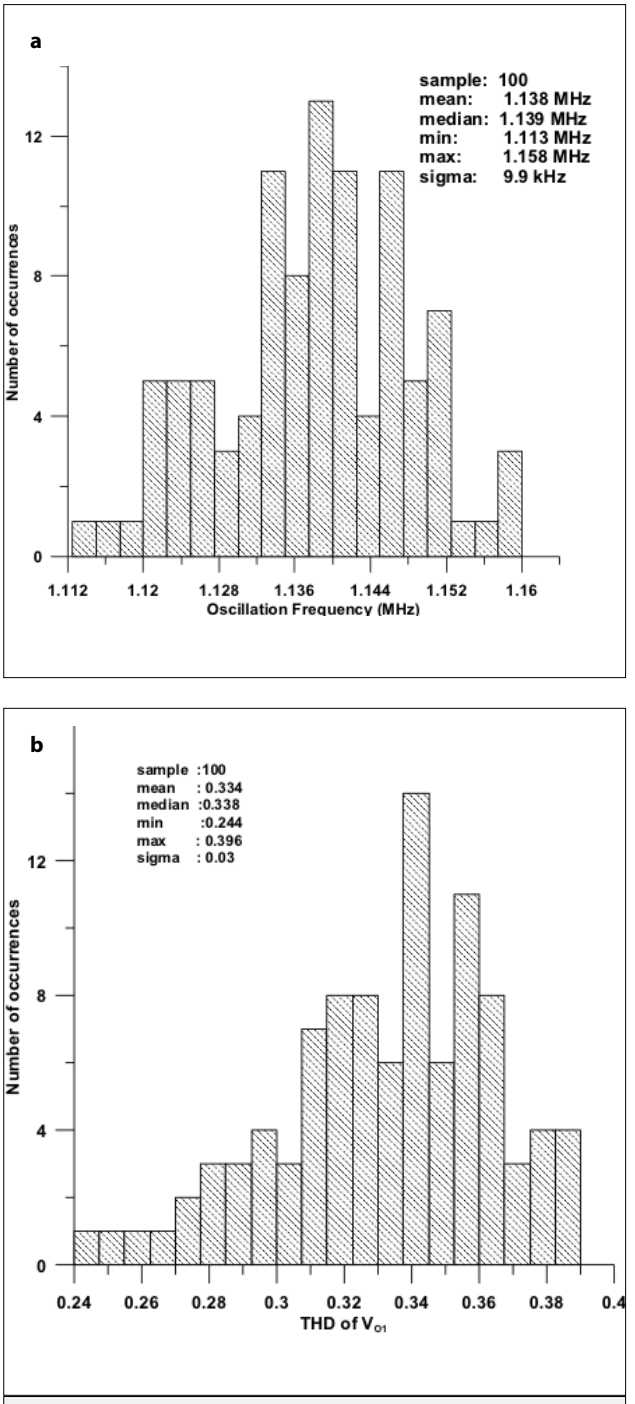

Figure 11. The histograms of (a) FO and (b) THD of VO1 distribution of the proposed oscillator circuit (100 times Monte Carlo Simulation)

Conclusions

New electronically tunable quadrature oscillator having a minimum number of active and passive elements is presented. It based on VDBA exhibits two voltage outputs and three current outputs. The influence of non-ideal effects of the VDBAs on the oscillator functionality has been investigated. Furthermore, the behaviors of the CMOS implementation of VDBA in Figure 4 with respect to passive elements have been evaluated and variation of between oscillation frequency and biasing current has also been given. It is easily observed simulation results that the proposed circuit enjoys low THD, feasibility of circuit and adjustment in a wide range.

References

1. A. S. Sedra, K. C. Smith, "Second-generation current conveyor and its applications," *IEEE Trans Circuit Theory,* vol. 17, pp. 132-134, 1970. [CrossRef]
2. C. Toumazou, F. J. Lidgey, D. G. Haigh, "Analogue IC design: The current mode approach," *IEE circuits and systems,* Peter Peregrinus, 1990.
3. E. A. Sobhy, A. M. Soliman, "Novel CMOS realizations of the inverting second-generation current conveyor and applications," *Analog Integrated Circuits and Signal Processing,* vol. 52, pp. 57-64, 2007. [CrossRef]
4. F. Khateb, N. Khatib, D. Kubanek, "Low-voltage ultra-low-power current conveyor based on quasi-floating gate transistors," *Radioengineering*, vol. 21 no. 2, pp. 725-735, 2012.
5. F. Yucel, E. Yuce "A new, single CCII-based, voltage-mode, first-order, all-pass filter and its quadrature oscillator application," *Scientia Iranica. Transaction D, Computer Science & Engineering, Electrical* vol. 22 no. 3, pp. 1068-1076, 2015.
6. J. W. Horng, H. Lee, J. Y. Wu "Electronically tunable third-order quadrature oscillator using CDTAs," *Radioengineering*, vol. 19 no. 2, pp. 326-330, 2010.
7. J. Jin, C. Wang, "CDTA-based electronically tunable current-mode quadrature oscillator," *International Journal of Electronics*, vol. 101, no. 8, pp. 1086-1095, 2014. [CrossRef]
8. J. Jin, C. Wang "Single CDTA-based current-mode quadrature oscillator," *AEU-International Journal of Electronics and Communications*, vol. 66, no. 11, pp. 933-936, 2012. [CrossRef]
9. W. Tangsrirat, D. Prasertsom, T. Piyatat, W. Surakampontorn, "Single-resistance-controlled quadrature oscillator using current differencing buffered amplifiers," *International Journal of Electronics,* vol. 95, no. 11, pp. 1119-1126, 2008. [CrossRef]
10. A.Ü. Keskin, "Voltage-mode high-Q band-pass filters and oscillators employing single CDBA and minimum number of components," *International Journal of Electronics*, vol. 92, no. 8, pp. 479-487, 2005. [CrossRef]
11. J.W. Horng "Quadrature oscillators using operational amplifiers," *Active and Passive Electronic Components*, (2011). [CrossRef]
12. W. Tangsrirat, W. Surakampontorn "Single-resistance-controlled quadrature oscillator and universal biquad filter using CFOAs," *AEU-International Journal of Electronics and Communications*, vol. 63, no. 12, pp. 1080-1086, 2009. [CrossRef]
13. A. Lahiri, W. Jaikla, M. Siripruchyanun, "First CFOA-based explicit-current-output quadrature sinusoidal oscillators using grounded capacitors," *International Journal of Electronics*, vol. 100, no. 2, pp. 259-273, 2013. [CrossRef]
14. A. M. Soliman, "Current feedback operational amplifier based oscillators," *Analog Integrated Circuits and Signal Processing*, vol. 23, no. 1, pp. 45-55, 2000. [CrossRef]
15. M. Kumngern, K. Dejhan, "DDCC-based quadrature oscillator with grounded capacitors and resistors," *Active and Passive Electronic Components*, (2009). [CrossRef]
16. A. Yesil, F. Kacar, K. Gurkan "Design and Experimental Evaluation of Quadrature Oscillator Employing Single FB-VDBA," *Journal of Electrical Engineering*, vol.67, no. 2, pp.137-142, 2016 [CrossRef]
17. U. E. Ayten, M. Sagbas, H. Sedef, "Electronically tunable sinusoidal oscillator circuit with current and voltage outputs," *International Journal of Electronics*, vol. 99, no. 8, pp. 1133-1144, 2012. [CrossRef]
18. B. Chaturvedi, J. Mohan, "Single active element based mixed-mode quadrature oscillator using grounded components," *IU-Journal of Electrical & Electronics Engineering*, vol. 15, no. 1, pp. 1897-1906, 2015.
19. D. R. Bhaskar, R. Senani, "New FTFN-based grounded-capacitor SRCO with explicit current-mode output and reduced number of resistors," *AEU-International Journal of Electronics and Communications*, vol. 59, no. 1, pp. 48-51, 2005.[CrossRef]
20. P. Kumar, R. Senani, "Improved grounded-capacitor SRCO using only a single PFTFN," *Analog Integrated Circuits and Signal Processing,* vol. 50, no. 2, pp. 147-149, 2007. [CrossRef]
21. U. Cam, A. Toker, O. Cicekoglu, H. Kuntman, "Current-mode high output impedance sinusoidal oscillator configuration employing single FTFN," *Analog Integrated Circuits and Signal Processing*, vol. 24, no. 3, pp. 231-238, 2000. [CrossRef]
22. F. Kacar, A. Yesil, A. Noori, "New CMOS realization of voltage differencing buffered amplifier and its biquad filter applications," *Radioengineering*, vol. 21, no. 1, pp. 333-339, 2012.

Abdullah Yeşil received his B.Sc., M.Sc. and Ph.D. degrees from İstanbul University, all in Electrical and Electronics Engineering 2009, 2011 and 2016. He is currently an assistant professor at Naval Architecture and Marine Engineering Department of Bandirma Onyedi Eylul University. His main research interests are active network synthesis, current-mode circuit design, low-noise implementation of continuous time filters, MOS-only filter design, electronic circuits for computer aided design and memristor.

Fırat Kaçar received his B.Sc., M.Sc. and Ph.D. degrees from İstanbul University, all in Electrical and Electronics Engineering 1998, 2001 and 2005. He is currently an professor at the Electrical and Electronics Engineering Department of İstanbul University. His current research interests include analog circuits, active filters, synthetic inductors, CMOS based circuits electronic device modeling and hot-carrier effect on MOS transistor.

İSTANBUL UNIVERSITY PRESS

RESEARCH ARTICLE

Electrica 2018; 18(1): 13-18

Recurrence Plot Analysis of Unsatured Polyester Samples Subjected to Contamination

Aysel Ersoy Yılmaz[1], Mehmet Murat İspirli[2]

[1]Department of Electrical and Electronics Engineering, İstanbul University School of Engineering, İstanbul, Turkey
[2]Department of Electrical and Electronics Engineering, Marmara University School of Technology, İstanbul, Turkey

Cite this article as: A. Ersoy Yılmaz, M. M. İspirli. "Recurrence Plot Analysis of Unsatured Polyester Samples Subjected to Contamination". *Electrica*, vol. 18, no. 1, pp. 13-18, 2018.

ABSTRACT

Polymer materials that are used in outdoor enviroments are exposed to humidity and polution. In addition, some insulation materials installed in water or embeded to slush containing serious pollutants for a long time. These conditions adversely affect the dielectric properties of insulating materials. In this study, the prepared unsaturated polyester (UPE) samples are stored in an ionized water solution for 8, 24, and 168 hours. This ionized water solution is considered to represent the polluted water in the outdoor environments. Further, the dielectric behaviors of the prepared polyester samples are investigated using the inclined plane test (IPT) method, whereas the leakage current data that are recorded during the experiment are analyzed using the recurrence plot (RP) method. The results of applying the inclined plane test on the unsaturated polyester samples depict that the lifetime of the samples decreased with an increase in the period of storage in the ionized water solution. Further, the results of the recurrence plot analysis reveal that the recurrence plot point density also depicted a decrease with an increase in the period of storage in the ionized water solution.

Keywords: Inclined plane test, surface tracking, recurrence plot analysis, tracking failure

Introduction

Today pollution is a key element which effects the quality of humans life and for electrical and electronics devices. Pollution can be gaseous, liquid or solid. Due to the increase of electrical device usage in every industrial sector the reliability and the continuity of the electric power systems gain importance. The intolerence to power outages force engineers to build more resistant materials against pollution and other enviromental factors. Pollution tests are become improtant and several test methods are introduced by several institutes such as IEC, VDE, ASTM, TSE, etc.

Polymers are widely used as insulating material in electrical systems due to their excellent dielectric properties [1-3]. Polymers are subjected to severe weather conditions such as rain, snow, storm, hail and environmental pollution under operating conditions [4]. Exposure of the material to a high electric field under these environmental conditions can cause the electrical insulation material to be degraded.

Progressive degradation of the surface of a solid insulating material by local discharges tend to form conducting or partially conducting paths [5]. Electrical tracking formed on the surface of polymeric materials is characterized by the formation of conductive paths [6]. The formation process of permanent conductive paths along the insulation surface under voltage stress is called tracking [7]. Due to pollution and humidity a conductive layer occurs on the surface of polymeric materials operating in the outdoor environment. When voltage is applied, leakage currents flow from this conductive layer. Heat is generated as a result of these flowing leakage currents. Along with the heat generated, a dry-band is formed on the insulation surface. The formation of the dry-band creates sparks which damage the insulation surface. Carbonization starts on the insulation surface due to these sparks. The resulting carbonization causes permanent discharges on the insulation surface. Due to permanent discharges, permanent

Address for Correspondence:
Mehmet Murat İspirli

E-mail:
mispirli@marmara.edu.tr

Received: 18.06.2017

Accepted: 30.12.2017

DOI: 10.5152/iujeee.2018.1803

conductive paths are formed on the insulation surface and these conductive paths spread with time. Finally, the insulation capability of surface between the electrodes completely is lost and breakdown initiated [8,9]. This phenomenon is known as electrical tracking failure.

Based on water absorption resistance polymeric materials can be classified into two class which are hydrophobicity or hydrophilicity. Hydrophobicity is one of the most useful properties of outdoor environment insulation materials [1]. If a material is hydrophobic, a conductive water layer does not form on the surface. Thus, surface discharges in the material are reduced. Energy loss is also reduced with reducing leakage currents flowing through the surface [1,10]. Unsaturated polyester (UPE) absorbs water in very small amounts to its structure. The amount of water absorbed to its structure are changed depends on the temperature and content of the water. In the study conducted by Dhakal et al., UPE samples were stored for 900 hours in water at room temperature and boiling water. As a result of this study, UPE samples absorbed about 0.5% water at room temperature and about 2% water at boiling water [11]. In a study conducted by Huang et al., samples are prepared using glass fiber fabric and unsaturated polyester absorbed about 1.5% of water after 21 days [12].

In this study, unsaturated polyester samples which are hydrophilic were stored in the electrolyte solution for 0, 8, 24, 168 hours respectively. These solution-waited samples were tested according to the IEC 587 Inclined Plane Test (IPT) method. After the tests, weight loss in the samples were measured. The recorded leakage current data was evaluated by the recurrence plot (RP) method, which is frequently used in the analysis of nonlinear time series. Using these results, the change of the dielectric properties of the polyester samples with storage time in the electrolyte solution were examined.

Material and Method

There are different test standards issued by IEC (International Electrotechnical Commission) and ASTM (American Society for Testing and Materials) organizations to evaluate electrical tracking resistance of polymer samples. In this study, Inclined Plane Test method determined by these organizations was used. IEC 60587 and ASTM D2303 are test method standards set by IEC and ASTM organizations, respectively. This test method was first published in 1964 as ASTM D2303 [13]. Then test method was later accepted by IEC and published in 1977 as IEC 60587 [14]. The test standard was last revised by IEC and ASTM organizations in 2007 and 2013, respectively [5,16]. Despite the small differences between these two test standards, they are based on the same theory. A schematic representation of the experimental setup based on these standards is shown in Figure 1. 4 kV AC voltage was applied to the samples. A resistance of 33 kΩ was connected in series to the test sample. The flow rate of the electrolytic liquid from the surface was set at 36 ml/h.

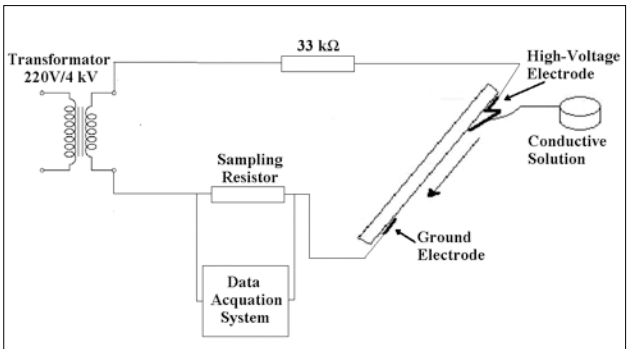

Figure 1. Schematic of experimental setup

According to the IEC and ASTM test standarts by the following conditions satisfied in the inclined plane test, tracking failure is occured [5,16];

- The value of the leakage current flowing from the sample surface is over 60mA for 2 s.
- The track length on the sample surface is 25 mm or more from the ground electrode
- Erosion on the sample surface [5,16].

All the samples used in this study were prepared by using 0.25% methyl-ethyl-ketone-peroxide (MEKP) and 0.25% accelerator (cobalt) by weight in polyester resin under the same laboratory conditions. Test samples were molded in dimensions of 120x50x9 mm.

Recurrence Plot Analysis

The recurrence plot method is an advanced nonlinear data analysis method. This method was presented in 1981 by Maizel and Lenk as a method of visual model analysis of a series of genetic nucleotides [17,18]. Fundamental structures of the recurrence plot analysis were developed by Eckman et al. [19]. Recurrence plot is a representation of the recurred behavior of the values of the m-dimensional phase space in the two-dimensional phase space. Both axis on the recurrence plots are time. Recurrence plots are a practical way of processing data since it is a graphical framework for extracting information from the time series. [17,20]. Leakage currents are chaotic signals. For this reason, the application of the recurrence plot technique is very useful for analyzing the leakage currents [17,21].

Dynamic systems with non-linear characteristics can be sampled using method in [17,22]. Recurrence plot method has the advantage of giving accurate results even for very short and unstable data [17,23]. According to Takens' embedding theorem, the time series is appropriately reconstructed as follows [17,24].

$$X_{(i)} = [x(i), x(i+\tau), \ldots, x(i+(m-1)\tau)], i = 1,2,3.. \quad (1)$$

Where;
$X_{(i)}$: Embedding Vector,
m : Embedding Dimension,
τ : Delay Time,
x(i) : Time series.

In this study, x(i) time series are defined as the leakage current data recorded from the system. Defining a function obtained from a time series in a dynamic characteristic as recurrence plot series is as follows.

$$R_{i,j} = H(\varepsilon - \left\| X_{(i)} - X_{(j)} \right\|_2), X_{(i)}, X_{(j)} \in R^m, i, j \in (1, M) \quad (2)$$

Where;
ε : Threshold value ,
||.||: Euclidean, maximum or manhattan norm,
H(x): Heaviside function
M: Number of $X_{(i)}$

Threshold value selection is very important when analyzing with the recurrence plot technique. The standard deviation of the time series is used when the threshold value (ε) is determined. If the threshold value is chosen extreme, irrelevant points will appear on the plot. If the threshold value is chosen too small, it will cause to loss of some data that might give the right result [17,25]. Selected threshold value and the values of the data in the embedding vector are processed in the Heaviside unit step function. As a result of this operation, the elements with value 1 are drawn with black in the recurrence plot, while those in value 0 are drawn with white.

Results

Prepared UPE samples in laboratory conditions were aged by waited in solution containing 0.1% NH_4Cl and 0.2% Triton X-100. While this aging was conducted, 3 groups of samples were waited in this solution for 8, 24 and 168 hours, respectively. Additionally alternative sample group under the same conditions was prepared without waiting session. 3 sample groups are exposed to aging process and a sample group was not exposed to aging process which were evaluated for surface tracking performance with the proposed experimental setup.

Surface Tracking Results

The samples aged in the solution were removed from the solution and dried. After drying, weights of the samples were measured with an analytical balance having a sensitivity of 0.1 mg. With this weights, the samples were compared with their weight prior to being stored in solution. Weight gains in the samples are given as a percentage in Figure-2. By the computational approach, the average of each sample group is taken within their scopes. UPE samples absorbed water 0.011%, 0.017% and 0.089% of their mass in solution at 8, 24 and 168 hours respectively. The water absorption rate of the UPE is decreased with the increased waiting time in the solution. Due to the saturation rate of the sample increases with time.

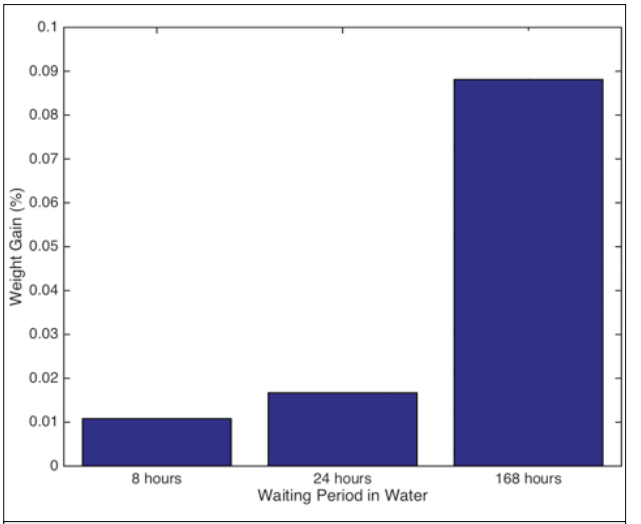

Figure 2. Weight gain of samples according to waiting time in solution

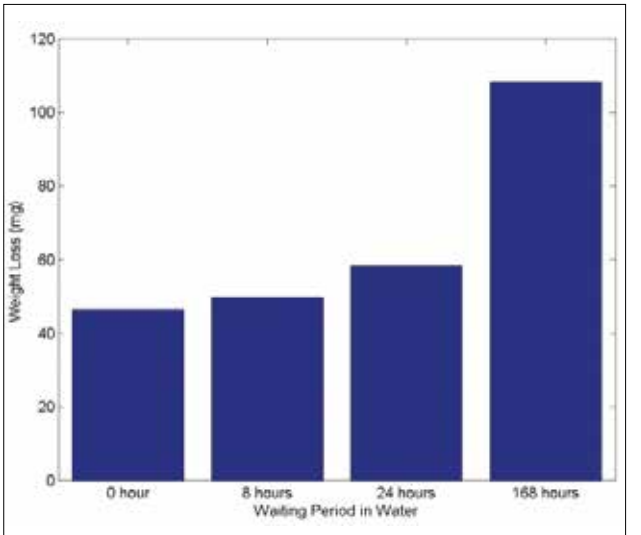

Figure 3. Weight loss of samples according to waiting time in solution

Before the test, sample weight was taken with a digital scale. Then the samples were tested on the prepared experimental setup according to IEC 587 standard. After each test, residues of carbon tracks formed on the sample surface were cleaned. Finally the sample weight was measured again. Averages of weight loss within each sample group were taken. The weight losses occurring in the sample groups according to the waiting times in the solution are given in Figure 3. Weight loss occurred in the samples waited for 8 hours in solution was about 7.5% higher than samples that were not waited. Weight loss of the sample that was waited for 24 hours in solution was about 25% higher than the sample that was not waited. Weight loss of the sample waited in the solution for 1 week (168 hours) is 2.3 times the weight loss of the sample that was not waited.

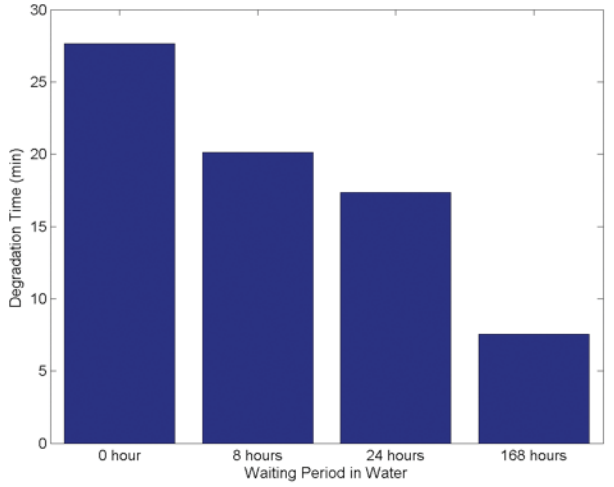

Figure 4. Degradation Time of samples according to waiting time in solution

In each test group the degradation time of samples were noted. When this procedure was carried out, the average of the degradation times of each test group is noted along with weight loss. The degradation time of the sample groups according to the waiting times in the solution are given in Figure 4. According to test results, the degradation time of the sample group that was waited for 8 hours in solution decreased by about 27% compared to the sample group that was not waited. The degradation time of sample groups waited in solution for 24 hours and 1 week (168 hours) decreased by 37% and 72.5%, respectively, when compared to the sample group that was not waited.

The tracking formed on the surface of the samples as a result of the experiments based on the ASTM D2303 standard are shown in Figure 5.

Recurrence Plot Results

For the recurrence plot analyze the leakage current flowing from the sample surface was recorded by Analog/Digital conversion device. The recorded data was analyze using the recurrence plot method. The relationship of leakage current data and waiting time of samples in solution was analyzed by this method. The last 3 seconds of the test procedure before the degradation of the sample was investigated by this analysis. The power frequency components have been filtered when the recurrence plot analysis is done. Fourier transform is used for eliminated 50 Hz Components (48-52 Hz). In this analysis, embedding dimensiın (m) is 3, delay time (τ) is 8 and threshold is 0.3·σ. σ is standart deviation of time series. Figure 6 shows the recurrence plots of samples from all sample groups. When the RP of the sample unwaited in the solution given in Figure 6a is compared with the RP of the sample waited in the solution for 8 hours in Figure 6b, it is seen that the black point density is more intense in the sample that was not waited. In other words, the density of the white space is higher in the RP belonging to

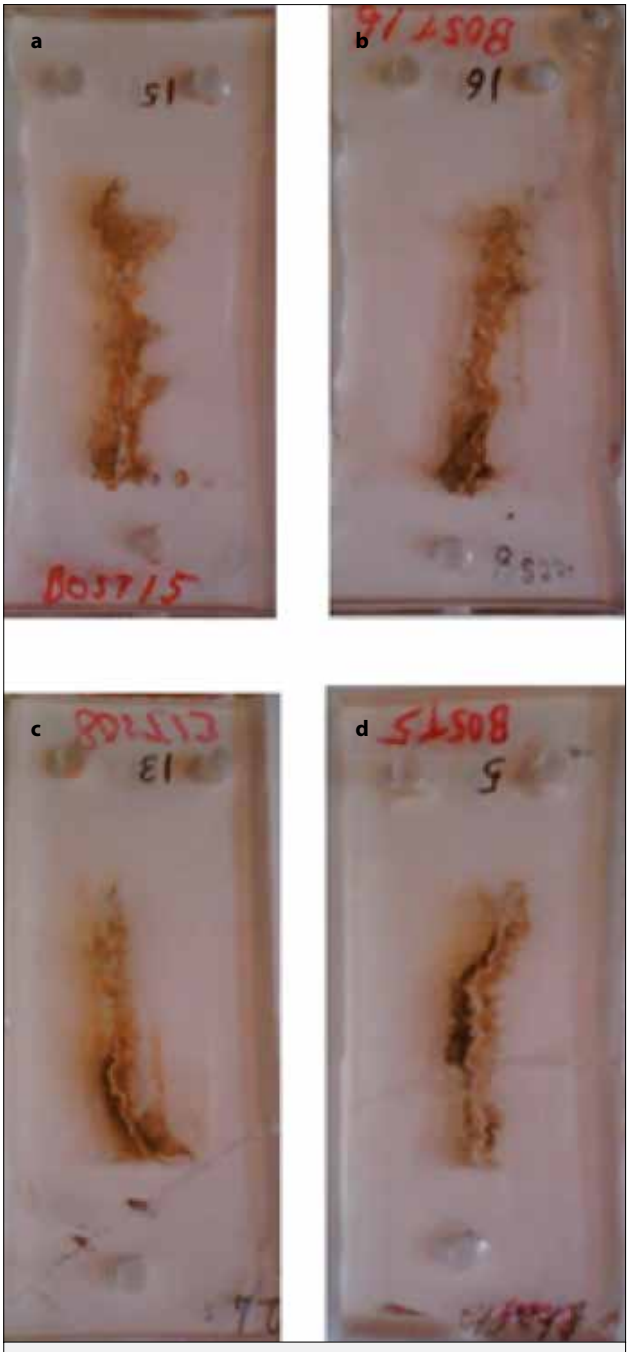

Figure 5. a-d. Observed tracking on UPE samples a) unwaited b) waited for 8 hours c) waited for 24 hours d) waited for 168 hours

the sample waited in the solution for 8 hours. Likewise, when the RP of the sample waited in the solution for 8 hours in Figure 6b is compared to the RP of the sample waited in the solution for 24 hours in Figure 6c, the black point density in the RP of the sample waited in the solution for 24 hours is less. When the RPs of all the samples were compared that were unwaited in the solution and waited in the solution for 8, 24, and 168 hours, the black point density was the maximum on the sample that was unwaited and it was the minimum on the sample that was

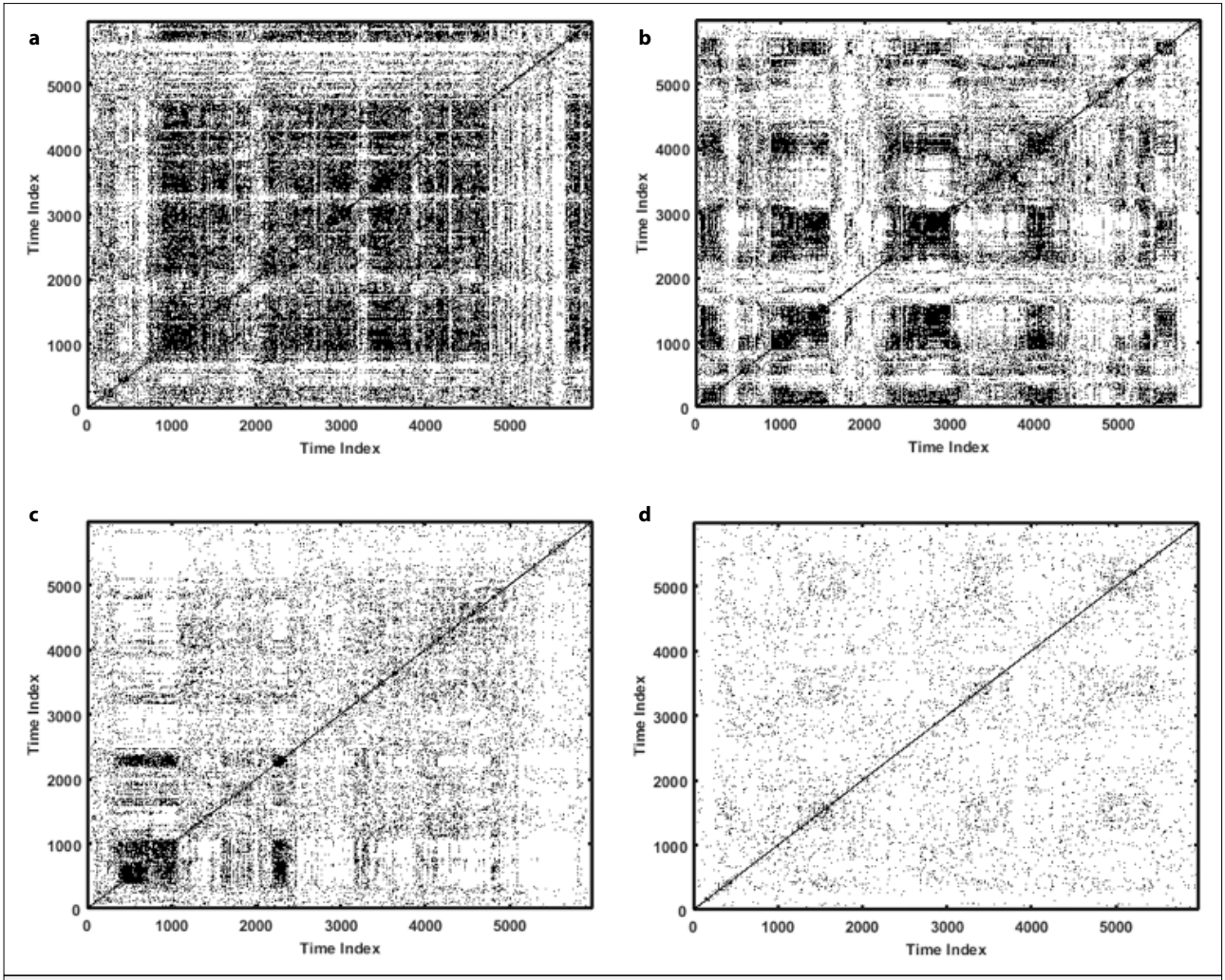

Figure 6. a-d. Recurrence Plots (a) unwaited (b) waited for 8 hours (c) waited for 24 hours (d) waited for 168 hour

waited in the solution for 168 hours. Namely, the density of the white space is the highest in the RP of the sample, which was waited in solution for 168 hours and shown in Figure 6d.

Conclusions

In this study, unsatureted polyester samples prepared under laboratory conditions were tested according to Inclined Plane Test method. As a result of the tests, weight loss in the samples were measured. The recorded leakage current data from the sample surface during the tests was analyzed by the recurrence plot method. As a result of these information;

1. Weight loss in the samples increased with increasing the waiting time of the samples in the solution
2. The degradation times of the samples were shortened with increasing the waiting time of the samples in the solution,
3. By increasing the waiting time of the samples in the solution, RP Point Density was decreased, White Space was increased. Thus, by increasing the waiting time of the samples in the water, the amplitude of the leakage currents flowing through the sample surface was increased.
4. The increase in the waiting time of the samples in the solution adversely affected the dielectric performance of the samples.

When all these results are evaluated, resistance to tracking of UPE is inversely proportional with waiting time in solution. Precautions like coating to prevent water absorption must be taken when unsaturated polyester materials used under wet and dirty conditions.

References

1. J. P Reynders, I. R. Jandrell, S. M. Reynders, "Review of aging and recovery of silicone rubber insulation for outdoor use," IEEE Transactions on Dielectrics and Electrical Insulation, vo. 6, no. 5, pp. 620-631, 1999. [CrossRef]
2. R. S. Gorur , E. A. Cherney, R. Hackam, T. Orbeck, "The electrical performance of polymeric insulating materials under accelerated

aging in a fog chamber," IEEE Transactions on Power Delivery, vol. 3, no. 3, pp. 1157-1164, 1988. [CrossRef]
3. R. G. Houlgate, D. A. Swift, A. Cimador, F. Purbaix, G. Marrone, P. Nicolini, "Field Experience and Laboratory Research on Composite Insulators for Overhead Lines," CIGRE 1986.
4. W. T. Shugg, and K.N. Mathes, "Handbook of electrical and electronic insulating materials", Vol. 995, IEEE press, New York, 1995.
5. Electrical insulating materials used under severe ambient conditions - Test methods for evaluating resistance to tracking and erosion, IEC 60587:2007 International Standard, 3rd ed., 2007.
6. R. F. Da Silva and S. V. Filho, "Analysis of electrical tracking by energy absorption during surface discharge in polymeric materials," IEEE Transactions on Dielectrics and Electrical Insulation, vol. 23, no. 1, pp. 501-506, 2016. [CrossRef]
7. K. Y. Lau and M.A.M Piah, "Polymer nanocomposites in high voltage electrical insulation perspective: a review," Malaysian Polymer Journal, vol. 6, no. 1, pp. 58-69, 2011.
8. L. Zhang, "Electrical Tracking Over Solid Insulating Materials for Aerospace Applications," Ph.D. Thesis, Diss. University of Manchester, 2011.
9. A. Mazen, A. Hussein, E. Ahdab, R. Roshdy, "High-Voltage Engineering: Theory and Practice, Revised and Expanded". Marcel Dekker Inc, New York, 2000.
10. H. Janssen, "The loss and recovery of hydrophobicity on silicone rubber surfaces." 10th International Symposium on High Voltage Engineering, Montreal, Canada. 1997.
11. H. N. Dhakal, Z.Y. Zhang, M.O.W. Richardson, "Effect of water absorption on the mechanical properties of hemp fibre reinforced unsaturated polyester composites," Composites Science and Technology, vol. 67, no. 7, pp. 1674-1683, 2007. [CrossRef]
12. G. Huang, H. SUN, 1Effect of water absorption on the mechanical properties of glass/polyester composites", Materials & design, vol. 28, no. 5, pp. 1647-1650, 2007. [CrossRef]
13. G. R. Mitchell, "Present Status of ASTM Tracking Test Methods," Journal of Testing and Evaluation vol. 2, no.1, pp. 23-31, 1974. [CrossRef]
14. Test method for evaluating resistance to tracking and erosion of electrical insulating materials used under severe ambient conditions, IEC 60587:1977 International Standard, 1st ed., 1977.
15. M. S. Naidu, V Kamraju, "High voltage engineering," Tata McGraw-Hill Education, New Delhi, India, 2013.
16. ASTM D2303-13, Standard Test Methods for Liquid-Contaminant, Inclined-Plane Tracking and Erosion of Insulating Materials, ASTM International, West Conshohocken, PA, 2013, www.astm.org.
17. M.M. İspirli and A. Ersoy Yılmaz, "Tracking failure and recurrence plot analysis for three different levels in the discharge on epoxy resin," Electrical, Electronics and Biomedical Engineering (ELECO), National Conference on. IEEE. pp. 349-353, 2016.
18. J.V. Maizel and P.L. Robert, "Enhanced graphic matrix analysis of nucleic acid and protein sequences," Proceedings of the National Academy of Sciences, vol. 78, no. 12, pp. 7665-7669, 1981. [CrossRef]
19. J-P. Eckmann, S. O. Kamphorst, D. Ruelle. "Recurrence plots of dynamical systems," EPL (Europhysics Letters), vol. 4 no. 9, pp. 973-977, 1987. [CrossRef]
20. Y. Liu and B. X. Du. "Recurrent plot analysis of leakage current on flashover performance of rime-iced composite insulator," IEEE Transactions on Dielectrics and Electrical Insulation, vol. 17, no.2, pp. 465-472, 2010. [CrossRef]
21. A. Wolf, J.B. Swift, H.L. Swinney, J.A. Vastanox, "Determining Lyapunov exponents from a time series," Physica D: Nonlinear Phenomena, vol. 16, no. 3, pp. 285-317, 1985. [CrossRef]
22. B. X. Du, Y. Gao, Y. Liu. "Effects of Gamma-Ray Irradiation on Tracking Failure of Polymer Insulating Materials." Nuclear Power-operation, safety and enviroment, Dr. Pavel Tsvetkov (Ed.), In Tech, 2011, DOI: 10.5772/17263 [CrossRef]
23. N. Marwan, M.C. Romano, M. Thiel, J. Kurths, "Recurrence plots for the analysis of complex systems," Physics Reports, vol. 438, no. 5, pp. 237-329, 2007. [CrossRef]
24. F. Takens, "Detecting strange attractors in turbulence", In Dynamical systems and turbulence, Warwick 1980 (pp. 366-381). Springer Berlin Heidelberg, 1981. [CrossRef]
25. B. X. Du, Y.G. Guo, Y. Liu, L Tian, "Effects of adding nanofiller on DC tracking failure of epoxy/MgO nano-composites under contaminated conditions," IEEE Transactions on Dielectrics and Electrical Insulation, vol. 21, no. 5, pp. 2146-2155, 2014. [CrossRef]

Aysel Ersoy Yılmaz was born in Eskişehir. She received her M.Sc. and Ph.D. degrees in Electrical and Electronics Engineering from İstanbul University in 2003 and 2007, respectively. She studied as a post doctorate researcher at Kettering University in USA between 2008 and 2009. Currently she is working as Assistant Professor in Electrical - Electronics Engineering Department of İstanbul University. Her research interests are high voltage techniques, dielectric materials and renewable energy applications.

Mehmet Murat İspirli was born in Çorum on May 14, 1991. He received his B.Sc. degrees in Electrical and Electronics Engineering from İstanbul University in 2015. He is an M.Sc. student at İstanbul University at Electrical-Electronics Engineering Department. Currently, he is working as Research Assistant in Electrical - Electronics Engineering Department of Marmara University. His research interests are high voltage technique, high voltage insulation materials, discharge phenomena, numerical analysis of electrostatic fields, protection against overvoltages and renewable energy materials.

İSTANBUL UNIVERSITY PRESS

RESEARCH ARTICLE

Electrica 2018; 18(1): 19-25

A Highly Linear Wide-Band Tunable Lna for Military Radio Applications

Hakan Doğan

Department of Electrical and Electronics Engineering, İstanbul Medipol University School of Engineering and Natural Sciences, İstanbul, Turkey

Cite this article as: Doğan. "A Highly Linear Wide-Band Tunable Lna for Military Radio Applications". *Electrica*, vol. 18, no. 1, pp. 19-25 , 2018.

ABSTRACT

A wide-band tunable Low-Noise Amplifier (LNA) was designed to be used in military radios. The LNA works in the frequency range of 30–512 MHz where military walkie-talkies operate. To cover the wide range of operating frequencies, the output of amplifier is divided into four sub-bands with four separate external inductors and integrated capacitor arrays. The first part of the study analyzes the performance parameters such as the gain, tuning, matching, noise figure, and distortion. Layout of the design was completed, and post-layout simulations, including the layout parasitic effects, were run to quantify the performance. The LNA achieves a minimum of 12-dB gain across the entire operating frequency range. The minimum rejections achieved by the LNA at 10% and 20% offset from the center-tuned frequency were 7 dB and 13 dB, respectively. The LNA achieves a worst-case noise figure of 4.6 dB, and the impedance-match parameter (S11) is better than –20 dB under all the conditions. The worst cases P1dB (1-dB Compression Point) and IIP3 (3rd Order Input Intercept Point) were 9.1 dBm and 18 dBm, respectively, across frequency and process–voltage–temperature corners. The design dissipates 20 mA from a 3.3-V power supply and uses a 1.5-V power supply for capacitor array termination.

Keywords: Tunable LNA, military radio, wide-band LNA, cascode amplifier, IIP3

Introduction

Professional personal and military radios that are used for tactical communication between various vehicles, military units and combatants have been around since before the World War I. There has been a steady improvement on the technology ever since. Until recently, these radios have mostly been used for simple voice communication across vast distances. With the developments in wireless technologies, these radios also incorporated video and other data links in addition to audio communications. All these advancements result in more rigorous specifications for the design of these radios, ranging from higher sensitivity requirements to greater resilience to blockers.

The usage scenarios for such equipment place various system requirements on the designer. Professional and military radios usually have multiple types, ranging from hand-held walkie-talkies to vehicle radios. While hand-held units have output power in the 30+dBm range, vehicle units can output as high as 45+dBm. This becomes a major concern when a hand-held unit is nearby a vehicle unit, since the high power transmitted by the vehicle unit will act as a blocker and de-sensitize the hand-held unit carried by the personnel. The signal power reaching the Low Noise Amplifier (LNA) input in this scenario can be as high as -10dBm. This requires careful filtering of the undesired signals by the receiver in order not to degrade performance. Since these wide-band systems have very high ratio between the highest channel frequency (512MHz for this design) and lowest channel frequency (30MHz), it becomes very cumbersome to design a tunable filter that can tune in the whole range. Owing to the very low bottommost channel frequency, integration of such filters is extremely burdensome due to large component values. As a result, these types of high performance radios are designed and built using discrete filters and amplifiers.

Since each of these filters and amplifiers can only cover limited number of frequency bands, multiple of these are used in parallel and switched in and out of operation depending on the operation band. Having large number of discrete components to design a system increases the complexity of a viable solution. Moreover, volume and power dissipation of the system, which are critical metrics, especially

Address for Correspondence:
Hakan Doğan

E-mail:
hdogan@medipol.edu.tr

Received: 09.06.2017

Accepted: 21.11.2017

DOI: 10.5152/iujeee.2018.1804

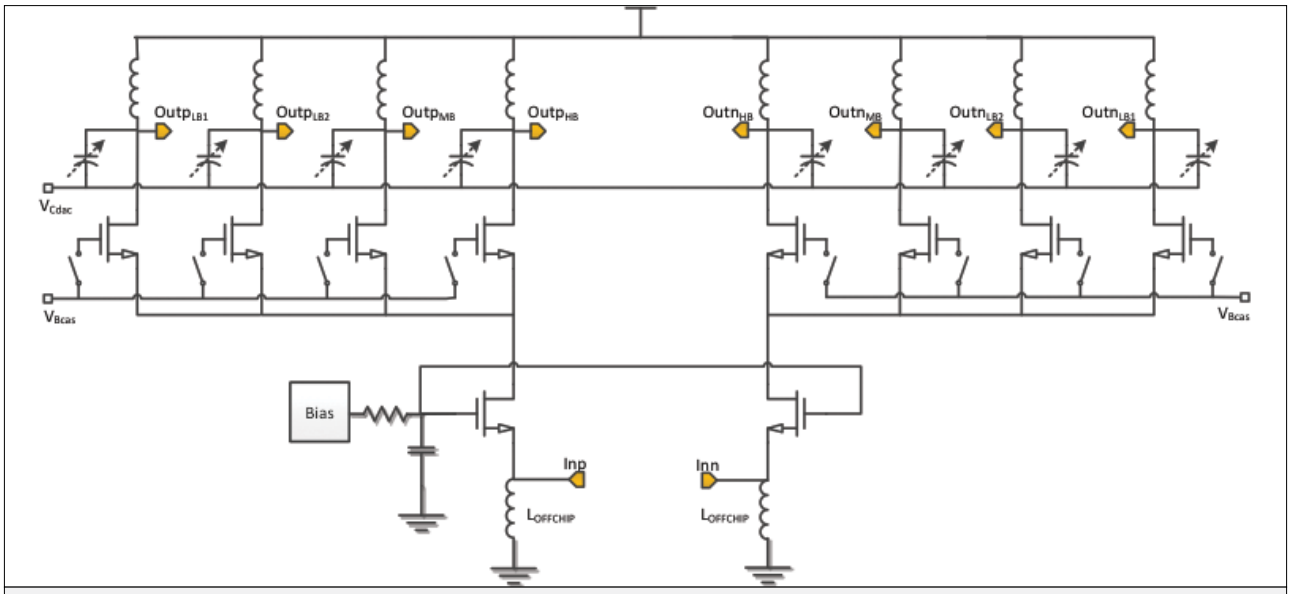

Figure 1. Transistor level schematic for the tunable wide-band LNA

for mobile military units, increase accordingly. This necessitates a drive towards higher integration to reduce size and power.

Although there are not many examples of amplifiers for such applications in the literature, various wide-band amplifiers exist that are aimed for Cable TV systems that works in the frequency range of 50-850MHz [1-3]. These amplifiers use standard design approaches with high power dissipation for linearity. Other solutions utilize feedback to linearize the wide-band amplifiers for better linearity [3-5]. Other solutions utilize noise cancellation to reduce noise in wide-band amplifiers [6].

In this work, we designed a tunable wide-band LNA that is suitable for use in professional civil and military radios. In order to meet the sensitivity goal of -120dBm for a 25KHz voice channel in the system it will be used, Noise Figure (NF) of the amplifier needs to be less than 5dB for a quadrature receiver with 8dB minimum SNR (Signal-to-Noise Ratio). Minimum gain of the amplifier will be limited to around 12dB at the center frequency and consequently blocker power will be kept near constant by rejecting the signal at 20% offset by around 12dB. In order for the system not to saturate with -10dBm blocker at 20% offset frequency and resolve -120dBm channels, the amplifier needs to have a 1dB compression point in access of 0dBm. Accordingly, while the desired signal at the output is amplified, the blocker power will be constant. Same LNA can be cascaded various times to realize a distributed type receiver where the blocker is kept at a level that doesn't overload the circuitry. Owing to relatively low top channel frequency of 512MHz, the design was realized using a well-established technology of 180nm CMOS from United Manufacturing Corporation (UMC). Metal-Insulator-Metal (MIM) capacitors were used due to their lower parasitic bottom plate capacitance which becomes extremely important when tuning in a wide range [7].

The organization of this paper is as follows. Part II gives design analysis and equations. Part III shows the simulation results and gives performance metrics for the design. Part IV summarizes work and gives conclusion remarks.

Design Analysis

The tough requirements for distortion performance of the LNA necessitates the employment of all the possible design methodologies to reduce distortion. The foremost is to use a differential approach to nullify the second order harmonic and intermodulation distortion terms since in such wide band systems, second order terms fall in band for most of the input channels. The only second order distortion terms generated in differential design is due to mismatch between the differential signal paths, which can be minimized with careful layout and calibration.

A differential cascode amplifier with the output divided into four sub-bands with four cascode branches is designed. The four outputs are connected back to a single node for the next stage input via a switch network and AC coupling capacitors. The top level schematic and the multiplexing network at the output of the design is given in Figure 1, 2 respectively and the subsections below discusses the design metrics.

Input Impedance Matching

In order to prevent reflections and maximize the power transfer from the antenna to the input of the amplifier, it needs to match to 50Ω differentially. Wide-band operation frequency of the amplifier limits the types of input topologies that can be used. Feedback has been used to achieve wide-band matching in some prior art [3-5], however this increases the complexity of the design, stability across frequency needs to be ensured and Noise Figure increases due to the feedback network. Additionally, feedback

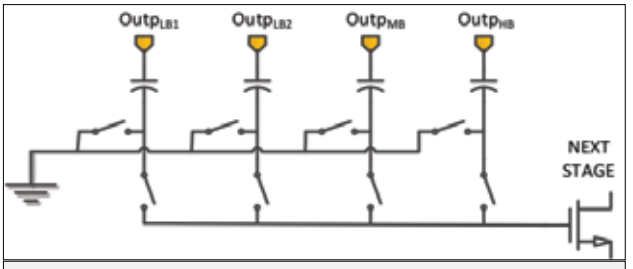

Figure 2. Output multiplexing network

creates a direct path from output to the input, which causes Local-Oscillator (LO) leakage into the antenna to increase. In order to mitigate these issues, a common gate amplifier is used to ensure matching in the whole frequency range.

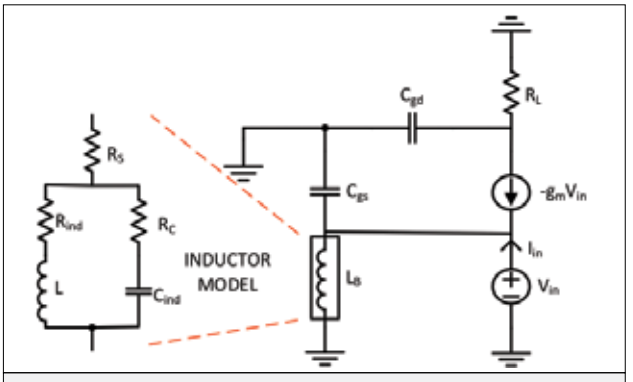

Figure 3. Small signal schematic of a common gate amplifier with off-chip inductor model

Figure 3 shows the single-ended input small signal network for the amplifier. This model can be used to calculate the input impedance equation using Kirchoff's Current Law (KCL) at the input node. The inductor used is an off-chip inductor selected from the Coilcraft products [8]. The main purpose of this inductor is to create a very low resistance bias path for the amplifier so that the transistors can be biased. This inductor is chosen to give a much higher impedance in the frequency range of 30-512MHz compared 25 ohms single-ended so that the input signal flows into the input devices rather than into the inductor. The inductance value chosen is around 780nH, which corresponds to an impedance value of j170Ω. Self-resonant frequency of the inductor is close to 600MHz, which is beyond the input frequency range of our system.

Inductor model given in Figure 3 is used to simulate the amplifier. However, for deriving the input impedance equation, only R_{ind} and C_{ind}, which are the dominant components are used for the sake of simplicity. Writing KCL equations, input impedance can be found to be:

$$R_{in} = \frac{V_{in}}{I_{in}} = \frac{1}{g_m + s(C_{gs}+C_{ind}) + 1/(R_{ind}+sL)} \quad (1)$$

where g_m, C_{gs} and C_{gd} are the transconductance, gate-source capacitance and gate-drain capacitance for the transistor. R_L represents the resistance seen at the drain of the input device.

For the design values of the C_{gs}, C_{ind}, R_{ind} and L, equation (1) approximates to $1/g_m$ in the frequency range of interest. This enables the designer to set the g_m value equal to 40mS for a near perfect matching at the input.

Gain and Output Tuning

As mentioned above, the very high dynamic-range requirements of these receivers require adequate filtering of the undesired signals. Employing larger order filters increases the selectivity of the amplifier at the cost of increased complexity, power and cost. Furthermore, resistive and capacitive parasitics in the circuit places a theoretical limit to the selectivity that can be achieved with a single amplifier. Because of these reasons, a simple tunable inductor-capacitor (LC) network is employed at the output of the amplifier to achieve at least 10dB rejection at 20% offset frequency from the received channel. The center frequency of a parallel LC tank circuit is given by [9,10]:

$$\omega_s = \frac{1}{\sqrt{LC}} \quad (2)$$

Equation (2) shows that in order to tune the output center frequency from 30MHz to 512MHz with a given inductor value, the capacitor value needs to change $(\omega_2/\omega_1)^2 = (512/30)^2$ times. This ratio is equal to 291, hence it is not possible to tune capacitors or varactors in such a wide range. Therefore, the output of the design is divided into 4 sub-bands in order to reduce the tuning range of the output capacitors. The four sub-bands that are used in the design are 30-50MHz, 50-100MHz, 100-200MHz and 200-512MHz. The highest tuning range for the sub-bands is for the high band and it is equal to $(512/200)^2 = 6.55$ times.

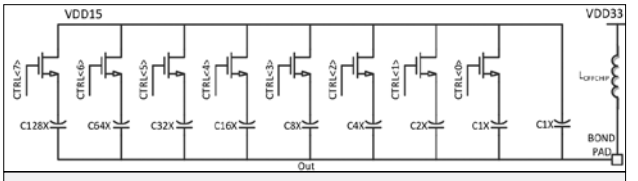

Figure 4. Capacitor DAC for tuning the output frequency

Figure 4 shows the capacitor array for each of the positive and negative output nodes. A binary weighted capacitor array is used to cover the frequency range of each of the four sub-bands. In order to maximize the capacitance density of the array, high density thin-oxide core MOS capacitors are used as long as the total parasitic capacitor permits. In order to comply with the reliability requirements of these devices, 1.8V lower than the gate drive voltage needs to be applied to the bottom plate terminal. This corresponds to 1.5V since the output of the amplifier has 3.3V DC through the load inductor, hence a DC supply of this value was used to terminate the bottom plate side of the capacitor. The use of 1.5V also enables the use of core devices as array switches, which is advantageous due to the reduces turn-on resistance and parasitic capacitance. Each time the array setting is incremented or decremented by one, the center frequency of the LC filter jumps up or down. The Least-Significant-Bit (LSB) of the array was chosen to give less than 1dB roll-off from the

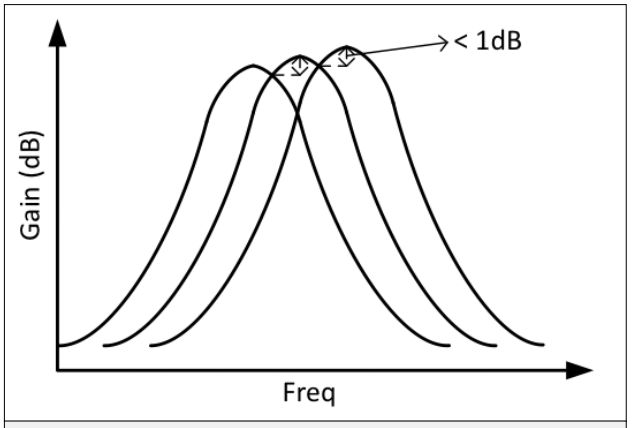

Figure 5. Gain vs. Frequency for different tuning settings of the amplifier

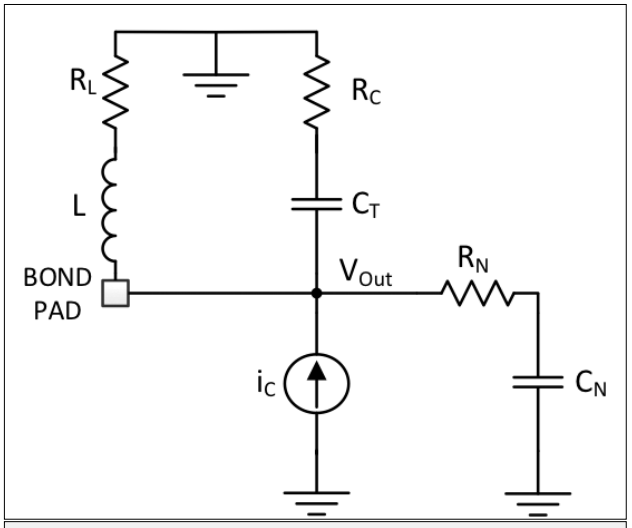

Figure 6. Schematic for the equivalent output load network.

center gain to the intersections of the gain curves for two subsequent tuning settings as shown in Figure 5.

Figure 6 shows the equivalent output impedance network for one of the output branches. The signal current from the cascode node is given by i_C and flows into the output impedance to generate the output voltage. L is the external inductor used for tuning at the output node and C_T is the equivalent total capacitance at the output. R_L and R_C denote the series resistances with the inductor and the capacitor respectively. R_L is composed of metal sheet resistance and R_C is composed of resistances of the switches in the capacitance array in addition to metal sheet resistances. These resistances have a big impact on reducing the quality factor (Q) of the output load network, hence they need to be minimized. C_N and R_N are the equivalent load capacitance due to the next stage and the series resistance due to signal routing traces and intrinsic gate resistances respectively.

In order to find the equivalent output network impedance, we can write KCL at the output node and derive $Z_{Out}=V_{Out}/i_C$. This analysis gives the output admittance to be:

$$Y_{Out} = \frac{1}{sL+R_L} + \frac{sC_T}{1+sC_TR_C} + \frac{sC_N}{1+sC_NR_N} \quad (3)$$

This equation is the most general form for the equivalent output admittance and it is difficult to get any insight from it. C_N is the gate capacitance for the next stage and is usually much smaller than C_T in the network. R_N is mostly the routing resistance and can be comparable or smaller than R_C since the latter is composed of routing and switch resistances. For the sake of simplicity, we can assume that the R_N-C_N network will be much smaller than the R_C-C_T branch, hence can be ignored. We then can write the equation for the output impedance as:

$$Z_{Out} = \frac{R_L+s(L+C_TR_CR_L)+s^2LC_TR_C}{1+sC_T(R_C+R_L)+s^2LC_T} \quad (4)$$

And the gain of the amplifier is given by:

$$A_V \cong g_m Z_{Out} \quad (5)$$

It is apparent from equation (4) that the network resonates at the frequency given in (2), where s^2 term is equal to $-1/LC_T$. When R_L and R_C values are close to each other and L is much larger than $C_TR_CR_L$ term, output impedance simplifies to:

$$Z_{Out} \cong \frac{L}{C_T(R_C+R_L)} \quad (6)$$

As expected, this equation suggests that for increasing R_C and R_L values, the equivalent load impedance goes down. Furthermore, a minimum L/C_T ratio has to be kept to ensure that the amplifier has the minimum required gain. This is another reason to divide up the whole frequency range to 4 sub-bands since a large tuning range for the capacitor increases its value to a range that may be comparable to L value. Figure 6 shows how the impedance of the load network varies for varying R_L and R_C values using the actual design values for L and C_T. It is apparent that as the R_L and R_C values increase a lot more than 1 Ω range, the output impedance scales down considerably. This has two consequences; the gain of the amplifier goes down and the rejection for blockers offset from the center frequency is reduced. It is apparent from the figure that even with 1 Ω series resistance with the inductor and capacitor, the rejection at 20% offset is around 10 dB, which is what we aim in this design. Consequently, layout techniques to reduce the series resistance with the external inductor and integrated capacitor array is very critical and are employed in this design.

Noise Figure

During operation, the amplifier is configured as a cascode amplifier working in one of the sub-bands mentioned in Part 2.2 above. Consequently, input referred noise of the amplifier will be that of a differential cascode amplifier and is given by [9, 10]:

$$\frac{\overline{v_{ir}^2}}{\Delta f} = 8kT\left[\frac{\gamma}{g_m} + \frac{(1+g_mR_s/2)^2}{R_Lg_m^2}\right] \quad (7)$$

where k is the Boltzman's constant, γ is a technology dependent scaling factor for the process used, R_L is the equivalent load resistance at the center frequency of the output tank and

R_s is the source resistances. Using (7), noise figure of the amplifier can be calculated to be:

$$NF = 1 + \frac{2\gamma}{g_m R_s} + \frac{2R_s}{R_L}\left[\frac{1+g_m R_s/2}{R_s g_m}\right]^2 \quad (8)$$

A perfect differential matching at the input of the amplifier requires that $1/gm = R_s/2$. Using (11), we can show that the equation simplifies to [10]:

$$NF = 1 + \gamma + \frac{2R_s}{R_L} \quad (9)$$

Equation (9) shows that the only way to control the NF of the amplifier is by increasing the gain by using a higher Q inductor. Otherwise, the NF is limited by the technology coefficients. Since the most important goal of this amplifier is to achieve higher filtering at the output by utilizing high-Q off-chip inductors, the design automatically minimizes the NF.

Distortion Analysis

In wide band receivers, linearity of the design blocks are extremely important due to the fact that the there is a wide range of incident frequencies that overload the system. As explained in the introduction, the specific system this amplifier is designed for may have a blocker of -10dBm at 20% offset when trying to receive a -120dBm desired signal and our design needs to be able to handle this power in full gain mode.

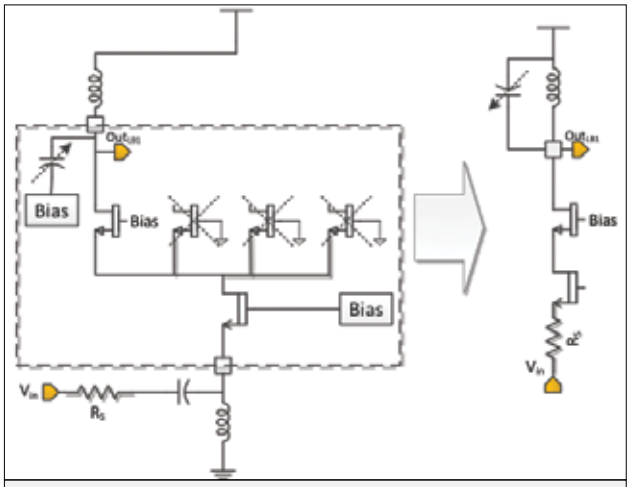

Figure 7. Schematic of half-circuit for distortion calculations

In order to understand the distortion performance of the amplifier designed, we can coarsely analyze it for linearity. Since the design is pseudo-differential, we can take half of the circuit and solve for distortion and the result will be the same for the differential amplifier for the fundamental tone and the odd harmonics. Even harmonics at the two outputs will be in phase and will cancel each other. One of the sub-bands of the amplifier will be on at a given time, so the equivalent circuit for distortion analysis reduces to the one on the right in Figure 7. At the frequencies of interest, the cascode device acts as a ideal current buffer, therefore doesn't introduce considerable distortion. Furthermore, for the sake of simplicity, we will assume that the programmable capacitor array at the output is biased at deep inversion, hence small-signal at the output doesn't cause considerable capacitance variation, which causes distortion. With these assumptions, the distortion of the single-ended amplifier is equal to that of a common gate amplifier with a source resistance. With Taylor Series expansion, the differential drain current of the amplifier can be written as [11]:

$$I_o = a_1 V_i + a_2 V_i^2 + a_3 V_i^3 \ldots \quad (10)$$

$$a_1 = \frac{g_m}{1+g_m R_S} \quad (11)$$

$$a_2 = 0 \quad (12)$$

$$a_3 = -\frac{2\left(\frac{\mu C_{OX} W}{2\ L}\right)^2 R_S}{(1+g_m R_S)^5} \quad (13)$$

where μ is the mobility of electrons, C_{ox} is the gate capacitance density and W/L is the gate-to-length ratio of the input transistors. It is apparent from Eq. (15) that for a fully matched amplifier, the second order distortion term is zero. Eq. (13) suggests that in order to minimize the third order distortion, W/L ratio needs to be minimized,

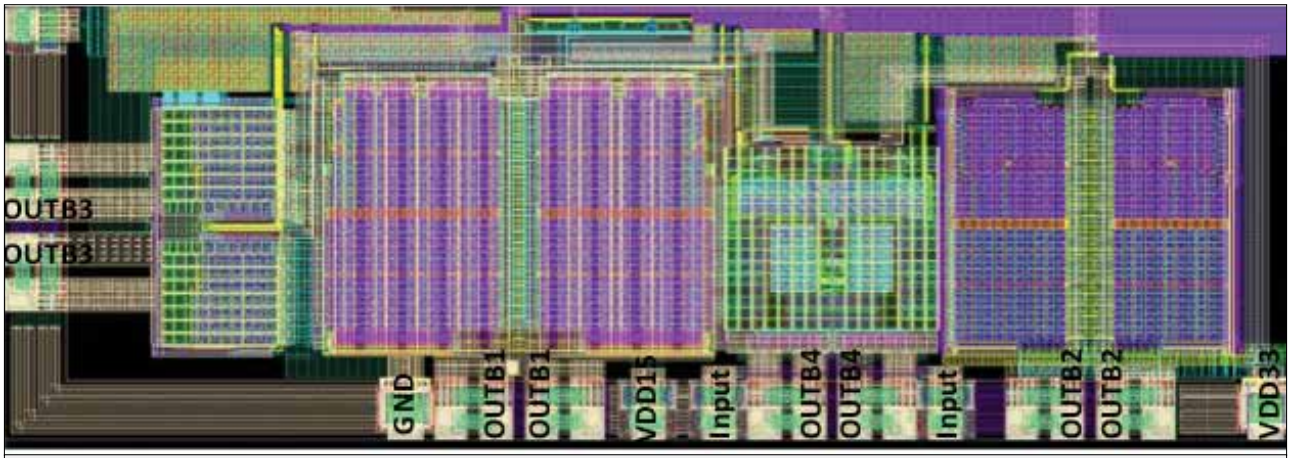

Figure 8. Layout of the wide-band LNA

while maximizing the g_m of the input device. Transconductance (g_m) of the input device is already decided on from Eq. (1) in order to have a adequate matching at the input port. Therefore, in order to minimize W/L ratio for a given gm value, V_{GS}-V_{TH} (also called V_{DSAT}) of the input device needs to be maximized. Additionally, careful design steps need to be taken to minimize the distortion due to secondary effects such as Channel Length Modulation. For this, the designer needs to make sure that the V_{DS} is maximized for all the transistors.

The amplifier was designed in 0.18um standard CMOS process and layout was optimized to minimize parasitic resistors that limits the Q of the inductors. For this purpose, two pads for each output node was used to double-bond the outputs to the package pins and reduce series resistor. This can be seen in the layout of the design in Figure 8. This figure shows the four subbands, the bonding pads for these, the input pads and the pads for supply and ground connections. The design occupies an area of 2200µm-by-700µm without the bonding pads and 2500µm-by-850µm with the bonding pads.

Table 1. Design Parameters

BAND	RS (Ω)	RC (Ω)	K	L-ind (nH)	Cind (fF)
30-50MHz	20	10m	165µ	81	56
50-100MHz	23	10m	72.2µ	35.7	59
100-200MHz	13	50m	48µ	21.9	54
200-512MHz	9	13m	32µ	12	58

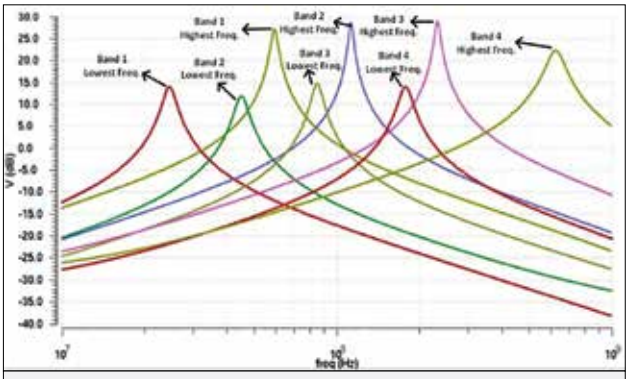

Figure 9. Minimum and maximum tuning for each band

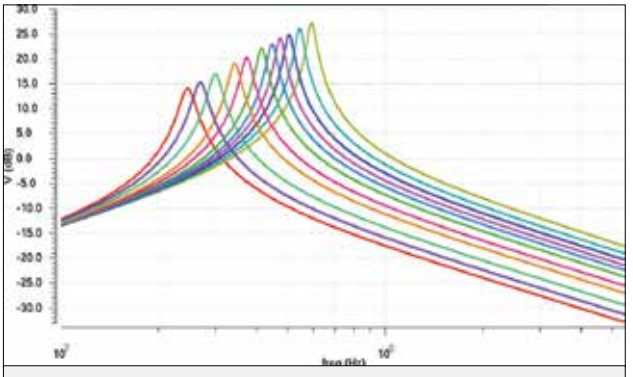

Figure 10. Minimum and maximum tuning for each band

Simulation Results

The design was verified across Process-Voltage-Temperature (PVT) using Cadence Spectre simulations. Post layout simulations were also performed to estimate the degradation in performance due to layout, bondwire and external inductor parasitics. The design works from 3.3V and 1.5V supplies for power supply and capacitor array terminations respectively, and consumes 20mA from the 3.3V supply.

Figure 3 shows the inductor model used to model the external inductors [12] and Table 1 shows the values and the coefficients for the inductors from Coilcraft.

Figure 9, 10 shows the gain and tuning curves for the amplifier. Figure 8 shows the lowest tuned frequency and highest tuned frequency for each of the sub-bands given in Table 1. Each band has overlap with the neighboring band at high and low ends of the range to make sure that there are no gaps in tuning in the whole frequency range of interest. The gain of the amplifier ranges from a minimum of 12dB to a maximum of 28dB across the whole band of 30-512MHz. This gain increase happens since the Q of the output tank increases as a function of frequency as we tune it higher within a sub-band. An attenuator following the amplifier can be used to limit the overall gain to a lower value in the case of high input power. Figure 9 shows how the amplifier tunes in the first sub-band of 30-50MHz by showing sample tuning settings that ranges from 0 to 255. Each sub-band has a total of 255 tuning steps as a result of 8 bit tuning control.

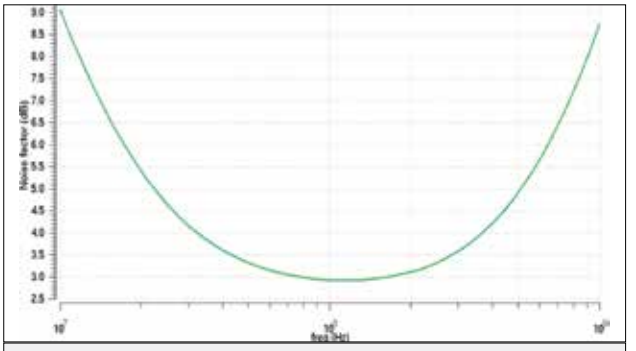

Figure 1 1. Noise Figure vs. Frequency for the high-end tuning of the 30-50MHz sub-band

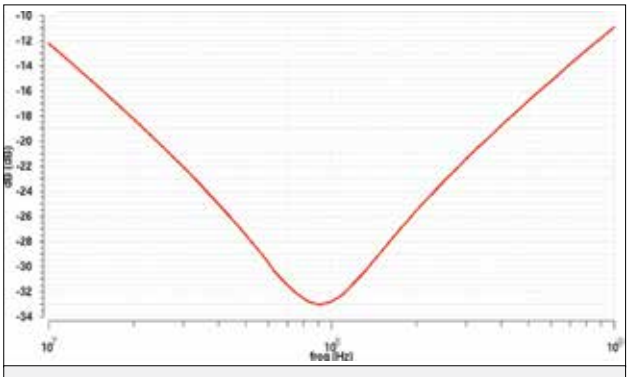

Figure 12. S11 vs. Frequency across the whole band

Table 2. Performance results

Band (MHz)	Freq (MHz)	NF (dB)	S11 (dB)	%10 offset rejection (dB)	%20 offset rejection (dB)	P1dB at 20% offset (dBm)	In-Band IIP3 (dBm)
30-50	30	4.6	-21	10	16.5	9.1	18
	50	3.4	-26	12	18.5	11	21
50-100	50	3.9	-26.5	11.2	17.5	9.8	21
	100	2.9	-33	15.6	22.1	13	21
100-200	100	3.3	-33.7	13.2	19.6	9.6	21
	200	2.8	-33	16.7	23.2	9.2	21
200-512	200	3.6	-31	9.9	16	9.5	21
	512	3.3	-21	7	12.8	9.2	21

NF: noise figure; P1dB: 1-dB compression point; IIP3: 3rd order input intercept point

Figure 11 shows the Noise Figure of the amplifier when the output is tuned to the high end of the 30-50MHz sub-band. As the amplifier is tuned to different frequencies, the frequency where the minimum NF is achieved moves with the center frequency. Table 2 shows the NF at the low and high ends of each sub-band. Worst case NF is 4.6dB across the whole frequency range.

Figure 12 shows the simulated impedance-match parameter (S11) result for the amplifier and it is less than -20dB across the whole frequency range of 30-512MHz. Table 2 gives S11 results at the low and high ends of each sub-band. The rejection of undesired signals at 10% and 20% frequency offset, which is one of the critical specifications for the design, are also given in Table 2. These rejection amounts are adequate to reject the incoming undesired signal enough to keep it under control at the output of the amplifier. The worst case 1dB compression point (P_{1dB}) and the third order input intercept point (IIP3) for the amplifier are 9.1dBm and 18dBm, respectively, across the whole band as given in Table 2.

Conclusion

In this paper, we have presented a wide-band tunable LNA that has been designed in 0.18µm CMOS process from UMC. The design has been laid-out and post layout simulations were run to include the parasitic effects. The design dissipates 66mW from a 3.3V supply to meet the tough requirements of military radios. In the first part of the paper, the proposed design has been analyzed for gain, tuning, matching, noise figure and distortion. The LNA works in the frequency range of 30-512MHz and achieves a minimum gain of 12dB across the whole range. Worst case Noise Figure was simulated to be 4.6dB and S11 is less than -20dB across frequency and PVT. The design is highly linear and achieves a minimum of 9.1dBm P_{1dB} and 18dBm IIP3 in worst case settings.

References

1. B Taddiken, W Ezell, E Mumper, K Clayton, J Douglass, V Birleson, J Esquivel, O Werther, A Schneider, Bolton J, et al. Broadband tuner on a chip for cable modem, HDTV, and legacy analog standards. In: IEEE RFIC Symposium; 10 - 13 June 2000; Boston, MA, USA. Piscataway, NJ, USA. pp. 17-20. [CrossRef]
2. M Hajirostam and K Martin. On-chip broadband tuner design for cable modem and digital CATV. In: IEEE 48th Midwest Symposium on Circuits and Systems; 7 - 10 August 2005; Cincinnati, OH, USA. pp. 1374 - 1377. [CrossRef]
3. D Im, I Nam, K Lee. A CMOS active feedback balun-LNA with high IIP2 for wideband digital TV receivers. *IEEE T-MTT,* 3566-3579, Dec. 2010.
4. J Kim and J Silva-Martinez. Wideband inductorless balun-LNA employing feedback for low-power low-voltage applications. *IEEE T-MTT*, 2833-2842, Sep. 2012.
5. EA Sobhy, AA Helmy, S Hoyos, K Entesari, E Sanchez-Sinencio. A 2.8mW Sub – 2dB Noise-Figure Inductorless Wideband CMOS LNA Employing Multiple Feedback. IEEE Trans. *Microwave. Theory Tech.,* pp. 652-664, 2011.
6. F Bruccoleri, EAM Klumperink, B Nauta. Wide-band CMOS low-noise amplifier exploiting thermal noise cancellation. *IEEE JSSC,* pp. 275-282, Feb. 2004.
7. PR Gray, RG Meyer. Analysis and Design of Analog Integrated Circuits. 3rd ed, New York, NY, USA: Wiley, 1993.
8. http://www.coilcraft.com/0603ls.cfm#table
9. TH Lee. Design of CMOS RF Integrated Circuits. Cambridge University Press, 1998.
10. B Razavi. RF Microelectronic. New Jersey, NJ, USA: Prentice Hall, 1997.
11. Meyer RG. EE242 Course Reader, UC Berkeley, Berkeley, CA, USA, Fall 1999.
12. http://www.coilcraft.com/0603CS.cfm

Hakan Doğan received his B.S. degree in electrical engineering from University of Southern California (USC), Los Angeles, in 1999, and the M.S. and Ph.D. degrees in electrical engineering from the University of California at Berkeley in 2001 and 2005, respectively. He is currently an Assistant Professor in the Electrical and Electronics Engineering Department at İstanbul Medipol University, İstanbul, Turkey. His research interests are in RF/Analog/Mixed Signal circuit design, end-to-end wireless and wireline communication system design. Previously, he was an Assistant Professor in the Electrical and Electronics Engineering Department at Istanbul Sehir University, Istanbul, Turkey, from 2013 to 2017. He was with Qualcomm-Atheros and Atheros Communications San Jose, CA from 2005 to 2013, where he was involved with dual-band wireless-LAN transceiver, Bluetooth transceiver, PLC transceiver and GPS receiver chipset designs. In the summer of 2000, he worked in HP Labs, where he was involved with the design of clock and data recovery circuits. During the two consecutive summers, he was with Maxim Integrated Circuits, involved with the design of cable modem tuners and satellite receivers.

İSTANBUL UNIVERSITY PRESS

RESEARCH ARTICLE

Electrica 2018; 18(1): 26-35

Comparison of ANN and ANFIS Methods for the Voltage-Drop Prediction on an Electric Railway Line

İlhan Kocaarslan[1], Mehmet Taciddin Akçay[2], Abdurrahim Akgündoğdu[1], Hasan Tiryaki[1]

[1]Department of Electrical and Electronics Engineering, İstanbul University School of Engineering, İstanbul, Turkey
[2]Diroctorate of Rail System, İstanbul Metropolitian Municipality, İstanbul, Turkey

Cite this article as: İ. Kocaarslan, M. T. Akçay, A. Akgündoğdu, H. Tiryaki. "Comparison of ANN and ANFIS Methods for the Voltage-Drop Prediction on an Electric Railway Line". *Electrica*, vol. 18, no. 1, pp. 26-35 , 2018.

ABSTRACT

Railway electrification systems are designed with regard to the operating data and design parameters. The minimum voltage rating required by traction during the operation should be provided. The maximum voltage drop on a line determines the minimum traction voltage. This voltage should be maintened within certain limits for the continuity of operation. In this study, the maximum voltage drop generated via traction was determined using artificial neural network (ANN) and adaptive neuro-fuzzy inference system (ANFIS) for a 25-kV AC-supplied railway. The voltage drop on line was calculated with regard to the operating data using ANN and ANFIS. ANN and ANFIS were explained, and the results were compared. The Levenberg–Marquardt (LM) algorithm was used for the ANN model. The LM algorithm is preferred because of the speed and stability it provides for the training of ANNs. The data created for one-way supply status were examined for simulation.

Keywords: ANFIS, ANN, electrification, railway, traction

Introduction

Mostly 25 kV 50 Hz. single-phase supply voltage is used for the traction force system on AC supplied railways. The single-phase supply voltage that the traction force uses is acquired through an interconnected network which has 154 kV phase to phase voltage. Two transformers of 154 kV/25 kV are present in the substations and the transformers can operate as back-up [1-6]. The equivalent circuit model of the AC railway is presented in Figure 1.

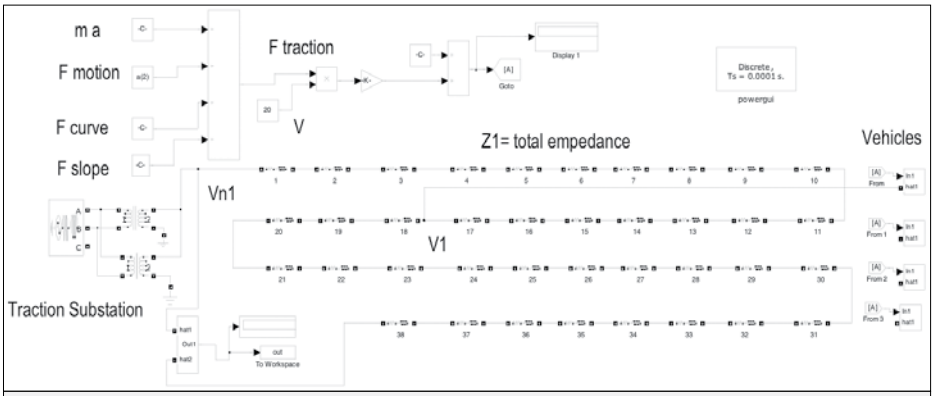

Figure 1. Chest X-ray showing right subdiaphragmatic free air

The equation regarding the supplying status from a single substation is given with Equation (1) which represents the total impedance from substation Z1 to the vehicle. The impedance values of the feeder cables were also added to Z1. Z1 value changes in accordance with the distance depending on the location of the vehicle. V1 is the voltage of the vehicle, Vn1 indicates the nominal

Address for Correspondence:
Mehmet Taciddin Akcay

E-mail:
taciakcay@gmail.com

Received: 24.06.2017

Accepted: 21.09.2017

DOI: 10.5152/iujeee.2018.1805

supply voltage, $I_{vehicle}$ indicates the vehicle current. The maximum traction force of the vehicles in the railway vehicles with a high power consumption can increase to 20 MVA [7-11].

$$V_1 = V_{n1} - I_{vehicle} \times Z1 \quad (1)$$

Neutral zones increase the operating capability by allowing to be supplied from different zones. Since the voltage drop occurring on the line and the currents drawn do not reach high values under normal operating conditions, the distances between the supply stations may be longer. As the number of traction supply stations and the efficiency of the traction force system increase, the voltage drop on the line and the losses decrease [12-16]. The traction system of the railway vehicle consists of a transformer, a three-phase PWM inverter and an asynchronous engine. In the course of regenerative braking, the asynchronous engine can function as a generator and enables energy transfer. This gain is more effective with the developed power electronics technology. With new research and studies, new traction force converters, various electric equipment used in railway vehicles also undergo a change [17-20]. The single-line scheme of the traction force supply diagram of an AC supplied railway is displayed in Figure 2.

The vehicle traction force ($F_{traction}$) consists of the sum of the resistance force against vehicle motion (F_{motion}), slope resistance force (F_{slope}), curve resistance force (F_{curve}) and the multiplication of acceleration and mass of the vehicle, which are given with (2), (3), (4) and (5). In the equations, V is the vehicle speed, m is the vehicle mass, A, B, C are the coefficients related to the vehicle characteristic, g is the gravitational acceleration, **γ** is the angle of inclination, R is the curve radius, C1, C2 and C3 are the coefficients used to calculate the curve force. In equation (5), the acceleration-mass (ma) value expresses the net force that affects the vehicle. The power equation of the vehicle is given with regard to the traction force and vehicle speed by Equation (6).

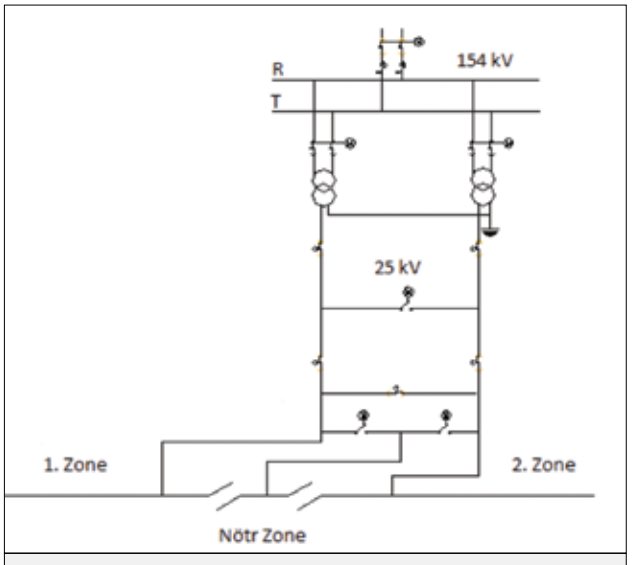

Figure 2. Single-Line scheme of the traction force supply diagram

$$F_{motion} = A + B \times v + C \times v^2 \quad (2)$$
$$F_{slope} = m \times g \times \sin(\gamma) \quad (3)$$
$$F_{curve} = (m \times g \div 1000) \times (C_1 - C_2 \times R) \div (R - C_3) \quad (4)$$
$$F_{traction} = F_{motion} + F_{slope} + F_{curve} + ma \quad (5)$$
$$P_{vehicle} = F_{traction} \times v \quad (6)$$

The vehicle power increases with the traction force and vehicle speed. The equivalent circuit given with Figure 1 was simulated with different operating parameters and 1000 data arrays were obtained regarding different operating conditions. Equations 1-6 were used to obtain different simulation datas given with Figure 1. 1000 simulation was done with different operation parameters for the best result for the prediction. The parameters used in the simulation are the number of vehicles, acceleration-mass value of the vehicle, vehicle motion resistance, curve radius, slope, the length of the supply line, internal consumption current of the vehicle, electric resistance and inductance of the line; the calculated value is the highest voltage drop value occurring on the line. Random values were assigned to all the input parameters used in the simulation. For the simulation, the number of vehicles varying between 0-10 was used and the vehicle placement was performed by taking the maximum voltage drop into consideration. The diversity of the parameters and the variability in operating conditions in the simulation render the solution of this problem complex. Artificial Intelligence is the science which deals with enabling machines to produce solutions to complex problems as humans. This is generally performed by taking the characteristic of human intelligence and applying it to the computer as an algorithm. In accordance with the demanded or desired needs, which mental attitude will be presented to which effect, less or more flexible or effective approaches can be displayed. Artificial intelligence was preferred in this study due to the stated advantages.

Material and Method

In this study, the artificial neural network and adaptive fuzzy inference system among the artificial intelligence applications were used for simulation. The ANN is a method which functions by imitating the way of work of a simple biological nervous system. The ANFIS is a hybrid artificial intelligence method which uses the parallel computing and learning capability of artificial neural networks and the inferential characteristic of fuzzy logic. Matlab program was used for simulations.

Artificial Neural Networks (ANN)

Artificial neural networks emerged as a mathematical method from the latest outputs of endeavors to study and imitate human nature. Artificial neural networks take computing and data processing power from their parallel distributed structure, their capability to learn and generalize. Generalisation is defined as artificial neural networks' producing proper reactions to the inputs which have not been experienced in the course of education or learning. These characteristics indicate the problem-solving capability of artificial neural networks [21-24].

The biological neuron consists of a nucleus, body and two extensions. The structure of the artificial neural network is given in Figure 3. The 1st layer is the input layer. Data are received from here and entered into the system. The 2nd layer is the hidden layer. Its use depends on the simulation. The 3rd layer is the output layer. Inputs are processed and received from here. Each sphere (nerve) has a function and a threshold value. Filled small circles indicate bonding weights [25-30].

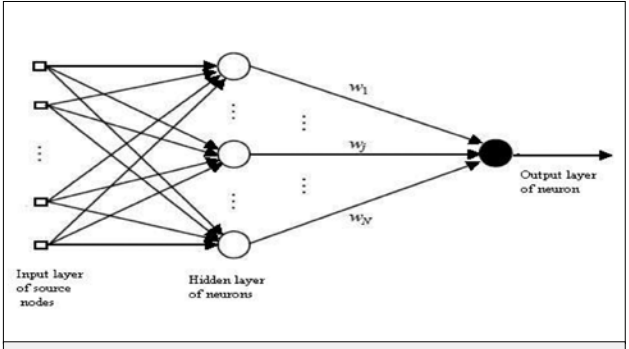

Figure 3. The structure of the artificial neural network

Levenberg-Marquardt Algorithm

The Levenberg-Marquardt algorithm is a least squares computing method based on the maximum neighborhood. This algorithm consists of the best features of the Gauss-Newton and gradient-descent algorithms and removes the restrictions of these two methods. This method is not affected by the slow convergence problem. The Levenberg-Marquart algorithm, which is the combination of the Gauss-Newton algorithm, is more efficient and rapid in optimization problems when compared to the sloping downward algorithm [25].

Adaptive Neuro Fuzzy Inference System (ANFIS)

The ANFIS is a class of adaptive networks functionally equivalent to the fuzzy inference system. The ANFIS can be given more integrated with some characteristics of controllers, learning ability, parallel processing, structured knowledge representation, other supervision and design methods. Fuzzy logic and neural networks are supplementary means used together in developing smart systems [31-34]. The ANFIS consists of 6 layers. This system is displayed in Figure 4. The node functions of every layer in the ANFIS structure and the operation of the layers are respectively as follows [34]. First layer is named the input layer. The input signals obtained from every node in this layer are transmitted to other layers. Second layer is named the fuzzification layer. In separating the input values into fuzzy sets, Jang's ANFIS model uses the Bell activation function generalized as a membership function. Here, the output of each node consists of membership degrees based on the input values and the membership function used and the membership values obtained from the 2nd layer are presented as and Third layer is the layer of rules. Each node in this layer expresses the rules established in accordance with the Sugeno fuzzy logic inference system and their number. The output of each rule node μ turns out to be the multiplication of membership degrees which arrive from the 2nd layer. The acquisition of μ values, on the condition that (j=1,2) and (i=1,….,n), is as follows:

$$y_i{}^3 = \Pi_i = \mu_{A_j}(x) \times \mu_{B_j}(y) = \mu_i \quad (7)$$

Here, represents the output values of the 3rd layer; n represents the number of nodes in this layer. Fourth layer is the normalization layer. Each node in this layer regards all the nodes coming from the rule layer as input values and computes the normalized ignition level of each rule. The computing of the normalized ignition level is performed in accordance with the following formula:

$$y_i{}^4 = N_i = \frac{\mu_i}{\sum_{i=1}^{n} \mu_i} = \overline{\mu_i} \ \text{(i=1,n)} \quad (8)$$

Fifth layer is the purification layer. The weighted resulting values of a given rule in each node in the purification layer are calculated. The output value of the ith node in the 5th layer is as follows.

$$y_i{}^5 = \overline{\mu_i}[p_i x_1 + q_i x_2 + r_i], \ \text{(i=1,n)} \quad (9)$$

The (pi , qi , ri) variables here are the outcome parameter set of the ith rule. Sixth is the sum layer. There is only one node in this layer and it is labeled as Σ.The output value of each node in the 5th layer is summed here so that the actual value of the ANFIS system is obtained. The computing of y, which is the output value of the system, is performed in accordance with the equation below [31].

$$y = \sum_{i=1}^{n} \overline{\mu_i} \, [p_i x_1 + q_i x_2 + r_i] \quad (10)$$

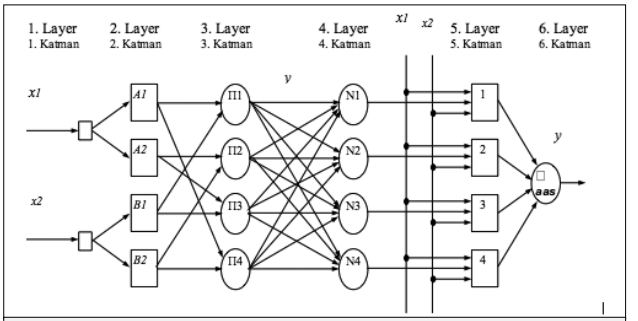

Figure 4. ANFIS structure

Mean absolute error (MAE)

The mean absolute error is the division of the absolute value of the difference between the measured values and predicted values by the measurement number. It is given by Equation (11), n represents the measurement number, e represents the difference between the actual value and estimated value [35-36].

$$MAE = \frac{1}{n}\sum_{i=1}^{n}|e_i| \quad (11)$$

Root mean squared error (RMSE)

The Root Mean Squared Error is acquired by dividing the real error sum of squares of a measuring line by the measurement number and by taking the square root of this calculated value. It carries out the most correct approach regarding the degree of accuracy of the measurements. In the RMSE equation given

by equation (12), xobs are the real values, xmodel are the predicted values, n is the measurement number [35-36].

$$RMSE = \sqrt{\frac{\sum_{i=1}^{n}(X_{obs,i}-X_{model,i})^2}{n}} \quad (12)$$

Relative absolute error (RAE)

The Relative absolute Error is acquired by dividing the sum of real error of a measuring line by the sum of predicted error. In the RAE equation given by equation (13), xobs are the real values, xmodel are the predicted values, model is the mean value of xmodel, n is the measurement number [35-36].

$$RAE = \frac{\sum_{i=1}^{n}|X_{obs,i}-X_{model,i}|}{\sum_{i=1}^{n}|\bar{X}_{model,i}-X_{model,i}|} \quad (13)$$

Root relative squared error (RRSE)

The Root relative squared error is acquired by dividing the real error sum of squares of a measuring line by the predicted error sum of squares and by taking the square root of this calculated value. In the RRSE equation given by equation (14), xobs are the real values, xmodel are the predicted values, model is the mean value of xmodel, n is the measurement number [35,36].

$$RRSE = \sqrt{\frac{\sum_{i=1}^{n}(X_{obs,i}-X_{model,i})^2}{\sum_{i=1}^{n}(\bar{X}_{model,i}-X_{model,i})^2}} \quad (14)$$

Findings

1000 data arrays different from each other were used for the calculation of the voltage drop created by the traction force. A portion of the data used is displayed in Table 1.

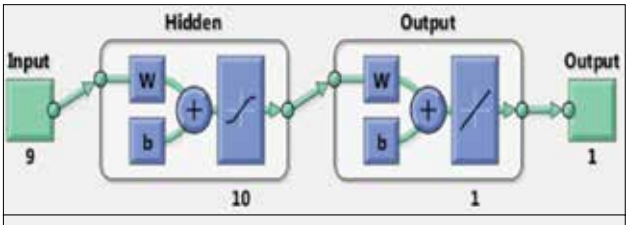

Figure 5. ANN architecture designed [MATLAB R2015b]

Simulation results with the ANN

As seen in Table 1, the system consists of 9 input and 1 output parameters. The ANN architecture used is given in Figure 5.

9 input data, 10 hidden neurons, 1 output neuron and 1 output data were used for the ANN architecture used in the design. 70% of the data used for simulation were used for education, 15% for validation, 15% for the test. As seen in Figure 6, the best validation value was reached at the 49th iteration by inhibiting overfitting in the simulation. The lowest mean squared error value is 152241.40. The training, validation and test data produced by the system displayed similar characteristics. Since the validation error value increased in the course of 6 iterations, the simulation was stopped at the end of 55 iterations.

The backpropagation gradient value is given on a logarithmic scale for each iteration with Figure 7. The difference between the test values and validation values is predicted. Validation checks and Matlab stop the simulation with the increase in the mse value of the validation values in order to inhibit overfitting at the end of 6 iterations. The mse performance is given with the training state graph. Gradient=718660.15 at epoch 55, mu=1000 at epoch 55 and the validation checks=6 at epoch 5.

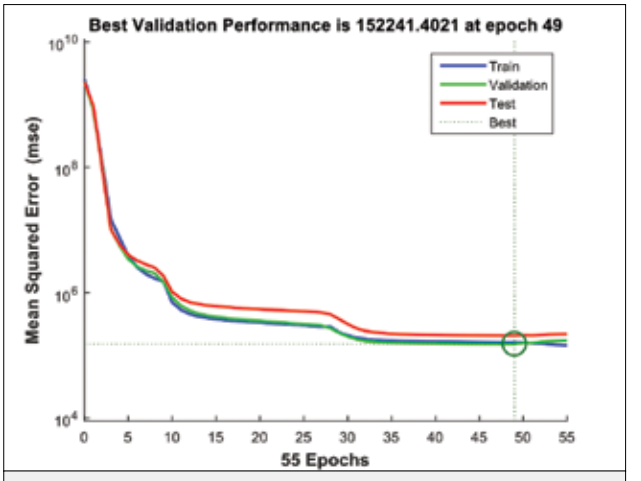

Figure 6. Best validation performance graph

Table 1. A portion of the data set that used

Inputs	Output Number of vehicles	Ma value (kilonewton)	Vehicle motion resistance (kilonewton)	Curve radius (meter)	Slope	The length of the supply line (kilometer)	Internal consumption current of the vehicle (amper)	Line resistance (ohm)	Line inductance (henry)	Voltage drop (volt)
6	235	65	910	0.0054	72	19.1	0.1271	0.001273	23525	
9	279	80	866	0.0177	68	19.1	0.1416	0.00146	46809	
2	210	65	890	0.0312	46	19.9	0.1236	0.001298	8100	
1	215	68	908	0.0292	96	22.3	0.1225	0.001272	11142	
1	223	69	939	0.0371	36	21.8	0.1107	0.001117	4022	

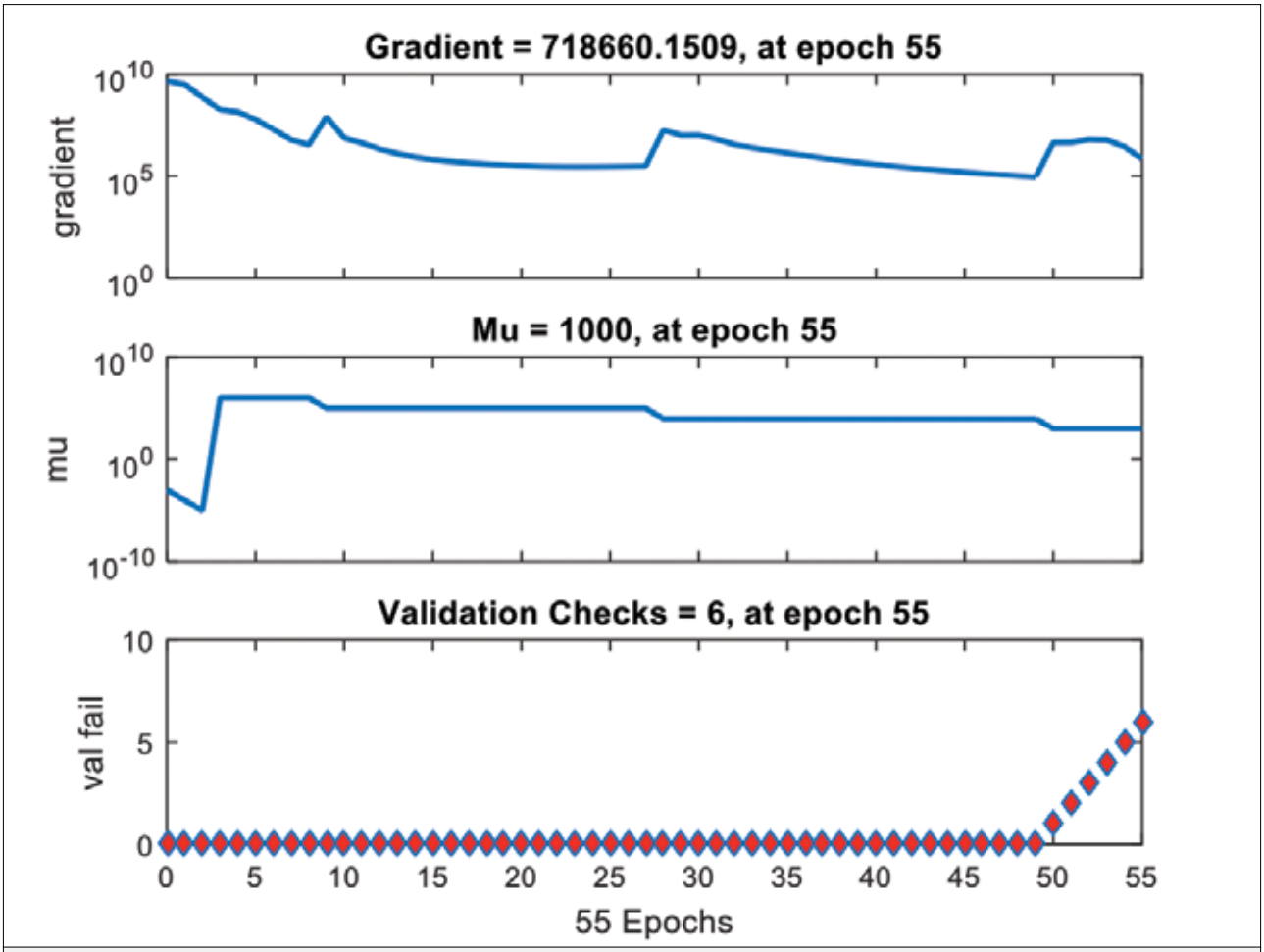

Figure 7. Training state graph, a) gradient, b) mu parameter, c) validation check

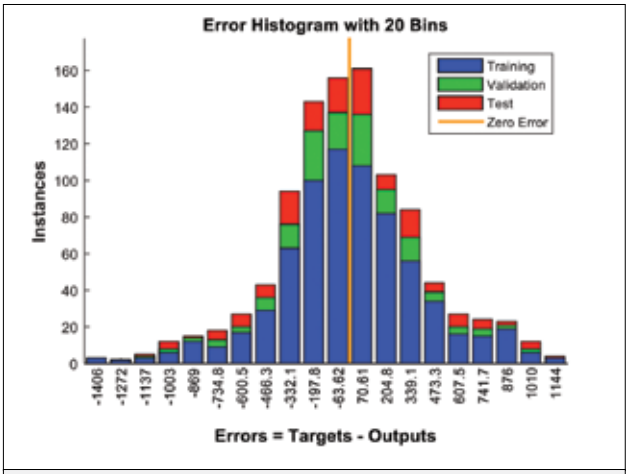

Figure 8. ANN Error histogram

The error histogram of ANN simulation is shown in Figure 8. The differences between the realized values and calculated values are seen with this graph. The distribution of the errors of the training data is shown with blue, validation data with green and test data with red. The errors mostly concentrate between -1137 and 1010.

The realized and calculated values of the training, validation and test data are seen in Figure 9. The regression value is shown with R, and as seen in the Figure 9, these values are 0.99962 for training, 0.9996 for validation, 0.99936 for the test data. The R value is 0.99959 for all data. As this value approaches 1, the accuracy of the data calculated by the system increases.

The realized data, calculated data and error values are shown in Figure 10. The realized data are given with blue, the calculated data are given with red, error values are given with yellow.

Simulation results with the ANFIS

The structure of the system created for the ANFIS and the simulation results are given below. A structure with 9 inputs 2 membership functions created for the ANFIS is given with Figure 11. 70% of the data used for simulation were used for education, 15% for validation, 15% for the test. A triangular-shaped membership function was used for the simulation.

Some of the rules established for the ANFIS are shown in Figure 12. 2^9=512 rules were established for the ANFIS design.

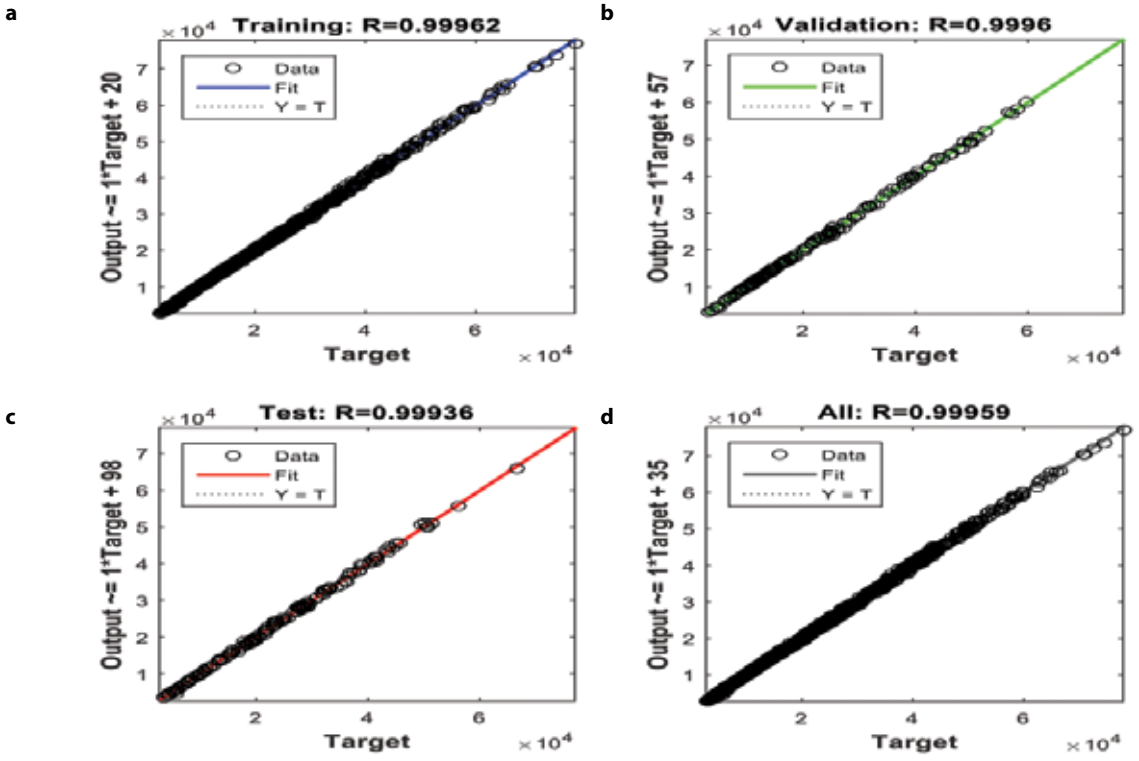

Figure 9. ANN regression graph, a) training, b) validation, c) test, d) all

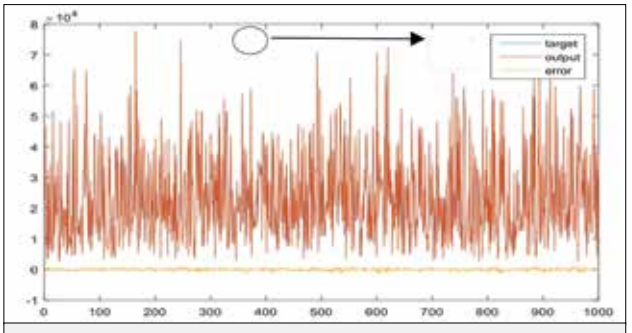

Figure 10. Output, prediction and error data graph of the YSA simulation

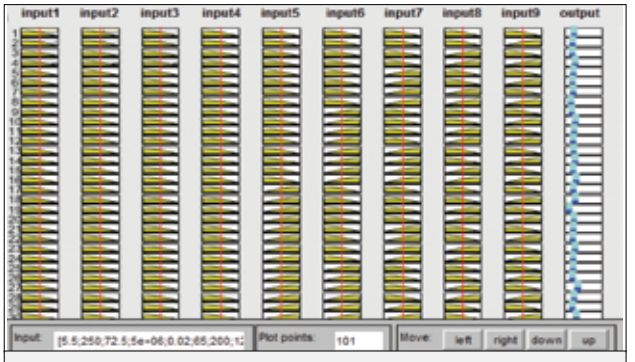

Figure 12. Rules established for the ANFIS

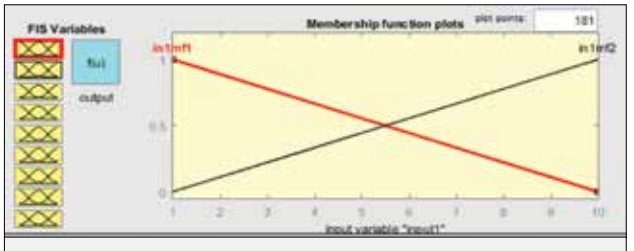

Figure 11. Triangular-shaped membership function

The ANFIS architecture is shown in Figure 13. The system consists of the input, input MF, Rule, output MF and output modules.

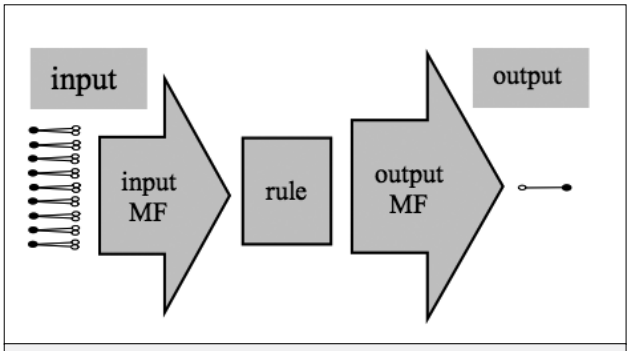

Figure 13. ANFIS architecture

The error histogram of ANFIS simulation is shown in Figure 14. The differences between the realized values and calculated values are seen with this graph. The distribution of the errors of the training data is shown with blue, validation data with red and test data with green. The errors mostly concentrate between -5456 and 3493.

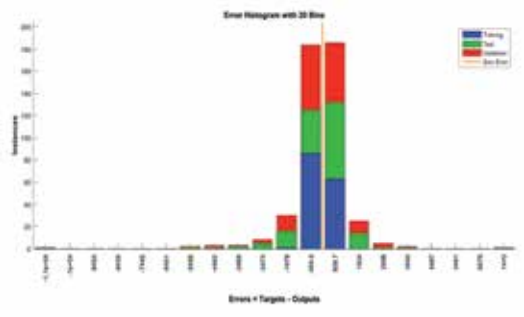

Figure 14. ANFIS Error histogram

The realized and calculated values of the training, validation and test data for ANFIS simulation are seen in Figure 15. The regression value is shown with R, and as seen in the Figure 15, these values are 0.99989 for training, 0.99685 for validation, 0.99425 for the test data. The R value is 0.99844 for all data. As this value approaches 1, the accuracy of the data calculated by the system increases.

The realized data, calculated data and error data are shown in Figure 16.

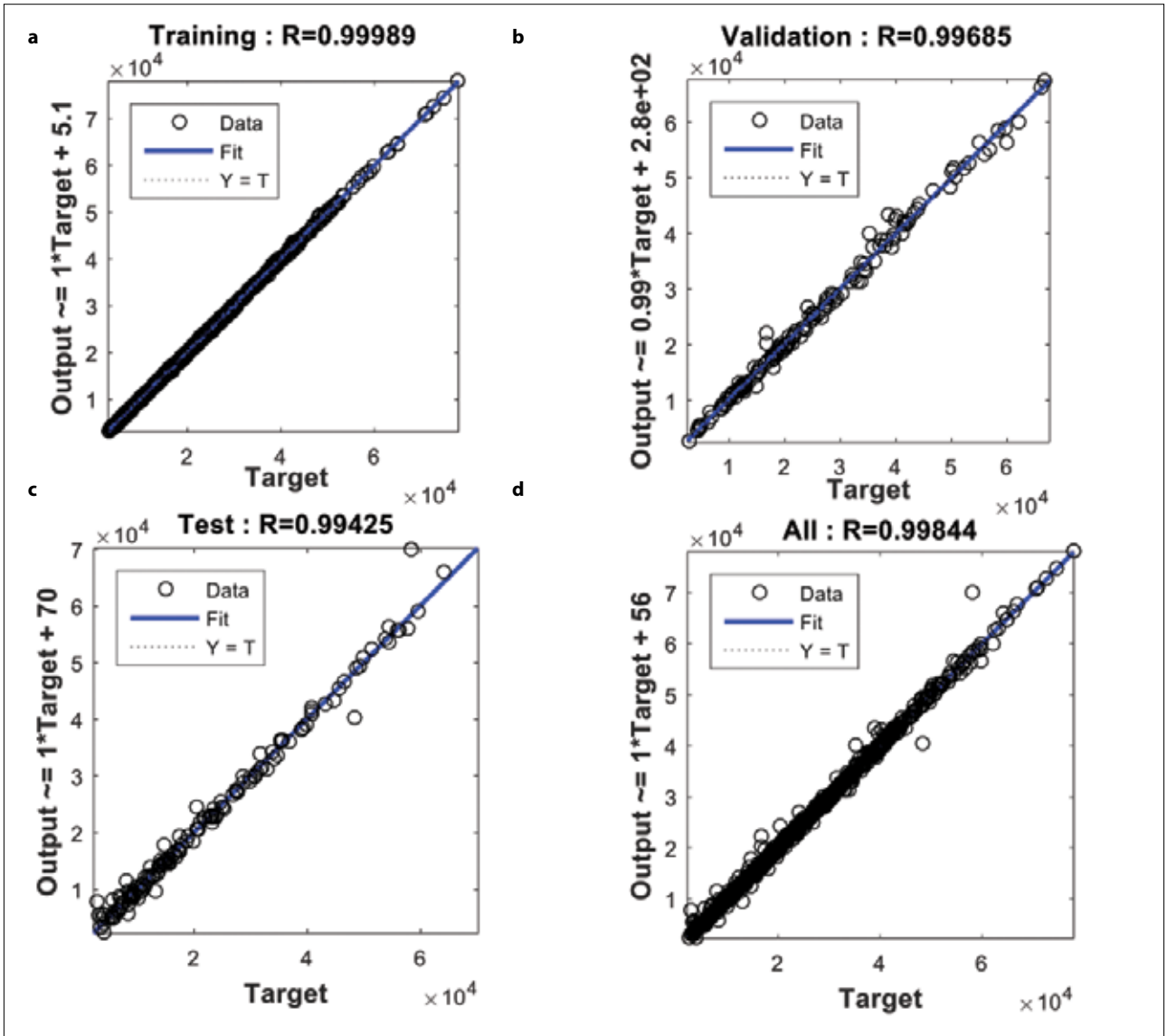

Figure 15. ANFIS regression graph, a) training, b) validation, c) test, d) all

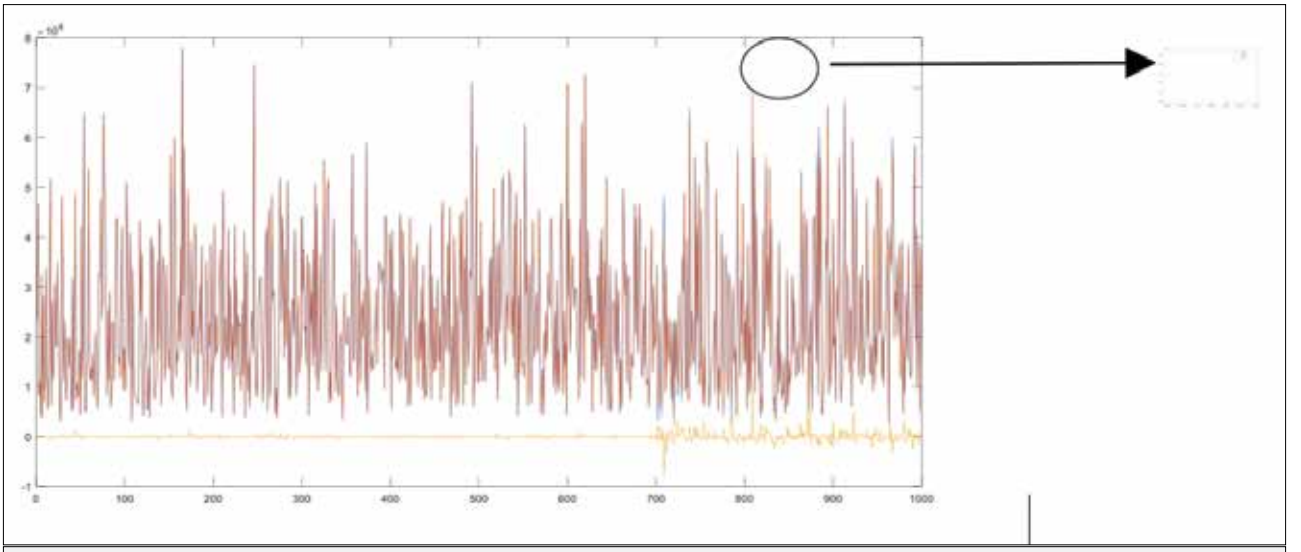

Figure 16. Output, prediction and error data graph of the ANFIS simulation

Table 2. The simulation results of both methods

Method	ANN	ANFIS
Mean absolute error (MAE)	305.3448	339.1464
Root mean squared error (RMSE)	407.4496	792.9189
Relative absolute error (RAE)	0.0266	0.0295
Root relative squared error (RRSE)	0.0288	0.0560
Total Number of Instances	1000	1000

ANN: artificial neural network; ANFIS: adaptive neuro-fuzzy inference system

The comparison of the ANN and ANFIS results

When the ANN and ANFIS results are compared, the ANFIS results are observed to be better. The simulation results of both methods are given in Table 2.

Conclusions

In this study, the prediction of the highest voltage drop created by the traction force on an AC supplied railway with regard to the operating data was performed. 1000 random input data arrays and the calculated output data were used for the simulation. In the analyses carried out, the ANN and ANFIS techniques were used. The voltage drop value was predicted. The RRSE value in the data obtained for the ANFIS in the calculations carried out is 5.6% and this value is 2.9% in the ANN. The RMSE values are 407 V for the ANN simulation and 793 V for the ANFIS. The MAE value acquired in the ANN is 305 V, this value is 339 V in the ANFIS. The RAE value in the ANN is 2.7%, this value is 3% in the ANFIS. When the data obtained from the simulations are compared, the prediction values produced with the ANN are observed to be better. When the prediction data produced for both techniques are compared with the real data, it is observed that errors are at an acceptable rate and that the prediction data produced are usable.

References

1. J. S. Huh, H.S. Shin, W. S. Moon, B. W. Kang, J. C. Kim, "Study on voltage unbalance improvement using SFCL in power feed network with electric railway system," *IEEE Transactions on Applied Superconductivity,* vol. 3: 3601004, 2013.
2. A. Ghassemi, S. S. Fazel, I. Maghsoud, S. Farshad, "Comprehensive study on the power rating of a railway power conditioner using thyristor switched capacitor," *IET Electrical Systems in Transportation*, vol. 4, pp. 97-106, 2014. [CrossRef]
3. G. Raimondo, P. Ladoux, A. Lowinsky, H. Caron, P. Marino, "Reactive power compensation in railways based on AC boost choppers," *IET Electrical Systems in Transportation*, vol. 2, pp. 169-177, 2012. [CrossRef]
4. K. Aodsup and T. Kulworawanichpong, "Effect of train headway on voltage collapses in high-speed AC railways," In: APPEEC 2012 Power and Energy Engineering Conference; 27-29 March 2012; Shanghai, China. New York, USA: IEEE. pp. 1-4. [CrossRef]
5. M. A. A. Baseri, M. N. Nezhad, M. A. Sandidzadeh, "Compensating procedures for power quality amplification of AC electrified railway systems using FACTS," In: PEDSTC 2011 Power Electronics Drive Systems and Technologies Conference; 16-17 Februrary 2011; Tehran, Iran. New York, USA: IEEE. pp. 518-521.
6. M. Brenna and F. Foiadelli, "The compatibility between DC and AC supply of the Italian railway system," In: Power and Energy Society General Meeting; 24-29 July 2011; San Diego, USA. New York, USA: IEEE. pp. 1-7. [CrossRef]
7. L. Abrahamsson, T. Kjellqvist, S. Ostlund, "High-voltage DC-feeder solution for electric railways," *IET Power Electronics*, vol. 5, pp. 1776-1784, 2012. [CrossRef]
8. S. V. Raygani, A. Tahavorgar, S. S. Fazel, B. Moaveni, "Load flow analysis and future development study for an AC electric railway," *IET Electrical Systems in Transportation,* vol. 2, pp. 139-147, 2012. [CrossRef]

9. C. J. Goodman and M. Chymera, "Modelling and simulation," In: REIS 2013 Railway Electrification Infrastructure and Systems Conference; 3-6 June 2013; London, England. New York, USA: IEEE. pp. 16-25. [CrossRef]
10. P. Ladoux, G. Raimondo, H. Caron, P. Marino, "Chopper-Controlled steinmetz circuit for voltage balancing in railway substations," *IEEE Transactions on Power Electronics,* vol. 28, pp. 5813-5822, 2013. [CrossRef]
11. H. S. Shin, S. M. Cho, J. C. Kim, "Protection scheme using SFCL for electric railways with automatic power changeover switch system," *IEEE Transactions on Applied Superconductivity*, vol. 20, 5600604, 2012.
12. H. S. Shin, S. M. Cho, J. S. Huh, J. C. Kim, D. J. Kweon, "Application on of SFCL in automatic power changeover switch system of electric railways," *IEEE Transactions on Applied Superconductivity* vol. 22, 5600704, 2012. [CrossRef]
13. V. Kolar, R. Hrbac, T. Mlcak T, "Measurement and simulation of stray currents caused by AC railway traction," In: EPE 2015 Electric Power Engineering Conference; 20-22 May 2015; Prague, Czech Republic. New York, USA: IEEE. pp. 764-768.
14. M. Chen, W. Jiang, J. Luo, T. Wen, "Modelling and simulation of new traction power supply system in electrified railway," In: ITSC 2015 IEEE 18th International Conference on Intelligent Transportation Systems; 15-18 September 2015; Las Palmas, Canada. New York, USA: IEEE. pp. 1345-1350. [CrossRef]
15. M. Soler, J. Lopez, J. Manuel, M. S. Pedro, J. Maroto, "Methodology for multiobjective optimization of the AC railway power supply system," *IEEE Transactions on Intelligent Transportation Systems*, vol. 16, pp. 2531-2542, 2015. [CrossRef]
16. Z. He, Y. Zhang, S. Gao, "Harmonic resonance assessment to traction power supply system considering train model in China high-speed railway," *IEEE Transactions On Power Delivery*, vol. 29, pp. 1735-1743, 2014. [CrossRef]
17. W. Song, J. Ma, L. Zhou, X. Feng, "Deadbeat predictive power control of single-phase three-level neutral-point-clamped converters using space-vector modulation for electric railway traction," *IEEE Transactıons On Power Electronics*, vol. 31, pp. 721-732, 2016. [CrossRef]
18. M. Shafighy, S. Khoo, A. Z. Kouzani, "Modelling and simulation of regeneration in AC traction propulsion system of electrified railway," *IET Electrical Systems in Transportation*, vol. 5, pp. 145-155, 2015. [CrossRef]
19. S. Kejian, W. Mingli, V. G. Agelidis, W. Hui W, "Line current harmonics of three-level neutral point-clamped electric multiple unit rectifiers: analysis," *Simulation and Testing, IET Power Electronics*, vol. 7, 1850-1858, 2014. [CrossRef]
20. P. Drabek, Z. Peroutka, M. Pittermann, P. Cedl, "New configuration of traction converter with medium-frequency transformer using matrix converters," *IEEE Transactıons On Industrıal Electronics,* vol. 58, pp. 5041-5048, 2011. [CrossRef]
21. H. Ozdemir, "Artificial neural networks and their usage in weaving technology," *Electronic Journal of Textile Technologies*, vol. 7, pp. 51-68, 2013.
22. M. Sahin, F. Buyuktumturk, Y. Oguz, "Light quality control with artificial neural networks," *Afyon Kocatepe University Journal of Science and Engineering*, vol. 13, vol. 1-10, 2013.
23. R. Bayindir, Ö. Sesveren, "Design of a visual interface for ANN based systems," *Pamukkale University Engineering Faculty Journal of Engineering Science,* vol. 14, pp. 101-109, 2008.
24. D. Askin, I. Iskender, A. Mamızadeh, "Dry type transformer winding thermal analysis usıng different neural network methods," *Journal of the Faculty of Engineering and Architecture of Gazi University*, vol. 26, pp. 905-913, 2011.
25. M. A. Cavuslu, Y. Becerikli, C. Karakuzu. "Hardware implementation of neural network training with levenberg-marquardt algorithm," *Journal of Computer Science and Engineering*, vol. 5, pp. 31-38, 2012.
26. İ. Dalkiran, K. Danisman, "Artificial neural network based chaotic generator for cryptology," *Turkish Journal Of Electrical Engineering And Computer Sciences*, vol. 18, pp. 225-240, 2010.
27. M. Ceylan, Y. Ozbay, O. N. Ucan, E. Yildirim, "A novel method for lung segmentation on chest ct images: complex-valued artificial neural network with complex wavelet transform," *Turkish Journal Of Electrical Engineering And Computer Sciences*, vol. 18, pp. 613-623, 2010.
28. S. Partal, İ. Senol, A. F. Bakan, K. N. Bekiroglu, "Online speed control of a brushless AC servomotor based on artificial neural networks," *Turkish Journal Of Electrical Engineering And Computer Sciences,* vol. 19, pp. 373-383, 2011.
29. S. Jashfar, S. Esmaeili, M. Z. Jahromi, M. Rahmanian, "Classification of power quality disturbances using s-transform and tt-transform based on the arti_cial neural network," *Turkish Journal Of Electrical Engineering And Computer Sciences,* vol. 21, pp. 1528-1538, 2013. [CrossRef]
30. M. Afsharizadeh, M. Mohammadi, "Prediction-Based reversible ımage watermarking using artificial neural networks," *Turkish Journal Of Electrical Engineering And Computer Sciences*, vol. 24, pp. 896-910, 2016. [CrossRef]
31. I. A. Ozkan, I. Saritas, S. Herdem, "Modeling of magnetic filtering with ANFIS," In: 12. National Conference on Electrical Electronic Computer Biomedical Engineering; 14-18 November 2007; Eskişehir, Turkey. Ankara, Turkey: CEE. pp. 415-418.
32. M. R. Minaz, A. Gun, M. Kurban, N. Imal, "Estimation of pressure, temperature and wind speed of bilecik using different methods," *Gaziosmanpasa Journal of Scientific Research*, vol. 3, pp. 100-111, 2013.
33. S. Sit, H. R. Ozcalik, E. Kilic, O. Dogmus, M. Altun, "Investigation of performance based on online adaptive neuro-fuzzy ınference system (ANFIS) for speed control of ınduction motors," *Cukurova University Journal of the Faculty of Engineering and Architecture,* vol. 31, pp. 33-42, 2016.
34. J. S. R. Jang, "ANFIS: Adaptive-network-based fuzzy inference system," *IEEE Transactions on Systems, Man, and Cybernetics,* vol. 23, pp. 665–685, 1993. [CrossRef]
35. S. Yurtcu and A. Ozocak, "Prediction of compression index of fine-grained soils using statistical and artificial intelligence methods," *Journal of the Faculty of Engineering and Architecture of Gazi University,* vol. 31, pp. 597-608, 2016.
36. C. J. Willmott and C. Matsuura, "Advantages of the mean absolute error (MAE) over the root mean square error (RMSE) ın assessing average model performance," *Climate Research*, vol. 30, pp. 79-82, 2005. [CrossRef]

İlhan Kocaarslan was born in Kırıkkale in 1964. He received his B.Sc. and first M.Sc. degrees in Electrical Engineering from Yıldız Technical University in 1983 and 1985 in Turkey, respectively. He received his second M.Sc. and Ph. D. degrees in Electrical Engineering from Bochum Ruhr University in 1986 and 1991 in Germany, respectively. He received the title of professor in 1999 in Turkey. Since 2008, he is working in Electrical-Electronics Engineering Department at İstanbul University, Turkey. His research interests are railway systems, control systems, automation, power generation, transmission and distribution.

Mehmet Taciddin Akçay was born in Kilis in 1984. He received his B.Sc. degree in Electrical Engineering from İstanbul Technical University in 2007 and M.Sc. degrees in Electrical and Electronics Engineering from Sakarya University in 2010. Since 2008 he is working in İstanbul Metropolitian Municipality, Directorate of Rail Systems. Since 2011 he is Ph. D. student in Electrical-Electronics Engineering Department at İstanbul University. His research interests are railway systems, power system analysis and energy management systems.

Abdurrahim Akgündoğdu was born in Bingöl in 1975. He received his B.Sc. and M.Sc. degrees in Electrical and Electronics Engineering and Biomedical Engineering from İstanbul University in 1995 and 2003, respectively. He received his Ph.D. degrees in Biomedical Engineering from İstanbul University in 2003 and 2010. He received the title of assistant of professor in 2014 in Turkey. Since 2000, he is working in Electrical-Electronics Engineering Department at İstanbul University, Turkey. His research interests are artificial intelligence, neural networks, automation, fuzzy logic.

Hasan Tiryaki was born in Denizli in 1980. He received his B.Sc. and M.Sc. degrees in Electrical and Electronics Engineering from Kırıkkale University in 2002 and 2005, respectively. He received the title of assistant of professor in 2016 in Turkey. Since 2012, he is working in Electrical-Electronics Engineering Department at İstanbul University, Turkey. His research interests are railway systems, control systems, automation, power generation, transmission and distribution.

İSTANBUL UNIVERSITY PRESS

RESEARCH ARTICLE

Electrica 2018; 18(1): 36-38

An Operational Transconductance Amplifier-based Memcapacitor and Meminductor

Yunus Babacan

Department of Electrical and Electronics Engineering, Erzincan University School of Engineering, Erzincan, Turkey

Cite this article as: Y. Babacan. 'An Operational Transconductance Amplifier-based Memcapacitor and Meminductor". *Electrica*, vol. 18, no. 1, pp. 36-38, 2018.

ABSTRACT

Previous studies have focused on the new mem-elements after the experimental realization of memristor which is the the fourth passive circuit element. This research presents a simple operational transconductance amplifier (OTA)-based memcapacitor and meminductor emulator circuit that does not comprise a mutator circuit. Each emulator was verified using the LTspice simulation program, and the simulation results were found to be compatible with the characteristic behaviors of the memcapacitor and meminductor.

Keywords: Memcapacitor, meminductor, emulator, OTA

Introduction

Leon Chua postulated the existence of a new basic passive circuit element, called the memristor, defined by a constitutive relationship between flux and charge linkage [1,2]. Researchers did not focused on the new element until fabricated a solid state implementation of the memristor [3]. The *n*-th order mem-elements are presented in the reference [4]. The mem-elements such as memcapacitor and meminductor attract interest therefore various SPICE models/circuits of memcapacitor and meminductor were showed by many researchers [5-10].

In this letter, Operational Transconductance Amplifier (OTA) based very simple memcapacitor and meminductor emulators that do not require any mutator to transform from memristor to memcapacitor or from memristor to meminductor is presented. The features of the proposed memelements are demonstrated via circuit simulations.

Memcapacitor Emulator Circuit

Current-mode structures have very low power consumption property (memristive elements have very low power consumption). For this reason OTA which is current mode circuit element is suitable for emulator design. The proposed memcapacitor circuit is shown in Figure 1. One output terminal of OTA is connected to the positive input terminal to provide resistive behaviour. Another terminal is connected to the C_2 capacitor to obtain memory effect of the proposed emulator. Negative input terminal of the OTA is connected to the voltage source which depends on the multiplication of the C_2 capacitor voltage and its integral [8]. The C_1 capacitor is initial capacitor of the proposed emulator.

Sinusoidal 100 mV input signals with various frequencies are applied to the input of the memcapacitor emulator and voltage-charge curves are obtained as shown in Figure 2a. The Figure 2b shows the input voltage-time and charge-time graphics.

Address for Correspondence:
Yunus Babacan

E-mail:
ybabacan@erzincan.edu.tr

Received: 17.08.2017

Accepted: 05.12.2017

DOI: 10.5152/iujeee.2018.1806

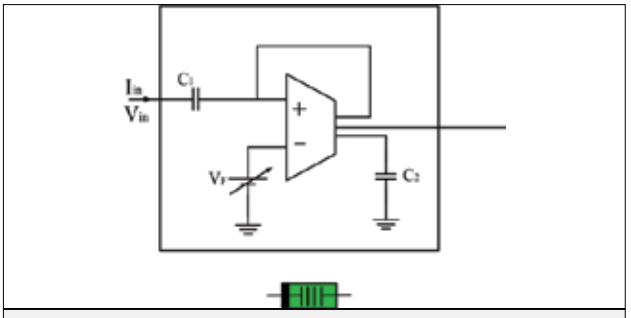

Figure 1. Memcapacitor emulator circuit based on OTA. Here C1=1nF, C2=1pF, gm=3mS

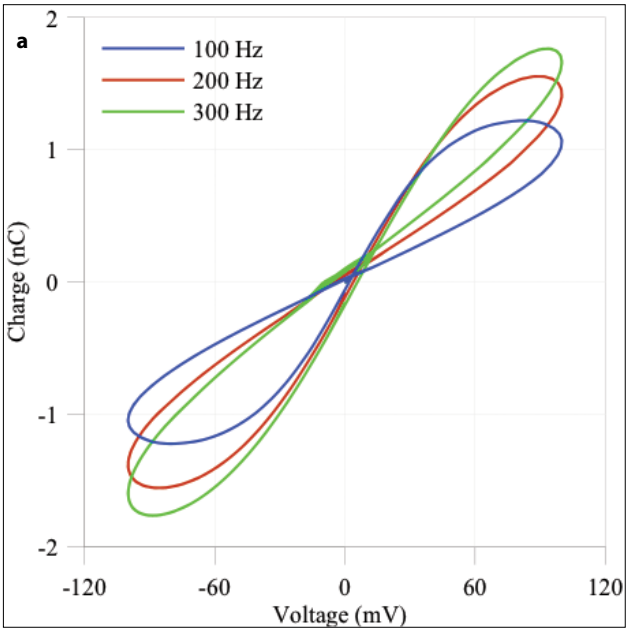

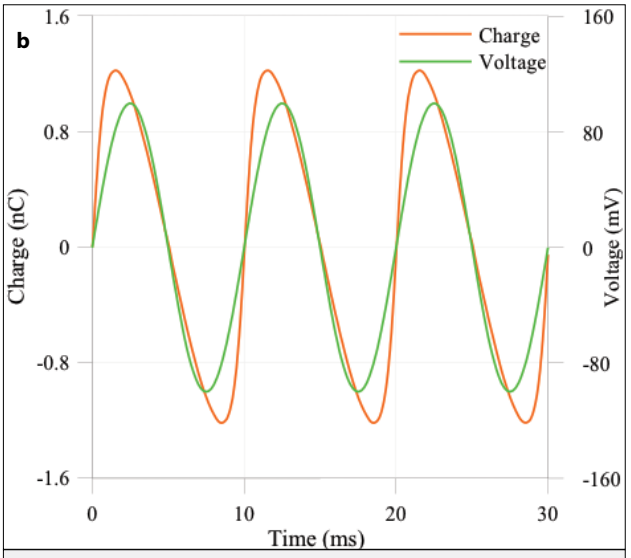

Figure 2. a,b. Simulation results under sinusoidal inputs for memcapacitor. a) Voltage-current relationship with various frequencies. b) Charge and input voltage of memcapacitor

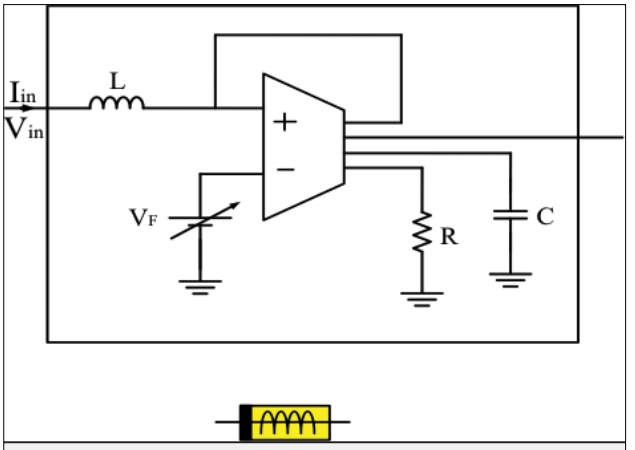

Figure 3. Meminductor emulator based on OTA. Here L=100 mH, C=1pF, R= 1 kΩ, gm=30 µS

The input current is given by:

$$I_{in} = C_1 \frac{d(V_{in} - V_F)}{dt} \quad (1)$$

This equation can be rewritten as below:

$$\frac{q(t)}{C_1} + V_F = V_{in} \quad (2)$$

$$V_F = V_{C2} \int V_{C2} = \frac{q(t)}{C_2^2} \int q(t)\,dt, (q(t) = C_2 V_{C2}) \quad (3)$$

q(t) is variable part of the proposed circuit that is why VF changes and provides the memcapacitive behaviour of the proposed emulator circuit.

Meminductor Emulator Circuit

Similar circuit topology used for meminductance design as shown in Figure 3. Negative input of the OTA is derivative of the multiplication of the resistor and capacitor voltages. One output of the OTA is connected to the its input to provide the resistive behaviour. The voltages on the capacitor and resistor provide the memory effect and inductance change ranges respectively.

The proposed meminductance emulator is operated under 100 nA sinusoidal input currents with 100, 300, 500 Hz respectively. Meminductor behaves frequency-dependent characteristic as shown in Figure 4a. The flux and current waveforms cross zero levels as shown in Figure 4b. Namely phase difference is zero between the both signals that is why hysteresis effects can be seen in current-flux relationship.

The fundamental relationship between flux and current is:

$$\varphi(t) = \int (V_{in} - V_F)dt = L\,i(t) \quad (4)$$

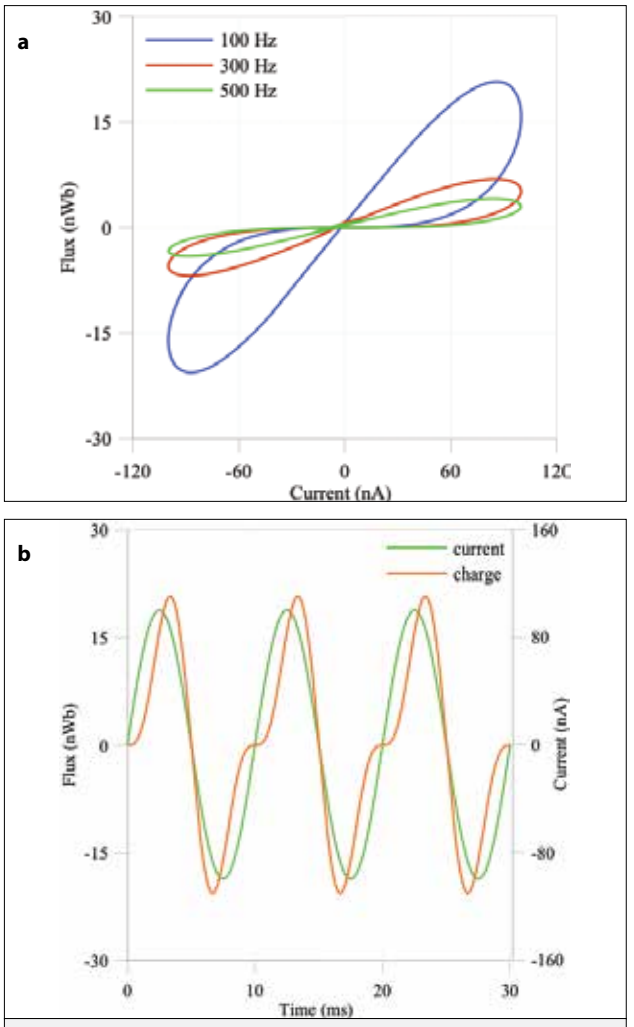

Figure 4. a,b. Various curves for meminductor emulator circuit. a) Hysteresis loops under periodic sinusoidal current input. b) Flux and input current of meminductor

The V_A voltage equals to the multiplication of resistor and capacitor.

$$V_A = V_R x V_C \qquad (5)$$

Here:

$$V_R = I_{in}(t) x R \text{ and } V_C = \frac{q(t)}{C} \qquad (6)$$

Negative input of the OTA,

$$V_F = \int V_A dt = \int \left(\frac{q(t) R I_{in}(t)}{C} \right) dt \qquad (7)$$

Equation (4) and (7) can be rearranged:

$$\varphi(t) = \left[L + \frac{q(t)R}{C} \right] I_{in}(t) \quad (8)$$

The flux change of the proposed circuit can be seen from equation (8) and the inductance changes according to the $\frac{q(t)R}{C}$.

Conclusions

Simple OTA based memcapacitor and meminductor emulator circuits are presented. Many memcapacitor and meminductor circuits or models consist of memristor element but proposed emulator is designed without any memristor circuit or models. Emulators which have no memristor circuit or models become more effectively according to the memristor based mem-elements so the proposed emulators are suitable for memcapacitor and meminductor based circuit applications. And also these emulators have simple structures. The behaviours of the proposed memelements are demonstrated via circuit simulations and all results compatible with previous studies.

References

1. L. O., Chua, "Memristor - the missing circuit element," *IEEE Trans. Circuit Theory*, vol. 18, pp. 507-519, 1971. [CrossRef]
2. L. O. Chua and S.M Kang, Memristive Devices And Systems. *Proceedings of The IEEE*, pp. 209-223, 1976. [CrossRef]
3. D. B. Strukov, G. S. Snider, D. R. Stewart, Williams, R. S., "The missing memristor found," *Nature*, vol. 453, 7191, pp. 80–83, 2008. [CrossRef]
4. L. O. Chua, "Nonlinear Circuit Foundations for Nanodevices, Part I: The Four-Element Torus," *Proceedings of the IEEE*, vol. 91, 11, pp. 1830-1859, 2003. [CrossRef]
5. M. P. Sah, R.K. Budhathoki, C. Yang, H. Kim, "Mutator-Based Meminductor Emulator for Circuit Applications", *Circuits Systems Signal Process,* vol. 33, pp. 2363–2383, 2014. [CrossRef]
6. D. Biolek and V. Biolkova, "Mutator for transforming memristor into memcapacitor", *Electronics Letters,* vol. 46, pp. 21, 2010. [CrossRef]
7. Y. V. Pershin and M. Di Ventra, "Memristive circuits simulate memcapacitors and meminductors", *Electronics Letters,* vol. 46, pp. 21, 2010. [CrossRef]
8. M.E. Fouda and A.G. Radwan, "Charge controlled memristor-less memcapacitor emulator", *Electronics Letters,* vol. 48, pp. 23, 2012. [CrossRef]
9. M.P. Sah, R.K. Budhathoki, C. Yang, H. Kim, "Charge Controlled Meminductor Emulator", *Journal of Semiconductor Technology And Science,* vol. 14, 6, pp. 750-754, 2014. [CrossRef]
10. D. Biolek, Z. Biolek, V. Biolkova, "Behavioral Modeling of Memcapacitor", *Radioengineering,* pp. 228-233, 2011.

Yunus Babacan received B.Sc., M.Sc. degrees in Electrical and Electronics Engineering at Atatürk University, 2008 and 2011 respectively. He received his Ph.D. degree in Electrical and Electronics Engineering at Istanbul University in 2016. His main research interests are memristive systems, analog circuit design and memristor based biological circuit/system design. He is currently working as an assistant professor at the Electrical and Electronics Engineering department of Erzincan University.

İSTANBUL UNIVERSITY PRESS

RESEARCH ARTICLE

Electrica 2018; 18(1): 39-44

A Molecularly Imprinted Polymer Based Biosensor for Electrochemical Impedance Spectroscopic Analysis

Feride Şermin Utku[1], Ozan Enver Özdemir[1,2], Melahat Sevgül Bakay[1,3]

[1]Department of Biomedical Engineering, Yeditepe University School of Engineering, İstanbul, Turkey
[2]Department of Metallurgical and Materials Engineering, İstanbul Technical University School of Engineering, İstanbul, Turkey
[3]Department of Electrical and Electronic Engineering, İstanbul Technical University School of Engineering, İstanbul, Turkey

Cite this article as: F. Ş. Utku, O. E. Özdemir, M. S. Bakay. "A Molecularly Imprinted Polymer Based Biosensor for Electrochemical Impedance Spectroscopic Analysis". *Electrica*, vol. 18, no. 1, pp. 39-44, 2018.

ABSTRACT

A molecularly imprinted polymer (MIP)-based impedimetric biosensor was developed for the electrochemical analysis of low-weight biological molecules. Synthetic polymeric matrices with specific and selective recognition sites, which are complementary to the shapes and sizes of the functional groups of analytes, can be prepared using the molecular imprinting method. In this study, a small molecule, tris(hydroxymethyl)aminomethane (TRIS), was used to coat a graphite pencil tip with a TRIS-containing polyacrylamide gel to fabricate a working electrode. The electrode modification and performance were evaluated using cyclic voltammetry and electrochemical impedance spectroscopy. The electrochemical properties of the modified electrodes were observed using an electrochemical cell comprising a Ag/AgCl reference electrode, a Pt wire as the counter electrode, and a pencil graphite tip as the working electrode using a redox-phosphate buffer solution with different concentrations of TRIS and Ethylenediaminetetraacetic acid (EDTA). The I–V and impedance performance of the chemically modified graphite pencil-tip electrodes exhibited decreased conductance and increased impedance correlating with the increase in TRIS concentration. Thus, MIP-based small-molecule biosensor prototypes can be promising economical replacements over other expensive sensors.

Keywords: Molecularly Imprinted Polymer, Cyclic Voltammetry, Electrochemical Impedance Spectroscopy, tris(hydroxymethyl)aminomethane, Pencil Graphite Electrode

Introduction

Biosensor, a device used in the detection of an analyte, combines a biological/chemical sensor component with a physicochemical transducer. The sensor and the transducer elements recognize and detect the analyte qualitatively and/or quantitatively [1-3]. The biological sensor element may be in the form of tissue, microorganism, organelle, receptor, enzyme, antibody, nucleic acid, molecule, etc., which may be attached to the metal, polymer or glass surface of the electrode through chemical and physical means.

A biological sensor element may be relatively short-lived and with complications in handling; therefore, they may be replaced with artificial elements that are components of a receptor-based sensing system. Molecular Imprinting Technology (MIT) is a method that aims to overcome these complications by producing selectively specific artificial receptors. It utilizes molecular imprinting polymer (MIP), formed as a dependable molecular recognition element with room temperature stability that mimicks natural recognition elements, such as antibodies and receptors. MIT is used in the detection, separation and purification of biological and chemical molecules, such as amino acids and proteins, nucleotids, toxins, drugs, etc. A 3D polymeric network is formed between the analyte and monomer through functional hydrogen bonds, dipole–dipole and ionic interactions. After polymerization, upon removal of the analyte, specific recognition sites that are in the shape, size and chemical structure of the analyte are formed in the polymer [4-11].

There are examples of MIP based sensors equipped more commonly with SPRS and QCM based transducers [4]. However, they have not been experimented in the detection of small

Address for Correspondence:
Feride Şermin Utku

E-mail:
sermin.utku@yeditepe.edu.tr

Received: 23.08.2017

Accepted: 23.11.2017

DOI: 10.5152/iujeee.2018.1807

molecules, such as metabolites formed during the various stages of cellular development using electrochemical transducers. Hydroxymethylaminomethane (TRIS), has been chosen as a small molecule used in established basimetric standard and buffer solutions, commonly used in biochemistry and molecular biology processes, such as protein and nucleic acid extraction and purification [12]. As the basic small molecule, TRIS has been used to produce the MIP electrode coated with TRIS containing polyacrylamide gel (PAGE) to produce TRIS receptor sites.

In this study, a MIP based sensor for TRIS made of pencil graphite electrode (PGE) was combined with electrochemical transduction techniques, i.e. cyclic voltammetry (CV) and electrochemical impedance spectroscopy (EIS) [13]. Upon binding of the analyte to the receptor sites on the gel surface, changes in I-V properties and impedance of the MIP modified PGE were expected to be detected using CV and EIS.

Materials and Experimental Method

Materials

Merck analytic quality chemicals were used in this study. For the electrochemical analysis, 20 mM $K_3[Fe(CN)_6]$ redox pair in phosphate buffer solution was used (redoks-PBS, 137mM NaCl, 2.7mM KCl, 10mM Na_2HPO_4, 1.8mM KH_2PO_4, pH 7.4) [14-16].

Three types of PGEs were prepared: (a) control electrodes (PGE), (b) positive control electrodes (PAGE-PGE), and (c) experimental electrodes for TRIS analysis (TRIS-PAGE-PGE). All electrodes were initially anodized in acetic buffer solution (ABS, 0.1 N acetic acid, 0.1 N sodium acetate, 20 mM NaCl, pH 4.8) for 60 seconds at +1.4V [15].

Five PGEs were used as control electrodes without further processing. PAGE-PGEs were prepared by coating PGEs with 12% polyacrylamide gel. TRIS-PAGE-PGEs were prepared by coating PGEs with 12% polyacrylamide gel containing 10M TRIS.

Instruments

Anodization and electrochemical analysis were conducted using a potentiostat (ZIVE SP2 Potentiostat/Galvonostat, Referans 600, Korea) equipped with ZMAN EIS data analysis program. The three-electrode cell consisted of Ag/AgCl as the reference electrode, platinum wire as the counter electrode, and PGE as the working electrode. The morphology of the coating on working electrodes was characterized by Scanning Electron Microscope (SEM) (Carl ZEISS EVO40).

Electrochemical Measurement Method

PGEs, PAGE-PGEs and TRIS-PAGE-PGEs were characterized electrochemically as stated below. Electrochemical measurements were conducted by immersing the working electrodes in solution at a depth of 2.5 cm and at a distance of 5 cm from the counter electrode.

Electrode modification was characterized using $K_3[Fe(CN)_6]$, a commonly used redox couple former $[Fe(CN)_6]^{4-}$ / $[Fe(CN)_6]^{3-}$ with well-defined electron transfer kinetics. Cyclic voltammetry was used at an applied potential varying between -500 and 500 mV relative to V_{ref} (step size: 20 mV, scan rate: 50 mV/s. I-V cycles were generated by swaying the potential initially anodically, then cathodically. In the forward scan, $Fe(CN)_6^{-4}$, is oxidized, generating an oxidative peak, followed by a reductive peak in the reverse scan [16].

$$Fe(CN)_6^{-4} \rightarrow Fe(CN)_6^{-3} + e^- \quad (1)$$

$$Fe(CN)_6^{-3} + e^- \rightarrow Fe(CN)_6^{-4} \quad (2)$$

The open cell potential (OCP) was measured in redoks-PBS solution till stabilization. The electrochemical impedance studies were conducted using AC voltage at an amplitude of +10 mV relative to OCP, between a frequency range of 10,000 and 0.01 Hz.

The CV and EIS response of the TRIS-PAGE-PGEs to the analyte was examined by introduction of incremental amounts of 0.25M TRIS to determine electrode response to TRIS (400, 600, 800, and 1000 µl, at a final concentration of 1.0, 1.5, 2.0 and 2.5 mM respectively). To confirm selectivity and specificity of the electrode to TRIS, incremental amounts of 0.25M Ethylenediamine tetraacetic acid (EDTA) was used (400, 800, and 1000 µl, at a final concentration of 1.0, 2.0 and 2.5 mM respectively).

Results

In this study, PGEs were modified to produce PAGE-PGEs and TRIS-PAGE-PGEs. Binding of TRIS to the TRIS-PAGE-PGEs was demonstrated using electrochemical methods as indicated with an increase in impedance. The selective specificity of the TRIS electrode was further confirmed by experiments involving EDTA, indicating that EDTA not bound to the surface increased solution conductivity and reduced impedance.

PGEs were anodized in ABS at +1.4V in order to limit the conductivity of PGEs [17]. In order to standardize the electrical conductivity of the electrodes, the initial 30 sec. anodization length (Figure 1) was extended to 60 sec. The PGEs were chosen among the low conducting anodized electrodes. Post 60 sec. oxidation, PGE conductivity was sufficiently decreased to values ranging between 42-142 µA.

The electrochemical properties of PGEs (C1 and E1) and PAGE-PGEs (C2 and E2) electrodes were determined in redoks-PBS solution using CV (Figure 2) and EIS (Figure 3).

The cell potential, the current amplitude and peak potential of PAGE-PGEs decreased with PAGE coating (Figure 2 and 4, C1-C2), while impedance was increased as expected (Figure 3, E1-E2). The I-V behavior of TRIS-PAGE-PGEs (Figure 2 and 4, C3-C6) displayed a decrease in current amplitude and a slight and gradual increase in peak potential and electrochemical cell potential; while in the EIS spectrum an increase in impedance,

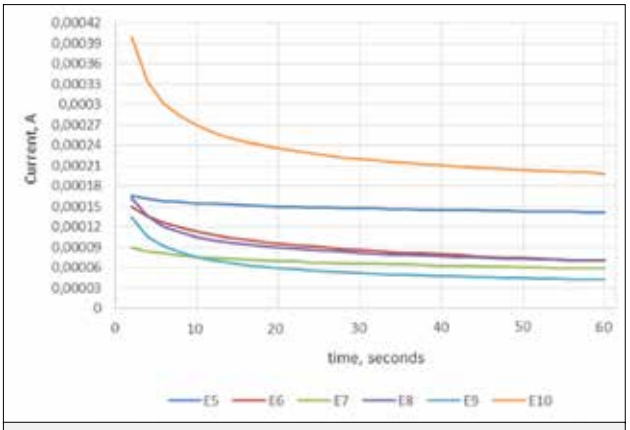

Figure 1. Current-time curve for PGEs anodized in ABS at +1.4V

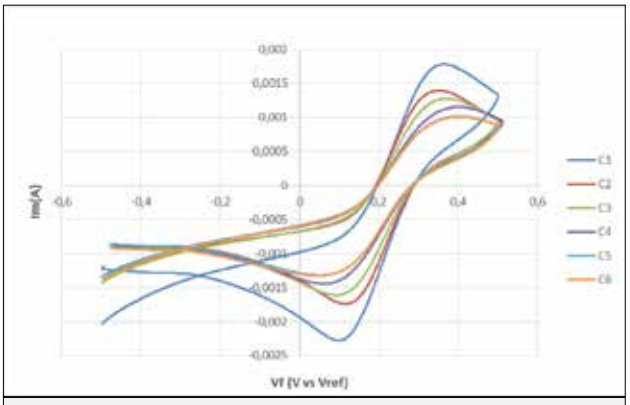

Figure 2. CV graphics in redoks-PBS solution. C1; PGE, C2; PAGE-PGE, C3-C6: TRIS-PAGE-PGE in TRIS-redoks-PBS solution; C3; 1 mM TRIS, C4; 1.5 mM TRIS, C5; 2 mM TRIS, C6; 2.5 mM TRIS

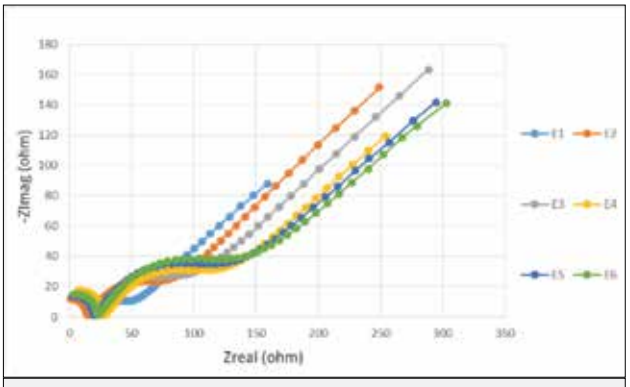

Figure 3. EIS graphics in redoks-PBS solution. E1: PGE, E2: PAGE-PGE, E3-E6: TRIS-PAGE-PGE in TRIS-redoks-PBS solution; E3: 1 mM TRIS, E4: 1.5 mM TRIS, E5: 2 mM TRIS, E6: 2.5 mM TRIS

correlating with the incremental increase in TRIS concentration was observed (Figure 3 and 4d, E3-E6).

The incremental increase in the EDTA concentration in redoks-PBS solution did not display a significant effect on the I-V behavior of TRIS-PAGE-PGEs (Figure 5). The EIS spectrum of TRIS-PAGE-PGEs exposed to an increase in EDTA concentration

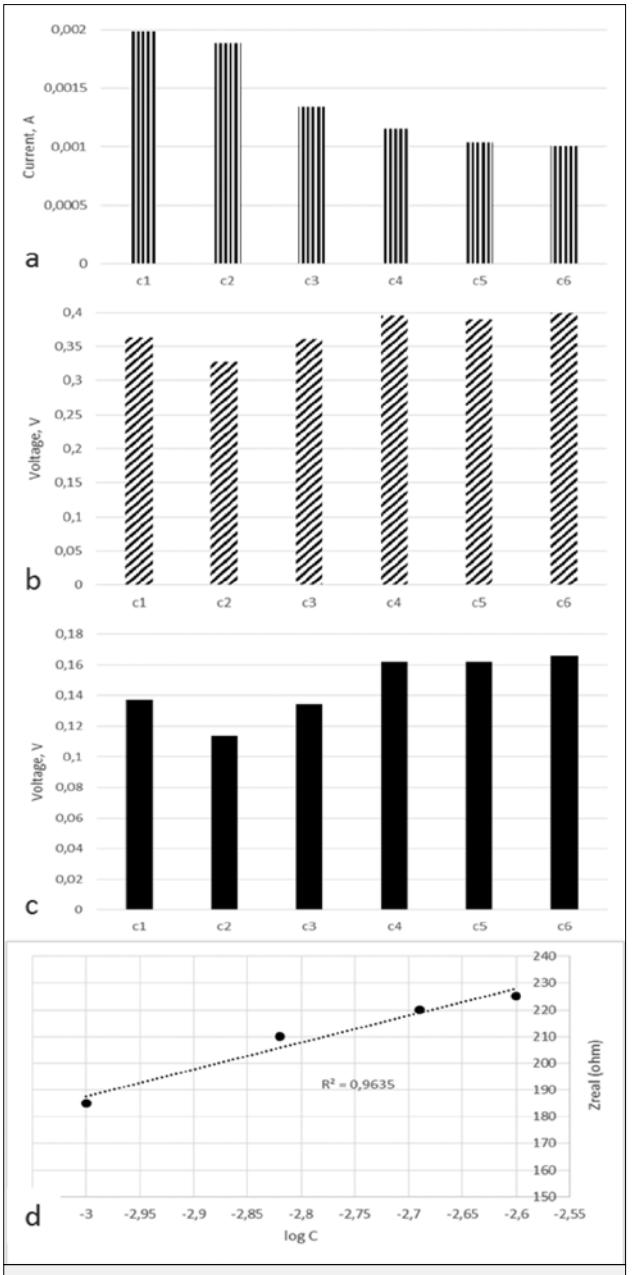

Figure 4. Electrochemical behavior of TRIS-PAGE-PGE in redoks-PBS solution in incremental amounts of TRIS. (a) peak current, (b) peak voltage, (c) electrochemical cell potential, (d) Zreal vs TRIS concentration

displayed a reduction in impedance (from 400 to 230 Ohms for Zreal and from 225 to 120 Ohms for -ZImag) with an apparent increase in solution conductivity as observed in the decrease in the radius of the semi-circular portion of the curve (Figure 6).

The morphology of the electrodes displaying the uncoated PGE surface (Figure 7a), the PAGE layer on PAGE-PGE surface (Figure 7b), and the TRIS-PAGE-PGE surface after electrochemical characterization in TRIS-redoks-PBS solution (Figure 7c) was characterized using SEM imaging.

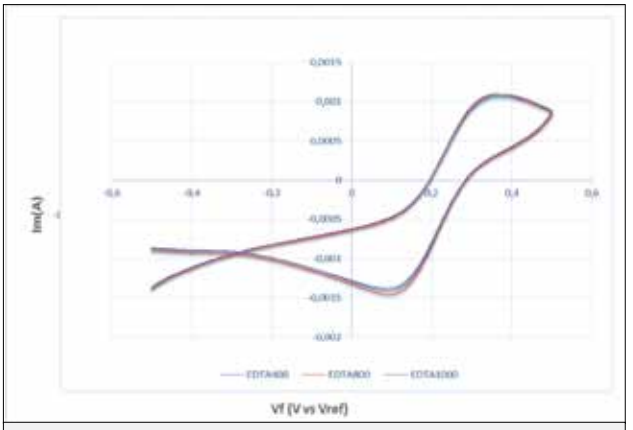

Figure 5. CV graphics for TRIS-PAGE-PGE in redoks-PBS solution in incremental amounts of EDTA in redoks-PBS solution. EDTA400/800/1000 with 1/2/2.5 mM EDTA

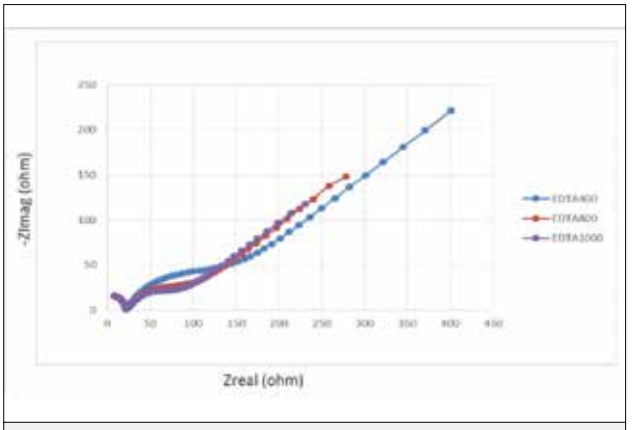

Figure 6. EIS graphics for TRIS-PAGE-PGE in redoks-PBS solution in incremental amounts of EDTA in redoks-PBS solution. EDTA400/800/1000 with 1/2/2.5 mM EDTA

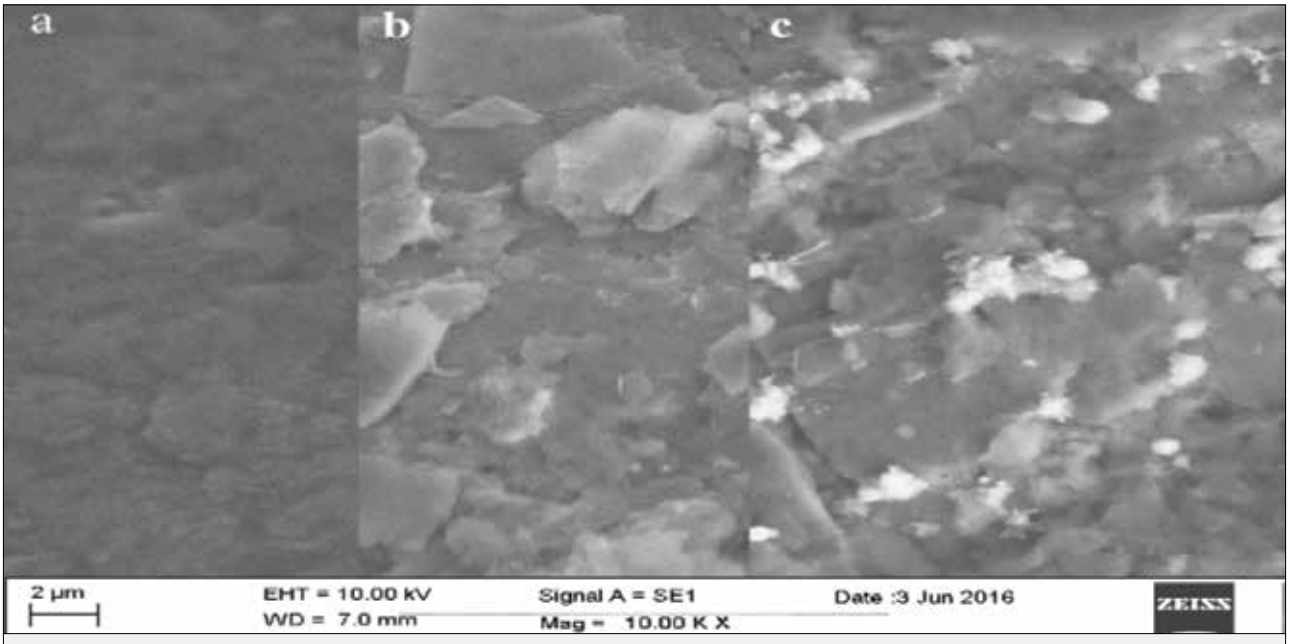

Figure 7. SEM images of (a) plain PGE surface, 10kX; (b) PAGE-PGE coated surface, 10kX; (c) TRIS-PAGE-PGE coated surface with TRIS crystals, 10kX

Discussion

In this study, a prototypic small molecule detecting biosensor, selectively specific to TRIS was produced using MIP-coated PGE as the sensing element and a potentiostat as the transducer in the conductance of CV and EIS analysis.

Graphite pencil leads, modified as PGE working electrodes are composite materials containing graphite (~65%), clay (~30%), and a binder (wax, resins, or high polymer) [18]. PGEs with high chemical and mechanical stability can be used in a wide range of working potentials [18]. PGEs are cheap, easily modified and convenient to use in quantification of a variety of analytes from a wide range of samples. With an active electrode surface area of approximately 0.255 cm^2, they can be used to analyse low concentrations of small volume samples without any preconcentration/deposition step [18].

PGEs are highly durable and stable, yielding reproducible signals and well-defined voltammetric peaks with good sensitivity and reproducibility. Background currents generated by clays and polymers contained in PGEs are much lower than those given by the conventional solid electrodes, such as glassy carbon, gold, and platinum; while displaying electron transfer rates similar to those of glassy carbon electrodes [18].

Variation in size and composition of PGEs result in differences in physical and chemical properties, thus, demonstrating vari-

ation in electrical properties. Anodization of PGEs in ABS solution leads to the oxidation of the carbon surface [17] and thus limiting current transmitted. CV studies in $K_4[Fe(CN)_6]$ have indicated that electron transfer rate correlates with an increase in diameter, generating higher amplitude signals used in quantitative determinations, while small diameter PGEs display better reversibility in qualitative investigations.

When the I-V behavior of TRIS-PAGE-PGEs and PAGE-PGEs is compared with the PGEs, a reduction in anodic and cathodic current (Figure 3) is demonstrated due to the reduced electron transfer rate of the redoks pair as a result of the polymer coating [16]. The decrease in oxidative and reductive peak current may be due to the changes in load transfer resistance of electrode surface [19,20]. In addition, the expected reduction in anodic and cathodic current in the TRIS-PAGE-PGEs has correlated with the incremental increase in TRIS concentration. It must be noted that the I-V behavior of TRIS-PAGE-PGEs in 2 and 2.5 mM TRIS-redox-PBS solution has displayed no apparent change at the higher concentration implying saturation of the polymer surface with TRIS (Figure 2, 3 and 7).

When the impedimetric behavior of TRIS-PAGE-PGEs and PAGE-PGEs is compared with PGEs, a reduction in electron transfer rate of the redox pair was displayed as a result of an increase in impedance (Figure 5) [13]. In addition, the expected increase in the impedance, i.e. the capacitance and diffusion resistance of TRIS-PAGE-PGEs correlated with the incremental increase in TRIS concentration as indicated by the increase in the semicircle diameter and load transfer resistance of the electrode [13]. It must be noted that the decrease in impedance of TRIS-PAGE-PGEs in 2 and 2.5 mM TRIS-redox-PBS solution being lower than expected at the higher concentration implies saturation of the polymer surface with TRIS (Figure 2, 3 and 7).

The CV and EIS results of TRIS-PAGE-PGEs (Figure 2, 3) indicated binding of the chosen analyte (TRIS) to the electrode. In order to determine the specificity of the biosensor to TRIS, the TRIS-PAGE-PGEs were experimented using EDTA. The results of these experiments indicated that the EDTA was not bound to TRIS-PAGE-PGEs since no apparent change in I-V behavior, i.e. a change in anodic and cathodic peak current, correlating with concentration was observed. EDTA, not bound to the electrode surface, remained in solution increasing solution conductivity and subsequently decreasing both solution and thus the total impedance. With the increase in EDTA concentration, the diameter of the semicircular portion of the curve corresponding to solution impedance was reduced and load transfer resistance was decreased.

Conclusions

In this study, a biosensor consisting of a TRIS-MIP sensor and an electrochemical transducer was developed. Electrode modification and performance was evaluated using CV and EIS. Graphite pencil tip was coated with polyacrylamide gel containing TRIS as the analyte and prepared as the working electrode. The electrochemical properties of the electrodes at various concentrations of TRIS and EDTA and $K_3[Fe(CN)_6]$ redox pair containing phosphate buffer solution, using Ag/AgCl reference electrode, platinum counter electrode and working electrode made of graphite pencil tip electrochemical cell were evaluated. The results indicate a correlation between the CV and EIS response and TRIS and EDTA solution concentration. With further research and improvements, the prototypic biosensor selectively specific to TRIS generated in this study can be a promising economical replacement for the commonly used expensive techniques.

Acknowledgements

We would like to thank Prof.s Dr. Ali Umit Keskin and Mustafa Culha, Assoc. Prof.s Levent Urgan and Erde Can from Yeditepe University, Faculty of Engineering.

References

1. A. Turner, I. Karube, G. S. Wilson, "Biosensors: Fundamentals and Applications", Oxford University Press, Oxford, U.K., 1987.
2. F. G. Banica, ed., "Chemical Sensors and Biosensors: Fundamentals and Applications", John Wiley & Sons, Hoboken, New Jersey, U.S.A., 2012. [CrossRef]
3. B. R. Eggins, "Chemical Sensors and Biosensors", John Wiley & Sons, Hoboken, New Jersey, U.S.A., 2002.
4. S. Yan, Y. Fang, Z. Gao, "Quartz crystal microbalance for the determination of daminozide using molecularly imprinted polymers as recognition element", *Biosensors and Bioelectronics*, vol. 22, no. 6, pp. 1087-1091, Apr, 2007. [CrossRef]
5. C. Alexander, H. S. Andersson, L. I. Andersson, R. J. Ansell, N. Kirsch, I. A. Nicholls, and M. J. Whitcombe, "Molecular imprinting science and technology: a survey of the literature for the years up to and including 2003", *J Molecular Recognition*, vol. 19, no. 2, pp. 106-180, Jan, 2006. [CrossRef]
6. W. Li and S. Li, "Oligomers-Polymer Composites-Molecular Imprinting", Springer, Berlin-Heidelberg, Germany, 2006.
7. G. Guan, B. Liu, Z. Wang, Z. Zhang, "Imprinting of molecular recognition sites on nanostructures and its applications in chemosensors", *Sensors*, vol. 8, no. 12, pp. 8291-8320, Dec, 2008. [CrossRef]
8. L. Ye and K. Haupt, "Molecularly imprinted polymers as antibody and receptor mimics for assays, sensors and drug discovery", *Analytical and Bioanalytical Chemistry*, vol. 378, no. 8, pp. 1887-1897, Jan, 2004. [CrossRef]
9. A. Bossi, F. Bonini, A. P. F Turner and S. A. Piletsky, "Molecularly imprinted polymers for the recognition of proteins: the state of the art", *Biosensors and Bioelectronics*, vol. 22, no. 6, pp. 1131-1137, Jan, 2007. [CrossRef]
10. E. Caro, N. Masqué, R. M. Marcé, F. Borrull, P. A. Cormack, and D. C. Sherrington, "Non-covalent and semi-covalent molecularly imprinted polymers for selective on-line solid-phase extraction of 4-nitrophenol from water samples", *J Chromatography A*, vol. 963, no. 1, pp. 169-178, July, 2002. [CrossRef]
11. G. Vasapollo, R. D. Sole, L. Mergola, M. R. Lazzoi, A. Scardino, S. Scorrano, and G. Mele, "Molecularly imprinted polymers: present and future prospective", *Int. J Mol Sci*, vol. 12, no. 9, pp. 5908-5945, Sept 14, 2011. [CrossRef]

12. G. Gomori, "Preparation of Buffers for Use in Enzyme Studies", *Methods Enzymol.*, vol. 1, pp. 138-146, 1955. [CrossRef]
13. E. Barsoukov and J. R. Macdonald, "Impedance spectroscopy: theory, experiment, and applications", John Wiley & Sons, Hoboken, New Jersey, U.S.A., 2005. [CrossRef]
14. B. Ozcan, B. Demirbakan, G. Yesiller and M.K. Sezginturk, "Introducing a new method for evaluation of the interaction between an antigen and an antibody: Single frequency impedance analysis for biosensing systems", *Talanta*, vol. 125, pp. 7-13, July**,** 2014. [CrossRef]
15. S. N. Topkaya, D. Ozkan-Ariksoysal, B. Kosova, R. Ozel and M. Ozsoz, "Electrochemical DNA biosensor for detecting cancer biomarker related to glutathione S-transferase P1 (GSTP1) hypermethylation in real samples", *Biosensors and Bioelectronics*, vol. 31, no. 1, pp. 516-522, Jan**,** 2012. [CrossRef]
16. E. Asav and M. K. Sezginturk, "A novel impedimetric disposable immunosensor for rapid detection of a potential cancer biomarker", *Int. J Biological Macromolecules*, vol. 66, pp. 273-280, May, 2014. [CrossRef]
17. L. Figueiredo, M. F. R., Pereira, M. M. A. Freitas and J. J. M. Orfao, "Modification of the surface chemistry of activated carbons", *Carbon*, vol. 37, no. 9, pp. 1379-1389, Dec**,** 1999. [CrossRef]
18. I. G. David, D.-E. Popa and M. Buleandra, "Pencil Graphite Electrodes: A Versatile Tool in Electroanalysis", *J Analytical Methods in Chemistry*, https://doi.org/10.1155/2017/1905968, Jan, 2017. [CrossRef]
19. I. S. Park and N. Kim, "Thiolated Salmonella antibody immobilization onto the gold surface of piezoelectric quartz crystal", *Biosensors and Bioelectronics*, vol. 13, no. 10, pp. 1091-1097, Nov, 1998. [CrossRef]
20. I. Markovich and D. Mandler, "The effect of an alkylsilane monolayer on an indium tin oxide surface on the electrochemistry of hexacyanoferrate", *J Electroanalytical Chemistry*, vol. 484, no. 2, pp. 194-202, Apr**,** 2000. [CrossRef]

Feride Sermin Utku received her B.S. degree in Biology and Chemistry ID from Earlham College, Richmond, IN, USA, and her MSc and PhD degrees in Biomedical Engineering from Bogazici University, İstanbul, Turkey in 2008. She has been teaching biomaterials at Yeditepe University, İstanbul, Turkey since 2013. Her research interests are biomaterials, surface coatings of implants, hard tissue biomineralization and ceramic materials.

Ozan Enver Özdemir received his B.S. degree in Biomedical Engineering from Yeditepe University, İstanbul, Turkey in 2016. This paper, based on his undergraduate thesis titled "MIP Based Biosensor for Impedance Spectroscopic Analysis" was presented at the Congress of Medical Technologies 2016.

Melahat Sevgül Bakay received her B.S. degree in Biomedical Engineering from Yeditepe University, İstanbul, Turkey in 2016. This paper, based on her undergraduate thesis titled "MIP Based Biosensor for Impedance Spectroscopic Analysis" was presented at the Congress of Medical Technologies 2016.

İSTANBUL UNIVERSITY PRESS

RESEARCH ARTICLE

Electrica 2018; 18(1): 45-51

Design and Implementation of a Smart Controller in Agriculture for Improved Productivity

V Sravani, Santhosh K V, Sanjay Bhargava, Verina D'Almeida

Department of Instrumentation and Control Engineering, Manipal Institute of Technology, Manipal Academy of Higher Education, Manipal, India

Cite this article as: V. Sravani, S. K. V., S. Bhargava, V. D'Almeida. "Design and Implementation of a Smart Controller in Agriculture for Improved Productivity". *Electrica*, vol. 18, no. 1, pp. 45-51, 2018.

ABSTRACT

Agricultural produce significantly depends on many crop parameters such as humidity, pH, temperature, sunlight, microbial activity, soil ions, air quality, and water quality. A higher production of crop can be achieved via maintaining all these parameters in the desired range. A smart system was developed to control the environmental parameters in the desired range via incorporating a multisensor to measure the parameters such as humidity, temperature, and sunlight; in addition, also a suitable controller was designed to control these parameters in the desired range. Sensors were placed to continuously monitor the field parameters such as temperature, humidity, sunlight, and soil moisture. All these parameters were remotely acquired using ZigBee to PC through myRIO boards. Fuzzy-based controllers were designed to operate the actuators to maintain the set point. The designed system on implementation was tested on a real-life model. The results show that the proposed technique maintained the parameters at the desired state and reduced human intervention and labor.

Keywords: Agriculture, fuzzy, humidity, light, soil moisture, temperature

Introduction

The Agricultural production of any country is predominantly volatile and depends on varied factors. The changing rainfall patterns, extreme variations in temperatures, soil and air quality have significant impact on the production yield. The rain-fed agricultural production system is vulnerable to seasonal variability which affects the livelihood of the farmers and landless laborers who depend on this system. Moreover population has significantly increased over past two decades, this led to urban land expansion due to increase in urban population which caused the degradation of agricultural land which in turn has affected the production of food growth. Hence various techniques have come into existence to increase the productivity by enhancing the natural and biological processes above and below the ground. Like in [1], discusses the influence of science and technology on agriculture in Africa. One way to increase the production and benefit the farmers is by continuously monitoring climatic parameters and notify them with present weather condition so that immediate action can be taken manually or automatically for the benefit of the crop. The parameters which are continuously monitored are temperature, soil moisture, light and humidity [2]. Due to advancement in field of science and technology, efficient sensors for all required ranges are available in the market with different sizes and different measurement principles. Technology also has led to wireless transmission of data from the sensors to remote location and without the intervention of humans, parameters can be controlled and monitored which has led to agricultural automation. Wireless sensor networks are most commonly used these day for continuous monitoring of the crops.

As food is essential for human survival, there is lot of work going in particular area to enhance the productivity and meet the demands of the people. There are several issues which are to be addressed for agricultural growth like climatic changes, drought, soil infertility etc. Authors in [3] have tried to address this issue by motivating farmers of one particular region to adopt climate-smart agriculture (CSA) technologies which focuses on productivity, mitiga-

Address for Correspondence:
Santhosh K V

E-mail:
kv.santhu@gmail.com

Received: 13.09.2017

Accepted: 24.10.2017

DOI: 10.5152/iujeee.2018.1808

tion in agriculture based on climatic conditions using different techniques under water-smart, energy-smart, nutrient-smart, carbon-smart, weather-smart, knowledge-smart technologies. As an extension to this proposed work in [4], authors have reported the rapid appraisal of climate smart agriculture system to discuss the influence of climate on agriculture. Authors in [5] have stated that the crop rotation can be one of the way to increase yield from crops and concluded that when winter wheat is grown after pea and winter barley crop, production of winter wheat is improved under varying climatic conditions.

The system approach to any problem always give a better idea to solve it, based on the same approach, agriculture also have different agriculture system models, which are discussed in [6], practiced from the year 1960 to present. They have stated that synchronization of these models with decision support systems can really help the society in terms of meeting the agricultural demands. In [7], use of technology acceptance model for precision agriculture. Authors in [8], talks about precision agriculture using Wireless Sensor Network (WSN) by placing sensor nodes at points, which have optimal periodic threshold sensitivity, region-based hybrid routing protocol and the data from the sensor node is passed to base station only when the parameters exceeds the threshold value there by reducing energy consumption by continuously sending the data. Development of a wireless sensor and actuation network based on decision support system which in turn realizes on fuzzy logic mimicking the farmer's action based on past experience for better water management is reported in [9]. Optimization of sensor data for precision agriculture monitoring for computing normalized difference vegetation index using sprectral response is reported in [10]. In [11], have reported use of thermal imaging to identify the requirements of water in a particular field and using cloud of things network which include internet of things and cyber physical system irrigation was done. Cloud computing based remote sensing application for soil moisture mapping is disscued in [12], for helping farmer in precision agriculture. In [13], use of Unmanned Aerial Vehicle (UAV) and Unmanned Ground Vehicle (UGV) for collection of soil data is reported. In [14], design of precision agriculture sensing system based on wireless multimedia sensor network is reported. They have formed a network of multiple sensors along with CMOS image sensor ,which is used to identify the diseases in crop and transmission of data was done using bitmap index based reliable data transmission protocol. Paper [15], said that plant productivity gets affected by soil moisture and atmospheric humidity in arid and semi-arid grassland systems. In [16], have reported design of fuzzy controller using MATLAB for automated land irrigation in simulation tool. The inputs to the fuzzy controller were taken as water level and time (day, afternoon, night) and outputs of the controller are tube well operation and power source (solar, hybrid, grid). Paper [17], have considered greenhouse control problem as non-linear and multi-variable. The performance of four different controllers was compared namely Proportional Integral Derivative (PID), Linear Quadratic Regulator (LQR), fuzzy PID, fuzzy immune PID controller taking air humidity and temperature as variables. From their experimental results they found that fuzzy immune PID gives better performance. Authors in [18], have stated that extreme temperature effect will certainly effect the plant in their reproductive stage and have significant impact on production of food grains and fruit. In [19], authors have examined impact of frost and heat shock on a wheat crop during different stages of its growth and using this information process-based crop models were formulated. Paper [20], discusses the impact of temperature and carbon dioxide on productivity of wheat and rice crop. In [21], a study to choose an ideal crop among apple, tomato, wheat and white potato for efficient use of the available land resources based on multiple aspects (climatic conditions) influencing simultaneously using Analytical Hierarchy Process (AHP) are reported. All the above reported literture discusses the current growth in precision or smart agriculture, as an initiative we are proposing a technique for monitoring of plant growth, by sensing the paramters influencing plant growth like soil moisture, humidity, sun light, and temperature. Further on take necssary action to manntain optimal parameters for good yeild in crops, if not in desirable range by implementing smart controllers.

Problems in conventional agriculture

The process of conventional agriculture system is: preparation of soil, sowing of seeds, adding manure and fertilizers, irrigation, harvesting and storage. All these steps are carried out with human intervention, which is a tedious task and each of the process requires a particular condition for having an efficient crop which produces maximum yield. The following are the challenges faced by the farmer these days:

i) Supplying adequate amount of water and fertilizers to the crop.
ii) Continuously predict the climatic conditions to take necessary action.

If the above stated challenges are not properly addressed by the farmer it will affect the yield from the crops in terms of quality and quantity. The excess amount of water and fertilizer used in cultivation may also damage the quality of the soil for the future use and will also lead to water shortage when required. It is also troublesome for the farmer to track the variations in climate as changes are sudden and difficult to predict.

If this conventional system is supported by technology then problems faced by farmers can be reduced and there will be significant growth in production of food grains to meet the demands of growing population. In view of all these, this paper aims at presenting a technology which can be an aid to farmers. The objectives of proposed technique are:

1) To make use of different sensors to monitor the current condition of the agricultural field.
2) To design a control algorithm, which will reduce the human intervention and increase the productivity as well as optimal use of water is done.

Methodology

This paper aims to provide a solution to difficulties faced by the farmer with the help of the smart agricultural monitoring technique. This paper focuses about measurement of four different parameters for monitoring the climatic conditions of the field namely temperature, light, humidity and soil moisture. The mentioned parameters will be grouped in two sets, first set consisting of temperature - light and second set with humidity-soil moisture which will form inputs to fuzzy rules and give out two outputs in terms controlling the speed of water pump and closing and opening of the shutter covering the specific area of interest. The fuzzy rule base is formed specifically for the two crops, rice and wheat, being staple food of the people. The proposed work is divided into two parts: 1) Data acquisition and 2) Control algorithm. The Figure 1, gives an overview of the proposed work. Data acquisition discusses about the sensors and other equipment's used for monitoring the current state of the crop. The control algorithm is a decision support system used to take necessary actions to meet the requirements of the crops for the proper growth.

Sensors

Temperature sensor: LM35 is used as the temperature sensor in the propsoed work, because of its sensitivtiy of 10mV/^{0}C. Operating range of -55 to 105^{0}C. Figure 2 shows the schematic of used temperature sensor.

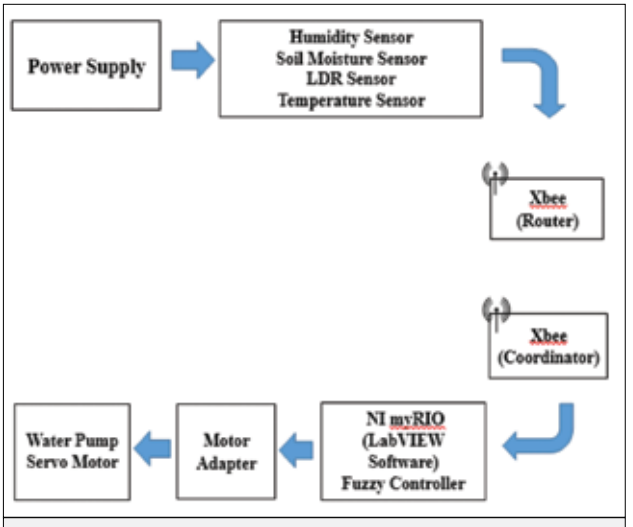

Figure 1. Block diagram of the proposed system

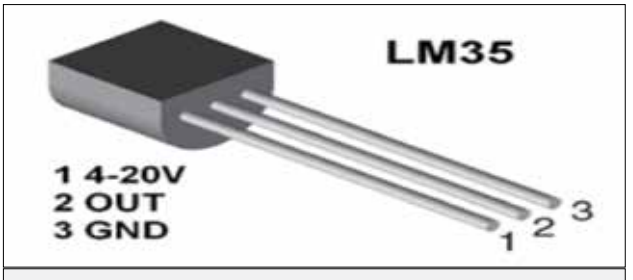

Figure 2. Temperature sensor

Light sensor: Light dependent resistor SEN133322 is used for sensing the light, light intensity is computed in lux. Lux is estimated based on change in resistance of light dependent resistor (LDR). Photosynthetically Available Radiation (PAR), PAR = (Lux/54). Figure 3 shows the schematic of the light sensor used in the proposed work.

Humidity sensor: Capacitive sensor HIH-4000 is used for measuring humidty in the proposed work, because of its range of 0 to 100 %RH. Figure 4 shows the representation of humidity sensor considered in the proposed work.

Soil moisture sensor: Conductive probe sensor is used to measure moisture content in soil. The conductive probe produces an output of 0 to 4.8 V. Figure 5 shows the representation of the soil moisture sensor considered.

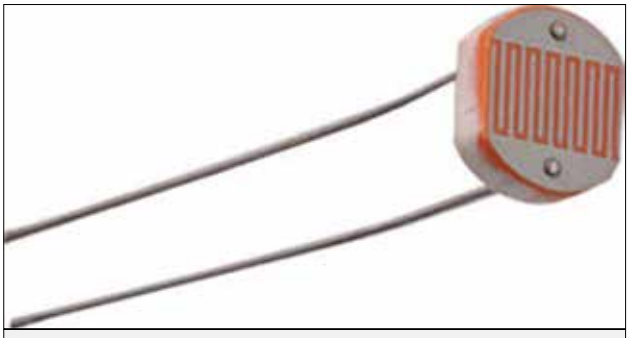

Figure 3. Light sensor

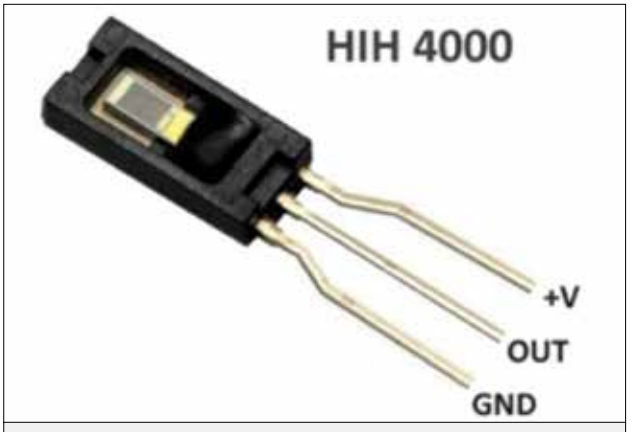

Figure 4. Block diagram of the proposed system

Figure 5. Block diagram of the proposed system

Data acquisition

The field parameters like humidity, moisture, light and temperature are collected from calibrated sensors to the RIO board via ZigBee communication for wireless transmission. The details of the sensors used is mentioned in Table 1. The output from the light sensor is converted to PAR from Lux as plant biologist consider this as more suitable unit for measurement of light. These sensors continuously monitor the field and transfer data wirelessly using ZigBee router (Xbee S2C) based on the IEEE 802.15.4 standard. XCTU software is used to configure ZigBee. The ZigBee (Router) is configured and paired with the other ZigBee (coordinator). The data is sent through Application program interface (API) mode. The analog data from the sensor is converted into digital form by ZigBee. The Analog to digital converter (ADC) on ZigBee radios are 10-bit. Each ADC inputs will have a separate 2 byte field in hexadecimal format in an API frame which is visible on console of XCTU software of ZigBee router and the same API frame is transmitted to ZigBee coordinator. The ADC value of voltage level is given by (1):

$$Voltage, V = \frac{ADC}{1024} * 1.2 \quad (1)$$

The coordinator ZigBee is connected to NI myRIO through UART. All the other necessary wirings are done from each of the components to the NI myRIO using adapters and power supply. Through NI myRIO data is acquired for further processing in LabVIEW.

The Wi-Fi of NI myRIO is connected to the PC to monitor all the parameters from a remote place. The real time program which is written on the LabVIEW is executed on the computer. The program starts and displays the values on the front panel. The sensors provide signals to ZigBee transmitter continuously and this sends the information regarding the atmosphere and the soil status remotely to the myRIO via ZigBee receiver. The system can be re-configured remotely depending on the soil and atmosphere conditions.

Control Algorithm

The climatic and soil conditions will have significant impact on the growth of the crops hence there is a need to have optimum values of temperature, light, soil moisture and air humidity. It is known that temperature- light have a collective impact on the heat requirements of the crops and air humidity-soil moisture have on necessary water requirement. This dependence has led to selection of fuzzy controller for optimizing the desired needs of the crops. Two different sets of Multi-Input-Single Output (MISO) fuzzy controllers are designed to analyze data received by various sensors. Two fuzzy controllers are defined based on the temperature and light for crops: Wheat and Rice which are the input membership functions shown in Figure 6, 7. Servo motor (considered as roof for a prototype) which rotates for a particular angle is the output membership function. Another fuzzy controller is defined based on the humidity and soil moisture requirement for both the crops which is the input membership functions and variation in pump is the output membership function. Since Humidity and Soil Moisture requirement for both the crops are almost same, only one fuzzy controller is designed for both. The sensor values when taken as input membership functions are categorized under three labels: high, medium and low. The output membership functions are defined as open, close, and partially open. Table 1 specifies about the rules chosen to form triangular membership function. Table 2 shows the parameters consider for cultivation of rice.

Table 1. Fuzzy rules for rice

#	Temperature	Light	Servo motor
1	Low	Low	Open
2	Low	Medium	Open
3	Low	High	Open
4	Medium	Low	Open
5	Medium	Medium	Partially open
6	Medium	High	Close
7	High	Low	Partially open
8	High	Medium	Close
9	High	High	Close

	Humidity	Soil moisture	Water pump
10	Low	Low	Open
11	Low	Medium	Open
12	Low	High	Open
13	Medium	Low	Open
14	Medium	Medium	Partially open
15	Medium	High	Close
16	High	Low	Partially open
17	High	Medium	Close
18	High	High	Close

Table 2. Parameter ranges for rice

Sensing parameter	Low	Medium	High
Temperature	8-26°C (cold)	25-35°C	33-50°C (hot)
Light	0-1000 (dark)	800-1800	1500-2500 (bright)
Humidity	0-50 (dry)	40-75	70-100 (humid)
Soil moisture	0-2 (dry)	1.5-3.5	3-5 (wet)

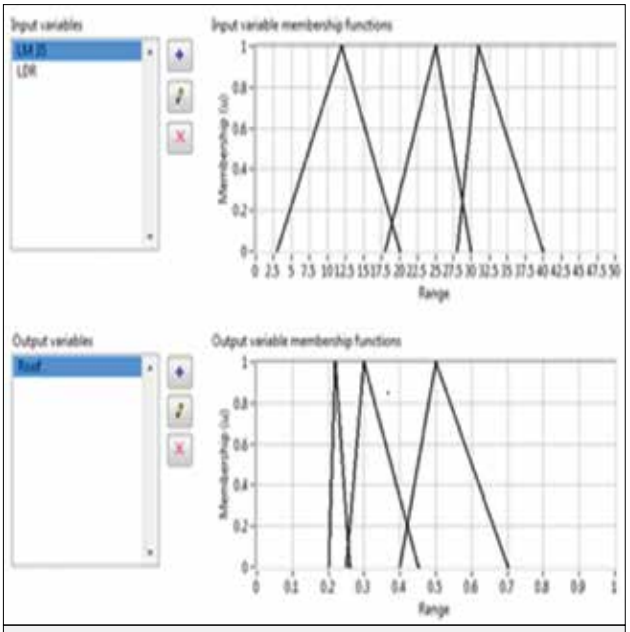

Figure 6. Fuzzy membership functions for rice

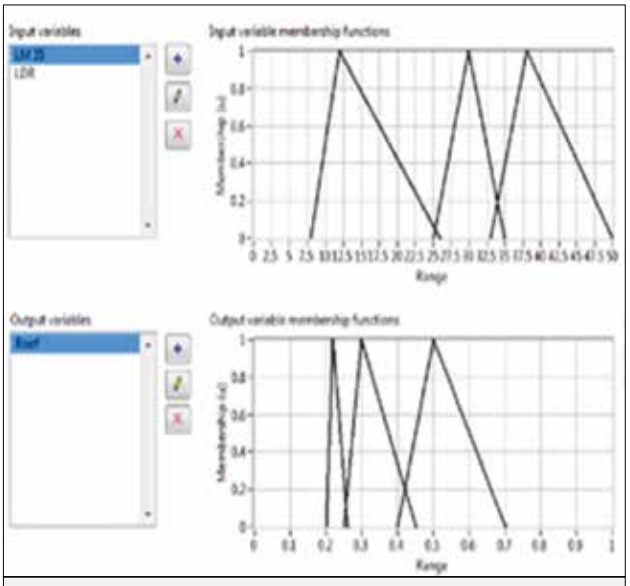

Figure 7. Fuzzy membership functions for wheat

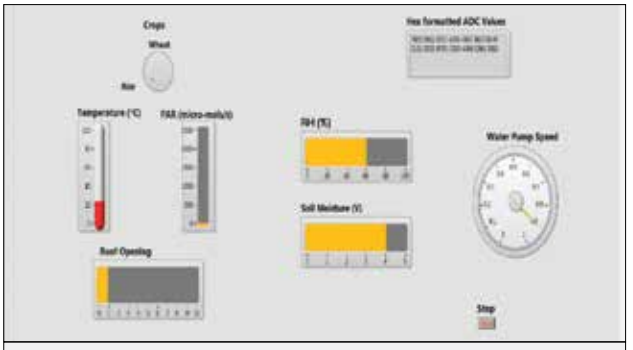

Figure 8. Front panel view of the proposed system interface

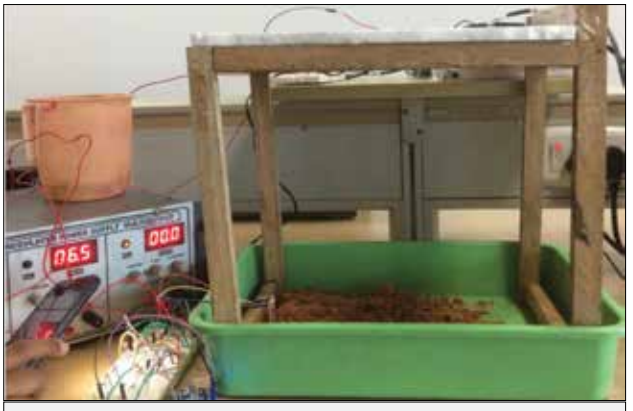

Figure 9. Laboratory setup showing closed roof

Figure 10. Model with roof partially opened

Results and discussion

Data from four sensors like temperature, light, humidity and soil moisture sensors are displayed on the front panel of LabVIEW. There is a knob to change the fuzzy algorithm for different crops. The data from temperature, light, soil moisture and humidity sensor are given to fuzzy controller which controls the roof opening through servo motor, and water pump speed. Figure 8 shows one set of measured values: when temperature is medium (25ºC) and light is low (10 micro-mols/s) which results in roof being opened completely (Duty cycle=1) to provide proper light energy for photosynthesis on the other side when humidity is medium (62 RH%) and soil moisture is high (4V) it results in the water pump speed being reduced completely (Duty cycle=0.9) which provides optimized use of water.

Figure 9-11 shows different position of roof being close, partially open, and open respectively so as to control the variations of temperature and light in the surrounding. Figure 12 shows the connection of ZigBee to the sensors.

Conclusion

An Automatic Fuzzy Controller based Smart Agriculture System (AgriSys) is developed using NI myRIO. AgriSys mainly

Figure 11. Model with fully opened roof

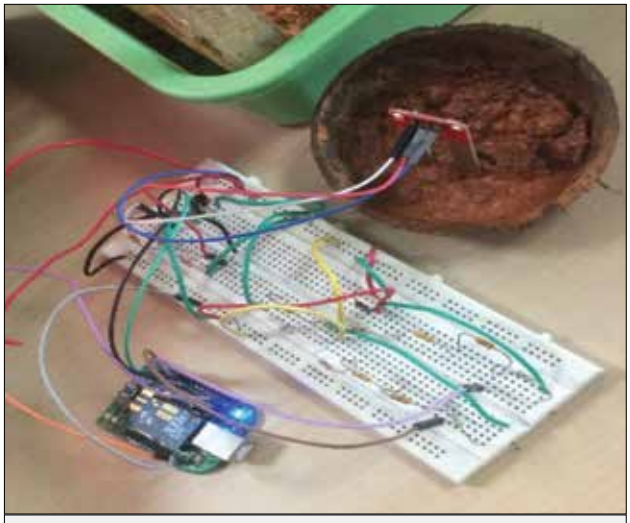

Figure 12. Placement and integration of humidity sensor

looks at inputs, such as temperature, light, humidity and soil moisture. Fuzzy controller is very robust and it can be easily modified. It can use multiple inputs and outputs sources. It is simple and very quick to implement. AgriSys can analyze an environment and intervene to maintain its adequacy. The system is easy to update and maintain over time and has an easy-to-upgrade bank of inference rules to control the agricultural environment. The system provides increased productivity and instant interventions and is able to automatically monitor the parameters and make necessary changes to the output. Incorporating Xbee makes it easier to send data to a remote place since the range of Xbee goes about more than 1000m.

References

1. X. Xu, X. Li, G. Qi, L. Tang, L. Mukwereza, "Science, Technology, and the politics of knowledge: The case of China's agricultural technology demonstration centers in Africa", *World Development*, vol. 81, pp. 82-91, 2016. [CrossRef]
2. J. W. Jones, J. M. Antle, B. Basso, K. J. Boote, R. T. Conant, I. Foster, H. C. J. Godfray, M. Herrero, R. E. Howitt, S. Janssen, B. A. Keating, R. Munoz-Carpena, C. H. Porter, C. Rosenweig, T. R. Wheeler, "Towards a new generation of agriculture system data, models, and knowledge products: State of agriculture systems science, *Agriculture Systems*, vol. 156, pp. 269-288, 2017. [CrossRef]
3. A. Chhetri, P. Aggarwal, P. K. Joshi, S. Vyas, "Farmer's prioritization of climate-smart agriculture (CSA) technologies", *Agriculture Systems,* vol. 151, pp. 184-191, 2017. [CrossRef]
4. C. Mwongera, K. M. Shikuku, J. Twyman, P. Laderach, E. Ampaire, P. V. Asten, S. Twomlow, L. A. Winowiecki, "Climate smart agriculture rapid appraisal (CSA-RA): A tool for prioritizing context-specific climate smart agriculture technologies, *Agriculture Systems*, vol. 154, pp. 192-203, 2017. [CrossRef]
5. M. Babulicova, "Enhancing of winter wheat productivity by the introduction of field pea into crop rotation", *Agriculture,* vol. 62, no. 3, pp. 101-110, 2016. [CrossRef]
6. J. Jones, J. Antle, B. Basso, K. Boote, R. Conant, I. Foster, T. Wheeler, "Brief history of agricultural systems modeling", *Agriculture Systems,* vol. 155, pp. 240-254, 2016. [CrossRef]
7. S. Far and K. Moghaddam, "Determinants of Iranian agricultral consultant's intentions toward precision agriculture:Integrating innovativeness to the technology acceptance model", *Journal of the Saudi Society of Agriculture Science.,* vol. 16, pp. 280-286, 2017. [CrossRef]
8. S. Maurya and V. K. Jain, "Energy-efficient network protocol for precision agriculture", *IEEE Consumer Electronics Magazine,* vol. 17, pp. 42- 51, 2017. [CrossRef]
9. F. Viani, M. Bertolli, M. Salcucci, A. Polp, "Low cost wireless monitoring and decision support for water saving in agriculture", *IEEE Sensors Journal,* vol. 17, no. 13, pp. 4299-4309, 2017. [CrossRef]
10. S. Askraba, A. Paap, K. Alameh, J. Rowe, C. Miller, "Optimization of an optoelectronics-based plant real-time discrimination sensor for precision agriculture", *Journal of Lightwave Technology,* vol. 31, no. 5, pp. 822-829, 2013. [CrossRef]
11. M. Roopaei, P. Rad, K. Choo, "Cloud of things in smart agriculture:Intelligent irrigation monitoring by thermal imaging", *IEEE Cloud Computing,* vol. 4, no. 1, pp. 10-15, 2017. [CrossRef]
12. L. Zhou, N. Chen, Z. Chen, C. Xing, "ROSCC: An efficient remote sensing observation-sharing method based on cloud computing for soil moisture mapping in precsion agriculture", *IEEE Journal of selected topics in applied earth observations and remote sensing,* vol. 9, no. 12, pp. 5588-5598, 2016. [CrossRef]
13. P. Tokekar, J. Hook, D. Mulla, V. Isler, "Sensor planning for a Symbiotic UAV and UGV sytem for precision agriculture", *IEEE Transactions on Robotics,* vol. 32, no. 6, pp. 1498-1511, 2016. [CrossRef]
14. Y. Shouyi, L. Leibo, Z. Renyan, S. Zhongfu, W. Shaojun, "Design of wireless multimedia sensor network for precision agriculture", *China Communications,* vol. 10, no. 2, pp. 71-88, 2013. [CrossRef]
15. C. Deng, K. Wang, J. Li, G. Zhao, Z. Shanggun, "Effect of soil mositure and atmospheric humidity on both plant productivity and diversity of native grassland across the Loess Plateau,China", *Ecological Engineering,* vol. 94, pp. 525-531, 2016. [CrossRef]
16. Z. Mustaq, S. Sani, K. Hamed, A. Alil, S. Belal, A. Naqvi, "Agricultural land irrigation sysytem by fuzzy logic", *International Conference on Information Science and Control Engineering*, pp. 871-875, 2016.
17. S. Revathi, T. Radhakrishnan, N. Sivakumaran, "Climate control in greenhouse using intelligent control algorithms" *American Control Conference*, pp. 887-892, 2017. [CrossRef]

18. J. Hatfield, J. Prueger, "Temperature extremes: Effect on plant growth and development", *Weather and Climate Extremes,* vol. 10, pp. 4-10, 2015. [CrossRef]
19. K. Barlowa, B. Chirsty, G. O'Leary, P. Riffkin, J. Nuttall, "Simulating the impact of extreme heat and frost events on wheat crop production:A review", *Field Crops Research,* vol. 171, pp. 109-119, 2015. [CrossRef]
20. S. Dwivedi, S. Kumar, V. Prakash, J. Mishra, "Effect of climate change on growth and physiology of rice-wheat genotypes", *Conservation Agriculture*, pp. 527-543, 2016. [CrossRef]
21. A. Sharififar, H. Ghorbani, H. Karim, "Integrated land evaluation for sustainable agricultural production by using analytical hierarchy process", *Agriculture,* vol. 59, no. 3, pp. 131-140, 2013. [CrossRef]

V Sravani is presently working as a faculty in of Manipal Institute of Technology, Manipal, India. She received her Bachelors and Masters from Jawaharlal Nehru Technological University, Hyderabad, India in year 2011 and 2013 respectively. She is currently pursuing her PhD in Manipal University, India. Her research interest are soft sensors, Computational Fluid Dynamics, and automation.

Santhosh KV is presently working as a faculty in Instrumentation and Control Engineering department of Manipal Institute of Technology, Manipal, India. He received his Bachelors and Masters from Visvesvaraya Technological University, Belgaum in year 2004 and 2006 respectively. He obtained PhD in the year 2013 from National Institute of Technology Silchar. His research interests include intelligent measurement, automation, sensor fusion, and image processing.

Sanjay Bhargava has received his Bachelors from Manipal Institute of Technology, Manipal in year 2017. Her area of interests are automation, LabVIEW.

Verina Preema D'Almeida is presently working as a Associate Software Engineer in Accenture, Bangalore, India. She received her Bachelors from Manipal Institute of Technology, Manipal in year 2017. Her area of interests are automation, IoT and PLC.

İSTANBUL UNIVERSITY PRESS

RESEARCH ARTICLE

Electrica 2018; 18(1): 52-59

Power-Efficient Viterbi Decoder Architecture and Field Programmeble Gate Arrays Fpga Implementation

Burcu Özbay, Serap Çekli

Department of Computer Engineering, Maltepe University School of Engineering, İstanbul, Turkey

Cite this article as: B. Özbay, S. Çekli. "Power-Efficient Viterbi Decoder Architecture and Field Programmeble Gate Arrays Fpga Implementation". *Electrica*, vol. 18, no. 1, pp. 52-59, 2018.

ABSTRACT

A Viterbi decoder system comprises a convolutional encoder and Viterbi decoder. In general, the code words generated from the input series of convolutional encoder arrive at the decoder through a noisy channel; however, the channel noise can cause corruption of code words. The Viterbi decoder extracts the original input message from the corrupted data using the Viterbi algorithm based on the maximum likelihood principle. A Viterbi decoder mainly comprises four essential units: a branch metrics unit, add-compare-select unit, path metrics unit, and survivor-path memory unit. Related complex calculations are repeated in these units at each clock cycle. In this study, a power- and area-efficient Viterbi decoder architecture that also reduces the computational complexity is proposed. Initially, a hard-decision Viterbi decoder system architecture design for Very Large Scale Integration (VLSI) realization was fulfilled without any further improvement to compare the performance of fundamental and improved designs with respect to power consumption. The initial design constitutes an essential base for the improved power- and area-efficient Viterbi decoder architecture. The improvements were made to achieve the less complex and power-efficient architectural system design. The performance of the proposed architecture was tested by a fieldprogrammable gate array (FPGA) platform, and the results have been reported. The architectural design is described using the Verilog hardware description language for comparing the related tests and performance of FPGA platform.

Keywords: Viterbi decoder architecture, FPGA implementation, forward error correction

Address for Correspondence:
Serap Çekli

E-mail:
serapcekli@maltepe.edu.tr

Received: 01.11.2017

Accepted: 28.12.2017

DOI: 10.5152/iujeee.2018.1809

Introduction

The transmission channel noise is the most influential and important problem on the impeccable data transmission on a communication system. Some error correction coding techniques are used according to the data size, activity field and the priority of the receiver to eliminate the effect of undesired channel noise. The coded data is transmitted to the receiver by decoders after the decoding process. An effective decoder provides intact data transfer after passing through a noisy channel. Viterbi decoders (VD) are the systems based on the aforementioned principle and they are employed frequently in fields such as wireless communication systems, Code Division Multiple Access (CDMA) systems, satellite and space communication systems, Mobile Communication Systems (GSM).

A VD system is comprised of the VD and convolutional encoder which generates forward error correcting code of the convolutional codes. Operation of a convolutional encoder is based on the finite state machine (FSM). Input message bits which provides states of encoder and state transitions could be expressed by using Trellis diagram.

Several approaches have been conducted for the digital system design of the Viterbi decoder, recently. These studies are focused mainly on the increasing the decoding speed [1-3], decreasing the hardware complexity for power efficient hardware design [4-14], changing the constraint length [8-10] and radix4 based digital architectures [15,16].

The designs which aim speeding up VD are carried out by transforming the serial architecture of a conventional Add Compare Select Unit (ACSU) to parallel design with an increase

of the number of states of Trellis diagram. Implementation of an architecture which uses that kind of principle has provided that 33% speed up for decoder [1]. Although, this architectural designs make possible the faster decoders, the power consumption is also increased as a result of the increased hardware complexityat the same time.

The studies which trying to provide the power efficiency focuses basicly on the power save by decreasing the hardware complexity. To reduce the hardware complexity, some researches have been done to use an algorithm which decreases the power consumption while tracing back the path for decoding [6,9,10,12]. Moreover, some studies have been put forward to change the architectural design of Survivor Path Memory Unit (SPMU) or ACSU [1,5-7,11,13,14] to decrease the usage of hardware resources.

The most successful approach for the power efficient design of the VD is defining a threshold value for ACSU. In this approach, the calculation load of decoder is reduced by avoiding the paths which have path metrics greater than the defined threshold value. This method is called T-algorithm and some design studies which use this algorithm have been put forward [11,13,14]. Decoder designs which based on this algorithm provides savings from storage areas Path Metrics Unit (PMU)[6]. By using the designs employing this kind of approaches also reduces power consumption by on Xilinx XCV1000 device [7].

In this study, convolutional code which is a forward error correction code is obtained by coding the input message code at first. VD which operates according to hard decision method is designed to turn out this code into non coded form after transmitting through a noisy channel before reaching at receiver. The initial decoder design is changed to power efficient form by some improvements. In this paper, improvement is the use of the T-algorithm. The power efficient decoder designed in this way has achieved 50% power saving in hardware based power consumption on Xilinx XC6SLX16 device.

The rest of the paper is organized as follows. Section 2 presents encoder structure, state diagram and operation of convolutional coder. The background of Viterbi algorithm and Trellis diagram are introduced for the suggested design in Section 2. In Section 3, the designed VD and in Section 4, the designed power efficient VD is proposed.The detailed implementation and comparisons results are given in the Section 5, and this paper concludes in Section 6.

Viterbi Algorithm Background and Convolutional Encoder

A convolutional encoder is based on a finite state machine. The coded sequence is generated from the input information series depending on the current and previous messages. The encoder consists of one or more D flip flops and logic gates as shown in Figure 1. The information on the flip flops changes according to each input message and indicates the current state of the encoder.

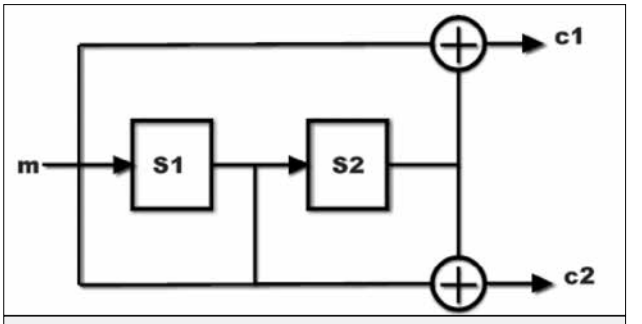

Figure 1. Convolutional encoder

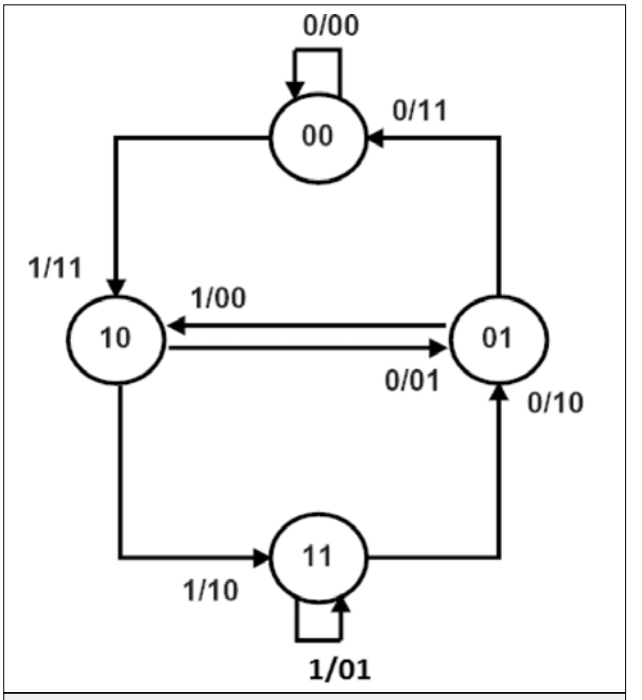

Figure 2. State diagram for the convolutional encoder

A convolutional code is expressed as *Cconv(n,k,K)*, where *k* is the length of the message bit; *K*, the length of the code bit; *n*, the constraint length, the memory of the encoder, and the depth of the code. It shows how many times each input bit is affected on output bit generation. The higher constraint length increases the power of the code but also increases the complexity of the encoder.

The *k*-bit message is collected according to modulo-2 summation, passing through the shift register which *K-1* memory elements, and an -bit output code is generated. The convolutional encoder can be defined by the status table and the trellis diagram. The states are a production of the encoder's shift register. The output code is a function of the message bit to be encoded and the current state.

The state diagram shows the output bits between time instants when an input message is encoded and the time instants when the other input message is encoded. The trellis diagram is a description of the state diagram.

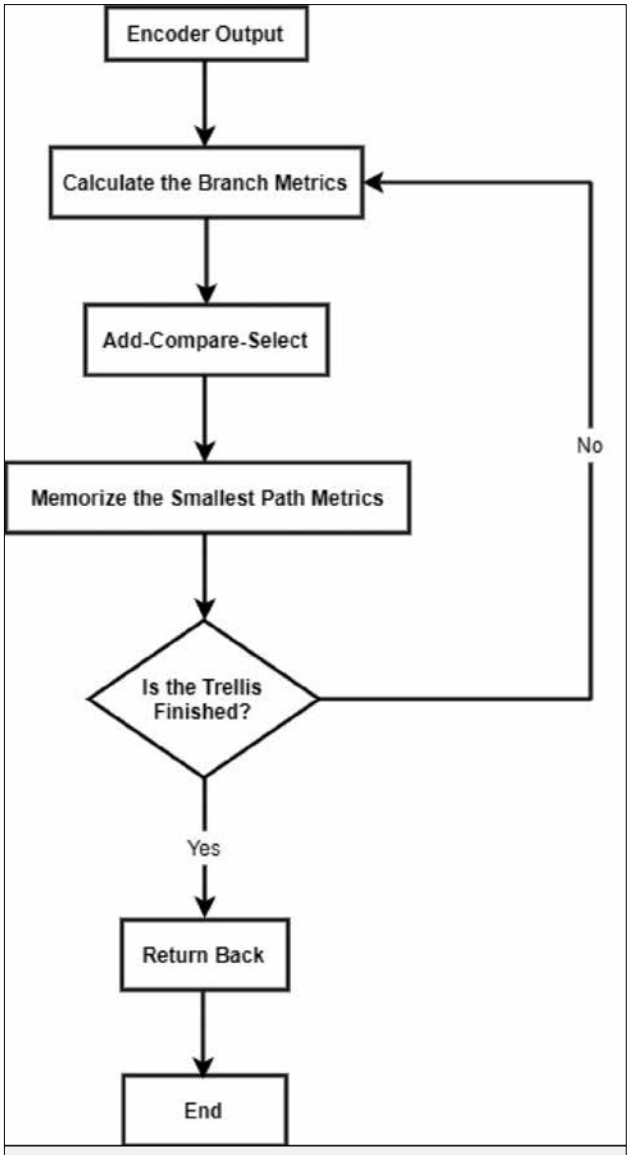

Figure 3. Flowchart of VA

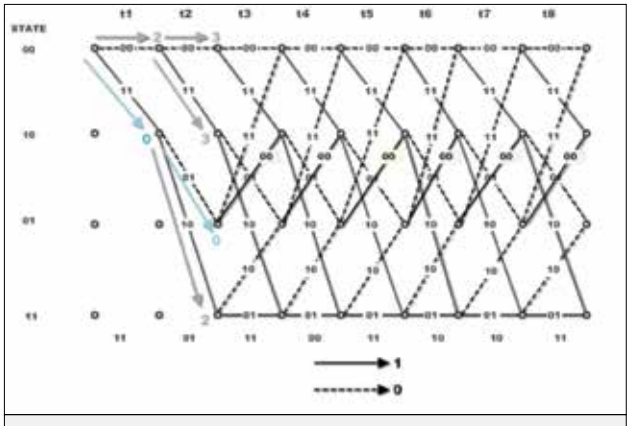

Figure 4. Trellis diagram for the input message sequence "100011" of the encoder

The encoder shown in Figure 1 is expressed as *Cconv*(2,1,3). According to this expression, one bit message is encoded as two bits. Each input message comes to the first memory element of the shift register and the bits which is hold in the memory elements shift to the right one bit. Thus, the encoder pass the next state. The encoder starts the encoding process with zero state. The encoding continues until all the bits in the input message enter the encoder and the encoder returns to zero state again.

The state diagram for the encoder shown in Figure 1 is shown in Figure 2, and the state table for this state diagram is shown in Table 1. This table shows which state encoder pass according to the input message bit and what the exit code is in this moment.

Viterbi Algorithm

Viterbi Algorithm (VA) is based on the Maximum Likelihood (ML) algorithm in solving the convolutional codes. The ML approach finds the most similar way in the trellis diagram for the convolutional encoder. The most similar path is composed of getting together the most similar branches.

Viterbi Algorithm can be defined as the most appropriate algorithm because of its success in reducing the error probability. The algorithm works by following the steps below. The related flowchart of the VA is given in Figure 3.

- The measures paths in the trellis diagram are calculated based on Euclidean Distance (ED) or Hamming Distance (HD).
- In ACSU, the shortest, or most similar path is selected for the code at each encoder output until the data transmission is complete. This path is memorized. These shortest paths are called survivor paths (SP).
- Encoded message against each branch of the selected SP is found by using an appropriate return algorithm.

Trellis diagram

Trellis diagram is generated from the state diagrams. Thanks to the trellis diagram, it is easy to see which output code the encoder produces when it moves from one state to another and which message comes to the encoder's input.

If the constraint length of the encoder is K, the number of states in the trellis diagram is $2^{(K-1)}$ [7].

Each branch in the trellis diagram carries some metrics that represent similarity between the encoded message and the receive message at this moment. According to HD, these values indicate how many bits are different between the recived code and the encoded one. Until the end of the diagram, branch metrics (BM) continue to be collect and thus path metrics (PM) occur. When the trellis diagram is completed, the path which have lowest PM among SPs that will ensure to decode correctly is chosen as the most similar path by VD.

Figure 4 shows the trellis diagram of the message sequence 100011 is encoded by the encoder given in Figure 1. The code sequence of 11 01 11 00 11 10 10 11 is obtained from the output of the encoder with this message sequence.

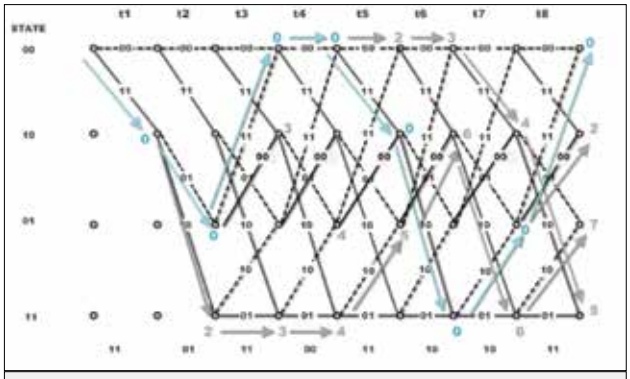

Figure 5. PMs of four possible paths for the input message sequence "100011" of the encoder

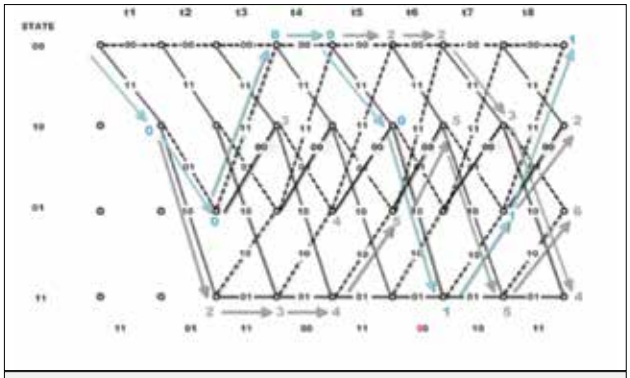

Figure 6. In the case of incorrect receiving, PMs of four possible path for the input message sequence "100011" of the encoder

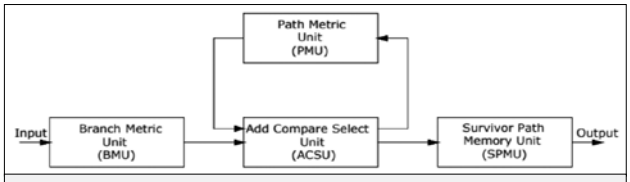

Figure 7. Basic units of VD

Trellis steps are continued by collecting the BMs until the encode process is finished. Thus, the PMs of all possible paths are calculated at the end of the trellis diagram. In Figure 5, four paths that can occur as SP when the trellis diagram is completed and their PMs are given. VD, in principle, chooses the route with a low PM. Here, the path with the metric of will be selected and the return algorithm will be applied over that path. Thus, the input code is approached to the highest level.

Assume that the code sequence 11 01 11 00 11 10 10 11 from the encoder output is detected as 11 01 11 00 01 10 10 11 by the decoder due to the noise in the channel. The 9th bit is misunderstood. As shown in Figure 6, because of the this bit error at the 9th bit, BM in the t_5 clock cycle becomes 1, although the smallest total BM in the first four time periods is 0. Due to there are no erroneous bits when the trellis diagram is complete, this path's PM will be 1. Compared to other SPs, the path which have the smallest PM is still this

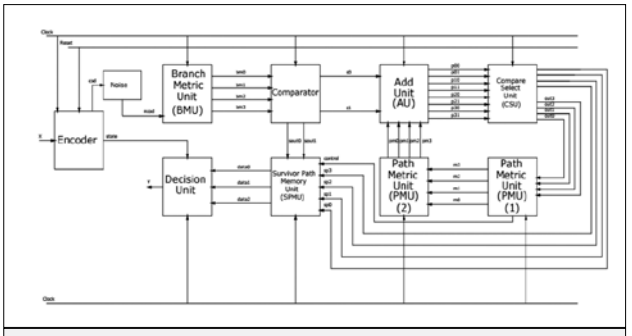

Figure 8. Structure of the designed VD

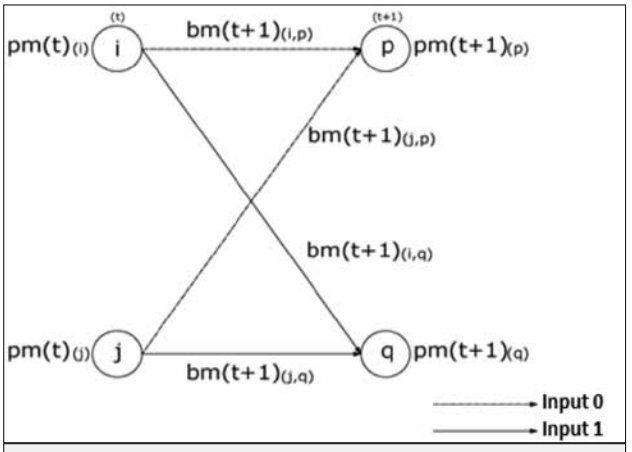

Figure 9. Butterfly structure of the ACSU [17]

path, so the decoder will go back over this path and decode the code 100011. Even though code receive wrong due to the noise in the channel the code is solved correctly thanks to VD.

Proposed Viterbi Decoder Architecture and Implementation

A Viterbi Decoder consists of four basic units as shown in Figure 7. Branch Metric, Add Compare Select, Path Metric, and Survivor Path Memory Unit. Other units different from these units are created by dividing these four basic units, and the design from the design may differ. But on the basis they do what these four units do. The designed VD units and connections between units are shown in Figure 8.

Branch metric unit

The first unit is called Branch Metric Unit. HD or ED can be used to calculate BMs according to the hard or soft decision method. If the decoder is designed according to soft decision method, ED are calculated. If it is designed according to hard decision method, HD are calculated. Although the soft decision decoder provides more information about the input message, the calculation complexity is more.The decoders designed for this study are working using hard decision method because it is aimed at power efficient design due to low complexity. The received code is compared with the encoded values bit by bit for every clock pulse end the difference between them is assigned as BM. The BMs are sent to ACSU to be selected as survivors.

Add compare select unit

ACSU is the unit where current PMs and current BMs are collected, compared and the path with the smallest PMs is selected. BMs are collected by the PMs coming from the previous time interval in this unit. The new PMs generated after this process are compared and the paths with the smallest PM are selected as SPs and sent to the SPMU. In addition, PMs, including this time interval, go to PMU for new calculations.

Figure 9 shows butterfly structure of ACSU. When the decoder is in the state of i and j, it goes to p or q according to the incoming message to the encoder. The PMs in the state of i and j are expressed as pm_t^i and pm_t^j. When BMs which are necessary for transition to p and q state are added to these values, the PMs in the state of p and q are formed and expressed as pm_{t+1}^p and pm_{t+1}^q $bm_{t+1}^{i,p}$, $bm_{t+1}^{j,p}$; are branch values that pass the state i and state j to state p and $bm_{t+1}^{i,q}$, $bm_{t+1}^{j,q}$; are branch values that pass the state i and state j to state q.

The addition process in acs unit is expressed by equations (1), (2), (3), (4) and the comparison process in acs unit is expressed by equations (5) and (6) [17].

$$pm_{t+1}^p = pm_t^i + bm_{t+1}^{i,p} \quad (1)$$

$$pm_{t+1}^p = pm_t^j + bm_{t+1}^{j,p} \quad (2)$$

$$pm_{t+1}^q = pm_t^i + bm_{t+1}^{i,q} \quad (3)$$

$$pm_{t+1}^q = pm_t^j + bm_{t+1}^{j,q} \quad (4)$$

$$pm_{t+1}^p = \min[(pm_t^i + bm_{t+1}^{i,p}), (pm_t^j + bm_{t+1}^{j,p})] \quad (5)$$

$$pm_{t+1}^q = \min[(pm_t^i + bm_{t+1}^{i,q}), (pm_t^j + bm_{t+1}^{j,q})] \quad (6)$$

Path metric unit

PMU is the unit where path metrics are calculated at intended time. Path metrics of the SPs are updated in this unit and returned to ACSU to gather new BMs which come from next time interval. The calculations made within the units of the VD shown in Figure 8, including ACSU and PMU are shown in Figure 10.

Survivor path memory unit

SPMU is the unit where the SPs which are traced to decoded are stored. In this work code is decoded by using TB method. The SPMU is needed for this method. The SPs are taken here in memory and the bits encoded per branch are decoded in the reverse order. The TB algorithm is applied on the lowest path of PM.

Proposed Power Efficient Viterbi Decoder Architecture and Implementation

The most common approach for a power-efficient VD is to reduce the computational and hardware complexity. In this study, with the comparator unit which added to the output of the BMU in the first designed decoder, some of the branches with large BM were eliminated and not involved in the calculation. Therefore, the first designed decoder is powerfully active according to a classical VD.

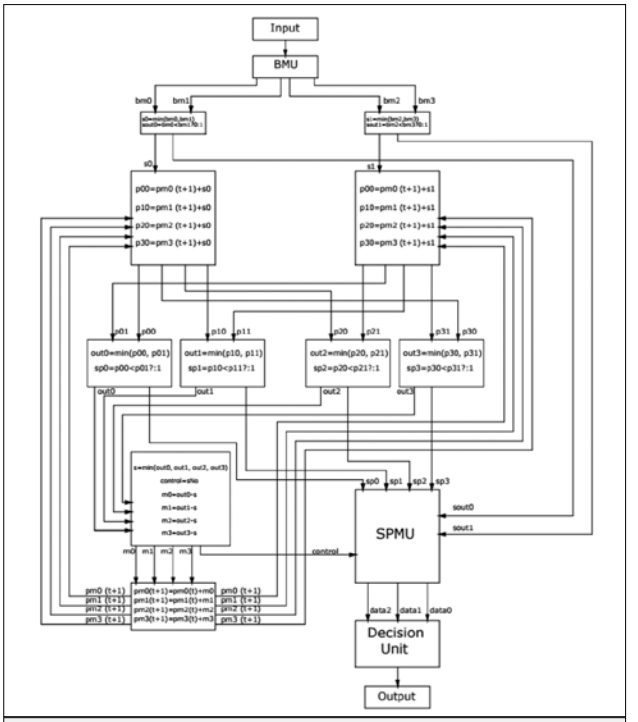

Figure 10. Operations in the ACSU and PMU of the designed VD

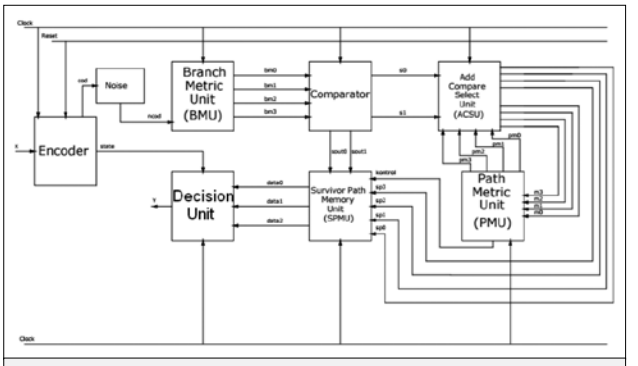

Figure 11. Structure of the designed power efficient VD

The decoder shown in Figure 11 is designed to make the designed decoder more power efficient. A threshold value for PMs has been defined, and the computational complexity of the decoder has been reduced by eliminating the paths that have PMs above this threshold value without comparison. Here, the choice of threshold value is important. Although, a low selected threshold value will reduce the computational complexity at high rate, may lead to the elimination of the path to be decoded. This means that the decoder is far from its most basic aim and it can not solve the code correctly. For this reason, the selected threshold value should be at the optimum level to ensure that the decoder operates most efficiently, without incorrect decoding. The threshold selection should be emprical. It can be attempted to reduce the threshold value until the incorrectly decoded. In this study, according to the input message, the maximum value of the PM is 1. For this reason, threshold is set to 0 which is the best value. Thus, paths with

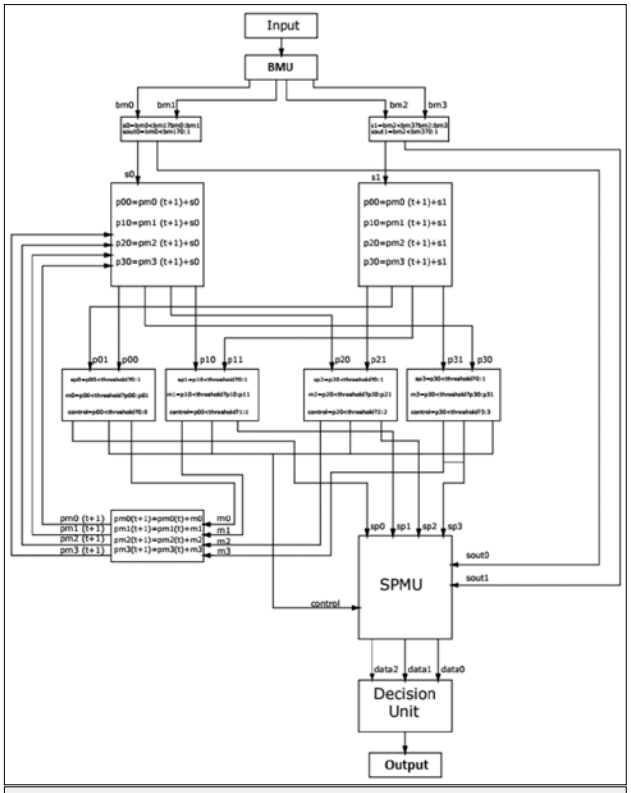

Figure 12. Operations in the ACSU and PMU of the power efficient designed VD

Table 1. State table for the convolutional encoder

Input Message m	State (t) S1 S2	State (t+1) S1 S2	Code c1	Code c2
-	00	00	-	-
0	00	00	0	0
1	00	10	1	1
0	01	00	1	1
1	01	10	0	0
0	10	01	0	1
1	10	11	1	0
0	11	01	1	0
1	11	11	0	1

erroneous decoding have been eliminated and only paths with zero distance to the encoded code are included in the calculation. In situations with large PMs, as the threshold value increases, the number of paths participating in the calculations and computational load of the decoder increases.

As shown in Figure 11, the power efficient VD has the same units as the decoder shown in Figure 8, except that ACSU and PMU are designed as a single unit. The calculations made in all units including ACSU and PMU are shown in Figure 12, and as seen here, the threshold value is defined in ACSU as the 'threshold', starting from here to reduce the calculation load.

Table 2. Viterbi decoder and power efficient Viterbi Decoder hardware utilization

Architectural design	Viterbi decoder	The power efficient viterbi	Hardware reduction
Number of registers	30	6	80%
Number of look up tables	253	110	57%
Number of GCLK (global clock)	1	1	-
Number of input/ output ports	4	4	-

Table 3. Viterbi decoder and power efficient Viterbi Decoder power consumption

Power consumption [W] \ Architectural design	Viterbi decoder	The power efficient viterbi	Power reduction
Logic block	0.004	0.002	50%
GCLK	253	110	-
(global clock)	0.005	0.005	-
Input/output port	0.002	0.002	-
Static device	0.020	0.020	-
Total on-chip	0.031	0.028	10%

Results

The number of employed registers and number of look up tables exhibits the hardware complexity and area utilization, evidently for a design which is implemented on the FPGA environment. The more number of register and look up table means the more number of logical operations and logical block utilization. If the aim is to design of a power efficient architecture then the number of registers and look up tables should be reduced due to the hardware complexity. For this purpose, the power efficient VD is designed by defining a threshold value. The PM values are compared with the defined threshold without compared with each other and the paths which are on the threshold are eliminated. In the power efficient design, the number of registers are reduced by and the number of look up tables are reduced by . This reductions are provided by the reduction of the number of PM comparison operations as well as the memory usage for

storing the comparison results, and the corresponding comparisons are given in the Table 2. In the power efficient VD design, the less number of logic blocks (LB) are used thus so, the power consumption resulting from the logic blocks is also less.

The power consumption analysis has been performed for the two FPGA implementations which are the VD and power efficient VD design. The power consumption of the VD design is 0.031 *Watt* and the power consumption of the power efficient VD design is 0.028 *Watt*. 0.020 *Watt* power dissipation is constant for the both VD designs and is 0.005 *Watt* also consumed for the clock source. 0.002 *Watt* is consumed for the Input/Output (IO) ports. The power consumption values are given in the Table 3.

When viewed in terms of total power consumption, power saving have correspond a value of 10% in the power-efficient decoder. This can be perceived as small value. But device based power consumption has been 64.5% of the total power consumption of VD and 71.4% of the total power consumption of the power efficient VD. And this static value can not be changed at all. Hence it is more meaningful to examine the power consumption of the logic blocks shown in Table 3. Because in this study the contribution is provided on this part.

The difference between the power consumption characteristics of two designs is resulted from the logic blocks. This result has been expected due to enhancements which are made on the logic block utilization of two designs. The power consumption of the hardware resource employment of the VD design is 0.004 *Watt*, however the power consumption of that of the VD design is 0.002 *Watt*. Therefore, the power consumption arising from the logic blocks has reduced by for the power efficient VD design in this study.

Conclusions

Viterbi decoding is the best technique for decoding the convolutional codes. Convolutional encoder with constraint length 3 and code rate 1/2 and the decoder decoding this code has been designed and implemented and decoder has been developed as power efficient. The key consideration is to decrease the power dissipation. In accordance with this purpose this paper has presented T-algorithm for power efficient management in VD. The ACSU consumes most of the power. The hardware complexity of the decoder is reduced by defining an appropriate selected threshold value in the ACSU and a power efficient VD which has the same ability to decode successfully as the first designed decoder in this study is obtained. Power consumption on hardware has been reduced to half. The different modules are designed using Verilog HDL (Hardware Description Language) and maped to Xilinx XC6SLX16 using Xilinx Integrated Software Environment (ISE).

References

1. I. Lee and J.L. Sonntag, "A new architecture for the fast Viterbi algorithm," IEEE Global Telecommunications Conference, San Francisco, vol. 3, pp. 1664-1668, Nov., 2000.
2. M. Benaissa, and Y. Zhu, "A Novel High-Speed Configurable Viterbi Decoder for Broadband Access," *EURASIP Journal on Applied Signal Processing,* pp. 1317-1327, 2003. [CrossRef]
3. Y. Zhu and M. Benaissa, "Reconfigurable Viterbi decoding using a new ACS pipelining technique," Proceedings of the 2003 IEEE international conference on Application-Specific Systems, Architectures, and Processors (ASAP2003), The Hague, The Netherlands, pp. 360-368., 24-26 June 2003. [CrossRef]
4. K. Page, P. M. Chau, "Improved Architectures for the Add-Compare-Select Operation in Long Constraint Length Viterbi Decoding," *IEEE J. Solid-State Circuits,* vol. 33, pp. 151-155, no. 1, January 1998.
5. I. Kang and A. Willson, "Low-Power Viterbi Decoder for CDMA Mobile Terminals," *IEEE J. of Solid-State Circ.,* vol. 33, no. 3, pp. 473-482, Mar. 1998. [CrossRef]
6. Y. Gang, T. Arslan, A. T. Erdogan, "An Efficient Pre-Traceback Approach for Viterbi Decoding in Wireless Communicationİ" ISCAS 2005, *IEEE International Symposium on Circuits and Systems,* vol. 6, pp. 5441- 5444, May, 2005.
7. R. Tessier, S. Swaminathan, R. Ramaswamy, D. Goeckel, W. Burleson, "A Reconfigurable, Power-Efficient Adaptive Viterbi Decoder," *IEEE Transactions On Very Large Scale Integration (VLSI) Systems,* vol. 13, no. 4, pp. 484-488, April, 2005.
8. A. Dinhand and H. Xiao, "A Hardware-Efficient Technique to Implement a Trellis Code Modulation Decoder," *IEEE Transactions On Very Large Scale Integration (VLSI) Systems,* vol. 13, no. 6, pp. 745-750, June, 2005.
9. Y.C. Tang, D. C. Hu, , W. Wei, W. C. Lin, H. Lin, "A Memory-Efficient Architecture for Low Latency Viterbi Decoders," 2009 International Symposium on VLSI Design, Automation and Test, 28-30 April, 2009.
10. K. Cholan, "Design and Implementation of Low Power High Speed Viterbi Decoder," *International Conference on Communication Technology and System Design,* vol.30, pp.61-68, 2011.
11. S.L. Latha and D.L. Kumari, "Low-Power Adaptive Viterbi Decoder for TCM Using T-Algorithm," *International Journal of Scientific and Research Publications,* vol. 3, no. 8, August, 2013.
12. N. Bhatt, M. Shah, B. Asodoriya, "FPGA Implementation Of Power Efficient Low Latency Viterbi Decoder," *Indianternational Journal of Engineering Research & Technology (IJERT)*, vol. 2, no 5, May, 2013.
13. R. I. Thakre, "Design of T-Algorithm Based High-Speed Low-Power Viterbi Decoder for TCM Decoders", *International Journal of Innovative Research in Electronics and Communications (IJIREC),* vol. 1, no. 1, pp. 33-38, April, 2014.
14. V.G. Kumar and A. C. Sudhir, "Implementation of Viterbi Decoder using T-algorithm for TCM Decoders," *International Journal of Innovative Research in Electrical, Electronics, Instrumentation and Control Engineering,* vol. 3, no 5, May, 2015.
15. P. J. Black and T. H. Meng, "A 140-Mb/s, 32-state radix-4 Viterbi Decoder", *IEEE J. Solid-State Circuits,* vol. 27, pp. 1877-1885, Dec. 1992. [CrossRef]
16. N. Bruels, E. Sicheneder, M. Loew, A. Schackow, J. Gliese, C. Sauer, "A 2.8 Gb/s, 32-State, Radix-4 Viterbi Decoder Add-Compare-Select Unit", *Symposium on VLSI Circuits Digest of Technical Papers,* pp. 170-173, June, 2004. [CrossRef]
17. I.C. Yilmaz, "Design and Simulation of Soft Decision Viterbi Decoder", Department of Electrical and Electronics Engineering, Çukurova University Institute of Natural and Aplied Sciences, MSc. Thesis, 2011.

Burcu Özbay was born in Besni on January 7th, 1990. She graduated from Marmara Private Science High School in 2007. She received her BSc. in Physics Engineering from Hacettepe University in 2012, and her MSc. in Computer Engineering from Maltepe University in 2017. She has been working in Computer Engineering Department of Maltepe University as a research assistant since 2013.

Serap Çekli was born in Germany in 1978. She received her BSc. degree in Electronics Engineering from İstanbul University in 2000, MSc. degree in Electronics and Communication Eng. from İstanbul Technical University in 2003. She has received PhD. degree from İstanbul University, Elect. Electronics Eng. Dept. in 2009. She worked for İstanbul University Engineering Faculty as a research assistant between 2001-2009. She has been working as an assistant professor at Maltepe University, Computer Engineering Department since 2009. Her research interests are digital systems, digital design, computer organization and architecture.

İSTANBUL UNIVERSITY PRESS

RESEARCH ARTICLE

Electrica 2018; 18(1): 60-71

A New Approach for Detection of Pathological Voice Disorders with Reduced Parameters

Haydar Ankışhan

Biomedical Equipment Technology, Başkent University Vocational School of Technical Sciences, Ankara, Turkey

Cite this article as: H. Ankışhan. "A New Approach for Detection of Pathological Voice Disorders with Reduced Parameters". *Electrica*, vol. 18, no. 1, pp. 60-71, 2018.

ABSTRACT

Voice data has demonstrated chaotic behavior in previous studies. Therefore, studying the linear properties alone does not yield successful results. This is valid for the examination of voice data as well. Therefore, conducting studies including chaotic features as well as existing technologies is inevitable. The main purpose of this study is to detect voice pathologies with fewer special features using new chaotic features. Both linear and nonlinear characteristics were used in this study. In this context, the largest Lyapunov exponents and entropy are preferred as chaotic properties because of their success in previous studies. Very few results with 100% accuracy were obtained in the experimental studies. In this study, multiple support vector machines (SVMs) were selected as a classifier because of their success in previous similar data types. Thus, the desired accuracy level was achieved using fewer features. Resultantly, the process complexity decreased and the system speed increased.

Keywords: Voice disorders, support vector machines, voice disorder detection

Introduction

Advanced evaluations in voice disorders are applied for diagnostic purposes in analysis laboratories with analyzing devices. Depending on the features, the results provide feedback for experts and patients, both visually and audiologically. It can be quite restrictive that human voice specialists, called foniatrists, work with a limited number of features to be examined on the axis of voice, frequency and time domain. This leads to inability to diagnose patients correctly in some special cases without going through the detailed investigations.

Although higher digital technologies have recently been used in acoustic signal analysis, it is still important to obtain meaningful and useful information. In signal processing studies, voice pathologies and problems have recently begun to be more carefully scrutinized [1,2]. Since the sounds have dynamic and complex characteristics, especially when different language constructions are taken into consideration, the complexity is increased depending on these different notations and emotions. For these reasons, the need for reliable software and analysis methods is increasing day by day. Language analysis can be done with the help of these methods and software, the diversity of pathologies can be examined and techniques can be investigated. Today, scientists are spending a lot of time developing tools that use different characters and traits and can predict different voice pathologies.

In clinical voice studies, patients' voice quality can be predicted by a sustained vocal phonetics or by mutual speaking. It is thought that sustainable vowels give useful results as they are avoided from linguistic artifacts and are observed to be sufficient in many sound estimations. Specialists examine whether or not it is possible for patients to maintain a sustainable vowel and their performances of voice analysis.

Voice quality analyzes can generally be performed in titles such as acoustics, aerodynamics, endoscopy, and a percentage of the patients' self-examination. It is observed that the

Address for Correspondence:
Haydar Ankışhan

E-mail:
hankishan@baskent.edu.tr

Received: 03.11.2017

Accepted: 05.12.2017

Available online at
http://dergipark.gov.tr/iujeee

DOI: 10.5152/iujeee.2018.1810

results of different methods are examined, in cases where the obtained results are uncertain [3]. It is shown from the literature that the acoustic properties of different features are evaluated together in the literature. Mostly preferred properties; fundamental frequency [4], jitter (frequency perturbation), shimmer (amplitude perturbation) [5-7], Harmonics to Noise Ratio [8] and Mel frequency celpstral coefficients (MFCC) [9,10].

According to [11], in vocal tract pathology, voice impairment is detected by interpreting the stimulation of the signal. It is observed that researchers devote a considerable amount of time to systems that can automatically calculate and group voice impairment with traditional diagnostic approaches. Some studies have shown that the correct diagnosis of the sound level increases the predictive accuracy of the noise impairment [1]. In addition to these studies, a universal method and approach is still not found for these kind of problems. Have obtained 100% accuracy with long-term average spectral properties, glottal noise measures and linear predictive modeling techniques [12]. Obtained 100% accuracy for diagnosed pathologies and 96.1% for ambiguous pathological conditions [13]. Has obtained 89.3% accuracy for Asthenia disease with MFCC, HNR, NNE, GTNE and PCA [14]. In [15] studies, adaptive time-frequency transform, octave max, octave mean, energy ratio, length ratio and frequency ratio together with Linear Discriminant Analysis (LDA) were used as properties and pathological classification was made. They obtained the 93.4% accuracy classification results. Again only used MFCC and obtained 96% accuracy with the help of the neural network – multi layer perceptron [16].

There are some other studies available in the literature, trying to detect vocal disorders by using different classification methods. For instance, [14] has helped to extract useful features. In their study, have shown that parameter reduction affects speech robustness in inner classificatios [17].

In some studies, acoustic signals and vocal cord images were combined for more precise analysis. Kymography and high-speed digital videoendoscopy (HSV) has played a major role in classifiying pathological disorders for clinicians [18]. In addition, [19], in their study, examined the correlation between the vocal cord vibration of the system and acoustic analysis of the voice.

Calculated the root mean square, delay spread and standard deviation of the voice signal. In the study, they have considered two situations; having disorders or not [11]. Additionally, 4 polyptical and 8 healthy person's wovel / a / or / i / were examined. Depending on the method, False alarm rate %0 and true negative 25% were calculated.

Some studies have used the Empirical mode decomposition (EMD) method to classify voice pathology. It was used by [20] at EMD Chemical plant controls. Could be classify into classes according to their pathology by using Maximum power spectral density of the intrinsic mode function as a feature [21]. For this operation used K-Nearest Neighbor (KNN) as a classifier. With the results of this process, they obtained 95.7% accuracy results.

In this study, fewer features were used than in previous studies, and features were calculated after voice modeling. In the aim of the study, classification of patients with 4 different pathologies was performed by using nonlinear, and linear time, frequency features with the help of the SVMs as a classifier. First, the sounds were recorded at specific phonetic intervals, then the LPC and MFCC coefficients were calculated and the voices were modeled with these coefficients. So, the modeled signals' features were then extracted, and pathological classification was performed with the SVMs depending on the characteristic values of the features. The flow chart of the events are given in Figure 1.

The study continuous as follows: second part is materials and methods, third part is results and discussions, and fourth part is conclusions.

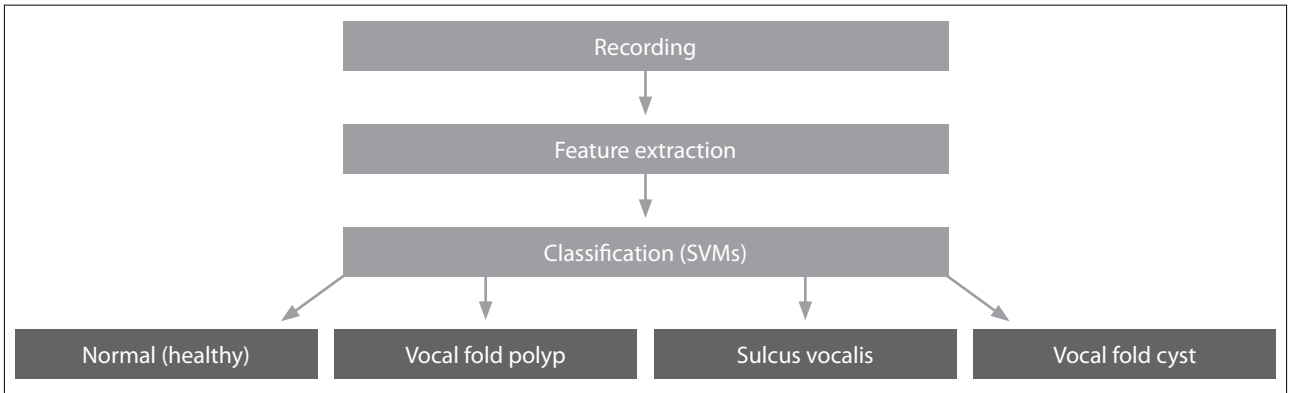

Figure 1. Block diagram of the proposed detection system

Materials and Method

Database

In this study, voice recordings were made through a dynamic one-way microphone (Shure SM58). EMU-Tracker Pre was preferred as the recording interface. The reason for this preference is that the recorded data can be used later in other programs. Recording was done in a sufficiently quiet room with a background noise of 45-60 dB. The sampling frequency of the recorded data is 44100 Hz and is in single channel PCM format with 16 bit resolution.

The sound data is recorded in different settings. A record of 10 seconds is executed for wovel / a /, and also, a paragraph is read about this time period. Many studies in the literature use this vowel because of the stationary acoustic features of / a /. 120 patients were examined in this study. The details of the patients are given in Table 1.

With the software developed for the study, the features of the sounds can be extracted and can be divided into sub classes depending on the features.

Table 1. Patient database knowledge

Pathology	Total	Women	Men
Vocal fold polyp	30	18	12
Vocal fold cyst	34	18	16
Sulcus vocalis	24	14	10
Normal (Healthy)	34	12	22

Methodology

In this study, differently from the previous ones, the sounds were modeled before the feature extraction using two different models; linear predictive coding (LPC) and Mel frequency cepstral coefficients (MFCC). The modelling process was carried out in three stages as given in Figure 2.

In the scope of the study, two different coefficient types were taken as basis for modeling of signals. LPC and MFCC coefficients of the signals were calculated after the preliminary steps were completed. The sound data is re-modeled with the calculated coefficients, and so the recorded speech is divided into two different signal types, clean and residual signals. In the aimed study, it was investigated whether some information was extracted from the signals obtained from the models.

Preprocessing

The modeling of the sounds and the calculation of the attributes from the modeled data are performed after some preprocessing. First, the audio data is automatically divided into sub-segments at specific lengths. Discretized signal is shown in the low-order linear difference model for use in the preprocessing steps as follows:

$$\hat{s}(n) = s(n) - \alpha s(n-1) \quad (1)$$

In this study, it is stated that it is appropriate to take α around 0.95 [17]. It is also assumed in this study that the characteristics of the voice data change slowly in time. In the scope of the study, the discrete M samples were taken and the sound windows with N samples were shown as follows;

$$x_l(n) = \hat{s}(Ml+n) \quad n = 0,1,...,N-1, l = 0,1,...,L-1 \quad (2)$$

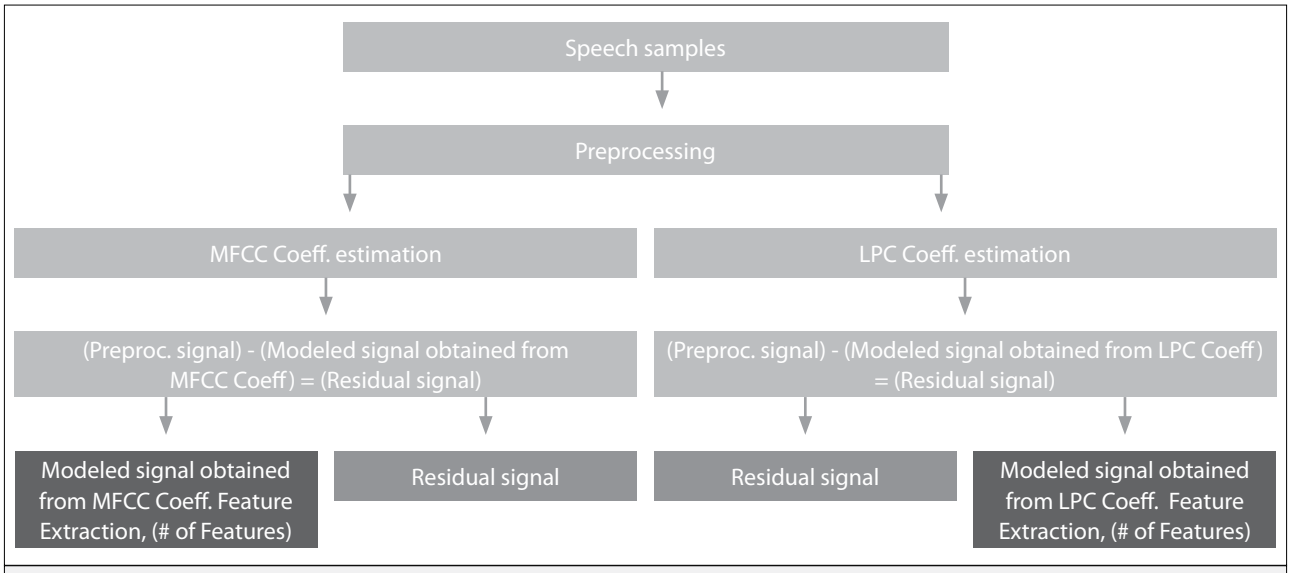

Figure 2. Flow chart of the modeled signal and residual signals from LPC and MFCC coefficients.

The purpose in the framing is to block the interruption of feature characteristics in the signal. Hamming windowing method is preferred for study by taking samples from similar studies. The window $w(n)$ is defined in interval $0 \le n \le N-1$, so the windowed signal is given as

$$\overline{x}_l(n) = x_l(n)w(n) \quad 0 \le n \le N-1 \tag{3}$$

Hamming windowing methods for this study is given as

$$w(n) = 0.54 - 0.46\cos\left(\frac{2\pi n}{N-1}\right) \quad 0 \le n \le N-1 \tag{4}$$

Linear Predictive Coding (LPC)

Linear predictive coding is one of the most important analysis techniques [22]. In particular, it has become a superior method for estimating audio parameters such as pitch, formant, spectrum, and vocal tract, when speech signals are stored and transmitted. The main ability of LPC is to be able to obtain a sound sample by linear combination from previous sound samples [22]. The sound data given at time n is expressed in linear form with p coefficients:

$$s(n) \approx a_1 s(n-1) + a_2 s(n-2) + \ldots + a_p s(n-p) \tag{5}$$

where $a_1 \; a_2 \; \cdots \; a_p$ denotes the parameter coefficients of the LPC. Once the autocorrelation of the window frames is established, these coefficients are obtained by the Levinson-Durbin method [23]. The signal modeled from the obtained coefficients is now cleaned from the recorded speech voice thanks to the coefficients.

Mel Frequency Cepstral Coefficients (MFCC)

The spectral coefficients of the windowed frames after the preprocessing are calculated using Fast Fourier Transform (FFT). In here, FFT gives the information of the amount of energy of each frequency band of the signal. The calculation of MFCC depending on the this procedure is given in Figure 3;

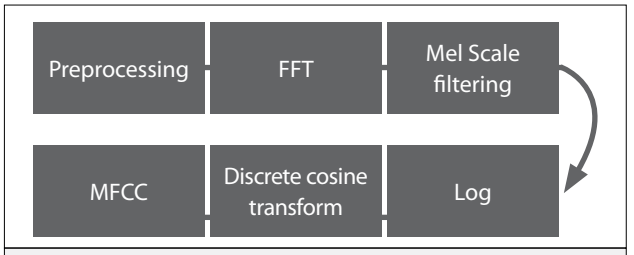

Figure 3. Flowchart of the MFCC coefficient estimations.

Human ears are not sensitive enough to detect sounds below 1000Hz [24]. Owing to these information, MFCC coefficient estimation is realized. Mel scaling frequency mapping isshown as linear below 1000Hz, logarithmic above 1000Hz [24]. Thus, at low frequencies, the corner and center frequencies are linear and logarithmic at high frequencies. Figure 4 gives information about this process.

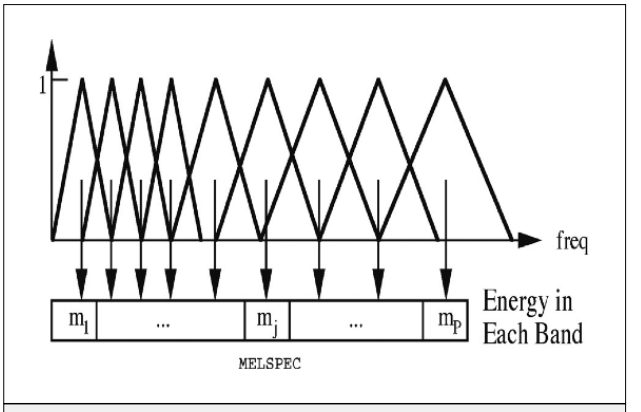

Figure 4. Mel Scale Filter Bank.

Mel scaling is given in (6),

$$Mel(f) = 2595\log_{10}\left(1 + \frac{f}{700}\right) \tag{6}$$

When this process occurs, the coefficients of each short time Fourier Transform (FT) are multiplied by the corresponding filter gain. So, the total is obtained by this process. Thus, DCT is applied to the log of Mel cesptral coefficients, so that MFCC is obtained.

Chaotic Model of System

The phase space must first be calculated before the chaotic model of a system can be obtained. According to Takens [25], if the size of the embedded dimension is chosen as large, the phase space of the time series can be constructed. One of the best techniques for the constructing phase space is the delay method.

An unknown dynamic system is defined as a time series $s(t)$. In this case, the m-dimensional $\tilde{s}(t)$ vector is obtained from the time delay of $s(t)$.

$$\tilde{s}(t) = \left[\; s(t), \quad s(t+\tau), \quad \ldots \quad s(t+(m-1)\tau) \; \right] \tag{7}$$

where τ and m represent the time delay and embedded dimension. These values are not known in practice and are calculated. In the study, it was observed that depending on the voice pathologies, the voice data have different characteristics, resulting in the reconstruction of phase space. The pathology related phase space representation is given in Figure 5.

When the figure 5 is examined, it is observed that the phase spaces obtained from the voices of the pathological signals also have different views.

Feature Extraction

In the study, features that can be evaluated in different characteristics, such as linear and nonlinear, were extracted. In here, before the features extraction, the voice signals were separated into frames, which were then used to calculate the features. In

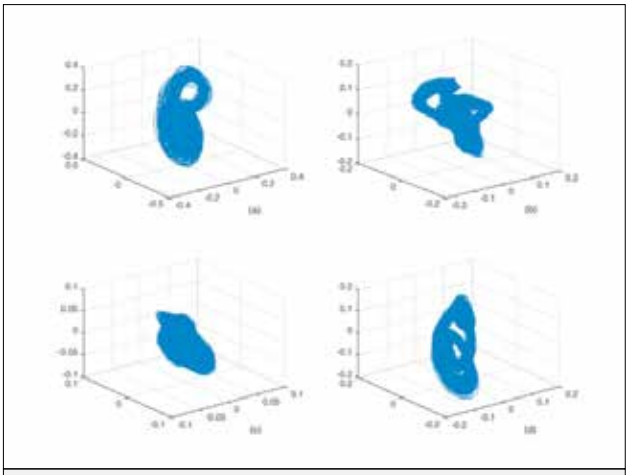

Figure 5. Phase space of the Cyst (a), Normal Person (b), Polyp (c), Sulcus (d) modeled signals.

this study, jitter, shimmer, skewness, kurtosis, entropy, and largest Lyapunov exponents (LLEs) were calculated.

Jitter

Jitter is known as the average approximate difference in divided time between consecutive periods [5-7].

$$jitter(relative) = \frac{\frac{1}{N-1}\sum_{i=1}^{N-1}|T_i - T_{i+}|}{\frac{1}{N}\sum_{i=1}^{N} T_i} \quad (8)$$

Where, T_i is the period length of the F_0 and *N* is the number of period of F_0 [5].

Shimmer

Shimmer is defined as the average approximate difference between the amplitudes of successive periods [5,6].

$$Shimmer(relative) = \frac{\frac{1}{N-1}\sum_{i=1}^{N-1}|A_i - A_{i+}|}{\frac{1}{N}\sum_{i=1}^{N} A_i} \quad (9)$$

where, A_i represents the amplitude of the peak to peak, and N is number of the extracted fundamental frequency F_0.

Skewness and Kurtosis

The skewness of any variable or signal $\tilde{s}(t)$ is defined as the standardized third moment of this signals [26].

$$Skew[\tilde{s}(t)] = E\left[\left(\frac{\tilde{s}-\mu}{\sigma}\right)^3\right] \quad (10)$$

where, E[.] represents the expected operator, μ represents average, and σ represents standard deviation.

The kurtosis of any variable or signals $\tilde{s}(t)$ is defined as the standardized fourth moment of the signals [27]. The kurtosis is given as,

$$Kurt[\tilde{s}(t)] = \frac{E[(\tilde{s}-\mu)^4]}{(E[(\tilde{s}-\mu)^2])^2} \quad (11)$$

Entropy

Entropy, the probability distribution of a random variable or signal $\tilde{s}(t)$, or a level of uncertainty [28]. Shannon has defined the definition of entropy as the uncertainty of a probabilistic distribution [28]. Shannon has proposed a method, which is a self-knowledge, has a logarithmic function, the values between 0 and 1. If the relational probability of the events is defined as $X = \tilde{s}_i, (i = 1,2, \dots, n)$. Then, self probability $h(p_i)$,

$$h(p_i) = log_2(\frac{1}{p_i}) \quad (12)$$

Entropy is derived as the weights of n number of self-information values.

$$H_k = \sum_{i=1}^{n} p_i log_2(\frac{1}{p_i}) \quad (13)$$

Largest Lyapunov Exponent (LLE)

Dynamic systems have characteristic exponents that determine the precision of the initial conditions. Attractors determine the convergence, the measure of the average ratio, or the divergence of the trajectory. According to Rosenstein [29], after the time delay vectors are reconstructed, the closest negihbour of the state in the phase space orbital is searched. The nearest neighbor pairs by LLEs in a given position are expressed by the divergence formula,

$$d_j(i) \approx C_j e^{\lambda_1(i,\Delta t)} \quad (14)$$

where, C_j represents the initial separation, Δt represents the sampling period, and $d_j(i)$ represents the nearest neighbour of the jth pairs. After taking the logarithm of the two sides,

$$lnd_j(i) \approx lnC_j + (i.\Delta t) \quad (15)$$

The LLEs are calculated as follows for the voice signals;

$$y(i) = \frac{1}{\Delta t}\langle lnd_j(i)\rangle \quad (16)$$

where, $\langle \dots. \rangle$ represents the average of the j values.

MultiClass Support Vector Machines (M-SVMs)

M-SVMs can be used in many different areas [30]. In the first stage, two different sets of data were used to separate each other under certain conditions. This process was done via binary SVMs. Later, it is also being used in multiple classification operations. According to Vapnik [30], if having training data $(x_i, y_i), i = 1,2, \dots, n$ and $x_i \epsilon R^d$ and $y_i \epsilon \{\pm 1\}$) and can transform it into a higher dimensional space, the feature space will be $\varphi(\dots), R^d \xrightarrow{\varphi(\dots)} R^H$.

$$\underset{w,\zeta,b}{Minimize} \quad \left\{\frac{1}{2}||w||^2 + C\sum_i \zeta_i\right\}$$
$$Subject\ to\ y_i(\varphi^T(x_i)w + b) \geq 1 - \zeta_i, \quad (17)$$
$$\forall_i = 1, \ldots, n, \quad \zeta_i \geq 0$$

Here, (w, b) defines a linear classifier in the features space. For forming two classes, SVMs force positive samples to +1 denominator and negative samples force -1 denominator lower. If these samples do not fulfill this condition, and if needing zero in the formulation, then there is a forcing/punishment in the objective function.

In (17), the included norm of w, checks whether margin is the maximum. The objective of $C\sum_i \zeta_i$ is to check the number of misclassified samples. When optimization is applied to solving the problem, there is a degradation between the classes due to uneven density of feature space clusters. In multiple SVMs, binary SVMs use different weight vectors and bias is applied for each class (w^j and b^j for $j\epsilon\{1,2,\ldots,k\}$). Classifier function of SVMs,

$$f(x) = arg.\max(\phi^T(x)w^i + b^j), j\epsilon\{1,\ldots,k\} \quad (18)$$

If equation(18) applies for each class,

$$\underset{w^j,b^j,\zeta_i^{j,m}}{Minimize} \left\{\frac{1}{2}\sum_{j=1}^{k}||w^j||^2 + C\sum_{j=1}^{k}\sum_{\substack{m=1\\m\neq j}}^{k}\sum_{i=1}^{n^j}\zeta_i^{j,m}\right\}$$
$$Subject\ to\ (\phi^T(x_i^j)w^j + b^j) - (\phi^T(x_i^j)w^m + b^m) \quad (19)$$
$$\geq 2 - \zeta_i^{j,m}, \zeta_i^{j,m}$$
$$\geq 0, \forall_j = 1, \ldots, k, \forall m = 1, \ldots, k(m \neq j), \forall i = 1, \ldots, n^j$$

where, x_i^j represents the ith samples of the jth class, n^j also represents the number of samples of training data. We have focused our study on non-linearly separable problems. To extend this simple model to solve non-linear separable problems, researchers have developed kernel based methods. This type of methods apply mapping functions on the input features and carry them into a very high dimension space and then construct a hyperplane in that feature space. The properties of the feature space depend on the kernel functions of the SVMs. The generally used kernel functions are polynomial, Radial Basis Function (RBF), and sigmoidal functions. To find out more about kernel functions and implementation of SVMs, the reader is referred to [30,31].

Results and Discussion

In this work, the preprocessing step has been carried out since the recording of the sound data. After the preprocessing, the recorded data are modeled by calculating LPC and MFCC coefficients. The modeled signals were first separated into subframes, then the characteristics of each frame were extracted and pathological classification was made depending on these features. When classification was performed, 30% of the data were randomly selected as test and 70% were randomly selected as training data.

The signals modeled from the coefficients are called clean data and are removed from the recorded data to generate the residual data. Thus, the main audio data is composed of two signal components, clean and residual. The signals split in two are analyzed in two dimensions. First, features extraction of the signals is performed. Features spaces of the clean signals owing to the different coefficients are given in Figure 6.

Figure 6 shows the spatial distribution of pathological data using 3 different features. When the entropy data obtained from the MFCC coefficients are analyzed, it is observed that the normal person and the patohological diagnosed person data can be distinguished from each other seriously. In the model based on LPC coefficients, this separation can be observed more clearly. Especially when the results of entropy, jitter and shimmer are examined, it is observed that the data can be separated from one another. Owing to the Student-T test results, the association of pathological and normal people with these traits can be distinguished, giving the following results.

When Table 2 is examined, it is observed that the signal obtained from the LPC-based model gives more meaningful results than the signal obtained from the MFCC-based model. The model features formed by LPC coefficients are seen from the results that pathological and normal person data can be separated from each other. Among the features, LLE is determined from the results that it does not give meaningful results in the analysis and separation of the data of pathological and normal person data. When the characteristics of the signals obtained from the MFCC coefficients are examined, it is observed that only the Shannon entropy feature values have distinctive meanings obtained from normal and pathological data.

Figure 7 shows histogram curves of voices based on feature values. By looking at the Figure 7, especially the entropy values, it can be said that their distributions are approximately separated from each other. This has also improved the sense of classification accuracy.

On the graph of entropy and skewness histogram, it is observed that the values are approximately separated from each other. Kurtosis, shimmer, and jitter, there is no clear separation. However, there is a small discrimination in the LLE values. When we use all the features together for the classifier, the differences are significant for the classifier.

BoxPlot graphs based on the values of the features are shown in Figure 8. Figure 8, information about the property-specific distribution of pathological and healthy people. Again, based on previous findings, similar results were obtained on the basis of the evaluations. In entropy values, it differs from the normal and pathological patients in distinguishing qualities. Is is ob-

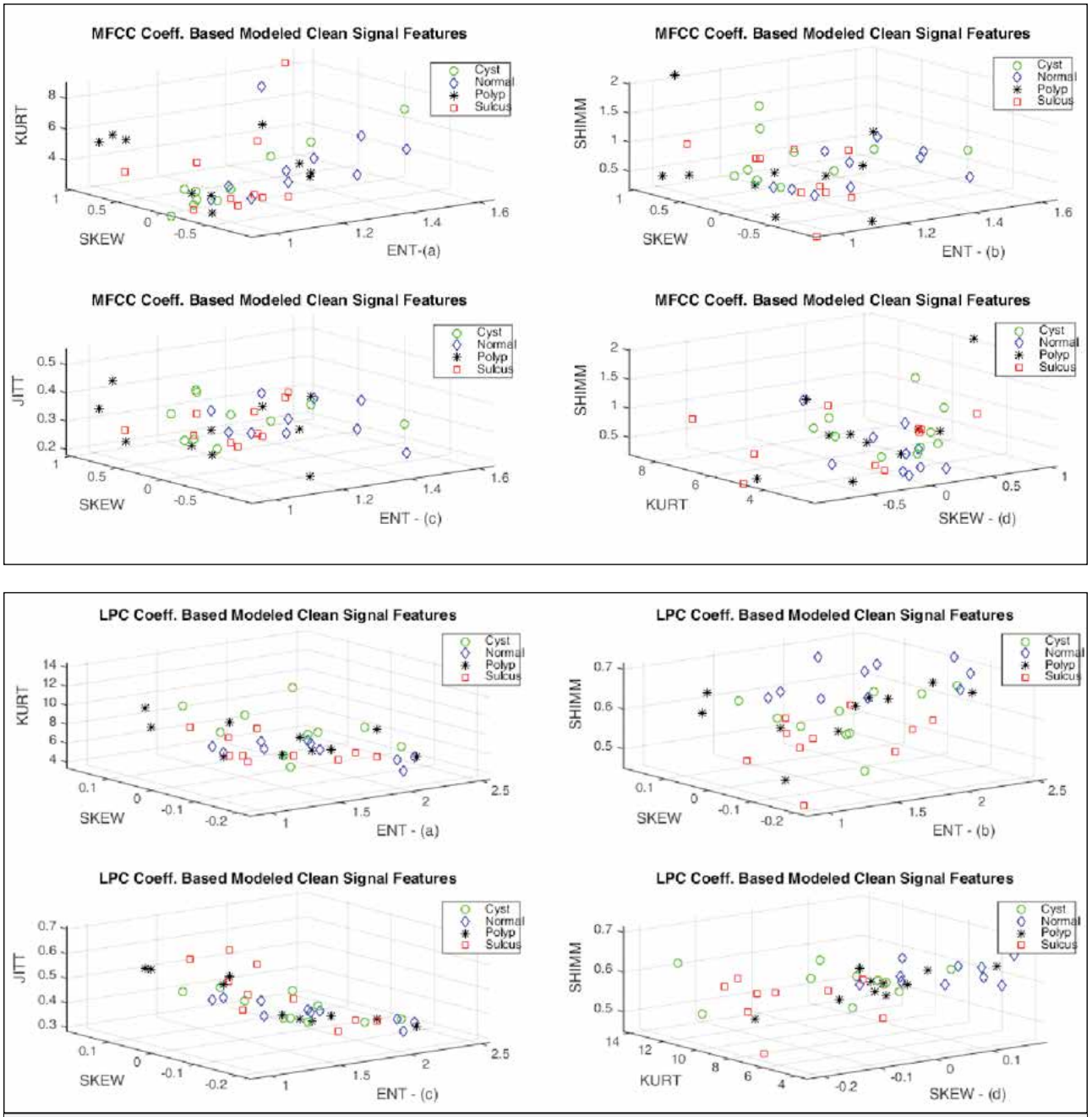

Figure 6. Features spaces of the pathological signals

served from the Figure 8 that while skewness and kurtosis are not determinant for cystic pathology, entropy, LLE and shimmer values are determinant. For sulcus pathologies, shimmer is the most defining feature.

Classifier Results

In the scope of the study, SVMs with multiple classification features were preferred. Especially in multiple classifications, the ability of SVMs to be high is the reason for selecting the classification and training accuracy in the same conditions to be high compared to some other classifiers [32].

Throughout this paper, it is carried out experiments using the one-against-all SVMs design scheme. Given a five-class problem, there are five binary SVMs and each is trained to separate one class of samples, which are positive in the experiments different than the others. The decision is made according to the maximal output among these binary classifiers [30]. It has been conducted the experiments using SVMs tool, which efficiently handles large-scale SVMs learning problems [33].

Gaussian kernel as kernel and 1e-5 as lambda value are selected. In case of experimental studies, the obtained experimental

Table 2. Student-t Test results

	Separation Group	LPC coeff. Based model signal	MFCC coeff. Based model signal
Jitter	N-P	0.005987885	0.651831
	N-S	7.43402E-07	0.248628
	N-C	0.000549804	0.159287
Entropy	N-P	0.0165838	0.006515
	N-S	2.27914E-06	0.01639
	N-C	0.007125662	0.033019
Kurtosis	N-P	0.545246	0.073383
	N-S	0.589144	0.189005
	N-C	0.587493	0.465145
Shimmer	N-P	0.005434	0.182185
	N-S	0.000626	0.122752
	N-C	0.021906	0.002425
Skewness	N-P	0.368412	0.945534
	N-S	0.001053	0.250572
	N-C	0.082233	0.349198
LLE	N-P	0.593211	0.173884
	N-S	0.839202	0.210503
	N-C	0.583968	0.433694

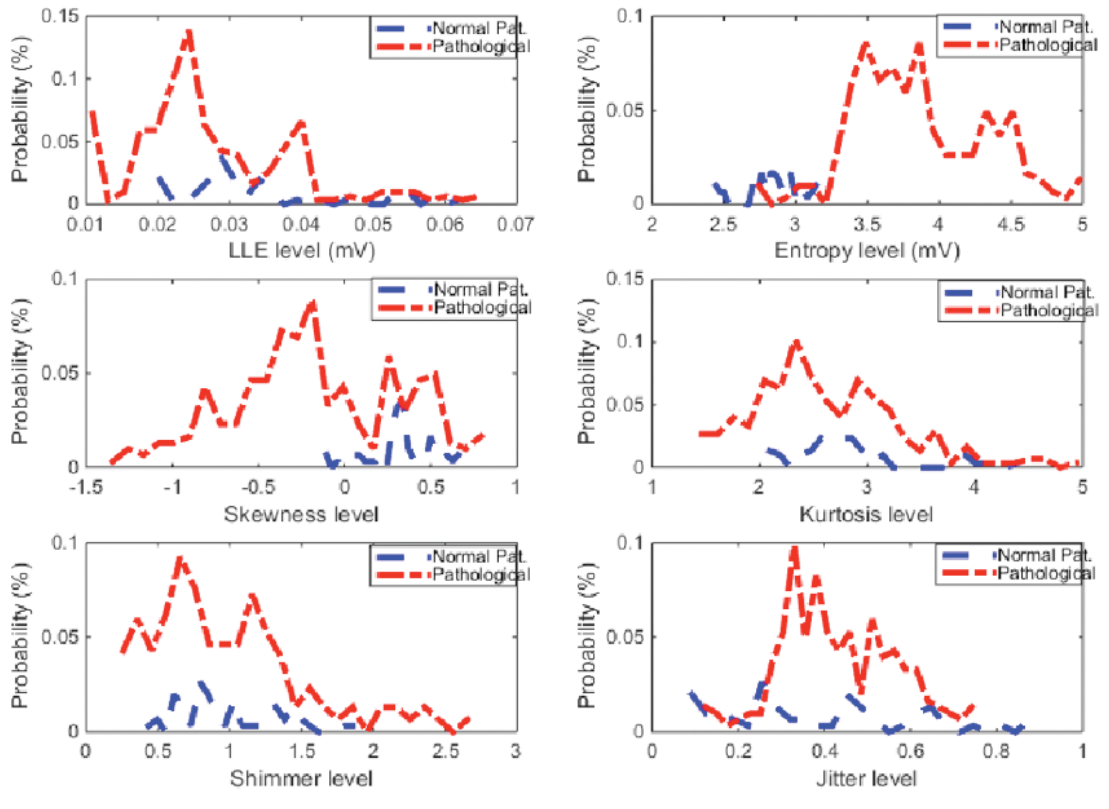

Figure 7. Histogram of the feature values

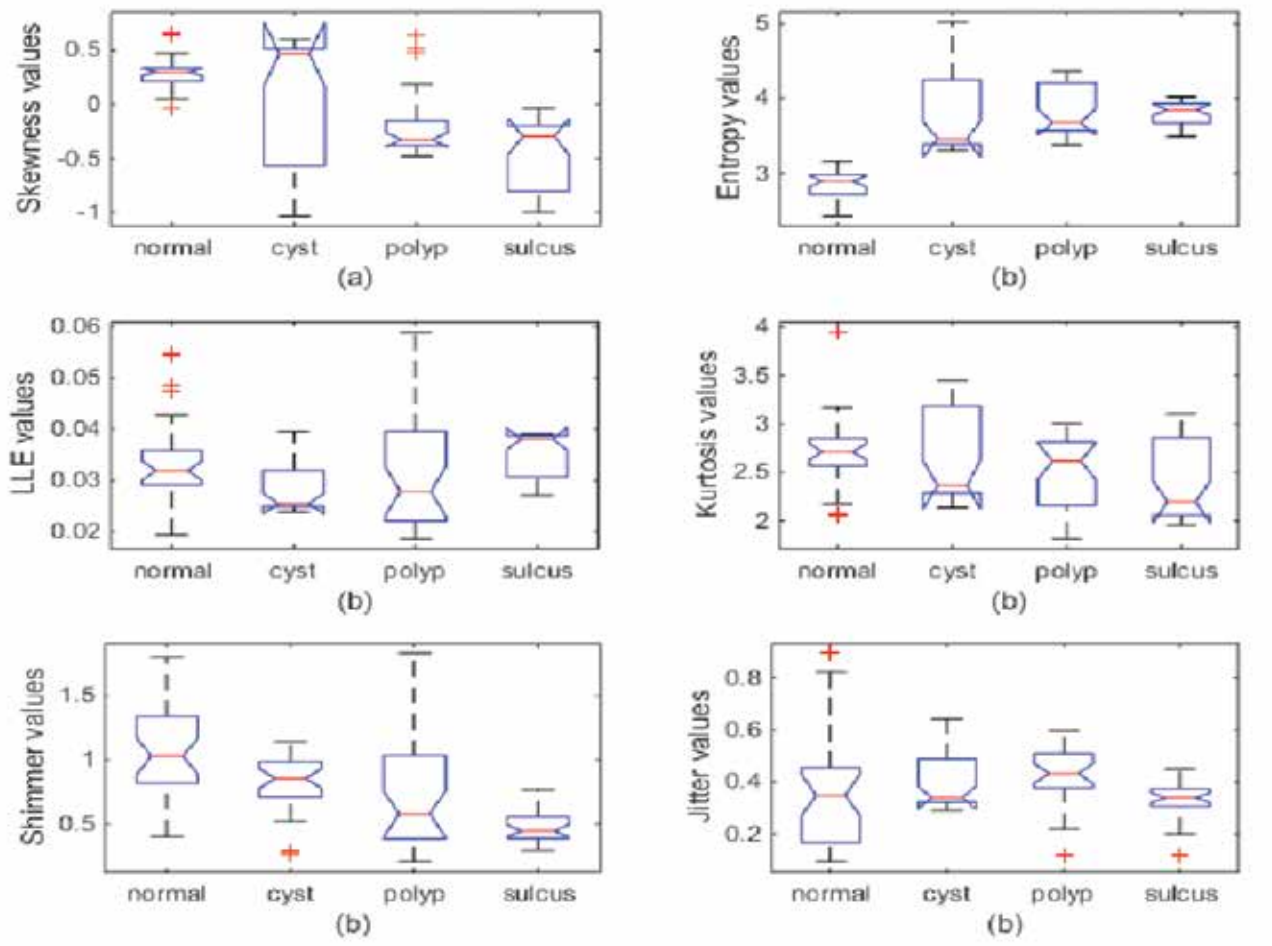

Figure 8. Boxplot graphs of the features

results have been compared with the other kernel functions (polynomial and sigmoid functions). However, the best (maximum classification results) results have been obtained with the Gaussian RBF. Classification results are given in Figure 8.

Entropy values play a critical role when looking at the classification results. Effect on the results of all classification, and other features, together with significant results. Entropy as well as the jitter that contributed most to the accuracy of the classification. It is observed from the results that the LLE is the least contribution feature. It can be seen from the student-t test the reason why we have to reach this results already. The effects that multiple features have added to the classifier are still observed on the Table 3. It can be seen from the Table 3 that each feature increased the classification accuracy of the test data results. Previous studies on the pathologic classification of voice data and a comparison of our study are given in Table 4.

When Table 4 is examined, it seems that working has some advantages. The number of features is reduced first. The process complexity is reduced and the system speed is increased. Especially in lesser numbers of reatures, the accuracy rate seems to be increased. On this count, the need for less data storage arises. In addition, chaotic analysis of the sounds was performed as a result of the operation of the proposed model. As well as pathological classification based on the characteristics of the data was performed. Thus, the study shows that pathological data can be separated less number of features.

Conclusions

In this paper, we showed multi-class SVMs whether can classify the pathological and normal voices into sub classes. It is concluded from the experimental results that multi-class SVMs provide good performance for classification of these voice data

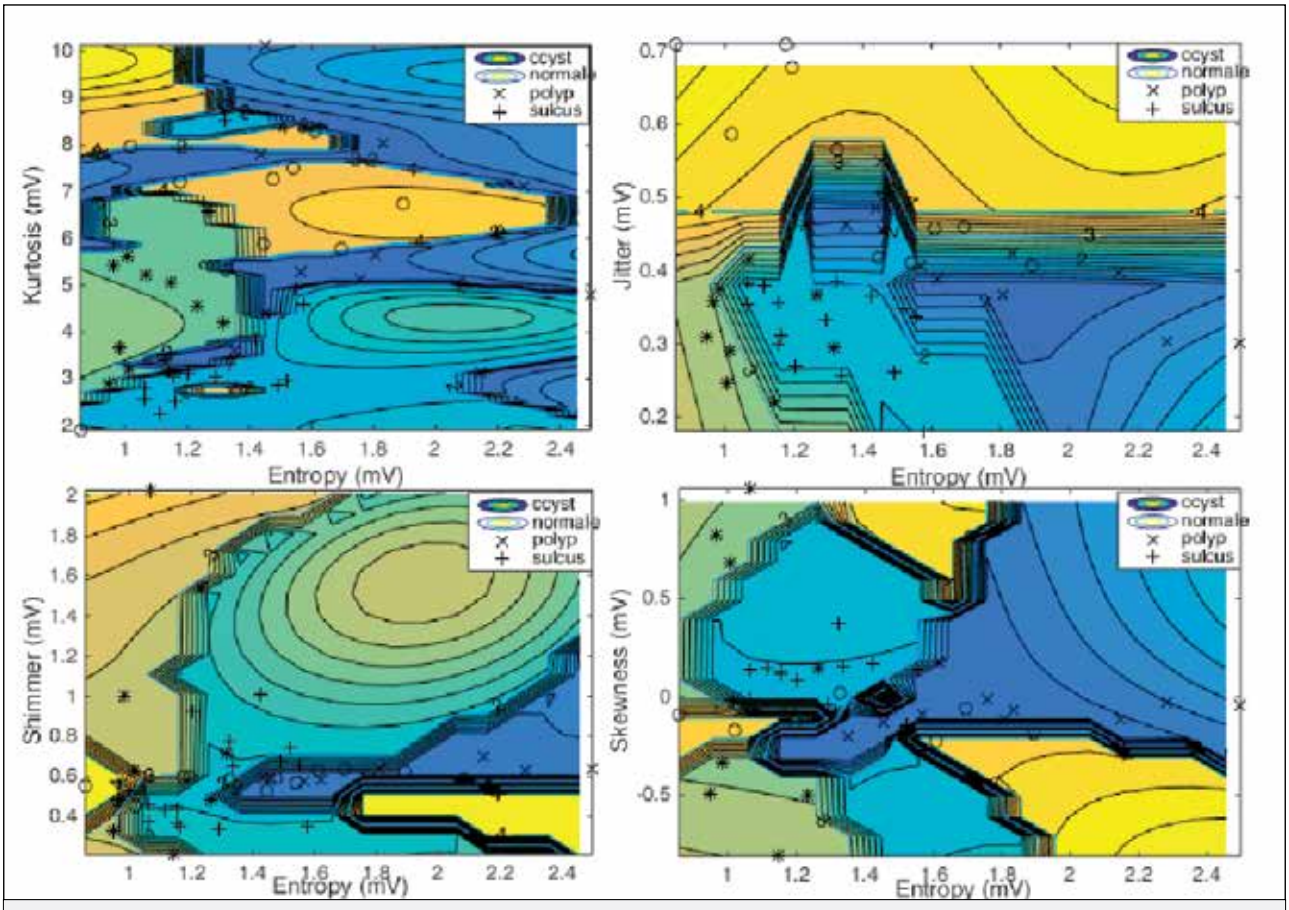

Figure 9. M-SVMs classification results depending on the related features

Table 3. M-SVMs classification results for the features

Features	Data	(%)
Entropy-Kurtosis	Training	100.00
	Test	93.45
Entropy-Jitter	Training	85.76
	Test	80.79
Entropy-Shimmer	Training	77.89
	Test	70.56
Entropy-Skewness	Training	72.67
	Test	66.60
Entropy-LLE	Training	78.87
	Test	67.00
Entropy-Kurtosis-Jitter	Training	100.00
	Test	94.57
Entropy-Kurtosis-Jitter-Shimmer	Training	100.00
	Test	96.60
Entropy-Kurtosis-Jitter-Shimmer-Skewness	Training	100.00
	Test	97.05
Entropy-Kurtosis-Jitter-Shimmer-Skewness-LLE	Training	100.00
	Test	97.20
10 features	Training	100.00
	Test	99.56

Table 4. Speech data classification studies and accuracy results

Methods			Database			
Post-Processing	**Classifier**	**Feat.No**	**Normal**	**Pathological**	**Accuracy (%)**	**Study**
-	M-SVMs	10	68	172	100.00	Proposed Study
GA and LDA	SMVs	18	53	240	98.3	[34]
LDA	SVMs	40	53	240	97.01	[35]
LDA and PCA	SVMs	64	53	67	100.00	[36]
LDA and PCA	SVMs	22	50	50	94.26	[37]
-	SVMs	26	53	173	98.23	[38]
-	ANN and LVQ	19	53	82	96	[10]

depending on used the features. For one-against-all SVMs, we proved that in associated with LLE, entropy, skewness, kurtosis, shimmer, jitter and LPC, MFCC based model coefficients, the SVMs classification performance is very good. Using the ten features, the accuracy rate of training data is 100 % for optimal C values and chossing Gaussian kernel, however, estimated accuracy rate for testing data is 99.56 %.

From the previous studies, [34-38] that showed that the related voices could be classified into normal / pathological as depending on sounds' characteristic features. On the other hand, their used classifier and methods, in [34] as accuracy rate 98.3%, in [35] as accuracy rate 97.01%, in [36] as accuracy rate 100%, in [37] as accuracy rate 94.26%, and in [38] as accuracy rate 98.23%. However, in this study we not only have increased accuracy rate of correct class for pathological and normal classification, but also are able to classify the related voices as four different classes, which are important for diagnosying speech voice' analysis. Additionally, with less number of features, obtaining the accuracy rate. So, the database storage could be reduced, not only processing complexity has gone to reduce, but also system performance being increased.

Additionally, we can easily see that gaussian RBF kernel provides good performance for classifying data. Finally, we demonstrated by computer experiment that multi-class SVMs can provide good result and can detect normal, voice sound segments.

Acknowledgements

The author would like to thank Dr. Derya Yılmaz and Dr. Mehmet Akif Kılıç for the related data.

References

1. J. R. O. Arroyave, J.F.V. Bonilla, E. D. Trejos, "Acoustic analysis and non linear dynamics applied to voice pathology detection: A review", *Recent Patents on Signal Processing,* vol. 2, pp. 1–11, 2012.
2. S. Fong, K. Lan, R. Wong, "Classifying human voices by using hybrid SFX time-series preprocessing and ensemble feature selection", *BioMed Research International,* vol. 1–27, 2013.
3. J. I. Godino-Llorente, N. S´aenz-Lech´on, V. Osma-Ruiz, S.Aguilera-Navarro, P. G´omez- Vilda, "An integrated tool for the diagnosis of voice disorders," *Medical Engineering & Physics,* vol. 28, pp. 276–289, 2006 [CrossRef]
4. C. Manfredi, M. D'Aniello, P. Bruscaglioni, A. Ismaelli, "A comparative analysis of fundamental frequency estimation methods with application to pathological voices," *Medical Engineering & Physics,* vol. 22, pp. 135–147, 2000. [CrossRef]
5. M. Farrus, J. Hernando, P. Ejarque, "Jitter and shimmer measurements for speaker Recognition," *Annual Conference of the International Speech Communication Association (Interspeech 2007),* Antwerp, Belgium, pp. 778–781, 2007.
6. P. Lieberman, "Some acoustic measures of the fundamental periodicity of normal and pathologic larynges", *The Journal of the Acoustical Society of America*, vol. 35, pp. 344–353, 1963. [CrossRef]
7. Y. Horii, "Vocal shimmer in sustained phonation," *Journal of Speech, Language, and Hearing Research,* vol. 23, pp. 202–209, 1980. [CrossRef]
8. E. Yumoto, W. J. Gould, T. Baer, "Harmonics-to-noise ratio as an index of the degree of hoarseness," *The Journal of the Acoustical Society of America*, vol. 71, pp: 1544–1550, 1982. [CrossRef]
9. L. R. Rabiner and B. H. Juang, "Fundamentals of Speech Recognition," Vol. 14, PTR Prentice Hall, Englewood Cliffs, NJ.
10. J. I. Godino-Llorente, P. Gomez-Vilda "Automatic detection of voice impairmentsby means of short-term cepstral parameters and neural network based detectors," *IEEE Trans. Biomed. Eng.,* vol. 51, pp. 380–384, 2004. [CrossRef]
11. Y. Zhang, et al. "Nonlinear dynamic analysis of voices before and after surgicalexcision of vocal polyps," *J. Acoust. Soc. Am.,* vol. 115, pp. 2270–2277, 2004. [CrossRef]
12. T. L. Eadie, P. C. Doyle, "Classification of dysphonic voice: Acoustic and auditory-perceptual measures," *Journal of Voice,* vol. 19, pp. 1–14, 2005. [CrossRef]
13. S. Hadjitodorov and P. Mitev, "A computer system for acoustic analysis of pathological voices and laryngeal diseases screening," Medical Engineering & Physics, vol. 24, p. 419–429, 2002. [CrossRef]
14. N. Saenz-Lechon, J. I. Godino-Llorente, V. Osma-Ruiz, M. Blanco-Velasco, F. Cruz-Roldan, "Automatic assessment of voice quality according to the GRBAS scale," 28th Annual International Con-

ference of the IEEE Engineering in Medicine and Biology Society, EMBS'06, New York, NY, USA, pp. 2478–2481, 2006. [CrossRef]
15. K. Umapathy, S. Krishnan, V. Parsa, D. G. Jamieson, "Discrimination of pathological voices using a time-frequency approach," *IEEE Transactions on Biomedical Engineering*, vol. 52, p. 421–430, 2005. [CrossRef]
16. J. I. Godino-Llorente, P. Gomez-Vilda, M. Blanco-Velasco, "Dimensionality reduction of a pathological voice quality assessment system based on Gaussian mixture models and short-term cepstral parameters," *IEEE Transactions on Biomedical Engineering,* vol. 53, p. 1943–1953, 2006. [CrossRef]
17. S. Jothilakshmi, "Automatic system to detect the type of voice pathology," *Applied Soft Computing,* 2014. [CrossRef]
18. A. Skalski, T. Zielinski, D. Deliyski, "Analysis of vocal folds movement in high speed videoendoscopy based on level set segmentation and image registration," *International Conference on Signals and Electronic Systems,* ICSES' 08, Krak´ow, Poland, pp. 223–226, 2008. [CrossRef]
19. D. D. Mehta, D. D. Deliyski, S. M. Zeitels, T. F. Quatieri, R. E. Hillman, "Voice production mechanisms following phonosurgical treatment of early glottic cancer," T*he Annals of Otology, Rhinology, and Laryngology,* vol. 119, p. 1, 2010. [CrossRef]
20. R. Srinivasan, R. Rengaswamy, R. Miller, "A modified empirical mode decomposition (EMD) process for oscillation characterization in control loops," *Control Engineering Practice* vol. 15, pp. 1135-1148, September, 2007. [CrossRef]
21. J. C. Saldanha, T. Ananthakrishna, R. Pinto, "Vocal fold pathology assessment using mel- frequency cepstral coefficients and linear predictive cepstral coefficients features," *Journal of Medical Imaging and Health Informatics,* vol. 4, pp. 168–173, 2014. [CrossRef]
22. L. Deng and O. Douglas O. "Speech processing: a dynamic and optimization-oriented approach," *Marcel Dekker,* pp. 41–48, 2003.
23. N. Levinson, "The Wiener RMS error criterion in filter design and prediction," *J. Math. Phys.,* vol. 25, pp. 261–278, 1947. [CrossRef]
24. M. Xu, et al. "HMM-based audio keyword generation," In Kiyoharu Aizawa; Yuichi Nakamura; Shin'ichi Satoh. Advances in Multimedia Information Processing – PCM 2004: 5th Pacific Rim Conference on Multimedia (PDF). Springer. [CrossRef]
25. Takens F. "Detecting strange attractors in turbulence", Dynamical Systemsand Turbulence, Warwick 1980, Springer, 1981, pp. 366–381.
26. N. L. Johnson, S. Kotz, N. Balakrishnan "Continuous Univariate Distributions," 1994, vol.1, 2nd Edition Wiley.
27. P. H. Westfall, " Kurtosis as Peakedness," 1905–2014. R.I.P., The American Statistician 68, 2014, p. 191–195. [CrossRef]
28. C. E. Shannon, "A mathematical theory of communication", *Bell System Technical Journal,* vol. 27, pp. 623–656, 1948. [CrossRef]
29. M. T. Rosenstein, J. J. Collins, C. J. De Luca. "A practical method for calculating largest Lyapunov exponents from small data sets," *Physica D,* vol. 65, pp. 117–134, 1993. [CrossRef]
30. V. Vapnik. "Statistical Learning Theory", New York, NY, USA: John Wiley&Sons, 1998.
31. T. Joachims, "Making large-scale SVM learning practical in Advances in Kernel Methods-Support Vector Learning", B. Schlkopf, C. J. C. Burges, and A. J. Smola, Eds., 1999, pp. 169–184, MIT Press, Cambridge, Mass, USA.
32. H. Ankışhan and D. Yılmaz, "Comparison of SVMs and ANFIS for Snore Related Sounds Classification by Using the Largest Lyapunov Exponents," *Computational and Mathematical Methods in Medicine*, vol. 2013, 2013.
33. C. W. Hsu and C. J. Lin, "A comparison of methods for multiclass support vector machines," *IEEE Transaction on Neural Networks,* vol. 13, pp. 415-426, May 2002. [CrossRef]
34. G. Hamzeh, T. K. Mehdi, K. A. Meisam, P. Mohammad "Detection of vocal disorders based on phase space parameters and Lyapunov spectrum," *Biomedical Signal Processing and Control*, vol. 22, p. 135–145, 2015. [CrossRef]
35. A. Akbari, M. K. Arjmandi, "Employing linear prediction residual signal of waveletsub-bands in automatic detection of laryngeal pathology," *Biomed. Signal Processing and Control* vol. 18, 293–302, 2015. [CrossRef]
36. M. K. Arjmandi, M. Pooyan, "An optimum algorithm in pathological voice qualityassessment using wavelet-packet-based features, linear discriminant analysisand support vector machine," *Biomedical Signal Processing and Control,* vol. 7, pp. 3–19, 2012. [CrossRef]
37. M. K. Arjmandi, et al. "Identification of voice disorders using long-time featuresand support vector machine with different feature reduction methods," *J. Voice,* vol. 25, pp. 275–289, 2011. [CrossRef]
38. J. D. Arias-Londono, et al. "Automatic detection of pathological voices using com-plexity measures, noise parameters, and mel-cepstral coefficients," *IEEE Trans. Biomed. Eng.* vol. 58, pp. 370–379, 2011. [CrossRef]

Haydar Ankışhan was born in Ankara, Turkey, 1979. He received th B.S. degree in electrical and electronics engineering from the Gaziantep University, M.S. and Ph.D. degrees in electronics/ electrical and electronics engineering from the Ankara University, Turkey, 2003, 2007, 2015., respectively. Currently, he works as an assistant professor since 2015 in Vocational School of Technical Sciences in Baskent University, Turkey. His main research interests are acoustic signal processing, biomedical signal processing and implementation, medical devices, simultaneous localization and mapping.

İSTANBUL UNIVERSITY PRESS

RESEARCH ARTICLE

Electrica 2018; 18(1): 72-77

A Comparative Study of Empirical and Variational Mode Decomposition on High Voltage Discharges

Cengiz Polat Uzunoğlu

Department of Electrical and Electronics Engineering, İstanbul University School of Engineering, İstanbul, Turkey

Cite this article as: C. P. Uzunoğlu. "A Comparative Study of Empirical and Variational Mode Decomposition on High Voltage Discharges". *Electrica*, vol. 18, no. 1, pp. 72-77, 2018.

ABSTRACT

Signal quality is the key issue for maintaining effective power transmission in electrical networks. In most cases, a high voltage (HV) is transmitted in power systems to decrease power loss. Power quality disturbances are monitored by observing the noise degradation of HV signals. Increased oscillations and high-frequency components of power signals exhibit nonstationary signal characteristics. In this study, a comparative analysis of empirical mode decomposition (EMD) and variational mode decomposition (VMD) was conducted on noisy discharge signals. These techniques were used for adaptive signal decomposition in the time domain, facilitating the evaluation of deeper characteristics of the investigated signal. The HV discharges were obtained using 0.4/40 kV and 8 kVA transformers in a laboratory, and all the current and voltage signal waveforms were recorded using high-frequency current and high-voltage probes. The results demonstrate distinct calculations of EMD and VMD techniques in terms of signal decomposition and extracting intrinsic mode functions (IMFs), which define low- and high-frequency components.

Keywords: Empirical mode decomposition, variational mode decomposition, intrinsic mode functions, discharge

Introduction

Electrical signal disturbance detection is of significant importance in electrical networks. The disturbances in signal quality may threat electrical devices which are vulnerable to these disturbances such as harmonics, sags, high frequency discharges [1] etc. There are various studies have been conducted for detection of these disturbances recently [2-5].

Most of the disturbances exhibit non-linear signal waveforms and oscillations. For this purpose, time-series signal analysis and frequency spectrum investigations are required for proper analysis. To improve the performance of the proposed techniques, time series decomposition has been investigated for detecting the oscillations [6-7]. Investigated signals (especially proposed HV discharges) may display time varying characteristics where adaptive time series decomposition is quite effective tool and required. In this study, a comparative research of empirical mode decomposition (EMD) and variational mode decomposition (VMD) is conducted.

As an efficient decomposition method, EMD has been introduced for non-linear signals (especially signals with non-stationary characteristics) [8]. EMD is used for effective decomposing of original time-series signal into signal components, which are called intrinsic mode functions (IMFs). Most of the EMD applications contain non-linear time series signal denoising approaches [9-13]. Due to the limitations of EMD, the improper (mode mixing error) IMFs or redundant IMFs can be obtained where the reconstruction of original signal could be challenging task [8].

Variational mode decomposition is a robust and recently introduced non-recursive adaptive time series decomposition method [14]. Unlike EMD, the VMD is computed in frequency domain by updating center frequencies for each mode, which is namely variational computation. In VMD, investigated signal is transformed into a few modes, in which these modes are updated by using Wiener filter. By the aid of the filter, VMD is not prone to background noise [14]. VMD has numerous

Address for Correspondence:
Cengiz Polat Uzunoğlu

E-mail:
polat@istanbul.edu.tr

Received: 05.11.2017

Accepted: 23.11.2017

DOI: 10.5152/iujeee.2018.1811

applications in literature such as biomedical signals, power signals, speech signals and mechanical systems signals [15-19] etc.

In order to investigate highly oscillated HV discharge signals a single-phase transformer with 0.4kV/40kV, 50Hz, 8kVA rated values is employed. During the tests, voltage signals and current signals are obtained and analyzed. Voltage signals are measured via capacitive HV probe (2000:1) and current readings are measured high frequency sensitive current probe. All the signal waveforms recorded via high-speed oscilloscope. After adaptive time series decomposition of voltage and current signals, the IMFs are obtained and analyzed for the comparison. Each IMFs cross correlation coefficients with investigated decomposed time series signal are computed.

This paper is organized as follows. In section 2, the test setup and employed equipment is introduced. In section 3 and section 4 the mathematical background of EMD and VMD methods are presented respectively. In section 5, the test results are provided. Finally, in section 6, the conclusion is given.

Test Setup

High voltage discharge signals are collected by using test setup, which is given in Figure 1. The discharge signal is generated approximately at 5.5kV. In the setup, transformer's secondary winding is open circuited and secondary voltage and discharge currents are recorded. In order to utilize all the aspects of the discharge current signal (evaluate all the frequency components) the current probe is employed. The current probe is capable of measuring frequency components up to 30MHz. Capacitive HV probe (2000:1 turn ratio) is used for measuring voltage of the transformer.

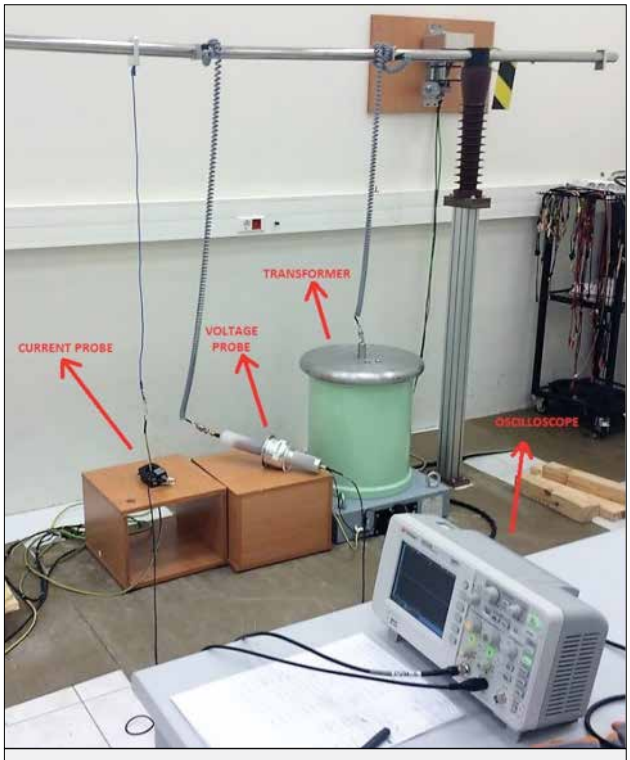

Figure 1. Test Setup

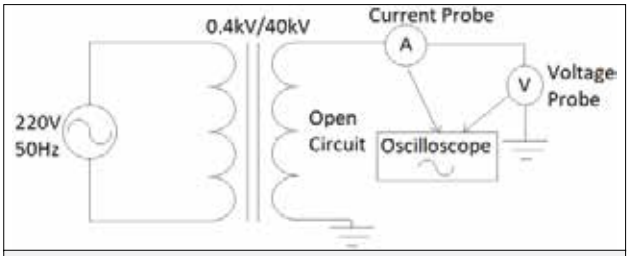

Figure 2. Block Diagram of Test Setup

The block diagram of the test setup is given in Figure 2. In order to eliminate time delay between voltage and current recordings an equal length data cables are used to connect high-speed oscilloscope and probes.

Empirical Mode Decomposition (EMD)

Empirical mode decomposition method is a novel method for decomposing nonlinear, multicomponent time series signals iteratively [8]. The decomposed time series functions (modes) are called IMFs, which exhibit instantaneous frequency and amplitude characteristics processed by Hilbert transform. The EMD algorithm is computed by experimental concept (empirical) rather than analytical calculations [20,21].

According to the EMD criterions, the IMFs should satisfy two limitations: (a) the number of extrema (over-shoot and under-shoot) and the number of zero crossing of the signal must be equal or they might be different at most by one; and (b) the average of the upper and lower envelope which is defined by the local extrema points should be zero everywhere. The local average is zero for each point [8].

EMD process is the iterative method, which is computed systematically. Initially the local extrema points are computed for a given time series signal $x(t)$. The envelope signals of local minima ($e_{min}(t)$) and local maxima($e_{max}(t)$) are obtained. The next step is to calculate local average [9-10]:

$$m(t)=\left[e_{\min}(t)+e_{\max}(t)\right]/2 \quad (1)$$

The IMFs are calculated recursively (by the i parameter) by using local average.

$$c_i(t)=x(t)-m(t) \quad (2)$$

The IMF function is checked for whether calculated IMF is valid according to the criterions mentioned previously. If IMF is not valid, the iterative process is repeated [8,18]. If IMF is valid then IMF is set to $z_1(t)=c_i(t)$.

$$x_1(t) = x(t) - z_1(t) \tag{3}$$

This iteration is repeated for *i=1….n* where signal decomposition is completed and IMFs are generated.

Variational Mode Decomposition (VMD)

Variational Mode Decomposition is a robust process, which decomposes the given signal into different signal waveforms (modes). These modes are characterized by their center frequencies [14]. As a variational approach, the modes (c_k) are evaluated for *k* values where sum of each mode (IMF) is equal to the given time series signal *x(t)*. Hilbert transform is conducted for obtaining frequency spectrum for each mode [14].

$$\left(\sigma(t) + \frac{j}{\pi t}\right) c_k(t) \tag{4}$$

By using computed center frequency, spectrum shifting is fulfilled for each mode where w_k is the center frequency.

$$\left[\left(\sigma(t) + \frac{j}{\pi t}\right) c_k(t)\right] e^{-jw_k t} \tag{5}$$

By definition the constrained variational evaluation for the given signal *x(t)* is the described as:

$$\min_{c_k, w_k} \left\{ \sum_k \left\| \partial_t \left[\left(\sigma(t) + \frac{j}{\pi t}\right) c_k(t) \right] e^{-jw_k t} \right\|_2^2 \right\}, \quad \sum_k c_k = x \tag{6}$$

where $c_k=c_1,c_2….c_k$ and $w_k=w_1,w_2….w_k$ are given. In order to solve variational problem the Lagrangian multipliers are used. In the given solution, a quadratic penalty term α and a Lagrangian multiplier (dual ascent) λ are used to solve unconstrained problem [14-15], [18].

$$\begin{aligned} L(c_k, w_k, \lambda) = \alpha \sum_k \left\| \partial_t \left[\left(\sigma(t) + \frac{j}{\pi t}\right) c_k(t) \right] e^{-jw_k t} \right\|_2^2 \\ + \left\| x(t) - \sum_k c_k(t) \right\|_2^2 + \left\langle \lambda(t), x(t) - \sum_k c_k(t) \right\rangle \end{aligned} \tag{7}$$

As an initial step, VMD process is employed for calculation of c_k^1, w_k^1 and λ^1, which are updated (c_k^{n+1}, w_k^{n+1} and λ^{n+1}) for further orders (n) in upcoming steps. The further calculations are conducted in frequency domain where parameters in frequency domain are given by ^ [18].

$$c_k^{n+1} = \left(\hat{x} - \sum_{i \neq k} \hat{c}_i + \frac{\hat{\lambda}}{2} \right) \frac{1}{1 + 2\alpha (w - w_i)^2} \tag{8}$$

The analyzed signal is decomposed into modes (c_k) by employing center frequencies (w_k) [14].

$$w_k^{n+1} = \frac{\int_0^\infty w \left| \hat{c}_k(w) \right|^2 dw}{\int_0^\infty \left| \hat{c}_k(w) \right|^2 dw} \tag{9}$$

According to the VMD algorithm, each mode is updated in the frequency domain and the center frequencies are re-calculated for each iteration.

Test Results

HV discharges are recorded and investigated via high-speed oscilloscope. High frequency discharges are observed on voltage and current waveforms. The voltage signal of the transformer secondary is given in Figure 3.

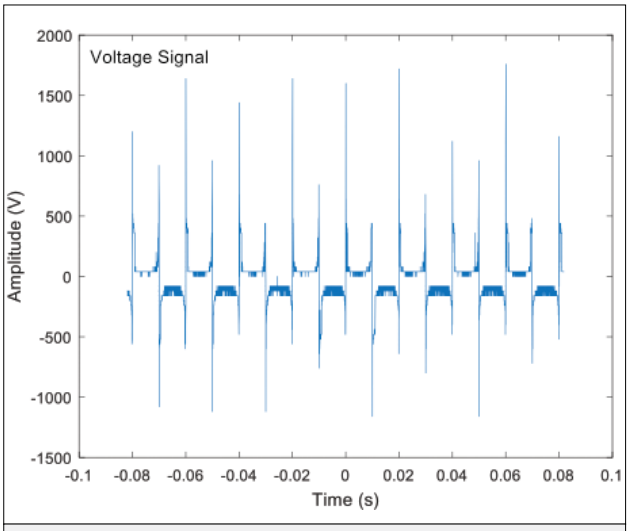

Figure 3. Voltage signal of transformer

The corresponding current signal of the transformer secondary is given in Figure 4.

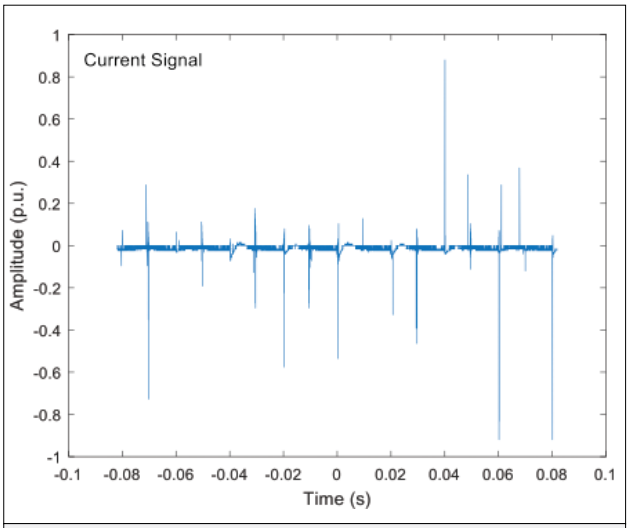

Figure 4. Current signal of transformer

HV discharges tend to produce harmonic components with high frequencies. In order to analyze frequency spectrum fast Fourier transform (FFT) of discharge signals are obtained. The frequency spectrum of voltage signal is given in Figure 5.

The frequency spectrum of current signal is given in Figure 6. Both voltage and current signals exhibit higher harmonics.

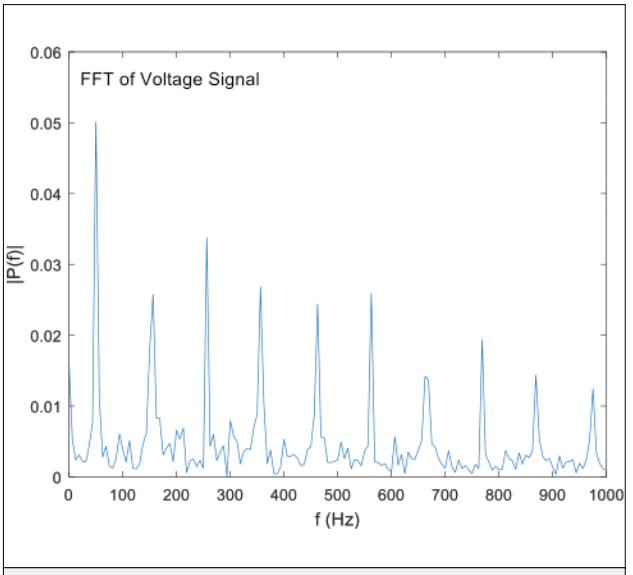

Figure 5. Frequency spectrum of voltage signal

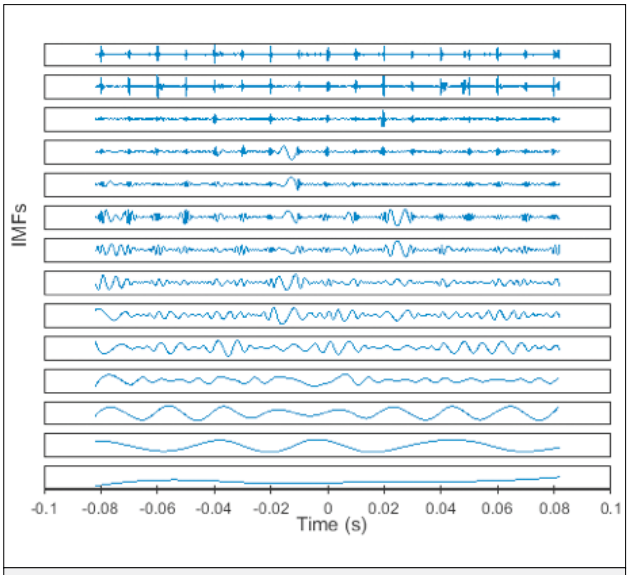

Figure 7. Decompositions of EMD on voltage signal

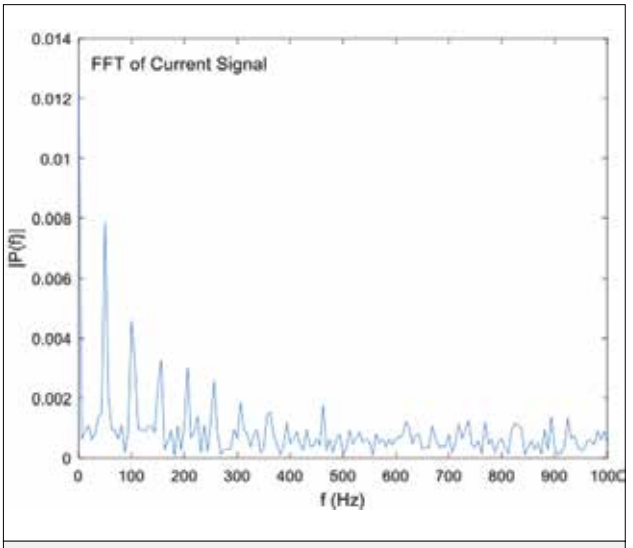

Figure 6. Frequency spectrum of current signal

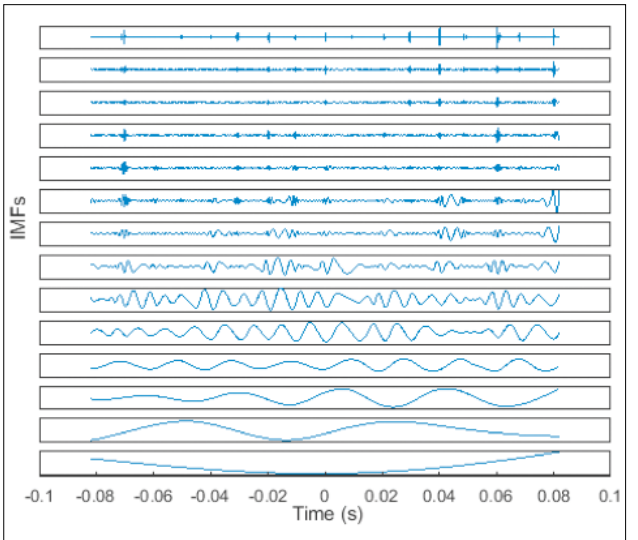

Figure 8. Decompositions of EMD on current signal

The time series current and voltage signals are analyzed by using EMD and VMD algorithms and IMFs are obtained. Decomposed modes are interpreted for comparison purposes.

EMD analysis

The non-linear signals contain higher harmonics where signal decomposition may reveal signal characteristics. In this study, EMD method is employed for time series analysis. The decomposed IMFs of EMD algorithm for voltage signal are given in Figure 7.

All the modes (IMFs) are expected to exhibit investigated signal characteristics in small scale. The decomposed IMFs of EMD algorithm for current signal are given in Figure 8.

Each IMF (mode) is given sequentially where IMFS are lined up according to their frequencies from high to low frequency modes. By definition, summation of all IMFs should generate original time series signal. In order to compare the produced IMFs and the correlation of the original signal, the cross correlation coefficients are calculated. To facilitate comparison between IMFs, cross-correlation coefficient analysis is quite effective tool [22]. The cross correlation coefficients of IMFs and original signals for EMD algorithm is given in Table 1.

The IMFs (intrinsic mode functions from first to fourteenth) are decomposed sequentially from high frequency based mode to low frequency based mode as mentioned. Considering current signal, high center frequency modes have higher correlation coefficients. However, voltage signal exhibit distributed characteristics in terms of mode coefficients.

Table 1. The cross correlation coefficients of IMFs and original signals for EMD algorithm

IMF	The correlation coefficients for current signal	The correlation coefficients for voltage signal
IMF1	0.470	0.195
IMF2	0.280	0.142
IMF3	0.208	0.174
IMF4	0.188	0.075
IMF5	0.153	0.116
IMF6	0.062	0.164
IMF7	0.085	0.233
IMF8	0.130	0.302
IMF9	0.144	0.209
IMF10	0.135	0.223
IMF11	0.191	0.303
IMF12	0.007	0.423
IMF13	0.017	0.025
IMF14	0.027	0.006

Table 2. The cross correlation coefficients of IMFs and original signals for VMD algorithm

IMF	The correlation coefficients for current signal	The correlation coefficients for voltage signal
IMF1	0.420	0.195
IMF2	0.458	0.142
IMF3	0.481	0.174

VMD Analysis

Unlike EMD, VMD have a few modes to reconstruct original non-linear signal. In this study, only there decomposed mode (IMF) is considered. The decomposed IMFs of VMD algorithm for voltage signal are given in Figure 9.

VMD is more efficient method than the EMD algorithm, since it is capable of decomposing given signal into lesser modes with non-recursive iteration. The decomposed IMFs of VMD algorithm for current signal are given in Figure 10.

The cross correlation coefficients are calculated by employing VMD algorithm for comparison purposes. The cross correlation coefficients of IMFs (intrinsic mode functions from first to third) and original signals for VMD algorithm is given in Table 2.

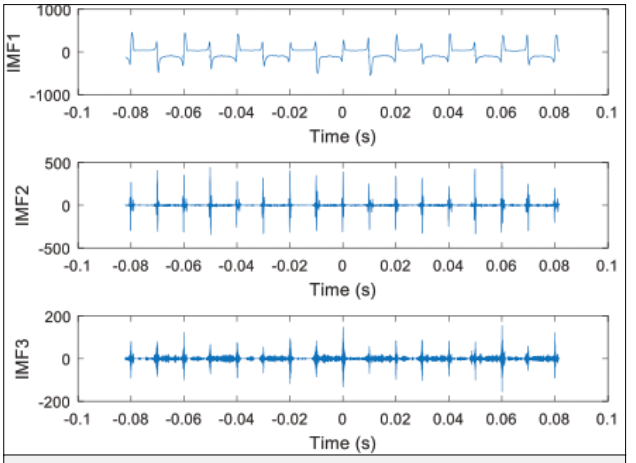

Figure 9. Decompositions of VMD on voltage signal

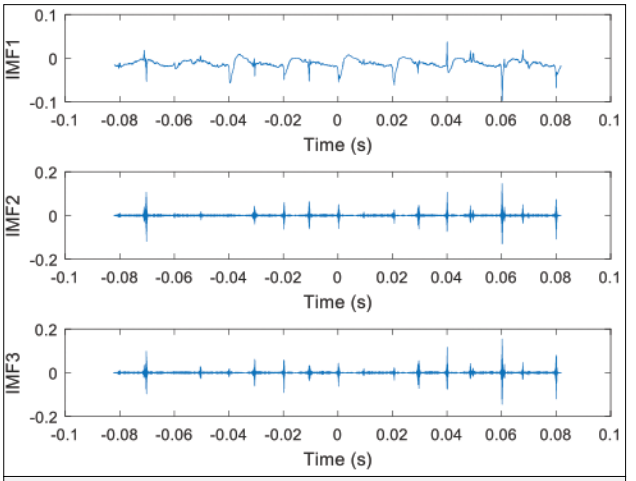

Figure 10. Decompositions of VMD on current signal

The correlation coefficients especially current signal coefficients are significantly displaying signal characteristic since they have higher coefficients. Additional modes have similar coefficients with the first three modes and hence proposed three VMD modes are assumed to be adequate. VMD algorithm can analyze characteristics of discharges with a few modes in contrast to EMD algorithm. Besides results have revealed that current characteristics of discharge signals are distinctive in terms of mode decomposition.

Conclusions

It is a quite challenging task to quantify non-linearity of discharge signals in electrical networks. Decomposing non-linear signals based on their distributed signal frequency components is an efficient technique to quantify non-linearity of a discharge signal. For this purpose, EMD and recently introduced VMD algorithms are employed to investigate HV discharge signals. A comparative study of EMD and VMD on non-linear HV discharge signals is conducted and modes (IMFs) are decomposed in time domain. In order to analyze obtained modes, cross correlation coefficients are computed and investigated. According to the

results, distinctive coefficients are observed on EMD and VMD algorithms for noisy signals. Especially current modes have higher correlation with the given noisy current signals. Besides VMD can reveal signal modes with a few decompositions rather than EMD algorithm. The proposed algorithms are capable of on-line monitoring of non-linear signal modes in time domain. By using these algorithms (especially VMD algorithm) an efficient detection of system signals with discharges is plausible.

Acknowledgement

I would like to show my gratitude and thank to the TÜBİTAK National Metrology Institute for the HV discharge tests which are conducted in Power and Energy Laboratory.

6. References

1. J. Thorp, "Disturbance Analysis for Power Systems [Book Reviews]", *in IEEE Power and Energy Magazine*, vol. 10, no. 3, pp. 89-90, May-June 2012. [CrossRef]
2. M. Biswal, Y. Hao, P. Chen, S. Brahma, H. Cao, P. De Leon, "Signal features for classification of power system disturbances using PMU data", *In Power Systems Computation Conference (PSCC)*, pp. 1-7, 2016. [CrossRef]
3. M. Sabarimalai Manikandan, S. R. Samantaray and I. Kamwa, "Simultaneous denoising and compression of power system disturbances using sparse representation on overcomplete hybrid dictionaries", *in IET Generation, Transmission & Distribution*, vol. 9, no. 11, pp. 1077-1088, 2015. [CrossRef]
4. L. Cai, N.F. Thornhill, B.C. Pal, "Multivariate Detection of Power System Disturbances Based on Fourth Order Moment and Singular Value Decomposition", *in IEEE Transactions on Power Systems*, vol. 32, no. 6, pp. 4289-4297, Nov. 2017. [CrossRef]
5. G. Rata, M. Rata, C. Filote, "Theoretical and experimental aspects concerning Fourier and wavelet analysis for deforming consumers in power network", *Elektronika Elektrotechnika (Electronics and Electrical Engineering)*, no. 1. pp. 62-66, 2010.
6. Z. Guo, L. Xie, A. Horch, Y. Wang, H. Su, X. Wang, "Automatic Detection of Nonstationary Multiple Oscillations by an Improved Wavelet Packet Transform", *Industrial and Engineering Chemical Research*, vol. 53, no. 40, pp. 15686-15697, 2014. [CrossRef]
7. A. N. I. Wardana, "A comparative study of EMD, EWT and VMD for detecting the oscillation in control loop", International Seminar on Application for Technology of Information and Communication (ISemantic), Semarang, pp. 58-63, 2016. [CrossRef]
8. N. E. Huang, Z. Shen, S.R. Long, M. C. Wu, H. H. Shih, Q. Zheng, H. H. Liu, "The empirical mode decomposition and the Hilbert spectrum for nonlinear and non-stationary time series analysis", *In Proceedings of the Royal Society of London A: mathematical, physical and engineering sciences*, vol. 454, no. 1971, pp. 903-995, 1998. [CrossRef]
9. Y. Lei, J. Lin, Z. He, M.J. Zuo, "A review on empirical mode decomposition in fault diagnosis of rotating machinery", *Mechanical Systems and Signal Processing*, vol.35, no.1, pp.108-126, 2013. [CrossRef]
10. D. P. Mandic, N. Rehman, Z. Wu, N. E. Huang, "Empirical mode decomposition-based time-frequency analysis of multivariate signals: The power of adaptive data analysis", *IEEE signal processing magazine*, vol. 30, no. 6, pp. 74-86, 2013. [CrossRef]
11. J. Dybala, R. Zimroz, "Rolling bearing diagnosing method based on empirical mode decomposition of machine vibration signal", *Applied Acoustics*, vol. 77, pp.195-203, 2014. [CrossRef]
12. S. Lahmiri, "Comparative study of ECG signal denoising by wavelet thresholding in empirical and variational mode decomposition domains", *in Healthcare Technology Letters*, vol. 1, no. 3, pp. 104-109, 2014.
13. G. Georgoulas, I.P. Tsoumas, J.A. Antonino-Daviu, V. Climente-Alarcon, C.D. Stylios, E.D. Mitronikas, A.N. Safacas, "Automatic pattern identification based on the complex empirical mode decomposition of the startup current for the diagnosis of rotor asymmetries in asynchronous machines", *IEEE Transactions on Industrial Electronics*, vol. 61, no. 9, pp. 4937-4946, 2014. [CrossRef]
14. K. Dragomiretskiy, D. Zosso, "Variational Mode Decomposition", *in IEEE Transactions on Signal Processing*, vol. 62, no. 3, pp. 531-544, Feb. 1, 2014. [CrossRef]
15. L. Zhao, C. Li, Y. Zhu, X. Chen, X. Guo, Y. Gao, "Power Transformer Partial Discharge Signal De-noising Based on Variational Mode Decomposition", *International Conference on Intelligent Systems Research and Mechatronics Engineering*, pp. 819-822, 2015. [CrossRef]
16. Y. Wang, R. Markert, J. Xiang, W. Zheng, "Research on variational mode decomposition and its application in detecting rub-impact fault of the rotor system", *Mechanical Systems and Signal Processing*, vol. 60, pp. 243-251, 2015. [CrossRef]
17. A. Upadhyay, R.B. Pachori, "Instantaneous voiced/non-voiced detection in speech signals based on variational mode decomposition", *In Journal of the Franklin Institute*, vol. 352, no. 7, pp. 2679-2707, 2015. [CrossRef]
18. U. Maji, S. Pal, "Empirical mode decomposition vs. variational mode decomposition on ECG signal processing: A comparative study", *International Conference on Advances in Computing, Communications and Informatics (ICACCI)*, Jaipur, pp. 1129-1134, 2016. [CrossRef]
19. K. P. Soman, P. Poornachandran, S. Athira, K. Harikumar, "Recursive Variational Mode Decomposition Algorithm for Real Time Power Signal Decomposition", *In Procedia Technology*, vol. 21, pp. 540-546, 2015.
20. G. Rilling, P. Flandrin, P. Goncalv`es, "On empirical mode decomposition and its algorithms", *in IEEE-EURASIP Workshop on Nonlinear Signal and Image Processing*, NSIP-03, 2003.
21. P. Flandrin, G. Rilling, P. Gonc¸alv`es, "Empirical mode decomposition as a filter bank", *IEEE Sig. Proc. Lett.*, vol. 11, no. 2, pp. 112-114, 2004. [CrossRef]
22. N. Pan, V. Mang, M. P. Un, P. S. Hang, "Accurate Removal of Baseline Wander in ECG Using Empirical Mode Decomposition," 2007 Joint Meeting of the 6th International Symposium on Noninvasive Functional Source Imaging of the Brain and Heart and the International Conference on Functional Biomedical Imaging, Hangzhou, 2007, pp. 177-180. [CrossRef]

Cengiz Polat Uzunoğlu received the M.Sc. and Ph.D. degrees in Electrical Electronics Engineering from İstanbul University, İstanbul, Turkey, in 2005 and 2011, respectively. From 2003 to 2017 he has worked as an Research Assistant at the Electrical and Electronics Engineering Department of İstanbul University, where he become an Assistant Professor in 2017. His main research interests include power systems, chaotic systems, high voltage engineering and non-linear systems.

İSTANBUL UNIVERSITY PRESS

RESEARCH ARTICLE

Electrica 2018; 18(1): 78-82

Corona Identification of Impulse Voltage and Current

Emel Önal

Department of Electrical Engineering, İstanbul Technical University School of Electrical and Electronics Engineering, İstanbul,Turkey

Cite this article as: E. Önal. "Corona Identification of Impulse Voltage and Current". *Electrica*, vol. 18, no. 1, pp. 78-82, 2018.

ABSTRACT

The corona effect in the power system has a dominant role in reducing the efficiency of the high-voltage lines. In this study, the current and voltage impulses, which are important in corona determination, have been examined in frequecy spectrogram base from test result. The frequency spectrogram graphs have been obtained from the current-time and voltage-time variation by Matlab program. With these graphs, frequency values have been found to provide an important clarification of the insulation performance of electrical equipment for reliable and accurate diagnosis. These values have been observed according to different conditions like pressure, polarity, and insulation ambient. This spectrogram analysis can be used to find the characteristic frequencies and eliminate the disturbance effect. The time between corona steps decrease when Sulphur hexafluoride (SF_6) gas pressure is increased. The time of second corona is close to leader's discharge time. Corona starts early when SF_6 amount is decreased in gas mixtures. The corona currents are large in the low SF_6 gas mixtures, this situation is related to the high insulation of the SF_6 gas. A feature which is dependent the frequency is not found.

Keywords: Corona, impulse, spectral analysis

Introduction

Impulse voltages are required in high voltage tests for basic investigations of stresses and breakdown in extreme stresses. This is a polar pulse of total short duration with a short rise time and longer fall time [1-3]. According to standards IEC 60060-1 and 60060-2, high voltage impulse tests ranging from several kV to MV are the foreground for electromechanical products to observe and investigate the breakdown mechanism of materials under high voltage and to determine compliance with international standards. Impulse voltages are measured by voltage dividers and peak voltmeters. At the measurement with voltage dividers, voltage dividers must be connected parallel to the unit during test. Since the voltage value is low, small peak impulse voltages can be measured without using a voltage divider. Impulse currents are measured by the magnetic probe, current transformer, and pure resistive shunt methods. Magnetic probe method is accomplished by the integration of the signal from a calibrated pickup loop coupled to the magnetic field of the impulse current. Current transformer method is accomplished by transformation of the current magnitude by means of a calibrated current transformer. Impulse voltage is a voltage that describes the voltage obtained in a building or electric line in the event of a lightning strike when a switch is turned on or off. Impulse voltages rise rapidly from zero to peak without significant vibrations and go back to zero again at a slower pace. Partial discharge (PD) can be produced by many cases. For a discharge to be recognized as a partial discharge, the induced current in the external conductor must be large enough to be perceived and generated with sufficient repetition speed to be perceived as something other than a random sound [4-6]. The detailed nature of the partial discharge waveform depends on the conditions of partial discharge generation, including gas types, gas pressures, charging, space conditions, and so on. In addition, the rise time and the fall time of partial discharge current pulse are influenced directly by electron avalanche and/or streamer/leader discharge extension, and by diffusion and recombination of charge carriers, respectively. In the physical understanding of electrical insulation degradation, analysis of partial

Address for Correspondence:
Emel Önal

E-mail:
eonal@itu.edu.tr

Received: 07.11.2017

Accepted: 20.11.2017

Available online at
http://dergipark.gov.tr/iujeee

DOI: 10.5152/iujeee.2018.1812

discharge waveform properties contributes [7-10]. There are many factors that affect corona losses. These factors are electrical factors, field around the conductor, athmospheric factors, heating of conductors according to load current, the beginning of the corona voltage and descructive critical voltage. The conditions of these factors affect corona losses directly or indirectly. Using the Matlab program, corona frequency intervals with corona time known from the current-time graph can be found. In this study, the current-time and voltage-time graphs of the events are examined in the time-frequency domain and the frequency magnitude of the corona is estimated with the help of spectrogram. The frequency component of the partial discharge pulses is an important issue in order to understand the discharge mechanism which must be made clear to reliably and correctly diagnose the insulation performance of the power apparatus [11-14]. About time-frequency imaging, there are a spectrogram represented by Short Time Fourier Transform (STFT) and a scalogram represented by wavelet. First, the time frequency is bounded by the uncertainty principle, because it divides a signal into short segments. The first is that the time resolution and the frequency resolution are uniform as long as they have the same observation time width over the entire frequency range. The second one changes the observation time width according to frequency. In the case of low frequency, the observation time width is extended and the frequency resolution is reduced. Conversely, in the case of high frequency, the time resolution is small and the frequency resolution is large [15]. In this study, short-time Fourier transform and spectrogram method will be tried to obtain results. By definition, the STFT, a complex valued function, conveys both modules and phase information necessary to reconstruct the signal. In practice, an energy density distribution, often referred to as a spectrogram, is preferred. The spectrogram of a signal is defined as the square size of the STFT [16]. In the spectrogram, dark regions correspond to high energy and open regions correspond to low-energy values. To determine the desired value, setting the time and frequency resolution of the spectrogram and the window size have an important role.

Test Set-Up

The experiment circuit is shown in Figure 1. In the experiment circuit, Marx Generator, pressure vessel, voltage divider, electrode system and oscilloscope are used. Figure 2 shows the experimental setup at high voltage laboratory. At this test, 1MV Marx impulse generator has been used with compensated voltage dividers 1:3080. HIAS 743 oscilloscope is used in system imaging. This oscilloscope is adjustable according to IEC 61083-1 and IEC 61083-2 standards and has 12-bit real vertical resolution at 120 MS / s. This oscilloscope allows automatic evaluation of all common impulse shapes and parameters and many functionalities like difference, parameter tolerance, STFT, step response, advanced evaluation etc. [9]. The gas insulations are used like 100% Sulphur hexafluoride (SF_6) and 1%SF_6 + 99% Nitrogen (N_2) as an environment. One of the variable parameter is pressure. The pressure is selected as 1 and 2 bar (Table 1).

Table 1. Three different athmosphere conditions

	Athmosphere	Pressure
Case 1	100% SF_6	1 bar
Case 2	1% SF_6 - 99% N_2	1 bar
Case 3	100% SF_6	2 bar

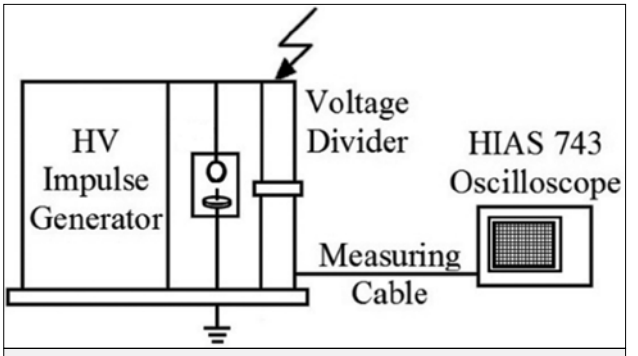

Figure 1 . Experimental set-up

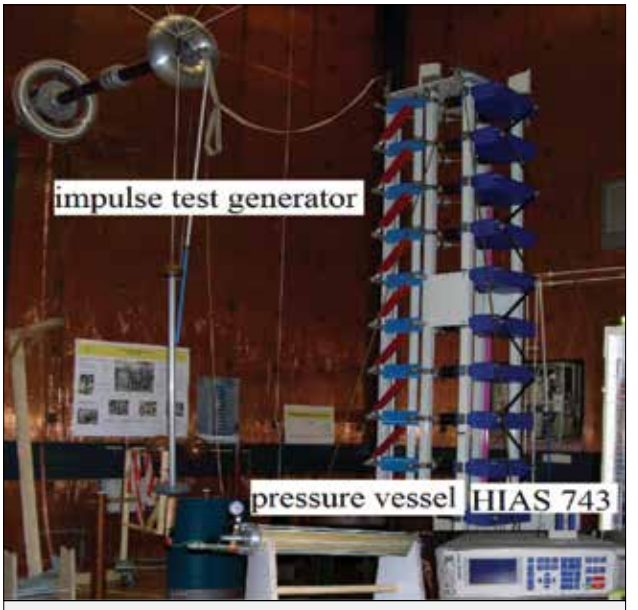

Figure 2 . Test set at high voltage laboratory

In the study, the electrode system is chosen as a spherical electrode of 5 cm diameter and a plane electrode 7.5 cm in length. In addition, the electrode system is completed by adding a 1 cm needle electrode to the plane electrode at shown in Figure 3. This is a non-uniform field representing most systems in practice. SF_6 gas is sensitive to irregularities in the field. In spite of weakness of SF_6, it is widely used today in electric power industry because of its high electrical strength and self recovery ability.

In the study, the results of the experiment are obtained under the following conditions. SF_6 and SF_6 gas mixtures commonly

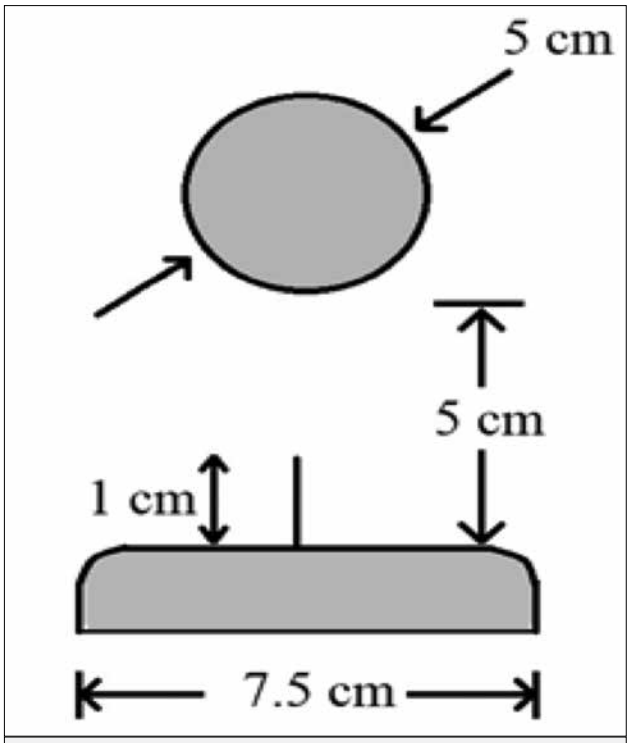

Figure 3. Electrode system

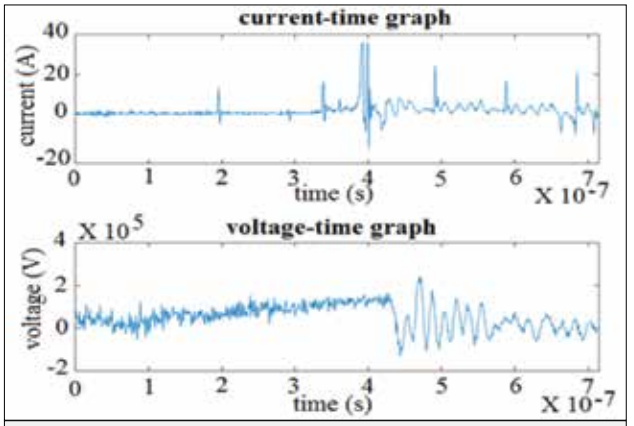

Figure 4. Current-time and voltage-time graphs of second case

used in circuit breaker as insulation ambient. Among the SF_6 gas mixtures investigated so far, SF_6-air, SF_6-CO_2 and SF_6-air appear very promising for technical applications. Although numerical methods are used in SF_6 gas mixtures, the superiority of experimental data is always present.

Spectral Analysis Using the Measurement Data

The experimental data obtained are processed in Matlab program to obtain partial discharge current-time and voltage-time graphs. Initially the peak values of the corona events observed before the breakdown discharge from the current-time graphs are determined. Then, based on the time of these values determined in the current-time graph, the values of the corona voltage are also found. Experimental data are reprocessed in the Matlab program using Spectrogram method to estimate the frequency values at corona moments and are tried to establish connection between these values and experimental data.

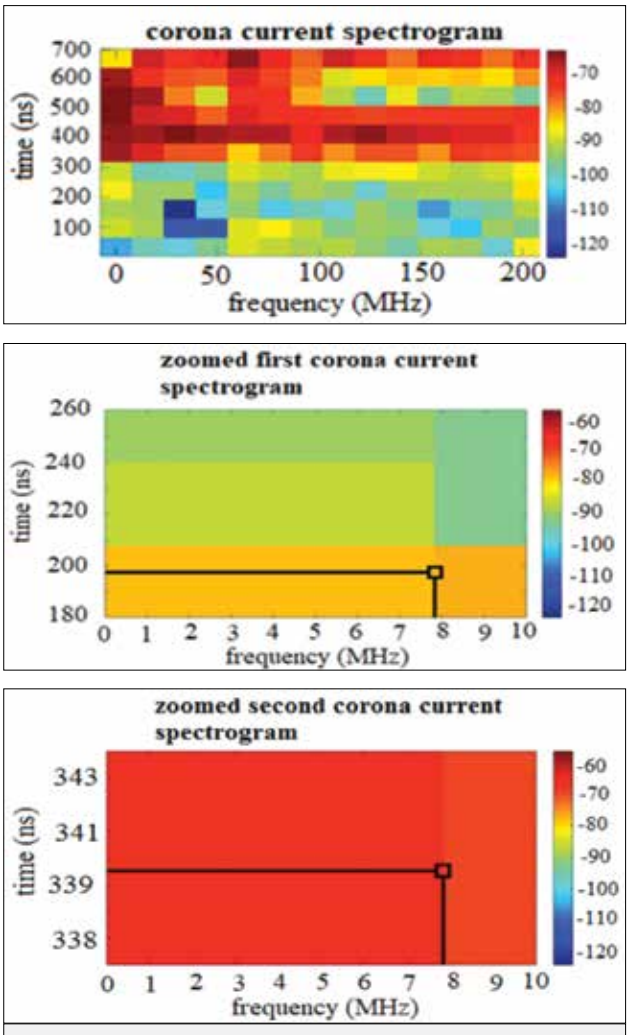

Figure 5. Second case spectogram and zoomed corona points

Case Study 1: 100% SF_6, 1 bar

At first 100% SF_6 and the pressure of 1 bar are selected. These pressures are used because the pressure intervals of the switchgears and circuit breakers used in practice are around 1-2 bar. The current value of the first corona at 4.89×10^{-7} s is determined to be 3.7625 A and the voltage value is found to be 141320,25 V. The first frequency value of this corona is found to be 6,945 MHz. The current value of the second corona at $9{,}48 \times 10^{-7}$ s is found to be 5,325 A and the voltage value is found to be 200020,25 V. The frequency value of second corona is seen 6,945 MHz.

Case Study 2: 1%SF_6+99%N_2, 1 bar

Due to the fact that SF_6 is electronegative gas, the prominence of SF_6 gas mixtures is gradually increasing. Nowadays, the re-

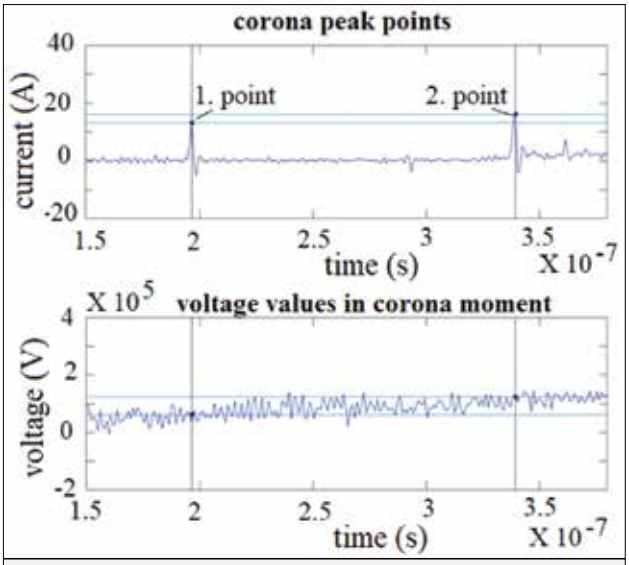

Figure 6. Current-time and voltage-time graphs of third case

Table 2. Parameters of corona moments according to cases

First corona	**Case 1**	**Case 2**	**Case 3**
Time (s)	4.89 E-07	1.96 E-07	7.30 E-07
Current (A)	3.7625	13.02	19.66
Voltage (V)	141320.25	61781.25	270020
Freq. (MHz)	6.945	7.82	23.44
Second corona	**Case 1**	**Case 2**	**Case 3**
Time (s)	9.48 E-07	3.39 E-07	8.25 E-07
Current (A)	5.325	16.01	3.725
Voltage (V)	200020.25	124150.5	262682.5
Freq. (MHz)	6.945	7.82	7.814

striction of use of SF_6 has brought about the use of SF_6 at low ratio. The most common of these mixtures is a mixture of SF_6 and N_2. Surveys show that the breakdown strength of SF_6 gas mixtures with few amount of SF_6 is higher than single gases. In this study, the corona discharges is examined rather than the breakdown stresses. As seen in Figure 4, the current value of the first corona at 1,96x10^{-7} s is determined to be 13,02 A and the voltage value is found to be 61781,25 V. The first frequency value of this corona is found to be 7,82 MHz. The current value of the second corona at 3,39x10^{-7} s is found to be 16,01 A and the voltage value is 124150,5V. The first frequency of this corona is seen 7,82 MHz. Environmental conditions in the second case (1% SF_6-99% N_2) play a decisive role. The second case, according to all the other cases, has the earliest first and second corona times and the largest first and second corona current values. The corona frequencies observed in the first and second case are the same.

In terms of being an example, case 2 analysis is given in detail in this study. The spectrogram analysis of the current of case 2 is shown in Figure 5.

Case Study 3:100%SF_6, 2 bar

The third case is related to 100% SF_6 and the pressure of 2 bar. The current value of the first corona at 7.30x10^{-7} s is determined to be 19,66 A and the voltage value is found as 270020 V. The first frequency value of this corona is 23.44 MHz. The current value of the second corona at 8.25x10^{-7} s is found as 3.725 A and the voltage value is found as 262682.5 V. The frequency of second corona is 7.814 MHz. The pressure parameter analysis can be performed by comparing the first and third cases. It is obvious that as the pressure rises, the corona voltage increases and the corona time also increases. Current-time and voltage-time graph of the case 3 is shown in Figure 6. The longest formation time of the first corona is seen in the third case. Also the biggest corona voltages are seen in this case. In this case, the first corona frequency is higher than the other cases and the second corona frequency is close to the other cases. According to the second case where both the environment and the pressure are different, in the third case, the current value formed by the first corona is larger and the current value formed by the second corona is larger in the second case. The largest first corona current value is seen in the third case, while the second largest corona current value is seen in the second case.

The results obtained from spectrogram analysis are suitable for the breakdown mechanism of the SF_6 gas mixture. The breakdown voltage is increased by the pressure. As pressure increases, the duration of breakdown also increases. The main focus here is on the corona frequencies. The frequencies of the corona can give us an idea of the cause and character of the corona. The values determined in the direction of all these graphs are given in the Table 2 below. At this study first and second corona inception values are obtained. From this data, standad deviation, mean value and 50% breakdown value can be computed. Moreover the electrical field near the sphere electrode (high voltage electrode) can be calculated via the Comsol Software Program. This proposal for detection of the corona impulse provides better results in removal of wideband noise, yielding a significant reduction of background noise for impulse measurement and breakdown analysis. The wavelet based decomposition analysis is a superior method for extracting noise. This method gives charge, phase, frequency and time information of corona signals.

Conclusion

In this study, current, voltage impulses, corona phenomena are investigated in spectrogram base. With the data obtained from the test results, current-voltage / time and spectrogram graphs are obtained with Matlab program. With these graphs, frequency values which have an important place in order to clarify the insulation performance of the electrical materials

for the reliable and correct diagnosis are estimated. It has been observed that these values react differently depending on different pressures, environments, conditions, and the values of current, voltage, time and frequency are differentiated. As a result, the corona spectrograms are used to find the source of noise and to suppress this noise. By examining the frequency spectrograms, the source of noise can be determined from the noise frequencies. The low frequencies of 500 kHz belong to the test circuit. It is known that the signals up to 10 MHz are due to electromagnetic disturbance and the frequencies above 10 MHz are from electronic digitizers [14-16]. It is necessary to examine the lower frequency bands to analyze the signals of the test circuit. Corona values tell us about streamer propagation. As pressure increases, streamer changes to leader propagation. This case refers to decreased corona data. Therefore, in future research, corona data can be examined in detail for atmospheric pressures. More experiments are needed for definite results. The fact that SF_6 is an electronegative gas and the creation of global warming indicates that future work will be based on SF_6 gas mixtures. For this analysis, the knowledge of resolution is also important. In the direction of this study, frequency identification in corona events can be made much simpler, faster and more innovative with the development of technological possibilities in the future.

Acknowledgements

Author presents their deepest appreciates to Prof. Stefan Tenbohlen, Prof. Kurt Feser and IEH researchers from Stuttgart University in Germany.

References

1. S. A. Boggs, "Partial discharge: overview and signal generation" *IEEE Electrical Insulation Magazine*, vol.6, no.4, pp. 33-39, 1990. [CrossRef]
2. A. Maglaras, T. Kousiouris, F. Topalis, D. Katsaros, L. A. Maglaras, K. Giannakopoulou, "Method of controlling corona effects and breakdown voltage of small air gaps stressed by impulse voltages". *arXiv.org, physics, arXiv: 1410.4189, Cornell University library*, 2014.
3. J. Wang, X. Wang, "Lightning Transient Simulation of Transmission Lines Considering the Effects of Frequency Dependent and Impulse Corona" *International Conference on Electrical and Control Engineering* (ICECE), 2011. [CrossRef]
4. H. Okubo, N. Hayakawa, A. Matsushita, "The relationship between partial discharge current pulse waveforms and physical mechanisms" IEEE Electrical Insulation Magazine, vol. 18, no. 3, pp.38-45, 2014. [CrossRef]
5. J. Kuffel, P. Kuffel, *High voltage engineering fundamentals*. Newnes. pp. 348-352, 2000.
6. J. S. Chang, P. A. Lawless, T. Yamamoto, "Corona discharge processes" *IEEE Transactions on plasma science*, vol. 19, no.6, pp. 1152-1166. 1991. [CrossRef]
7. L. Wang, S. Liu, M. Wei, H. Xiao, F. Wang. "Time-frequency analysis of nonlinear and non-stationary weak signals of corona discharge". *Journal of Physics: Conference Series.* IOP Publishing, vol. 418, no.1, 2013. [CrossRef]
8. L. Zhu, J. Zhu, F. Lü, Y. Liu, Q. Geng, "De-noise of the high frequency corona current with wavelet analysis method" *Applied Mechanics and Materials* vol. 385, pp. 1394-1397, 2013. [CrossRef]
9. M.B. Priestle. "*Non-linear arid Non-stationary Time Series Analysis,*" Academic Press, New York, 1988.
10. S. Tenbohlen, G. Schroder. The Influence of Surface Charge on Lightning Impulse Breakdown of Spacers in SF_6 *IEEE Transactions on Dielectrics and Electrical Insulation,* Vol. 7, No. 2, April 2000. [CrossRef]
11. P. N. Mavroidis, P. N. Mikropoulos, C. A. Stassinopoulos, A. Dodos, P. Zannias, M.B. Priestle. "Discharge Characteristics in short rod-plane gaps with Dielectric-Covered Rod under Lightning Impulse Voltages" *17. International Conference on Gas Discharges and Their Applications*, 2008.
12. M. Hasmi, M. Lehtonen, M. Nordman, R. Jabbar, S. Qureshi, "Wavelet based de-noising of on-line PD signals captured by Pearson coil in covered-conductor overhead distribution networks" *Journal of Electrical Power Energy Systems,* 43 pp. 1185-1192, 2012. [CrossRef]
13. J. Tang, W. Li, Y. Liu, "Blind source separation of mixed PD signals produced by multiple insulation defects in GIS", *IEEE Transaction on Power Delivery*, vol. 25, pp. 170-176, 2010. [CrossRef]
14. H. Zhang, T. Blackburn, B. Phung, D. Sen, "A novel wavelet transform technique for on-line partial discharge measurements. 2. On-site noise rejection application", IEEE *Transaction on Dielectrics and Electrical Insulation*, 14, pp. 15-22, 2007. [CrossRef]
15. D. ZhaoHeng, L. ShangHe, W. Lei, "Selection of the optimal wavelet bases for wavelet de-noising of partial discharge signal", *2nd International Conference on Signal Processing Systems (ICSPS)*, vol. 3, pp. 400-404, July 2010.
16. E. Onal, K. Yumak, S. Seker. "The Wavelet-Based Filtering Method as an Alternative to *k*-Factor Filtering for High-Voltage Impulse Signals" Arabian Journal for Science and Engineering, pp 1-10, November, 2017. [CrossRef]

Emel Önal was born in İstanbul, Turkey. She received B.Sc, M.Sc. and Ph.D. degrees from İstanbul Technical University (ITU) in Electrical and Electronics Faculty in İstanbul, Turkey. She worked as a visiting researcher at IEH Stuttgart University about GIS technology and transformers between 2006 and 2007. She is currently working as a Assoc. Professor in electrical engineering department at ITU and her interest areas are in the areas of discharge phenomena, electrical power systems, insulation and protection techniques in power systems, generation and measurement of high voltages, signal processing, soft computing and condition monitoring techniques.

İSTANBUL UNIVERSITY PRESS

RESEARCH ARTICLE

Electrica 2018; 18(1): 83-89

Suboptimal Frequency-Selective Transceiver Design for Multicarrier Millimeter Wave MIMO Systems

Nihat Kabaoğlu

Department of Electrical and Electronics Engineering, İstanbul Medeniyet University School of Engineering and Natural Science, İstanbul, Turkey

Cite this article as: N. Kabaoğlu. "Suboptimal Frequency-Selective Transceiver Design for Multicarrier Millimeter Wave MIMO Systems". *Electrica*, vol. 18, no. 1, pp. 83-89, 2018.

ABSTRACT

Fifth-generation (5G) cellular communication systems aim to obtain a higher data rate, decreased latency time, higher performance even at high mobility speeds, decreased system complexity, lower transmission cost, and an increased system capacity and coverage area. Many of these goals can be achieved because of the studies devoted to the physical layer of 5G cellular networks. In this respect, solutions to the problems of beamforming (steering and precoding or precoding and combining) and channel estimation that are encountered in the physical layer of 5G cellular networks are the key points to achieve the aforementioned goals. Thus, a two-stage beamforming method is proposed in this study. The proposed method is a suboptimal method that minimizes the difference between outputs obtained when fully digital and hybrid beamforming methods are used. The analytical results, which are validated through simulations, demonstrate that the proposed method is an effective solution and, hence, the preferred beamforming approach for 5G millimeter wave band-based wireless systems.

Keywords: Millimeter wave communications, hybrid beamforming, precoding and combining

Introduction

With intelligent devices taking an important role in our lives, demand for high data rate and system capacity is increasing day by day. The Long Term Evolution (LTE) standard, which is the standard of today's fourth-generation (4G) systems, has been able to meet these demands to a certain extent by using Orthogonal Frequency Division Multiplexing (OFDM) and Multiple-Input Multiple-Output (MIMO) technology on a network designed from the outset. However, with the extraordinary demand for applications that require more bandwidth, such as very high resolution video applications, the contradiction between capacity requirements and spectrum constraints has become more apparent. It is not possible to meet this demand with existing cellular network technology, which has a very limited bandwidth and a fairly crowded spectrum. Due to the aforementioned bandwidth bottleneck, research has been initiated to provide innovative solutions for 5G cellular communication systems to support the total mobile user network traffic expected to increase 1000 times by 2020 [1]. Millimeter wave (mmW) communication for physical layers of personal Wireless Area Networks (WPAN), Local Area Networks (LAN) and Metropolitan Area Networks (MAN) has already been standardized [2,3] and has a data rate potential of Gbits at the moment, mmW communication has also become a strong candidate for 5G cellular networks.

The mmW band is the frequency range defined as 30 GHz - 300 GHz (3 GHz to 30 GHz according to some studies). There are several advantages to be gained by using mmW band in 5G cellular networks. The first one of them is that the mmW band provides a wide spectrum. The other is that the communication in this band is short-range one due to the severe path loss, and thus it is possible to reuse the frequency at short distances and hence it is possible to extremely increase the capacity. Another is that very high data rates can be achieved by communicating with antenna arrays consisting of several

Address for Correspondence:
Nihat Kabaoğlu

E-mail:
nihat.kabaoglu@medeniyet.edu.tr

Received: 16.11.2017

Accepted: 05.12.2017

DOI: 10.5152/iujeee.2018.1813

antennas since antenna dimensions are very small in this band. The last one is that higher levels of privacy and security can be achieved if the beam width of the antenna arrays can be narrowed sufficiently. Since all these points strongly indicate that mmW band communication can be used in 5G cellular networks, studies on the channel characteristics of mmW band and the study of device technologies that can work on this band have started to take place in the literature in recent years [4,5].

Since signal propagation in the mmW band has a different characteristic than the propagation in the traditional band, the vast majority of the published work is on the physical layer of mmW systems. These studies are usually focused on beamforming and/or channel estimation. In particular, beamforming is crucial for achieving a reasonable link budget and for overcoming high path loss problem in cellular mmW systems. It is possible to achieve higher gain because the mmW frequencies have the ability to fit several tens of antennas into small volumes. However, it is almost impossible to allocate a Radio Frequency (RF) chain (consisting of amplifier, mixer, analog-to-digital converter and analogue converter units) for each antenna element in this array due to the high cost and power consumption that will arise. Therefore, it is not possible to use digital beamforming methods. For this reason, the past studies proposed analog beamforming methods that operate according to the principle of controlling the phase of the signal radiated from each antenna by using RF phase shifter circuitry [2,6,7]. These solutions are based on the principle of recursively obtaining the beamformer coefficients in systems that do not have channel information. Similar to [2,6] proposed a dual beam-training algorithm that selects a beam pattern from a codebook. In order to minimize duration of beam-training, a multi-beam structure was used in [8]. The methods proposed in these studies tend to converge to a single communication beam, despite the reduction of complexity in [2]. Hence, they are not capable of providing the desired multiplexing gain in parallel transmission of multiple data sequences. In summary, the solutions presented in the studies on analogue beamforming are not adequate due to hardware limitations.

Hybrid beamforming solutions are presented to enable higher data rate and antenna array gain [9-13]. [9] presents a hybrid beamforming solution that maximizes channel capacity, while matching one or more RF beam pairs for predefined RF beam clusters in the receiver and transmitter. The performance of the proposed method in that work is based on the diversity of the codebook for each selected RF spectrum pair since it determines the best precoder by exploring the codebook in detail (which results a high computational burden). Moreover, it is inevitable that the method continuously needs feedback information. Assuming that the receiver knows the channel perfectly, [10] proposes a simple, hybrid beamforming method that uses mmW channel sparsity. Under the assumption that the receiver partly knows the channel, a hybrid beamforming method is described in [11] similar to [10]. All of the methods proposed in these studies require the channel estimation and beamforming operations to be done together, since they need partial or complete channel state information during determination of the precoding matrix. Therefore, a fairly high computational burden occurs at the channel estimation stage of these proposed methods, which prevents their practical implementation. Since MIMO techniques causes a trade-off between multiplexing gain and diversity, studies on application of hybrid beamforming methods to them has been proposed in recent years. In this context, in [12], it is shown that spatial multiplexing and beamforming can be executed one after the other in actual channel models. [13] discusses the advantages and disadvantages of hybrid beamforming and low resolution combining that are two possible MIMO mmW architectures. As a result, analogue beamforming is exploited to avoid path loss in short distance communications; the hybrid beamforming is exploited to balance the trade-off between performance and complexity for new generation outdoor cellular networks.

In this work, we propose a suboptimal frequency selective transceiver design that configures the beam via the two-stage serial optimization method unlike other transceiver designs in the literature that jointly configure the beam in both Base Station (BS) and Mobile Station (MS) sides. Thus, the computational complexity of the classic transceiver algorithm is reduced by transforming the multi-parametric and multi-dimensional optimization problem into fewer parametric and lower dimensional two-parallel optimization problems.

System Model

The considered system in this work is a mmW MIMO-OFDM system. It is assumed that transmitter BS and receiver MS communicates each other with N_S length-M data symbol blocks over frequency selective fading channels via their one dimensionally antenna arrays. Transmitter and receiver have N_{BS} and N_{MS} antenna elements respectively, and N_{RF} RF chains. The transmitted symbol vector $\mathbf{s}(m) \in C^{N_S}$ on the m sub-carrier of the BS has zero-mean and $\mathbb{E}\left[\mathbf{s}(m)\mathbf{s}(m)^H\right] = \left(P_t / MN_S\right)\mathbf{I}_{N_S}$, where P_t is the average total transmit power. $\mathbf{s}(m)$ at each sub-carrier is precoded by digital precoding matrix $\mathbf{P}_{BB}(m) \in C^{N_{RF} \times N_S}$, and then the resulting symbol blocks are transformed into time domain using N_{RF} M-point IFFT assuming that all sub-carriers are used and data blocks length is equal to number of sub-carriers. After adding cyclic prefix and applying RF precoding by $\mathbf{P}_{RF} \in C^{N_{BS} \times N_{RF}}$ each element of which has constant module, we finally obtain the following discrete-time complex baseband signal on the m-th sub-carrier

$$\mathbf{x}(m) = \mathbf{P}_{RF}\mathbf{P}_{BB}(m)\mathbf{s}(m). \quad (1)$$

The signal in (1) is transmitted to the MS by the BS through frequency selective quasi-static channel whose discrete impulse response on m-th sub-carrier is $\mathbf{H}(m) \in C^{N_{MS} \times N_{BS}}$ and the

maximum excess delay is the same as length of a symbol. After combining the received signal by $\mathbf{C}_{RF} \in C^{N_{MS} \times N_{RF}}$ and removing cyclic prefix from it, the resulting signals are transformed back to frequency domain using N_{RF} M -point FFT first, and then obtained symbols on each sub-carrier are combined by digital combining matrix $\mathbf{C}_{BB}(m) \in C^{N_{RF} \times N_S}$. The received signal on sub-carrier m can be eventually obtained as

$$\begin{aligned}\mathbf{r}(m) &= \mathbf{C}_{BB}^H(m)\mathbf{C}_{RF}^H\mathbf{H}(m)\big(\mathbf{x}(m)+\mathbf{w}(m)\big)\\ &= \mathbf{C}_{BB}^H(m)\mathbf{C}_{RF}^H\mathbf{H}(m)\mathbf{P}_{RF}\mathbf{P}_{BB}(m)\mathbf{s}(m)\\ &+\mathbf{C}_{BB}^H(m)\mathbf{C}_{RF}^H\mathbf{w}(m),\end{aligned} \tag{2}$$

where $\mathbf{w}(m) \sim \mathcal{N}\big(\mathbf{0}, \sigma_w^2 \mathbf{I}_{N_{MS}}\big)$ is the zero mean circularly symmetric complex Gaussian noise.

Problem Formulation

The aim of this work proposes a low computationally complex hybrid beamforming method for the system model given in Section 2, which maximizes the achievable rate subject to the transmit power constraint at BS side. Assuming that the mobile station is using the optimal nearest decoding method with fully digital hardware, it is possible to decouple the problems of designing beamforming and combining matrices from each other. This makes it possible to design a hybrid precoder that will maximize the common information of the system. The classic solution to this problem is given below.

$$\begin{aligned}\max_{\mathbf{P}_{RF},\mathbf{P}_{BB}(m),\mathbf{C}_{RF},\mathbf{C}_{BB}(m)} & \mathcal{I}\big(\mathbf{P}_{RF},\{\mathbf{P}_{BB}(m)\}_{m=1}^M,\mathbf{C}_{RF},\{\mathbf{C}_{BB}(m)\}_{m=1}^M\big)\\ s.t.\ & \mathbf{P}_{RF} \in \mathcal{P}_{RF} \text{ and } \mathbf{C}_{RF} \in \mathcal{C}_{RF}\\ & \sum_{m=1}^{M} \big\| \mathbf{P}_{BB}(m) \big\|_F^2 \le P_t\end{aligned} \tag{3}$$

where $\mathcal{P}_{RF}$ and $\mathcal{C}_{RF}$ are general set of matrices with constant modulus entries or the quantized codebooks, and

$$\begin{aligned}\mathcal{I}\big(\mathbf{P}_{RF},\{\mathbf{P}_{BB}(m)\}_{m=1}^M,\mathbf{C}_{RF},\{\mathbf{C}_{BB}(m)\}_{m=1}^M\big) &= \log_2 \det\big(\mathbf{I}_{N_{MS}}\\ &+\frac{\gamma}{N_s}\big(\mathbf{C}_{RF}\mathbf{C}_{BB}(m)\big)^H\mathbf{H}(m)\mathbf{R}\mathbf{H}(m)^H\mathbf{C}_{RF}\mathbf{C}_{BB}(m)\big)\end{aligned} \tag{4}$$

is the mutual information of the system, with $\gamma = \frac{P_t}{M\sigma_w^2}$ and $\mathbf{R} = \mathbf{P}_{RF}\mathbf{P}_{BB}(m)\big(\mathbf{P}_{RF}\mathbf{P}_{BB}(m)\big)^H$. The problem in (3) is a non-convex and it needs multiparameters and multi-dimensional non-convex optimization, but it has a closed form solution.

Channel Model

In mmW band, free-space propagation path loss is extremely higher than traditional microwave band. Since mmW propagation enviorement is well characterized by a clustered channel model, mmW channel model at almostly all works in the literature such as [3,14-20] is based on Saleh-Valenzualle geometric channel model in [21]. Since the author believes that the best representation among them is the representation in [20], he adopt the same channel model with L clusters, each of which has a time delay $\tau_l \in R$, and Angle of Arrival (AoA) and Angle of Departure (AoD) $\theta_l, \phi_l \in [0, 2\pi]$. Each ray has a relative time delay τ_{r_l}, relative angle of arrival and departure shift ψ_{r_l}, φ_{r_l}, and complex path gain α_{r_l}. The number of rays and path loss between BS and MS are R_l and ρ respectively. $p_{RC}(\tau)$ represents raised-cosine pulse shaping function for T_s -spaced signaling evaluated at τ seconds. Delay- d MIMO channel matrix $\mathbf{H}(d)$ can be expressed as [15]

$$\begin{aligned}\mathbf{H}(d) = \sqrt{\frac{N_{BS}N_{MS}}{\rho}}\sum_{l=1}^{L}\sum_{r_l=1}^{R_l}&\alpha_{r_l}p_{RC}(dT_s-\tau_l-\tau_{r_l})\\ &\times\mathbf{a}_{MS}(\theta_l-\psi_{r_l})\mathbf{a}_{BS}^H(\phi_l-\varphi_{r_l}),\end{aligned} \tag{5}$$

where $\mathbf{a}_{MS}(\theta)$ and $\mathbf{a}_{BS}(\phi)$ are antenna array response vetors of MS and BS, respectively. Given the delay- d MIMO channel model in (5), the channel at sub-carrier m, $\mathbf{H}(m)$ can be written as [22],

$$\mathbf{H}(m) = \sum_{d=0}^{D-1}\mathbf{H}(d)\exp(-j\frac{2\pi m}{M}d). \tag{6}$$

Proposed Suboptimal Transceiver Design

Nearly all previous work on hybrid beamforming for mmW systems uses block diagonalization method such as [23-27] since it has low complexity. Thus, a hybrid beamforming method based on the block diagonalization technique is proposed in this study. The proposed method is based on the finding of the hybrid beamformer matrices that make the received signal $\mathbf{r}(m)$ be the nearest to the signal $\mathbf{r}_d(m)$ obtained using digital beamformer matrices. As a metric of this closeness, the way to minimize the Mean Square Error (MSE) between the received signal $\mathbf{r}(m)$ and the signal $\mathbf{r}_d(m)$ to be received if a digital beamformer was used, was chosen. In this context, we calculate the MSE between $\mathbf{r}_d(m)$ and $\mathbf{r}(m)$ as follows:

$$\mathbf{r}_d(m) = \mathbf{s}(m) + \mathbf{U}^H(m)\mathbf{w}(m) \tag{7}$$

where $\mathbf{r}_d(m) = \mathbf{C}_{opt}^H(m)\mathbf{H}(m)\mathbf{P}_{opt}(m)\mathbf{s}(m)+\mathbf{C}_{opt}^H(m)\mathbf{w}(m)$ with both fully digital combiner matrix $\mathbf{C}_{opt}$ and precoding matrix $\mathbf{P}_{opt}$. Minimizing e_m for $\forall m$ with respect to parameter set $\{\mathbf{P}_{RF},\mathbf{P}_{BB}(m),\mathbf{C}_{RF},\mathbf{C}_{BB}(m)\}$ under the constraints in (3) gives optimum hybrid precoder matrices $\mathbf{P}_{RF}$ and $\mathbf{P}_{BB}(m)$, and combiner matrices $\mathbf{C}_{RF}$ and $\mathbf{C}_{BB}(m)$, but it still requires needs M -dimensional non-convex optimization such as in [19] and [20]. However, this problem can be more easily solved when channel state information is available in MS side (this assumption is a reasonable, since channel reciprocity can be assumed when BS communicates to MS in time division duplexing mode). In that case, $\mathbf{r}_d(m)$ can be expressed as

$$\mathbf{r}_d(m) = \mathbf{s}(m) + \mathbf{U}^H(m)\mathbf{w}(m), \tag{8}$$

where $\mathbf{C}_{opt}(m) = \mathbf{U}(m)$ and $\mathbf{P}_{opt}(m) = \mathbf{V}(m)\square(m)$, and $\mathbf{U}(m)$, $\mathbf{Ó}(m)$ and $\mathbf{V}(m)$ can be obtained by using singular value decomposition of $\mathbf{H}(m)$. Using (8), (7) can be arranged as follows:

$$
\begin{aligned}
e_m = \mathbb{E}\Big[\Big\| & \mathbf{s}(m) + \mathbf{U}^H(m)\mathbf{w}(m) \\
& - \mathbf{C}_{BB}^H(m)\mathbf{C}_{RF}^H\mathbf{H}(m)\mathbf{P}_{RF}\mathbf{P}_{BB}(m)\mathbf{s}(m) \\
& - \mathbf{C}_{BB}^H(m)\mathbf{C}_{RF}^H\mathbf{w}(m)\Big\|_F^2\Big] \\
= \mathbb{E}\Bigg[\Bigg\| & \underbrace{\Big(\mathbf{I} - \mathbf{C}_{BB}^H(m)\mathbf{C}_{RF}^H\mathbf{H}(m)\mathbf{P}_{RF}\mathbf{P}_{BB}(m)\Big)\mathbf{s}(m)}_{signal\ part,\ e_m^s} \\
& + \underbrace{\Big(\mathbf{U}^H(m) - \mathbf{C}_{BB}^H(m)\mathbf{C}_{RF}^H\Big)\mathbf{w}(m)}_{noise\ part,\ e_m^n}\Bigg\|_F^2\Bigg].
\end{aligned}
\tag{9}
$$

(9) can be directly optimized to obtain exact solution as follows:

$$
\min_{\mathbf{C}_{RF},\mathbf{C}_{BB}(m),\mathbf{P}_{RF},\mathbf{P}_{BB}(m)} \sum_m \mathbb{E}\Big[e_m\Big], \tag{10}
$$

or can be first partitioned into two parts like as signal parts and noise part, and then each part can be separately optimized to obtain a suboptimal solution. Since the aim of this work is to design a suboptimal hybrid beamformer, we have made a separate optimization of each of the signal part and the noise part. Those problems in either case are still non-convex. Each of two optimization problem can be solved by a single singular value decomposition over concatenated matrices. Let's define those concatenated matrices as

$$
\begin{aligned}
\overline{\mathbf{P}}_{opt} &= \Big[\mathbf{P}_{opt}(1)\ \mathbf{P}_{opt}(2)\ldots\mathbf{P}_{opt}(M)\Big] \in C^{N_{BS}\times MN_S}, \\
\overline{\mathbf{P}}_{BB} &= \Big[\mathbf{P}_{BB}(1)\ \mathbf{P}_{BB}(2)\ldots\mathbf{P}_{BB}(M)\Big] \in C^{N_{RF}\times MN_S}, \\
\overline{\mathbf{C}}_{opt} &= \Big[\mathbf{C}_{opt}(1)\ \mathbf{C}_{opt}(2)\ldots\mathbf{C}_{opt}(M)\Big] \in C^{N_{MS}\times MN_S}, \\
\overline{\mathbf{C}}_{BB} &= \Big[\mathbf{C}_{BB}(1)\ \mathbf{C}_{BB}(2)\ldots\mathbf{C}_{BB}(M)\Big] \in C^{N_{RF}\times MN_S}.
\end{aligned}
\tag{11}
$$

We can now define final form of the considered problem as

$$
\begin{aligned}
\min_{\mathbf{C}_{RF},\overline{\mathbf{C}}_{BB}} \sigma_w^2\ & Tr\Big[\Big(\mathbf{C}_{opt}^H - \overline{\mathbf{C}}_{BB}^H\mathbf{C}_{RF}^H\Big)\Big(\mathbf{C}_{opt}^H - \overline{\mathbf{C}}_{BB}^H\mathbf{C}_{RF}^H\Big)^H\Big] \\
& s.t.\ \ \mathbf{C}_{RF} \in \mathcal{C}_{RF}
\end{aligned}
\tag{12}
$$

$$
\begin{aligned}
\min_{\mathbf{P}_{RF},\overline{\mathbf{P}}_{BB}} \frac{P_t}{MN_S}\ & Tr\Big[\Big(\mathbf{I} - \hat{\overline{\mathbf{C}}}_{BB}^H\hat{\mathbf{C}}_{RF}^H\mathbf{U}\boldsymbol{\Sigma}\mathbf{V}^H\mathbf{P}_{RF}\overline{\mathbf{P}}_{BB}\Big) \\
& \Big(\mathbf{I} - \hat{\overline{\mathbf{C}}}_{BB}^H\hat{\mathbf{C}}_{RF}^H\mathbf{U}\boldsymbol{\Sigma}\mathbf{V}^H\mathbf{P}_{RF}\overline{\mathbf{P}}_{BB}\Big)^H\Big] \\
& s.t.\ \ \mathbf{P}_{RF} \in \mathbf{P}_{RF}
\end{aligned}
\tag{13}
$$

where $\hat{\overline{\mathbf{C}}}_{BB}$ and $\hat{\mathbf{C}}_{RF}$ are the matrices obtained from the solution of (12). Since this problem has a smilar structure as its single carrier part form in [28], it can be extended to multicarrier case and then it can be solved using Orthogonal Matching Pursuit (OMP) algorithm leveraged from the compressive sensing domain. The optimization procedure can be defined into two steps. In the first step, the noise part is optimized and suboptimal combiner matrices $\hat{\overline{\mathbf{C}}}_{RF}$ and $\hat{\overline{\mathbf{C}}}_{BB}$ are obtained. In the second step, these suboptimal combiner matrices are inserted into the signal part, and then the signal part is optimized to obtain suboptimal precoder matrices $\hat{\overline{\mathbf{P}}}_{RF}$ and $\hat{\overline{\mathbf{P}}}_{BB}$. Spesifically, we apply the OMP algorithms in Table 1 for both two steps to obtain suboptimal solution of the considered problem.

Table 1. OMP Algorithms

Algorithm for Eq. (12)	
Step 1	Initialize
	$\mathbf{C}_{res} = \overline{\mathbf{C}}_{opt} = \mathbf{U}$
	$\mathbf{C}_{RF} = [\ ]$
Step 2	while $i \le N_{RF}$ do
	(2.1) $\boldsymbol{\Xi}_C = \mathbf{A}_d^H\mathbf{C}_{res}$
	(2.2) $k = \arg\max_j \Big[\boldsymbol{\Xi}_C^H\boldsymbol{\Xi}_C\Big]_{j,j}$
	(2.3) $\mathbf{C}_{RF} = \Big[\mathbf{C}_{RF}\Big|\mathbf{A}_d(:,k)\Big]$
	(2.4) $\tilde{\overline{\mathbf{C}}}_{BB} = \Big(\mathbf{C}_{RF}^H\mathbf{C}_{RF}\Big)^{-1}\overline{\mathbf{C}}_{opt}$
	(2.5) $\mathbf{C}_{res} = \dfrac{\overline{\mathbf{C}}_{opt} - \mathbf{C}_{RF}\tilde{\overline{\mathbf{C}}}_{BB}}{\Big\|\overline{\mathbf{C}}_{opt} - \mathbf{C}_{RF}\tilde{\overline{\mathbf{C}}}_{BB}\Big\|_F}$
Step 3	Normalize $\tilde{\overline{\mathbf{C}}}_{BB}$, $\tilde{\overline{\mathbf{C}}}_{BB} = \dfrac{\tilde{\overline{\mathbf{C}}}_{BB}}{\Big\|\mathbf{C}_{RF}\tilde{\overline{\mathbf{C}}}_{BB}\Big\|_F}$
Algorithm for Eq. (13)	
Step 1	Initialize
	$\mathbf{P}_{res} = \overline{\mathbf{P}}_{opt} = \Big(\tilde{\overline{\mathbf{C}}}_{BB}^H\hat{\mathbf{C}}_{RF}^H\mathbf{U}\boldsymbol{\Sigma}\mathbf{V}^H\Big)^{-1}$
	$\mathbf{P}_{RF} = [\ ]$
Step 2	while $k \le N_{RF}$ do
	(2.1) $\boldsymbol{\Xi}_P = \mathbf{A}_d^H\mathbf{P}_{res}$
	(2.2) $k = \arg\max_j \Big[\boldsymbol{\Xi}_P^H\boldsymbol{\Xi}_P\Big]_{j,j}$
	(2.3) $\mathbf{P}_{RF} = \Big[\mathbf{P}_{RF}\Big|\mathbf{A}_d(:,k)\Big]$
	(2.4) $\tilde{\overline{\mathbf{P}}}_{BB} = \Big(\mathbf{P}_{RF}^H\mathbf{P}_{RF}\Big)^{-1}\overline{\mathbf{P}}_{opt}$ ^
	(2.5) $\mathbf{P}_{res} = \dfrac{\overline{\mathbf{P}}_{opt} - \mathbf{P}_{RF}\tilde{\overline{\mathbf{P}}}_{BB}}{\Big\|\overline{\mathbf{P}}_{opt} - \mathbf{P}_{RF}\tilde{\overline{\mathbf{P}}}_{BB}\Big\|_F}$
Step 3	Normalize $\tilde{\overline{\mathbf{P}}}_{BB}$, $\tilde{\overline{\mathbf{P}}}_{BB} = \sqrt{\dfrac{P_t}{MN_S}}\dfrac{\tilde{\overline{\mathbf{P}}}_{BB}}{\Big\|\mathbf{P}_{RF}\tilde{\overline{\mathbf{P}}}_{BB}\Big\|_F}$

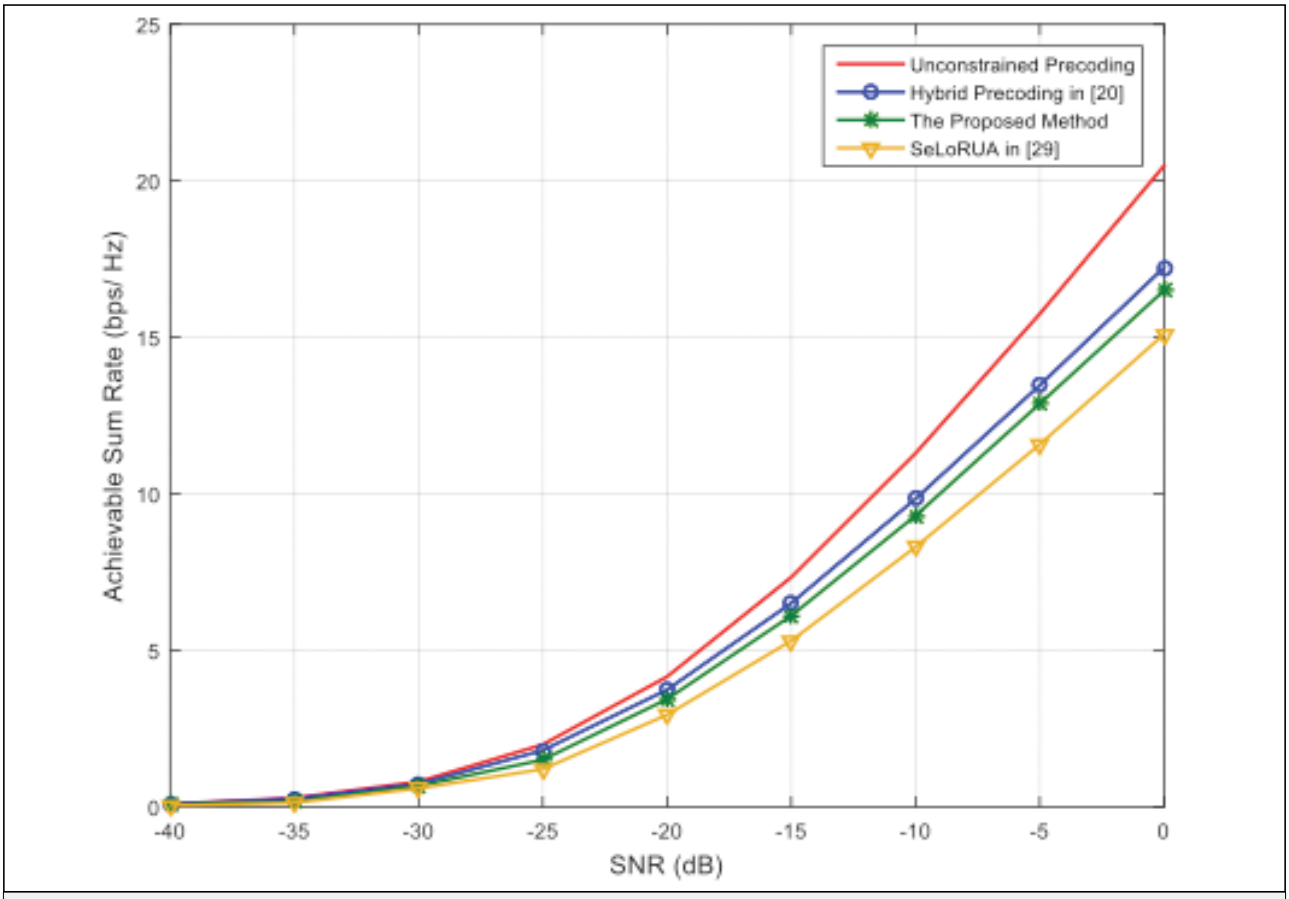

Figure 1. Achievable sum rate versus *SNR*

Computer Simulations

In this section, we present computer simulation results to reveal the performance of the proposed transceiver which consists of hybrid precoder and combiner. It is assumed a mmW system operating at 28 GHz where transmitter BS and receiver MS have multiple antennas and limited number of RF chains. BS and MS are equipped with Uniform Linear Array (ULA), number of antennas in each of which are $N_{BS}=64$ and $N_{MS}=16$ respectively with $N_{RF}=3$. The AoA and the AoD are assumed to be uniformly distributed in $\left[0,2\pi\right]$ with angle spread of 10° for ULAs. The number of clusters for the mmW channel is $L=8$, and each cluster has $R_l=7$ rays and unity average power. Complex path gain of the channel α_{r_l} are i.i.d. and follow the complex distribution $\mathcal{N}\left(0,\sigma_{r_l}^2\right)$. The number of subcarriers is $M=512$, and the cyclic prefix length is 128. All the simulation results are generated by averaging 2000 randomly chosen channel realizations.

In Figure 1, the performance of the proposed suboptimal method is compared with different schemes. In this simulation, The number of transmitted streams is fixed at $N_S=3$. As can be seen from this figure, the suboptimal method proposed in this study exhibits a better performance than the method proposed in [29], but shows almost the same performance with the method proposed in [20]. This performance is quite good for a suboptimal method.

Figure 2 shows the comparison of the performance of the proposed suboptimal algorithm with the digital unconstrained solution for different numbers of transmission data streams. First, the performance of both coding methods increases and then decreases. The reason for this decrease is the sparse structure of the mmW channel and allocating of power equally between the different streams. The solution to this problem is what is called multimodal pre-coding. In addition, this figure shows that the difference between the proposed suboptimal solution and the digital unconstrained solution is small when the number of data streams has both the small and the large values. This is why the mmW channels are sparse.

Conclusion

In this work, we have presented a suboptimal hybrid precoding and combining design for downlink of a multicarrier massive MIMO system. It has a simple implementation and relatively lower computational complexity since it partitiones the objec-

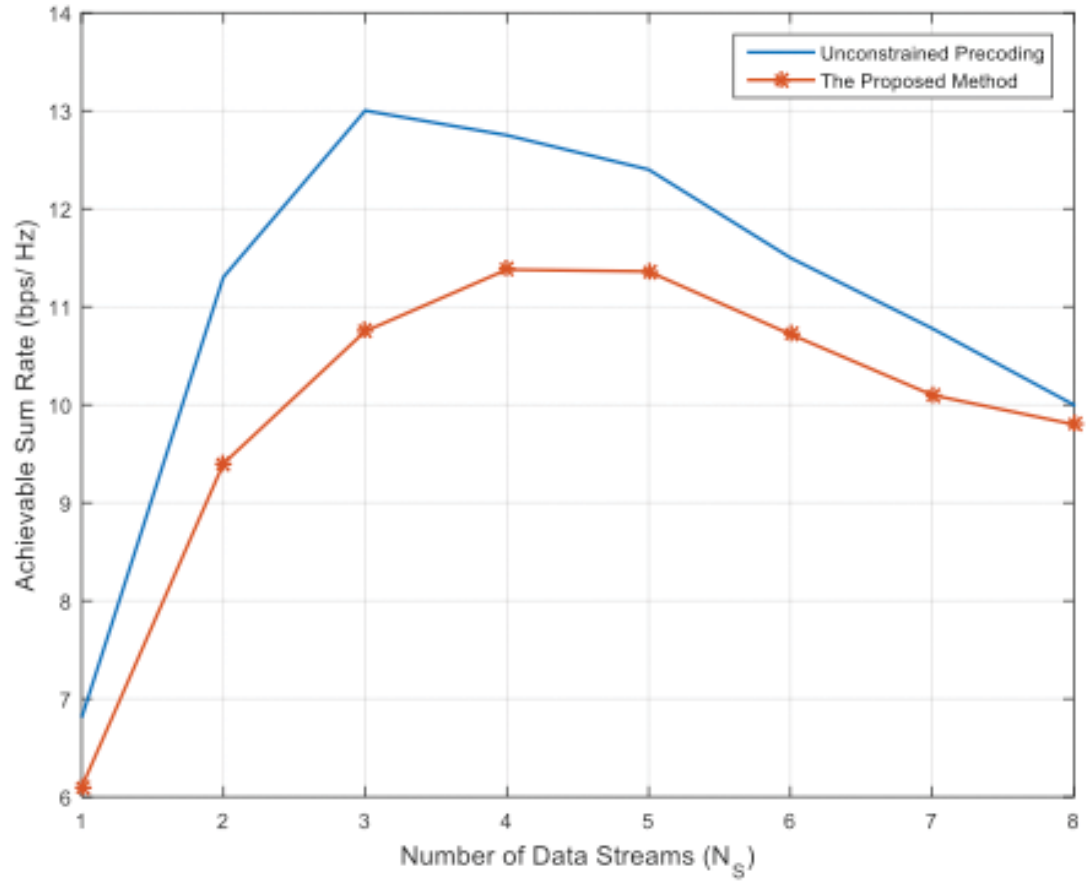

Figure 2. SER versus number of iterations for different N_s

tive function into two parts such as signal part and noise part. The reason for this is that the multi-parameter and multi-dimensional optimization problem is transformed into two parallel optimization problems with fewer parameters and fewer dimensions. The optimization procedure can be defined into two steps. In the first step, the noise part is optimized and suboptimal combiner matrices are obtained. In the second step, these suboptimal combiner matrices are inserted into the signal part, and then the signal part is optimized to obtain suboptimal precoder matrices. The performance of the proposed algorithm is sufficient. Simulation results show that it outperforms the precoding algorithm in [29], and has a close performance to the state of the art sparse precoding algorithm in [20].

References

1. A. Osseiran, V. Braun, T. Hidekazu, P. Marsch, H. Schotten, H. Tullberg, M. A. Uusitalo, M. "Schellman, The foundation of the mobile and wireless communications system for 2020 and beyond: Challenges, enablers and technology solutions". *In: 2013 IEEE 77th Vehicular Technology Conference (VTC Spring)*, pp. 1–5, 2013.
2. IEEE standard for information technology– local and metropolitan area networks– specific requirements– part 15.3: Amendment 2: Millimeter-wave-based alternative physical layer extension. *IEEE Std 802.15.3c-2009 (Amendment to IEEE Std 802.15.3-2003)*, 1–200, 2009.
3. Iso/iec/ieee international standard for information technology–telecommunications and information exchange between systems–local and metropolitan area networks–specific requirements-part 11: Wireless lan medium access control (mac) and physical layer (phy) specifications amendment 3: Enhancements for very high throughput in the 60 ghz band (adoption of IEEE std 802.11ad-2012). *ISO/IEC/IEEE 8802-11:2012/Amd.3:2014(E)*, 1–634, 2014.
4. Z. Pi, F. Khan, "An introduction to millimeter-wave mobile broadband systems," *IEEE Communications Magazine*, vol. 49, pp. 101–107, 2011. [CrossRef]
5. M. R. Akdeniz, Y. Liu, M. K. Samimi, S. Sun, S. Rangan, T. S. Rappaport, E. Erkip, E, "Millimeter wave channel modeling and cellular capacity evaluation," *IEEE Journal on Selected Areas in Communications*, vol. 32, pp. 1164–1179, 2014. [CrossRef]
6. J. Wang, "Beam codebook based beamforming protocol for multi-gbps millimeter-wave wpan systems," *IEEE Journal on Selected Areas in Communications*, vol. 27, pp. 1390–1399, 2009. [CrossRef]

7. S. Hur, T. Kim, D. J. Love, J. V. Krogmeier, T. A. Thomas, A. Ghosh, "Millimeter wave beamforming for wireless backhaul and access in small cell networks," *IEEE Transactions on Communications* vol. 61, pp. 4391–4403, 2013. [CrossRef]
8. Y. M. Tsang, A. S. Y. Poon, S. Addepalli, "Coding the beams: Improving beamforming training in mmwave communication system," *In: 2011 IEEE Global Telecommunications Conference - GLOBECOM 2011*, pp. 1–6, 2011. [CrossRef]
9. T. Kim, J. Park, J. Y. Seol, S. Jeong, J. Cho, W. Roh, "Tens of gbps support with mmwave beamforming systems for next generation communications," *In: 2013 IEEE Global Communications Conference (GLOBECOM)*, pp. 3685–3690, 2013.
10. O. E. Ayach, S. Rajagopal, S. Abu-Surra, Z. Pi, R. W. Heath, "Spatially sparse precoding in millimeter wave mimo systems," *IEEE Transactions on Wireless Communications*, vol. 13, pp. 1499–1513, 2014. [CrossRef]
11. A. Alkhateeb, O. E. Ayach, G. Leus, R. W. Heath, "Hybrid precoding for millimeter wave cellular systems with partial channel knowledge," *In: 2013 Information Theory and Applications Workshop (ITA)*, pp. 1–5, 2013. [CrossRef]
12. S. Sun, T. S. Rappaport, R. W. Heath, A. Nix, S. Rangan, "Mimo for millimeter-wave wireless communications: beamforming, spatial multiplexing, or both?" *IEEE Communications Magazine,* vol. 52, pp. 110–121, 2014. [CrossRef]
13. A. Alkhateeb, J. Mo, N. Gonzalez-Prelcic, R. W. Heath, "Mimo precoding and combining solutions for millimeter-wave systems," *IEEE Communications Magazine,* vol. 52, pp. 122–131, 2014. [CrossRef]
14. T. S. Rappaport, S. Sun, R. Mayzus, H. Zhao, Y. Azar, K. Wang, G. N. Wong, J. K. Schulz, M. Samimi, F. Gutierrez, "Millimeter wave mobile communications for 5g cellular: It will work!", *IEEE Access* 1, 335–349, 2013. [CrossRef]
15. P. Schniter, A. Sayeed, "Channel estimation and precoder design for millimeter-wave communications: The sparse way," *In: 2014 48th Asilomar Conference on Signals, Systems and Computers*, pp. 273–277, 2014. [CrossRef]
16. M. K. Samimi, T. S. Rappaport, "Ultra-wideband statistical channel model for non line of sight millimeter-wave urban channels," *In: 2014 IEEE Global Communications Conference*, pp. 3483–3489, 2014. [CrossRef]
17. C. E. Chen, "An iterative hybrid transceiver design algorithm for millimeter wave mimo systems," *IEEE Wireless Communications Letters* vol. 4, pp. 285–288, 2015. [CrossRef]
18. X. Yu, J. C. Shen, J. Zhang, K. B. Letaief, "Alternating minimization algorithms for hybrid precoding in millimeter wave mimo systems," *IEEE Journal of Selected Topics in Signal Processing* vol. 10, 485–500, 2016. [CrossRef]
19. S. Park, R. W. Heath, "Frequency selective hybrid precoding in millimeter wave ofdma systems," *In: 2015 IEEE Global Communications Conference (GLOBECOM)*, pp. 1–6, 2015. [CrossRef]
20. A. Alkhateeb, R. W. Heath, "Frequency selective hybrid precoding for limited feedback millimeter wave systems," *IEEE Transactions on Communications*, vol. 64, pp. 1801–1818, 2016. [CrossRef]
21. A. Saleh, R. Valenzuela, "A statistical model for indoor multipath propagation," *IEEE Journal on Selected Areas in. Communications*. (2006).
22. W. U. Bajwa, J. Haupt, A. M. Sayeed, R. Nowak, "Compressed channel sensing: A new approach to estimating sparse multipath channels," *Proceedings of the IEEE,* vol. 98, pp. 1058–1076, 2010. [CrossRef]
23. L. Liang, W. Xu, X. Dong, "Limited feedback-based multi-antenna relay broadcast channels with block diagonalization," *IEEE Transactions on Wireless Communications*, vol. 12, pp. 4092–4101, 2013. [CrossRef]
24. X. Xue, T. E. Bogale, X. Wang, Y. Wang, L. B. Le, "Hybrid analog-digital beamforming for multiuser mimo millimeter wave relay systems," *In: 2015 IEEE/CIC International Conference on Communications in China (ICCC)*, pp. 1–7, 2015. [CrossRef]
25. G. Kwon, H. Park, "An efficient hybrid beamforming scheme for sparse millimeter wave channel," *In: 2015 IEEE Global Communications Conference (GLOBECOM)*, pp. 1–6, 2015. [CrossRef]
26. N. Song, H. Sun, T. Yang, "Coordinated hybrid beamforming for millimeter wave multi-user massive mimo systems," *In: 2016 IEEE Global Communications Conference (GLOBECOM)*, pp. 1–6, 2016. [CrossRef]
27. R. Rajashekar, L. Hanzo, "Iterative matrix decomposition aided block diagonalization for mm-wave multiuser mimo systems," *IEEE Transactions on Wireless Communications,* vol. 16, pp. 1372–1384, 2017. [CrossRef]
28. A. Alkhateeb, O. El Ayach, G. Leus, R. W. Heath, "Channel Estimation and Hybrid Precoding for Millimeter Wave Cellular Systems," *IEEE Journal of Selected Topics in Signal Processing,* vol. 8, pp. 831-846, 2014. [CrossRef]
29. J. Zhang, A. Wiesel and M. Haardt, "Low rank approximation based hybrid precoding schemes for multi-carrier single-user massive MIMO systems," *IEEE International Conference on Acoustics, Speech and Signal Processing (ICASSP)*, Shanghai, pp. 3281-3285, 2016, [CrossRef]

Nihat Kabaoğlu received the B.S. and M.S. degrees in electronics engineering from İstanbul University, and the Ph.D. degree in electronics and telecommunication engineering from İstanbul Technical University, İstanbul, Turkey, in 1997, 2000, 2005 respectively. After working in different positions at İstanbul University, The Scientific and Technological Research Council of Turkey, Kadir Has University and Maltepe University, he joined to İstanbul Medeniyet University as an associate professor in 2015. His general research interests cover estimation theory, statistical signal processing, communication theory, wireless sensor networks and array processing. His current research areas are focused on wireless communication concepts with specific attention to channel estimation for spread-spectrum and multicarrier systems, on beamforming design for next generation systems and on optimal power allocation in wireless sensor networks.1

İSTANBUL UNIVERSITY PRESS

RESEARCH ARTICLE

Electrica 2018; 18(1): 90-94

Classification of Texture Images Based on the Histogram of Oriented Gradients Using Support Vector Machines

Hasan Demir

Department of Electronics and Communication Engineering, Namık Kemal University Çorlu School of Engineering, Tekirdağ, Turkey

Cite this article as: H. Demir. "Classification of Texture Images Based on the Histogram of Oriented Gradients Using Support Vector Machines". *Electrica*, vol. 18, no. 1, pp. 90-94, 2018.

ABSTRACT

Herein, using support vector machines, texture images were classified based on the histogram of oriented gradients, from which feature vectors were obtained. In addition, the success rate was examined for the feature vectors with different dimensions and the minimum length of a feature vector for performing classification was determined to be 288 elements.

Keywords: Texture classification, Support vector machines, Histogram of oriented gradients

Introduction

Texture analysis is the mostly used method in image processing. It is possible to get knowledge about segmentation and classification of spatial parameters in images by texture analysis. Texture analysis is frequently utilized in medical image processing, remote sensing, and control systems. Features of texture can be extracted with variety of methods such as statistics, geometry, model-based, and signal processing etc. [1-8]. Those features are classified by machine learning techniques such that support vector machines, artificial neural networks. Histogram of oriented gradients method has been primarily used for pedestarian detection [9]. In addition, this method has been used to solve problems about human detection, crowd detection, 3D segmentation, sign language recognition [10-13]. Support vector machines is proposed by Cortes and Vapnik for the purpose of solving two dimensional classification problem [14]. It can also be used to solve for multiclass classifying problem [15]. In addition, svm can be implemented for linear or nonlinear classification problems. In this study, hog and feature vector extraction will be discussed at first for texture images, and classification of feature vectors via support vector machine will be mentioned.

Histogram of Oriented Gradients

At first, image has been partitioned into piece of blocks and cells, and features of the image are obtained by calculating the gradient for every cell [9]. Therefore, images are represented with respect to local histograms. Vertical and horizontal gradient of the images are calculated with the help of Sobel filters. Lets assume I(x,y) is the image, f_x is horizontal gradient whose Sobel filter coefficients are [1.0,-1], and f_y represents the vertical gradient whose Sobel filter coefficients are $[1,0,-1]^T$. I(x,y) represents the intensity of the image at (x,y) point. Then gradient will be calculated as:

$$f_x(x,y) = I(x+1,y) - I(x-1,y) \quad (1)$$

$$f_y(x,y) = I(x,y+1) - I(x,y-1) \quad (2)$$

Address for Correspondence:
Hasan Demir

E-mail:
hdemir@nku.edu.tr

Received: 20.12.2017

Accepted: 04.01.2018

DOI: 10.5152/iujeee.2018.1814

In addition,

$$f(x,y) = \sqrt{f_x^2 + f_y^2} \quad (3)$$

$$\Theta = \arctan \frac{f_y(x,y)}{f_x(x,y)} \quad (4)$$

where f(x,y) represents the magnitude and Θ stands for the phase of the gradient.

Support Vector Machines

Support vector machines classify the group of data by using optimal hyperplane [14]. It is illustrated for 2-D data in Figure 1. Problem is to calculate w and b parameters with a constraint on optimum hyperplane such that wx+b=0, and X_i can either be +1 or -1.

Texture Classification via HOG

Texture data have been gathered from Salzburg Texture Image Database [16]. Size of the texture images are 512x512. Just three of the texture data: fabric, metal and tree textures are shown in Figure 2-4.

Implementation has been made by using Python programming language, and opencv machine learning library has been used. Texture images are converted into gray level images, and following methods are applied to those images.

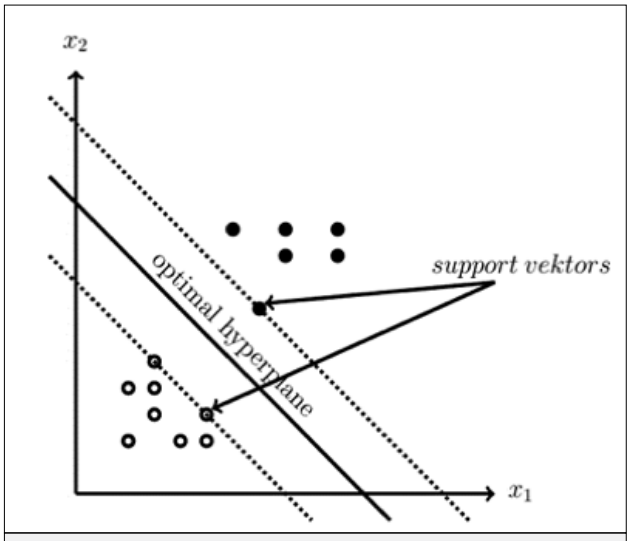

Figure 1. Support vectors and optimal hyperplane

Figure 2. Texture image of fabric

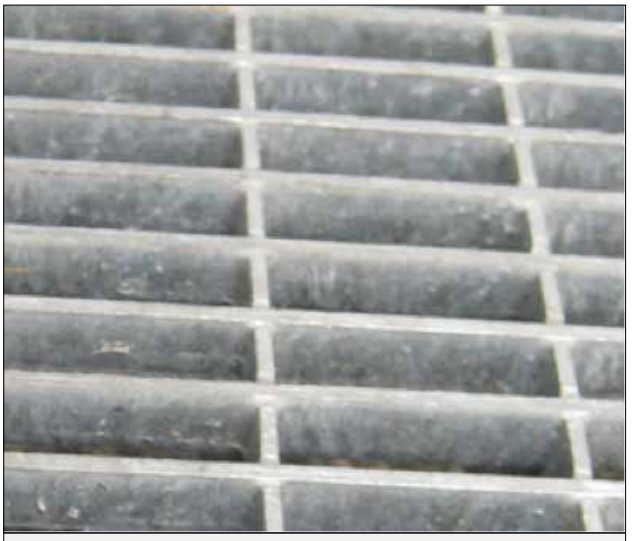

Figure 3. Texture image of metal

Figure 4. Texture image of tree

Method 1
Calculate the vertical and horizontal gradient for the images of size 512x512. Calculate amplitude and angle of the gradients. Histogram of angles are calculated by dividing [0.180) degree into 9 equal pieces. For every subimage, amplitude values are accumulated for each angle in the same piece. Therefore, 9 dimensional feature vector is obtained.

Method 2
Calculate the vertical and horizontal gradient for the images of size 512x512. Calculate amplitude and angle of the gradients. Histogram of angles are calculated by dividing [-180, 180) degree into 18 equal pieces. For every subimage, amplitude values are accumulated for each angle in the same piece. Therefore, 18 dimensional feature vector is obtained.

Method 3
Texture image is divided into four piece with a size of 256x256. Calculate vertical and horizontal gradient for these subimages. Calculate amplitude and angle of the gradients. Histogram of angles are calculated by dividing [0.180) degree into 9 equal pieces. For every subimage, amplitude values are accumulated for each angle in the same piece. Therefore, 9 dimensional feature vector is obtained. Concatenate all feature vectors together, and obtain 4x9=36 dimensional feature vector.

Method 4
Texture image is divided into four piece with a size of 256x256. Calculate vertical and horizontal gradient for these subimages. Calculate amplitude and angle of the gradients. Histogram of angles are calculated by dividing [-180, 180) degree into 18 equal pieces. For every subimage, amplitude values are accumulated for each angle in the same piece. Therefore, 18 dimensional feature vector is obtained. Concatenate all feature vectors together, and obtain 4x18=72 dimensional feature vector.

Method 5
Texture image is divided into 16 piece with a size of 128x128. Calculate vertical and horizontal gradient for these subimages. Calculate amplitude and angle of the gradients. Histogram of angles are calculated by dividing [0.180) degree into 9 equal pieces. For every subimage, amplitude values are accumulated for each angle in the same piece. Therefore, 9 dimensional feature vector is obtained. Concatenate all feature vectors together, and obtain 16x9=144 dimensional feature vector.

Method 6
Texture image is divided into four piece with a size of 128x128. Calculate vertical and horizontal gradient for these subimages. Calculate amplitude and angle of the gradients. Histogram of angles are calculated by dividing [-180, 180) degree into 18 equal pieces. For every subimage, amplitude values are accumulated for each angle in the same piece. Therefore, 18 dimensional feature vector is obtained. Concatenate all feature vectors together, and obtain 16x18=288 dimensional feature vector.

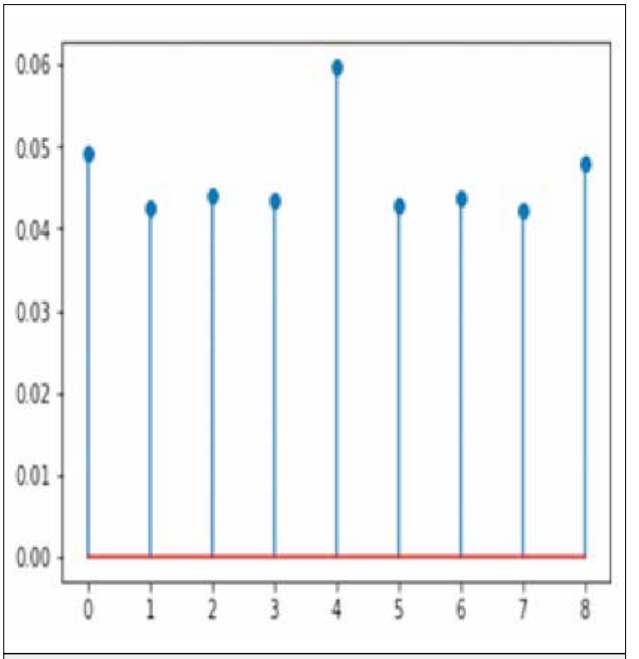

Figure 5. Feature vector calculated with Method 1.

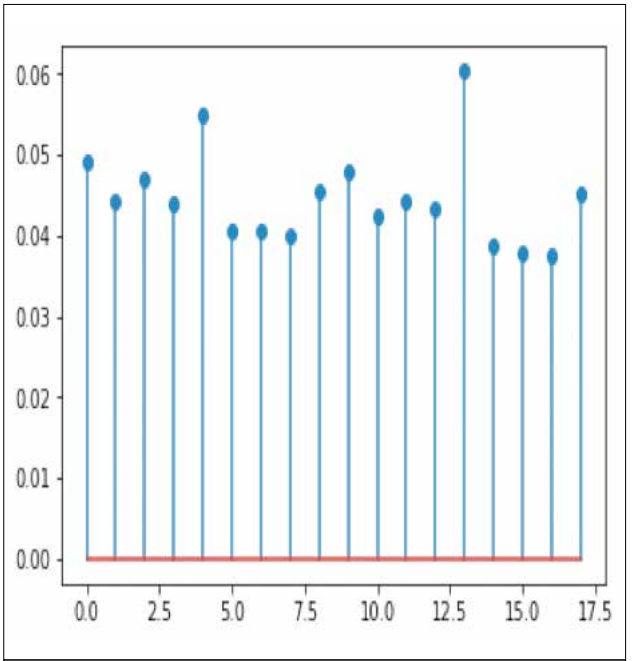

Figure 6. Feature vector calculated with Method 1.

Normalized feature vectors are calculated with all the methods before mentioned for the texture image in Figure 2. In addition, all feature vectors are shown in Figure 5-10.

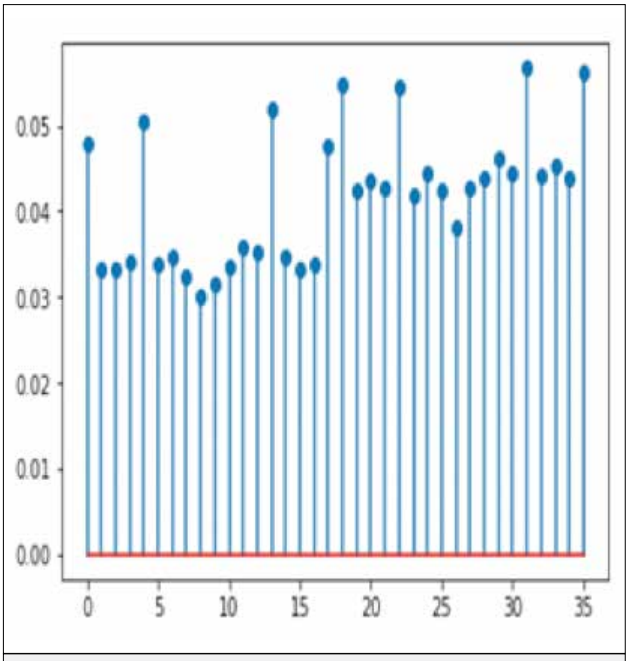

Figure 7. Feature vector calculated with Method 3

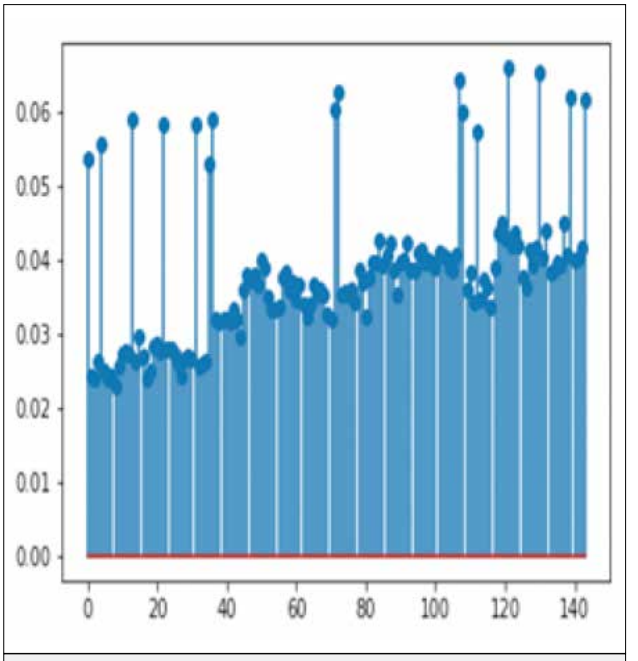

Figure 9. Feature vector calculated with Method 5

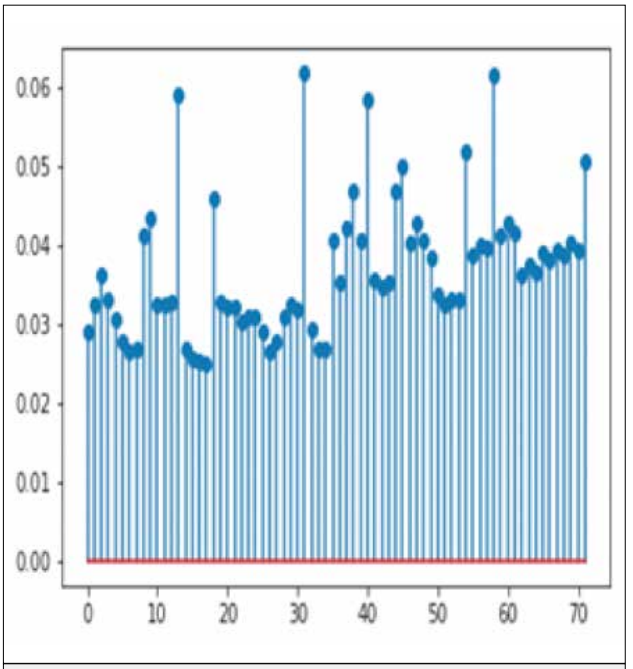

Figure 8. Feature vector calculated with Method 4

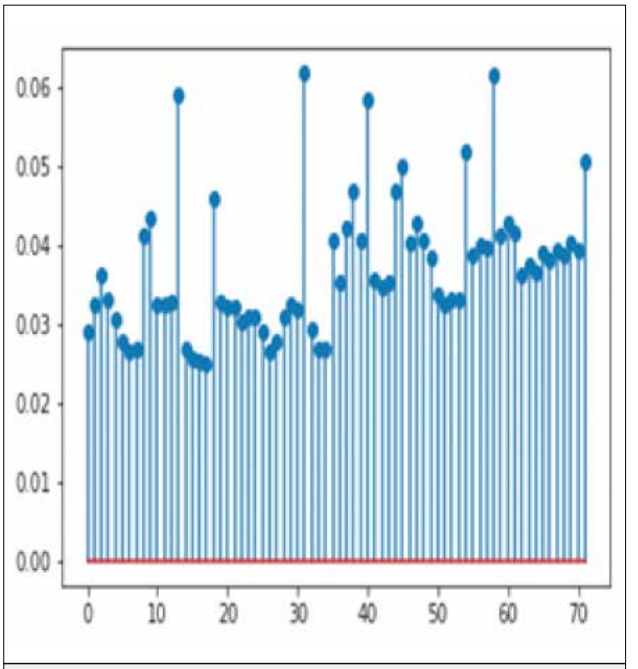

Figure 10. Feature vector calculated with Method 6

Results and Discussion

Opencv library has been used for the classification. Histogram intersection kernel is also utilized for the support vector machine. 230 of texture images which belong to 6 different class have been used as a training data, and 16 texture images have been utilized as a testing data. Success rate of classification are given in Table 1.

In the literature, size of feature vector using histogram of oriented gradients have been reported 3780 elements [18]. In the method 6, size of feature vector has obtained 288 elements.

Conclusions

Methods which are related with generating 18 piece of histograms with an angles between [-180, 180) have better perfor-

Table 1. Success rates of classification

Method	Success rate
1	43.75%
2	25%
3	50%
4	62.25%
5	31.25%
6	81.25%

mance results than other methods, i.e Method 4 and Method 6. For those methods consisting of 18 piece of histograms have better success rates when the numbers of feature vectors are increased. Method 6 is the best method when success rates are taken into account.

References

1. M. Tuceryan, A. K. Jain, "Texture analysis - Handbook of Pattern Recognition & Computer Vision," World Scientific Pub Co Inc., Singapore City, 1993.
2. D. Marr, "Vision", Freeman, Chap 2, pp. 54-78, 1982.
3. H. Voorhees, T. Poggio, "Detecting textons and texture boundaries in natural images", Proceedings of the First International Conference on Computer Vision. pp 250-258, 1987.
4. M. Tuceryan, A. K. Jain, "Testure segmentation using Voronoi polygons," *IEEE Transactions on Pattern Analysis and Machine intelligence* vol. 12, pp. 211-216, 1990. [CrossRef]
5. F. Tomita, S. Tsuji, "Computer Analysis of Visual Textures," Springer, New York, 1990. [CrossRef]
6. L. S. Davis, S. A. Johns, J. K. Aggarwal, "Texture Analysis Using Generalized Co-Occurrence Matrices," *IEEE Transactions on Pattern Analysis and Machine Intelligence*, vol. PAMI-1, Issue: 3, July 1979. [CrossRef]
7. N. Ahuja, B. J. Schachter, "Pattern Models", John Wiley, 1983.
8. M. Clark, A. C. Bovik, W. S. Geisler, "Texture Segmentation Using Gabor Modulation/Demodulation," *Pattern Recognition Letters,* vol. 6, pp. 261-267, September 1987. [CrossRef]
9. N. Dalal, B. Triggs. "Histograms of Oriented Gradients for Human Detection", *IEEE Computer Society Conference on Computer Vision and Pattern Recognition*, vol.1, pp. 886–893, June 2005. [CrossRef]
10. T. Watanabe, S. Ito, K. Yokoi, "Image Feature Descriptor using Co-occurrence Histograms of Oriented Gradients for Human Detection," *The Journal of the Institute of Image Information and Television Engineers,* vol. 71, pp. J28, 2017. [CrossRef]
11. H. Fu, H. Ma, "Real-time crowd detection based on gradient magnitude entropy model," Proceedings of the ACM International Conference on Multimedia, November 03-07, 2014, Orlando, Florida, USA. [CrossRef]
12. C. Bhole, N. Morsillo, C. Pal, "3D segmentation in CT imagery with conditional random fields and histograms of oriented gradients", Proceedings of the Second international conference on Machine learning in medical imaging, p. 326-334, September 18, 2011, Toronto, Canada. [CrossRef]
13. P. Jangyodsuk, C. Conly, V. Athitsos, "Sign language recognition using dynamic time warping and hand shape distance based on histogram of oriented gradient features", Proceedings of the 7th International Conference on PErvasive Technologies Related to Assistive Environments, May 27-30, 2014, Rhodes, Greece. [CrossRef]
14. C. Cortes, V. Vapnik, "Support-Vector Networks", *Kluwer Academic Publishers Machine Learning,* vol. 20, pp. 273-297, 1995. [CrossRef]
15. A. Wang, W. Yuan, J. Liu, Z. Yu, H. Li, "A novel pattern recognition algorithm: Combining ART network with SVM to reconstruct a multi-class classifier," *Computers and Mathematics with Applications*, vol. 57, pp. 1908-1914, 2009. [CrossRef]
16. R. Kwitt, P. Meerwald, "Salzburg texture image database," Available online: http://www.wavelab.at/sources/STex/
17. A. Barla, F. Odone, A.Verri "Histogram intersection kernel for image classification" *Image Processing,* 2003. ICIP 2003. Proceedings. 2003 International Conference on, vol. 3.
18. C.Tomasi,"Histograms of Oriented Gradients", http://www.cs.duke.edu/courses/fall15/compsci527/notes/hog.pdf, 2017.– Accessed: 20.11.2017

Hasan Demir was born in Elbistan, 1972. He received his bachelor's degree from Yıldız Technical University Electronics and Communication Engineering Department in 1994, Master's Degree in from Institute of Science, İstanbul University in 1998, and his Ph.D. degree from İstanbul University, Institute of Science in 2008. Between 1994 and 1998, He worked as an assistant at T.Ü. Çorlu Engineering Faculty, and between 1998-2008 he worked as a research assistant in the Department of Electrical and Electronics Engineering at the I.U. Faculty of Engineering. Currently, he is an Assistant Professor in the Department of Electronics and Communication Engineering at Çorlu Engineering Faculty, N.K.U. He works on artificial neural networks, image processing, wavelet analysis.

İSTANBUL UNIVERSITY PRESS

RESEARCH ARTICLE

Electrica 2018; 18(1): 95-99

Lossy/Lossless Grounded Inductance Simulators Using Current Feedback Operational Amplifier (CFOA)

Muhammed Emin Başak[1], Fırat Kaçar[2]

[1]Yıldız Technical University School of Naval Architecture and Maritime, İstanbul, Turkey
[2]Department of Electrical and Electronics Engineering, İstanbul University School of Engineering, İstanbul, Turkey

Cite this article as: E. Başak, F. Kaçar. "Lossy/Lossless Grounded Inductance Simulators Using Current Feedback Operational Amplifier (CFOA)". *Electrica*, vol. 18, no. 1, pp. 95-99, 2018.

ABSTRACT

Active elements are critical in implementing active filters, oscillators, rectifiers, and signal processing circuits. We observe that several active circuits have been proposed in the literature. In this study, we have proposed four inductance simulators that employ only one active circuit current feedback operational amplifier and three or four passive components. The first and fourth topologies are designed for series lossy inductance, whereas the second and third topologies are designed for lossless negative inductance simulators. A passive RLC filter is used to demonstrate the effectiveness of the proposed inductance simulators. The simulations performed with the LTSpice program and the results agree with the theoretical analysis.

Keywords: CFOA, filter, CMOS

Introduction

Inductance is the source of many problems in electronic circuits and systems. It stands to reason that inductance radiates magnetic energy, it places a larger footprint in the integrated circuit, and it contains more parasitic noises than other components. Bulky and expensive passive inductors motivated the researchers to design the alternative circuits can be worked as inductors. Inductance simulators are widely used, especially for high frequencies, instead of inductors. Therefore, for designing filters or oscillator, for eliminating electromagnetic interferences the inductance simulators are used.

Recently, a considerable literature has grown up the theme of active inductance realization. Several active inductance simulators have been proposed such as operational transconductance amplifier (OTA) [1-3], operational transresistance amplifier (OTRA) [4,5], current-feedback operational amplifier (CFOA) [6-12] current differencing buffer amplifer (CDBA) [13,14], four terminal floating nullor (FTFN) [15], voltage differencing buffer amplifer (VDBA) [16-18], differential voltage current conveyor (DVCC) [19], second generation current conveyor (CCII) [20,21], dual-X current conveyor (DXCCII) [22-24]. Most of the reported circuits are commercially unavailable such as OTRA, CDBA, DVCC, DXCCII. Some of them such as FTFN [15] can be realized using two active devices such as AD844 CFOA can be commercially available. CFOA is a low-cost, general purpose device that has good AC and DC performance. CFOA is current mode circuit so it has some inherantel advantages over the voltage mode operational amplifers such as wider bandwidth, wider dynamic range and greater linearity. It also allows high slew rate capability and it is free from the slew rate boundries that are basic characteristics of the traditional operational amplifiers.

Address for Correspondence:
Muhammed Emin Başak

E-mail:
mebasak@yildiz.edu.tr

Received: 07.11.2017

Accepted: 04.01.2018

DOI: 10.5152/iujeee.2018.1815

Four different inductance simulators employing a single CFOA and three or four passive components were presented in [6]. Three different generic structures were also presented in [11] which employing a single CFOA and three or four passive components. The circuits [25-27] are not operated commercially available devices such as AD844, LM741. The circuits [4,28-31] can be constructed with more than one AD844.

The overall structure of the study takes the form of four sections. The first section is an introduction, the second section gives the proposed four grounded inductance simulator topologies and parallel resonant circuit is constructed with the proposed inductance simulator, the third section gives the simulation results and the last section is the conclusion. It is expected that the proposed circuit will provide different opportunities to the designers accomplishing of analog integrated circuit applications.

The Proposed Inductor Simulators

The equivalent circuit of CFOA is shown in Figure 1. In the ideal case, current gain and voltage gains are $\alpha = 1$ and $\beta_1 = \beta_2 = 1$, respectively. So; CFOA whose electrical symbol ideally specified as $I_y = 0$, $I_z = I_x$, $V_x = V_y$ and $V_w = V_z$, are going to be stated by the following equation:

$$\begin{bmatrix} I_y \\ I_z \\ V_x \\ V_w \end{bmatrix} = \begin{bmatrix} 0 & 0 & 0 \\ \alpha & 0 & 0 \\ 0 & \beta_1 & 0 \\ 0 & 0 & \beta_2 \end{bmatrix} \begin{bmatrix} I_x \\ V_y \\ V_z \end{bmatrix} \quad (1)$$

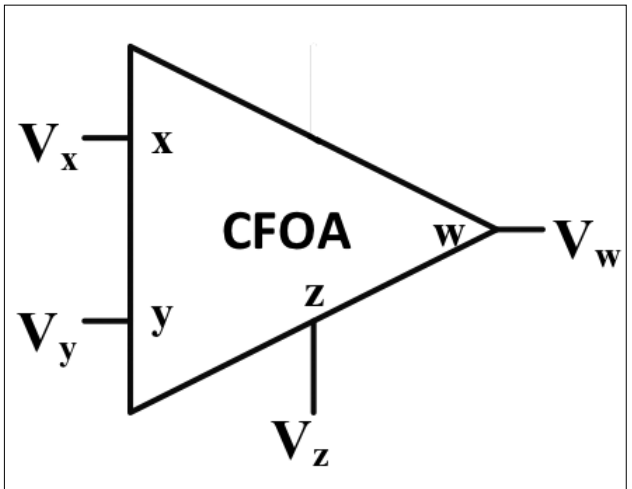

Figure 1. Equivalant circuit of CFOA

Table 1. Equivalent impedances of proposed inductance simulators

Circuit	Non-ideal impedances (Z_{eq})	Ideal impedances (Z_{eq})
Figure 2 (a)	$\frac{R_1}{1+Cs\alpha(\gamma-\beta)R_2}+\frac{R_2}{1+Cs\alpha(\gamma-\beta)R_2}+\frac{Cs\alpha\gamma R_1R_2}{1+Cs\alpha(\gamma-\beta)R_2}$	$R_1+R_2+CsR_1R_2$
Figure 2 (b)	$-\frac{CR_1R_2s}{\beta\gamma+CR_2s(-1+\beta\gamma)}$	$-CR_1R_2s$
Figure 2 (c)	$\frac{C_2R_1R_2s}{C_2R_2s-\alpha\beta\gamma-C_1R_2s\alpha\beta\gamma}$	$\frac{C_2R_1R_2s}{-1-C_1R_2s+C_2R_2s}$
Figure 2 (d)	$\frac{R_1}{1-Cs(-1+\alpha\beta\gamma)R_2}+\frac{CsR_1R_2}{1-Cs(-1+\alpha\beta\gamma)R_2}$	$R_1+CsR_1R_2$

Table 2. Equivalent admittances of proposed inductance simulators ideal and non-ideal cases

Circuit	Non-ideal admittances (Y_{eq})	Ideal admittances (Y_{eq})
Figure 2 (a)	$\frac{1}{R_1+R_2+Cs\alpha\gamma R_1R_2}+\frac{Cs\alpha(-\beta+\gamma)R_2}{R_1+R_2+Cs\alpha\gamma R_1R_2}$	$\frac{1}{R_1+R_2+CsR_1R_2}$
Figure 2 (b)	$-\frac{\beta\gamma}{CR_1R_2s}+\frac{1-\beta\gamma}{R_1}$	$-\frac{1}{R_1R_2Cs}$
Figure 2 (c)	$\frac{1}{R_1}-\frac{C_1\alpha\beta\gamma}{C_2R_1}-\frac{\alpha\beta\gamma}{C_2R_1R_2s}$	$\frac{1}{R_1}-\frac{C_1}{C_2R_1}-\frac{1}{C_2R_1R_2s}$
Figure 2 (d)	$\frac{1}{R_1+CsR_1R_2}+\frac{Cs(1-\alpha\beta\gamma)R_2}{R_1+CsR_1R_2}$	$\frac{1}{R_1+CsR_1R_2}$

The proposed CFOA based inductor simulators are shown in Figure 2 a-d. The first inductance simulator consists of one CFOA and three passive components while the others consist of one CFOA and four passive components. Transfer functions of the proposed circuits are given in Table 1, 2. According to the equivalent impedance of the first and fourth simulators are intended for lossy series inductors. The second simulator is intended to negative lossless inductance simulator. The third one is also intended to negative lossless inductance simulator if C_1 and C_2 capacitors and R_1 and R_2 resistors are equal to each other.

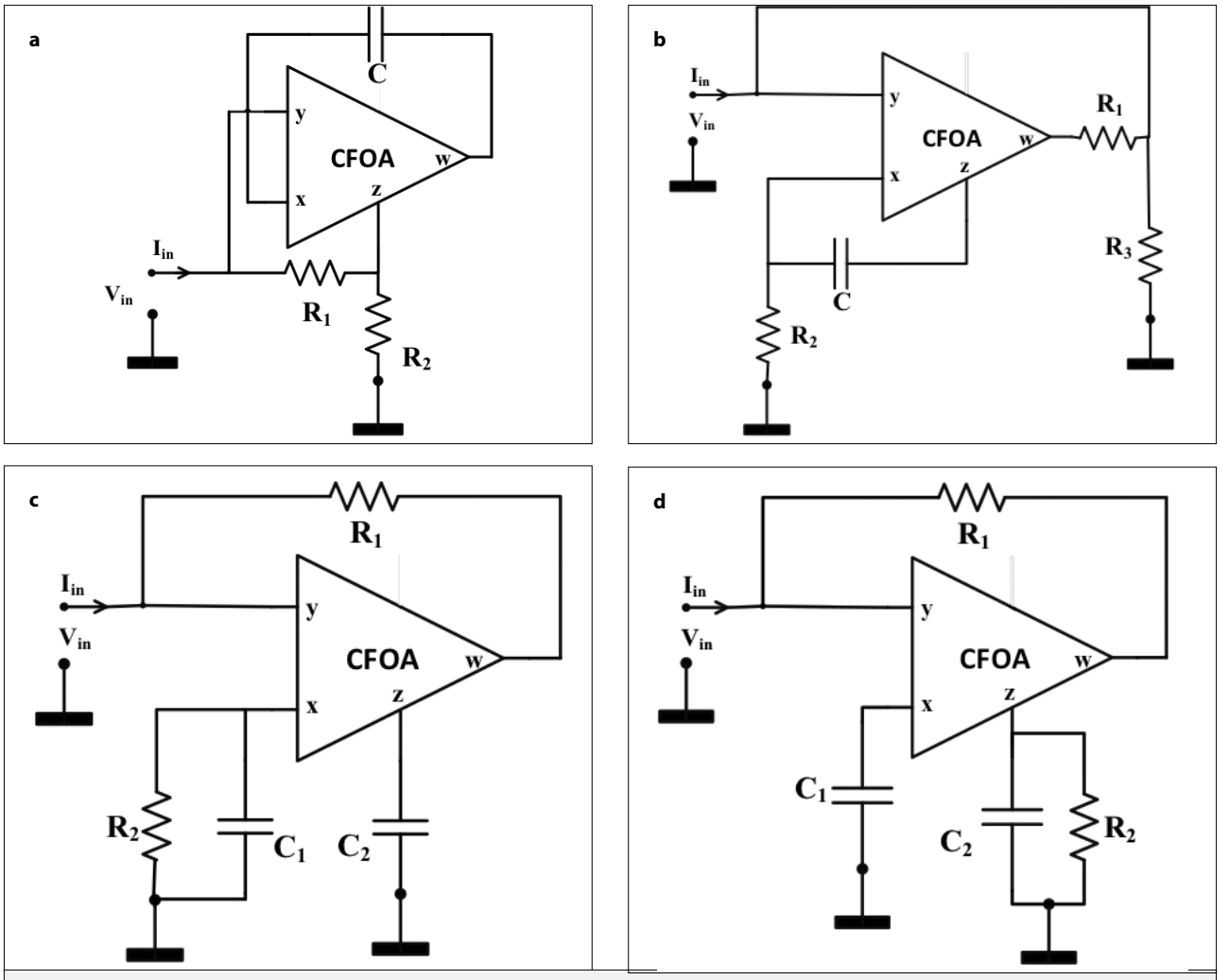

Figure 2. a-d. Proposed inductance simulators made with CFOA

Simulation Results

As long as higher value inductances occupy a bigger area in chips, Inductor will be a central ingredient in deciding the total chip area because higher inductance values imply larger area consumption. In order to solve this problem, it is more convenient to use active implementations of an inductor which offer less area consumption.

LTSpice program is used to explain the performance of the presented inductance simulator. The simulated frequency response of input impedance for the inductor simulator is given in Figure 2b. The magnitude of impedance of the presented inductance simulator is given in Figure 3. The inductive characteristic extends from 1 kHz to 50 MHz.

RLC filter is presented as an application example to demonstrate the performance of the presented inductance simulator. Inductance simulator with a parallel capacitor and resistor formed as a resonant circuit shown in Figure 4. In this Figure actively simulated induc-

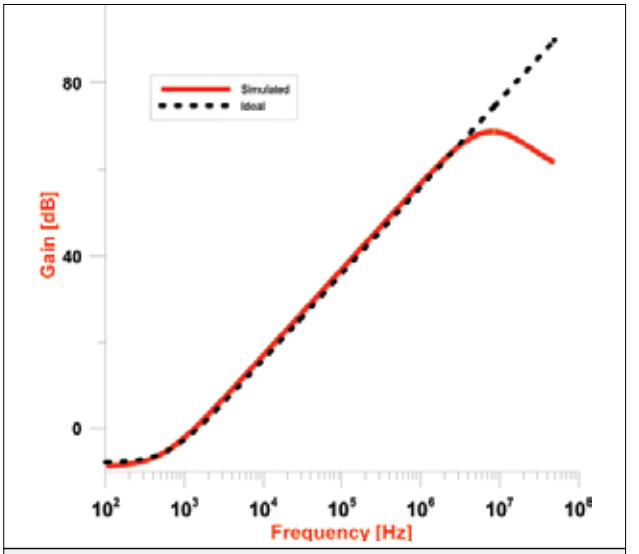

Figure 3. Simulated magnitudes of impedance of presented inductance simulator in comparison with ideal inductance

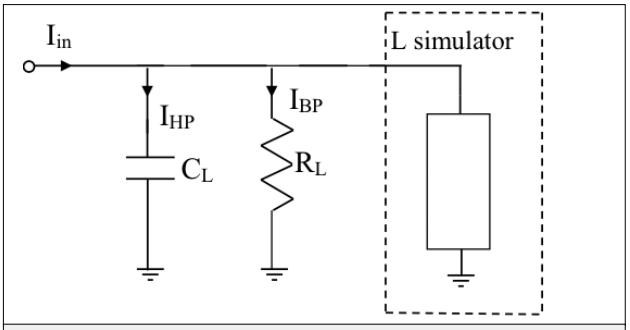

Figure 4. RLC Filter application of the proposed inductance simulator

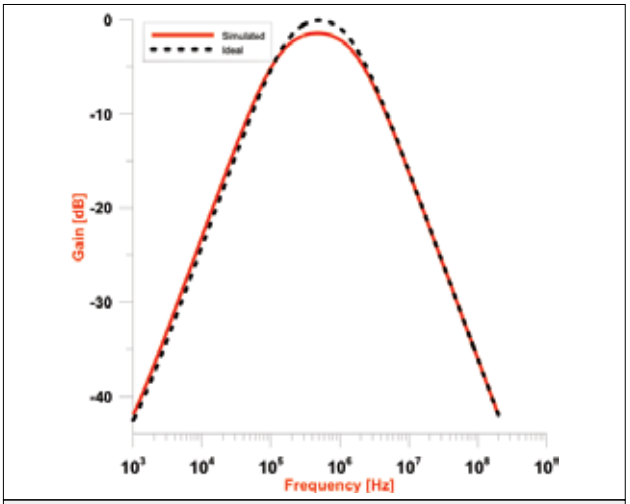

Figure 5. Simulated bandpass response of the filter

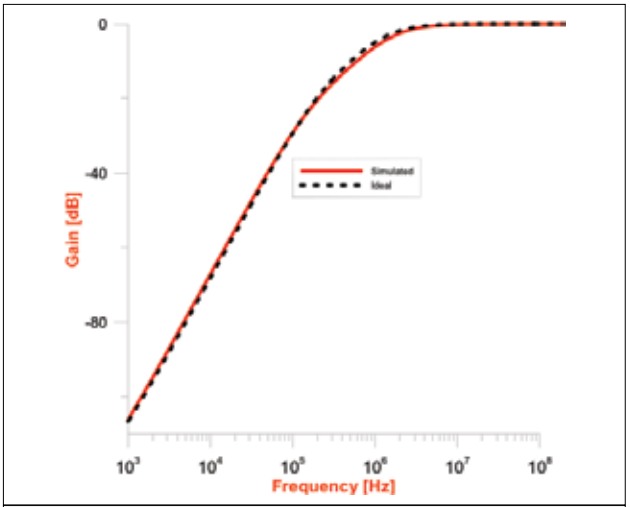

Figure 6. Simulated highpass response of the filter

tance simulator circuit in Figure 2b replaces the parallel inductor. The transfer functions are given by the following equations:

$$\frac{I_{HP}}{I_{in}} = \frac{s^2}{s^2 + \frac{G_L}{C_L}s + \frac{1}{L_{eq}C_L}} \quad (2)$$

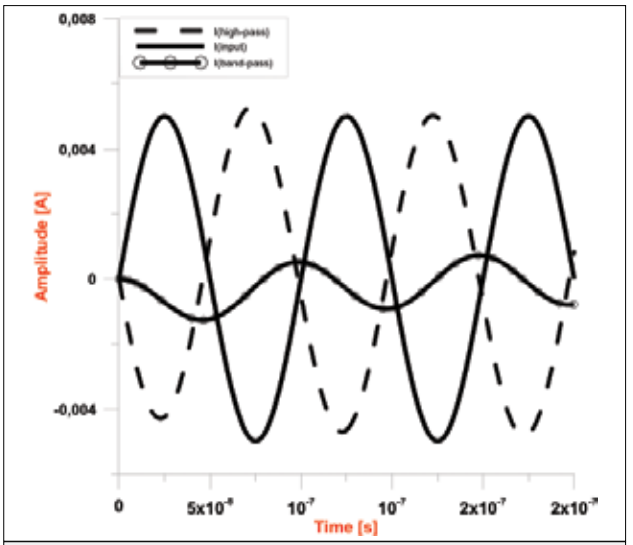

Figure 7. Time domain response of RLC filter high-pass and band-pass filter for 10mA peak-to-peak 10MHz sine wave input

$$\frac{I_{BP}}{I_{in}} = \frac{\frac{G_L}{C_L}s}{s^2 + \frac{G_L}{C_L}s + \frac{1}{L_{eq}C_L}} \quad (3)$$

The realized filter is simulated with LTSpice program using AD844. Supply voltages are taken as V_{DD} = 12V and V_{SS} = –12 V. Simulation result of the filter responses, very good agreement with the predicted theory, is given in Figure 5 and Figure 6 respectively. The component values of the accomplished filter are chosen as follows: C_L=1nF, R_L=100Ω R_1= R_2=R_3=1kΩ and C=50pF, thus an inductor L_{eq}=100μH is obtained. In order to analysis time responses of RLC filter, peak-to-peak 10 mA and 10 MHz sinusoidal inputs are applied. The time domain analysis result is given in Figure 7 for bandpass and highpass filter configuration for the circuit in Figure 4.

Conclusions

In this study, A CFOA based inductor simulators are proposed. The proposed circuit consisted only one single of CFOA, and three or four passive components. The aim of the present research was to propose the inductance simulators which consists three or four passive components in addition to single active device named CFOA. In order to show the effectiveness of the proposed inductance simulators, LTSpice simulation tests were put into practice. This study sets out provide the further possibilities to the designers in the realization of analog integrated circuits such as filters and oscillator applications.

References

1. P. Soni, B. P. Singh, and M. Bhardwaj, "Design of OTA based floating inductor," in 2011 International Conference on Devices and Communications, ICDeCom 2011 - Proceedings, 2011. [CrossRef]
2. R. Banchuin, B. Chipipop, and B. Sirinaovakul, "Novel practically applicable passive equivalent circuit model of the alternatively structured higher performance practical OTA-based floating inductor," in 2007 International Symposium on Intelligent Signal Processing and Communications Systems, ISPACS 2007 - Proceedings, pp. 447–450, 2008.

3. R. Banchuin, R. Chaisricharoen, B. Chipipop, and B. Sirinaovakul, "In depth analysis of the CMOS OTA-based floating inductors," in 2006 International Symposium on Intelligent Signal Processing and Communications, ISPACS'06, pp. 239–242, 2007.
4. U. Çam, F. Kaçar, O. Cicekoglu, H. Kuntman, and A. Kuntman, "Novel two OTRA-based grounded immitance simulator topologies," *Analog Integr. Circuits Signal Process.,* vol. 39, no. 2, pp. 169–175, 2004. [CrossRef]
5. B. C. Nagar, S. K. Paul, "Negative inductance simulator using OTRA," vol. 3, no. 2, pp. 2–4, 2016. [CrossRef]
6. F. Kaçar and H. Kuntman, "CFOA-based lossless and lossy inductance simulators," *Radioengineering,* vol. 20, no. 3, pp. 627–631, 2011.
7. O. Çiçekoğlu, "Precise simulation of immittance functions using the CFOA," *Microelectronics J.,* vol. 29, no. 12, pp. 973–975, Dec. 1998. [CrossRef]
8. M. T. Abuelma'Atti, S. K. Dhar, "CFOA-based floating negative inductance, positive frequency dependent resistance and resistance-controlled capacitance and resistance emulator," *Int. Conf. Electron. Information, Commun. ICEIC* 2016, pp. 3–5, 2016.
9. M. Taher, "A New CFOA-Based Low Frequency Lowpass Filter for Biomedical Applications," pp. 1–4, 2016.
10. M. Taher, "New CFOA-Based Floating Lossless Negative Immittance Function Emulators," pp. 0–3, 2015.
11. M. T. Abuelma'atti, "New grounded immittance function simulators using single current feedback operational amplifier," *Analog Integr. Circuits Signal Process.,* vol. 71, no. 1, pp. 95–100, 2012. [CrossRef]
12. E. Yuce, "Novel lossless and lossy grounded inductor simulators consisting of a canonical number of components," *Analog Integr. Circuits Signal Process.,* vol. 59, pp. 77–82, 2009. [CrossRef]
13. J. K. Pathak, A. K. Singh, R. Senani, "New canonic lossy inductor using a single CDBA and its application," Int. J. Electron., vol. 103, no. 1, pp. 1–13, 2016. [CrossRef]
14. S. Minaei, E. Yuce, "A simple CMOS-based inductor simulator and frequency performance improvement techniques," *AEU - Int. J. Electron. Commun.,* vol. 66, no. 11, pp. 884–891, 2012. [CrossRef]
15. U. Çam, O. Çiçekoğlu, H. Kuntman, "Novel lossless floating immitance simulator employing only two FTFNs," *Analog Integr. Circuits Signal Process.,* vol. 29, no. 3, pp. 233–235, 2001. [CrossRef]
16. O. Channumsin, J. Pimpol, C. Thongsopa, W. Tangsrirat, "VDBA-based floating inductance simulator with a grounded capacitor," in Proceedings - 2015 7th International Conference on Information Technology and Electrical Engineering: Envisioning the Trend of Computer, Information and Engineering, ICITEE 2015, 2015, pp. 114–117. [CrossRef]
17. A. Yeşil, F. Kaçar, K. Gürkan, "Lossless grounded inductance simulator employing single VDBA and its experimental band-pass filter application," *AEU - Int. J. Electron. Commun.,* vol. 68, no. 2, pp. 143–150, 2014. [CrossRef]
18. A. Yesil and F. Kacar, "VDBA-based lossless and lossy inductance simulators and its filter applications," in 2016 24th Signal Processing and Communication Application Conference (SIU), 2016, pp. 909–912. [CrossRef]
19. A. Abaci and E. Yuce, "Modified DVCC based quadrature oscillator and lossless grounded inductor simulator using grounded capacitor(s)," *AEU - Int. J. Electron. Commun.,* vol. 76, pp. 86–96, 2017. [CrossRef]
20. E. Yuce, O. Cicekoglu, S. Minaei, "CCII-based grounded to floating immittance converter and a floating inductance simulator," *Analog Integr. Circuits Signal Process.,* vol. 46, no. 3, pp. 287–291, 2006. [CrossRef]
21. G. Ferri, N. Guerrini, E. Silverii, A. Tatone, "Vibration damping using CCII-based inductance simulators," *IEEE Trans. Instrum. Meas.,* vol. 57, no. 5, pp. 907–914, 2008. [CrossRef]
22. A. Yeşil and F. Kaçar, "New dxccii-based grounded series inductance simulator topologies," İstanbul Univ. - J. *Electr. Electron. Eng.,* vol. 14, no. 2, pp. 1785–1789, 2015.
23. I. Myderrizi, S. Minaei, E. Yuce, "DXCCII-based grounded inductance simulators and filter applications," *Microelectronics J.,* vol. 42, no. 9, pp. 1074–1081, 2011. [CrossRef]
24. B. Metin, "Supplementary inductance simulator topologies employing single DXCCII," *Radioengineering,* vol. 20, no. 3, pp. 614–618, 2011.
25. M. Incekaraoglu and U. Çam, "Realization of Series and Parallel R-L and C-D Impedances Using Single Differential Voltage Current Conveyor," *Analog Integr. Circuits Signal Process.,* vol. 43, no. 1, pp. 101–104, Apr. 2005. [CrossRef]
26. E. Yuce, "Comment on 'realization of series and parallel R-L and C-D impedances using single differential voltage current conveyor,'" *Analog Integr. Circuits Signal Process.,* vol. 49, no. 1, pp. 91–92, 2006. [CrossRef]
27. H. Y. Wang and C.T. Lee, "Systematic synthesis of R-L and C-D immittances using single CCIII," *Int. J. Electron.,* vol. 87, no. December 2011, pp. 293–301, 2000.
28. H. Y. Wang and C. T. Lee, "Realisation of R-L and C-D immittances using single FTFN," *Electron. Lett.,* vol. 34, no. 6, p. 502, 1998. [CrossRef]
29. M. O. Cicekoglu, "Active simulation of grounded inductors with CCII's and grounded passive elements," *Int. J. Electron.,* vol. 85, no. 4, pp. 455–462, 1998. [CrossRef]
30. E. Yuce and S. Minaei, "A modified CFOA and its applications to simulated inductors, capacitance multipliers, and analog filters," *IEEE Trans. Circuits Syst. I Regul. Pap.,* vol. 55, no. 1, pp. 266–275, 2008. [CrossRef]
31. O. Çiçekolu, A. Toker, and H. Kuntman, "Universal immittance function simulators using current conveyors," *Comput. Electr. Eng.,* vol. 27, no. 3, pp. 227–238, 2001. [CrossRef]

Muhammed Emin Başak received his B.Sc., M.Sc., and Ph. D. degrees from İstanbul University in all in Electrical and Electronics Engineering 2005, 2008, 2014, respectively. Başak has performed research from 2007 to 2008 in l'ESIGELEC, IRSEEM Institutes, Rouen, France. He is currently an Assistant Professor at Faculty of Naval Architecture and Maritime at the Yıldız Technical University. His general research interests modelling, simulation of electronic devices and electronic circuits.

Fırat Kaçar received his B.Sc., M.Sc. and Ph.D. degrees from İstanbul University in all in Electrical and Electronics Engineering 1998, 2001 and 2005. He is currently Professor at the Electrical and Electronics Engineering Department of İstanbul University. His current research interests include analog circuits, active filters, synthetic inductors; CMOS based circuits' electronic device modeling and hot-carrier effect of MOS transistors. He is the author or co-author of about 80 papers published in scientific journals or conference proceedings.

İSTANBUL UNIVERSITY PRESS

RESEARCH ARTICLE

Electrica 2018; 18(1): 100-108

Monitoring, Surveillance, and Management of the Electromagnetic Spectrum: Current Issues in Electromagnetic Spectrum Monitoring

Ali Boyacı[1], Ali Rıza Ekti[2], Serhan Yarkan[3], Muhammed Ali Aydın[4]

[1]Department of Computer Engineering, İstanbul Commerce University School of Engineering, İstanbul, Turkey
[2]Department of Electrical and Electronics Engineering, Balıkesir University, Balıkesir, Turkey
[3]Center for Applied Research on Informatics Technologies (CARIT), İstanbul Commerce University, İstanbul, Turkey
[4]Department of Computer Engineering, İstanbul University School of Engineering, İstanbul, Turkey

Cite this article as: A. Boyacı, A. R. Ekti, S. Yarkan, M. A. Aydın. "Monitoring, Surveillance, and Management of the Electromagnetic Spectrum: Current Issues in Electromagnetic Spectrum Monitoring". *Electrica*, vol. 18, no. 1, pp. 100-108, 2018..

ABSTRACT

This paper discusses the current aspects of the surveillance and management of the electromagnetic spectrum under various topics that are vital to wireless communications. On the basis of the recent technological advancements in conjunction with the discussions on the global approaches toward electromagnetic spectrum monitoring, the paper addresses short-, medium-, and long-term strategies in wireless communications for monitoring, governing, and managing the electromagnetic spectrum of leading countries and multinational organizations. Furthermore, it proposes a novel spectrum monitoring strategy for next-generation wireless systems and outlines the implications of the proposed strategy.

Keywords: Flexible licensing, spectrum monitoring, spectrum refarming, wireless communications

Introduction

Wireless communication has become a necessity in modern life. Ubiquitous connectivity and mobility support without the need for a physical connection are the main features of contemporary wireless communication technologies. Such features attract ever-increasing number of users to utilize a wide variety of wireless services and applications. It is predicted that by the year 2020, seven billion people will be served by seven trillion wireless devices [1].

Aforementioned increase is not only limited to the number of users but also includes the volume of data carried by wireless communication systems. The increase in data volume is not surprising given the availability of vastly diverse and high quality services carried over wireless technologies. Today, any smartphone that has an Internet connection could provide many services beside the traditional voice communications such as file transfer, multi-media sharing, video chat, and online gaming. The predictions indicate that next stage of the evolution of wireless communications will expand into cyber-physical systems such as Internet of Everything (IoE) which is believed to cover virtual and augmented reality; high-definition and interactive television broadcast; a vast variety of sensor applications; smart homes, cities, and infrastructures [2].

The most important step towards the predictions that indicate IoE is the successful realizations and deployment of large scale wireless communication networks and systems. Coexistence of many large-scale networks along with the emergence of recent technologies requires a more comprehensive terminology than large-scale wireless networks. In this regard, next generation wireless networks (NGWNs) are considered to be a generic umbrella term for wireless communication systems which are designed to carry high-volume data and provide a very wide range of services with mobility support to a large number of users with the motivation of "being online anywhere, anytime" via several both inter- and intra-networking strategies.

Address for Correspondence:
Serhan Yarkan

E-mail:
syarkan@ticaret.edu.tr

Received: 06.08.2017

Accepted: 24.01.2018

Available online at
http://dergipark.gov.tr/iujeee

DOI: 10.5152/iujeee.2018.1816

NGWNs are based on different forms of connection types; macro cellular and small coverage cellular base stations; and WiFi access points and vehicle-to-everything (V2X) communication platforms. Such diversity leads to heterogeneous structures. It is clear that the true realization of IoE mandates several criteria to be met simultaneously. The prominent criteria are providing high-quality performance under every circumstance for vast variety of services; accommodating increasing number of users seamlessly; achieving low latencies with high-order diversity and so on. Obviously, in order for NGWNs to satisfy those needs, all available resources should be exploited in an optimum way. Electromagnetic spectrum (EMS) is regarded the most important resource among all for wireless communications. In conjunction with the previous discussions, ever-increasing number of users for wireless communications introduces the "spectral crowd and scarcity problem." On the other hand, measurement reports bring out the fact that EMS is underutilized rather than being scarce.

Many of the natural resources are finite and subjected to be exhausted when overused. However, unlike other resources, EMS is theoretically an unlimited and infinite one. But due to wireless propagation characteristics and sizes of the portable devices, only a part of the EMS can be used effectively for NGWNs. From this standpoint, EMS could be considered to be a limited resource in practice. Therefore, NGWNs should utilize the EMS to the greatest extent given the ever-increasing demand observed for wireless communications within the last three decades.

The transmission power is also a very important and a limited resource such as EMS. Battery life of mobile devices manifests one of the aspects of this limitation. The other aspect reveals itself when EMS is accessed by multiple nodes within the same local geographical area, which is known as multi-user interference (MUI). MUI affects negatively all of the elements of wireless systems in various ways. It reduces the performance of receivers, causes the overall capacity of the system to drop, leads to disruptions to the communication link, and so on. One should keep in mind that dominating the communication channel by increasing transmit power seems to be a solution at first glance. However, such a strategy leads to a more severe interference scenario along with a shorter battery life and with a dramatic drop in the overall system capacity. Therefore, when interference is unavoidable, transmit power as a resource should be handled more delicately.

In light of the discussions above, one could conclude that both EMS and the transmission power are fundamental and crucial design concepts for all sorts of wireless communication systems. Therefore, they need to be steadily observed and strictly controlled under certain rules, guidelines, regulations, and standards. It is worth mentioning that EMS should always be considered as the first in comparison with the transmission power at design stages. This stems from the fact that propagation characteristics of electromagnetic waves are dramatically different from each other at different portions of EMS. Hence, in practice, transmission frequencies and their relevant propagation characteristics are taken into account before considering the transmission power requirements of the system to be designed.

Although EMS is a national resource, propagation behavior and standards render EMS as an international resource. This implies that the observation and control tasks are carried out both at national and international level. The rules, guidelines, and standards used in the supervision of EMS are determined by the United States and European countries for historical reasons. The Federal Communications Commission (FCC) in the United States and the International Telecommunication Union (ITU) at the international level stand out in this regard.

Monitoring and Governance of Electromagnetic Spectrum

As a natural but practically limited resource, the most important characteristic of EMS is that it is not used up in contrast to other natural resources such as oil, natural gas, and its derivatives. Because EMS is not only an inexhaustible but also a limited resource in practice, its utilization is crucial. First step of utilization is to manage EMS and the most important component of EMS management is the spectrum monitoring. Spectrum monitoring involves the recording, processing, and evaluation of collected spectrum data. It is important to bear in mind that spectrum data are obtained in traditional domains such as time, frequency, and space as well as in other artificial domains such as code domain driving the code division multiple access technology (CDMA).

In order to better understand why spectrum monitoring is the most important component in the management of the EMS, it is sufficient to check how the EMS is generally classified. Furthermore, scenarios based on this classification provide an extra insight into the importance of spectrum monitoring. The EMS is generally overviewed in three classes: the exclusive, licensed, and unlicensed spectrum. Exclusive bands are specifically allocated to specific purposes, institutions and/or organizations. Examples include bands that are reserved for space and astrophysics research. Licensed bands are those which require special permissions and regulations to carry out transmission. Mobile phone operators provide their services through the use of licensed bands. Unlicensed bands are the bands that everyone can use provided that they abide by various rules and regulations. Industrial, scientific, and medical (ISM) purposes bands fall into the unlicensed bands category. Therefore, the following scenarios are relevant for all spectrum classes.

Scenario I. Identification and supervision of authorized broadcasts of any spectrum class

Scenario II. Identification and supervision of unauthorized broadcasts of any spectrum class

Scenario I involves the collection of usage statistics for the spectrum band of interest; identification of broadcast; evaluation of whether these broadcasts are authorized, license types are appropriate and their validity is approved, depending on whether the band is licensed or unlicensed. The supervision process covers evaluating the competence of the broadcasts with the local, national and/or international regulations and the compliance with the regulations of the band concerned. Scenario II includes the cases where unauthorized broadcasts are of interest.

As can be understood from Scenario I and Scenario II, the efficient use of a highly valuable natural source such as the EMS depends on a very detailed observation of the EMS in temporal, frequency, and spatial domains (and all possible natural and artificial domains such as code) steadily. Spectrum monitoring, therefore:

- Should be the first step to identify, quantify, track, and control the wireless interference present in all domains at local, national, and international scale.
- Provides ways of identifying whether devices used and techniques/algorithms that they employed comply with protocols, rules, regulations, and standards defined by both national and international institutions and organizations
- Helps identify the infrastructural requirements of local and national governments by obtaining coverage data. Combined with wireless interference map, coverage information paves the way for environmentally-friendly communication technologies by preventing further power consumption and not wasting of national wealth via optimizing installation locations and settings of base stations.
- Ensures that local and/or national television/radio broadcasts can be received by everyone seamlessly, without any problems. It reduces the time and increases the effectiveness in resolving emerging problems.
- Guarantees that broadcasts on the licensed bands, in particular, meet local, national and/or internationally applicable standards (spectrum masks, transmission power, etc.) in high resolution.
- Enables to collect and process valuable real-time usage and occupancy statistics. As a result of processing these data:
  - Dynamics of EMS in all domains could be analyzed and understood in a detailed manner via versatile reporting tools.
  - Problems could be identified almost instantaneously via high-resolution statistics. Anomalies which might lead to serious problems in the future could be detected at their early stages.
  - Future plans and predictions could be established accurately by taking into account the evolution of the real-world data. Therefore, waste of such a valuable resource is avoided.

Classification of Monitoring of Electromagnetic Spectrum

Monitoring the EMS has many aspects since the EMS is a multi-dimensional phenomenon as discussed above. Each dimension or domain plays an important role not only in determining both the quality and the quantity of data to be collected but also in estimating the size of the requirements such as equipment, software, and communication infrastructure to be used. However, when importance of the EMS as a national and international resource is considered, it becomes clear that the most general classification will be based on spatial domain, namely the size of the area to be monitored. From this perspective, the classification can be divided into the following subcategories: national; regional; local; outdoors; and in-doors.

Similarly, monitoring in frequency domain can be classified as narrowband; broadband; and wideband. Classification in temporal domain can be categorized as instantaneous; short-term (minute, hour); medium-term (hour, week); and long-term (month, year). In Figure 1, prominent classification classes and their subcategories are presented.

One of the fundamental issues in spectrum monitoring is to store and/or transfer the data collected. Sizes of the data to be collected are generally significant since, as shown in Figure 1, high-resolution spectrum monitoring accommodates multiple domains with high degrees of freedom. In this regard, measurement resolution should also be included into the classifi-

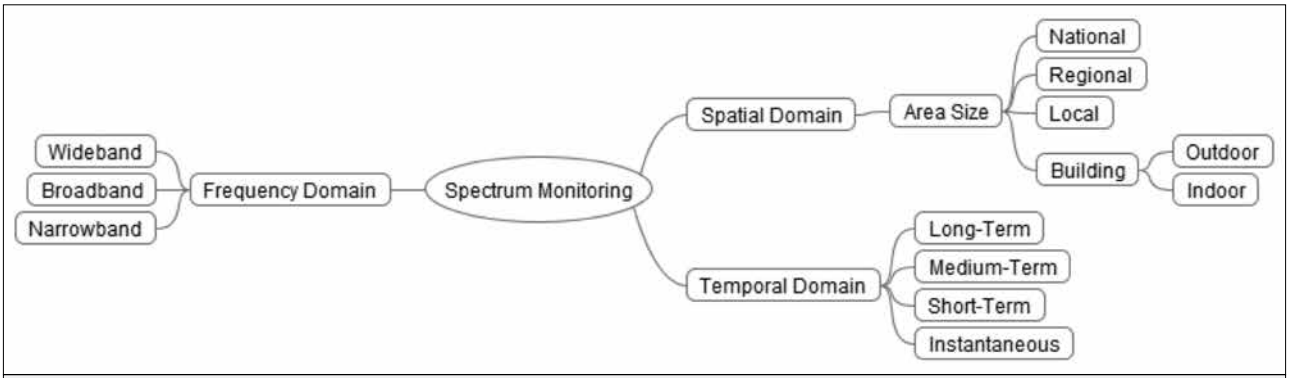

Figure 1. Prominent classification types for spectrum monitoring

cation not maybe as a new domain but as a parameter such that High-resolution sampling (above Nyquist rate); Critical sampling; Low-resolution sampling (below Nyquist rate). There is a direct ratio between the bandwidth used in the frequency domain and the monitoring resolution. Since the number of monitoring data points in the spatial domain will be equal to the number of data sets, the size of the total monitoring data is given as:

$$C \propto N \times B \times T \times S \quad (1)$$

where the total number of monitoring points is equal to , the size of the total monitoring data is given as ; denotes the total bandwidth measured/monitored at one time instant; stands for the monitoring duration, and represents the sampling rate.

Techniques

Detection and locationing of unauthorized broadcasts and/or interference sources are at the forefront of main goals of spectrum monitoring. Sophisticated radio wave propagation characteristics, physical and geographical obstacles between the source and measurement location make it difficult to determine the precise location of the interference source solely by using EMS data. For this reason, the first step in determining the location of the source is to find the direction of the emission. It is worth mentioning that beside its direction, the EMS can be monitored to classify and extract a very large set of features, parameters, and/or identifiers, such as the type of modulation used in emission or any signal received.

There are many direction finding techniques and methods in the literature. In case the direction finding is performed on a single channel, three classes are prominent in the literature: amplitude-based, phase-based, or hybrid forms. The same classes could be considered for multi-channel systems except for infrastructure required by multi-channel systems. Hence, it is sufficient to review single-channel methods for direction finding.

The most frequently encountered methods for single-channel applications are:

- Watson-Watt [3]
- Doppler and pseudo-Doppler [4]
- Correlative vector [5]
- High-resolution direction finding [6,7]
- Maximum likelihood model
- Principal component analysis

There are, of course, some other methods present in the literature, which demonstrate a certain degree of high performance. Algorithms that employ subspace separation of the received signal [8] and the use of linear prediction [9] based approaches are two examples that stand out. Phase-locked loop assisted direction finding methods are also present in the literature [10].

The above-mentioned methods could generally be regarded as deterministic methods since they draw conclusions at the result of following a certain statistical construction. Apart from deterministic methods, there are direction finding algorithms relying on heuristic strategies. There are studies in the literature benefiting from both evolutionary methods [11] and heuristic methods supporting subspace-based algorithms [12] as well.

Monitoring Area

Size of the area to be monitored shows considerable variability in scale due to the propagation behavior (reflection, diffraction, scattering, etc.) of the radio waves and the losses to be experienced within the environment. Especially in large cities demographic structure changes rapidly due to the construction of large buildings (skyscrapers, shopping malls, etc.) and/or the demolishing of existing buildings in a very short period of time. Such changes imply that the usage statistics fluctuates dramatically because of the rapid alteration of the demographic structure. Coverage area and all related transmission parameters will be different as well. Hence, handover rates, traffic loads, and resource allocation mechanisms and many other metrics will be affected. Therefore, reliability of the measurements taken especially in densely populated regions, downtowns, and metropolitan areas should be checked and verified very frequently by validating measurement setup, devices, and parameters. Hidden node issues, out-of-coverage measurement problems, and uncalibrated device recordings are some of the prominent topics that need to be contemplated.

Equipment

With the great advances in digital technology, spectrum monitoring equipment has been reduced in size and become cheaper. Putting the antenna dimension issues aside, monitoring devices equipped with computationally powerful and multi-tasking chips have become available on a considerably larger scale [13, 14]. Furthermore, monitoring hardware is generally software reconfigurable; therefore, it can be customized to serve for any desired purpose. With a few simple plug-ins, the monitoring data can be processed directly onsite and only the results can be transferred to desired locations and/or centers.

The aforementioned equipment will also enable authorities and institutions to take advantage of high altitude platforms, unmanned aerial vehicles, and other remotely controllable equipment. Such diversified options will bring extreme agility and flexibility into operational capabilities of institutions and/or organizations performing the spectrum monitoring tasks [15].

Current Issues in Electromagnetic Spectrum Monitoring

Importance of spectrum monitoring for public safety agencies and first responders is slightly different from that for commercial and governmental agencies since radio communications

for public safety agencies and first responders is a life-critical operation. Any problem, disruption or failure in communications might lead to death and/or serious injuries and/or severe damage. From this point of view, (i) spectrum bands dedicated to public safety agencies and/or organizations should always be available. Furthermore, (ii) these bands should not be occupied by any other parties apart from authorized agencies. Considering the ever-increasing demand and services, one should anticipate that some of the dedicated bands could be densely populated whereas some of them are totally vacant. Therefore, (iii) the spectral load should be distributed uniformly and future plans and predictions could be established accordingly. Spectrum monitoring is the only solution for the issues indicated in (i)-(iii).

This chapter will cover a variety of emerging topics in spectrum monitoring around the globe on both national and international scale. Concepts of reallocating and refarming the spectrum proposed by several countries will be discussed as well.

Refarming the EM Spectrum

Refarming the spectrum is a recent concept which aims to distribute the occupancy statistics of spectrum bands in a uniformly manner. As can be inferred, the driving force behind spectrum refarming is the underutilization of some of the bands. Of course, underutilized spectrum is not the sole motivation. Significant progress has been made in communication and digital signal processing techniques. With the recent advances, many wireless services are provided with less bandwidth but with a higher quality. For example, terrestrial analog television broadcasts have been replaced by digital technology in the United States, and 698-806MHz has been emptied and reopened for further use. Since a similar process will also take place in the rest of the globe soon, new concepts and paradigms such as interference temperature, spectral white holes, spectrum leasing and bidding, and band aggregation will arise. In this regard, legislators and auditors will have to go beyond traditional approaches previously employed in spectrum monitoring for fair usage, security, privacy, and so on. Preparation towards spectrum refarming concept should start with collecting, analyzing, and interpreting space, time, and frequency usage patterns and statistics of EMS. Next, resource planning, licensing, and pricing procedures and processes should be reviewed and revised in the near future especially taking into account the paradigm so-called "flexible licensing" [16].

It is important to emphasize one more time that spectrum refarming aims to ensure that the occupancy in the EMS is homogeneous. This way, white bands could be taken advantage of more efficiently and contribute to wealth and economy. However, maximum utilization comes at the expense of a highly detailed, continuous, and super resolution monitoring, which implies high volume of data storage, process, and transfer infrastructures.

Emerging Technologies and Non-Civilian Usage

Beside the refarming paradigm, emerging technologies, applications, and services which penetrate the market rapidly should be observed as well. One of the prominent examples is the deployment of high-altitude platforms when the coverage area needs to be expanded and/or capacity within certain geographical areas drops below a certain threshold. Similarly, unmanned aerial vehicles and their derivatives with wireless broadcasting capability, both for civil and non-civilian use, are now being used for a variety of purposes [17]. Another instance of recently emerging technologies and mass penetration to market is related to intelligent transport systems (ITS). The European Union has initiated formal studies to ensure that ITS are employed in all European Union countries via embedding appropriate infrastructures into roads and vehicles manufactured after 2018. For instance, 77GHz radars for vehicles already included in ITS for parking and roadblocks.

IoE and many other technologies are among the services and applications that will need to be included into the horizons of spectrum management in the very near future. Spectrum monitoring therefore should be established in such a way that institutions and organizations in charge need to take into account all of the emerging technologies along with their possible extensions.

Disaster Communication

Disasters manifest the importance of spectrum management/monitoring in a very dramatic manner. For instance, when the great Düzce earthquake occurred, cellular base stations in the local region were out and physical infrastructure damaged. There was a long-term communication blackout in the region. This posed several problems. People who were exposed to the disaster were not able to communicate outside the region and vice versa. Furthermore, people who were not in the region attempted to communicate and failed due to the network congestion. Blackout in the region coupled with congestion hampered the coordination, collaboration, and cooperation of public safety agencies and first responders. Unable to react rapidly to the disaster region disrupted the rescue operations and led to loss of many lives.

In order not to experience such tragedies due to communications failures, the spectrum should be continuously monitored in both large and small scale geographical regions. Monitoring data should be examined with the aid of advanced statistical methods such as anomaly detection and machine learning. In case an anomaly or problem is identified, the relevant institutions and/or organizations should be informed instantaneously so that management, command and control can be carried out as efficiently as possible. Monitoring the spectrum on both large and small scale is the key to determining and identifying the physical locations exposed to disasters. Also, spectrum monitoring helps first responders and public safety agencies act in coordination with each other in the most effective way.

Impact on Health

There are scientific studies on the negative effects of electromagnetic radiation on health. Studies report that the operation of cardiac pacemakers is impaired or completely stopped under electromagnetic radiation and serious health problems occurred or triggered [18, 19]. This suggests that monitoring the spectrum is a necessity, especially in the areas where hospitals and healthcare professionals provide healthcare.

Installing base stations within and/or around living spaces in an unauthorized manner can also be examined under this topic. Detection and identification of stations which broadcast with non-standard parameters are also possible with continuous, wide-area, and high-resolution spectrum monitoring activities. This way, the conditions that negatively affect social health could be eliminated.

Environment-friendly Communication

Cellular network service providers have been incorporating more and more base stations in order to meet the requirements of the ever-increasing number of users and maintain the quality of the services provided. The increasing number of base stations naturally implies high volume of energy consumption [20, 21] as well. Surveys reveal that the information and communication technology industry receives 0.5% of total global energy consumption and this share is expected to increase further in the near future. As shown in Figure 2 and Figure 3, communication networks consist not only of base stations but also of users, transmission lines carrying mobile data traffic to the core network, and many other system components operating within the network. It is evident that such a complicated and crowded topologies increase energy consumption and should be taken seriously from green communications perspective.

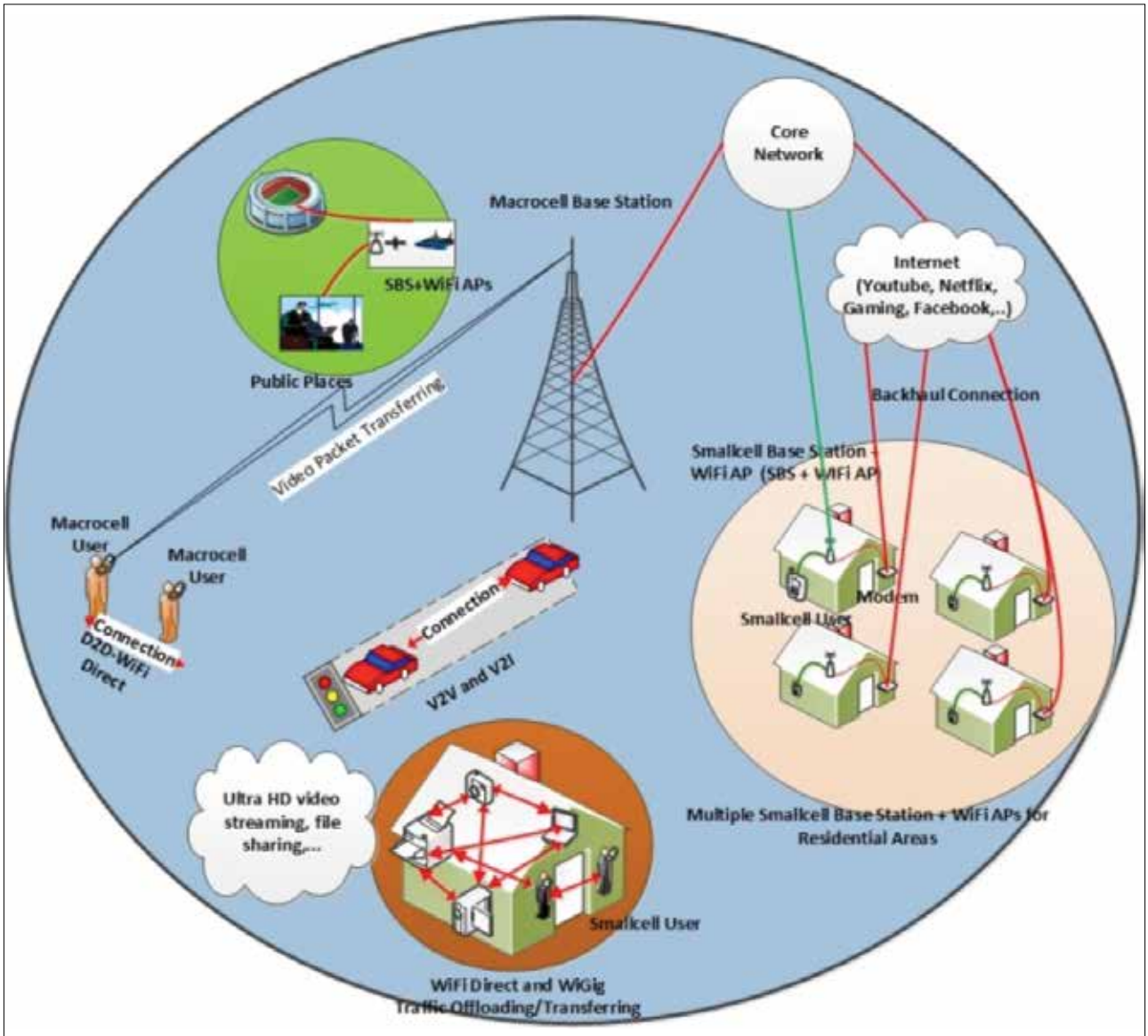

Figure 2. A conceptual framework for heterogeneous next generation wireless networks

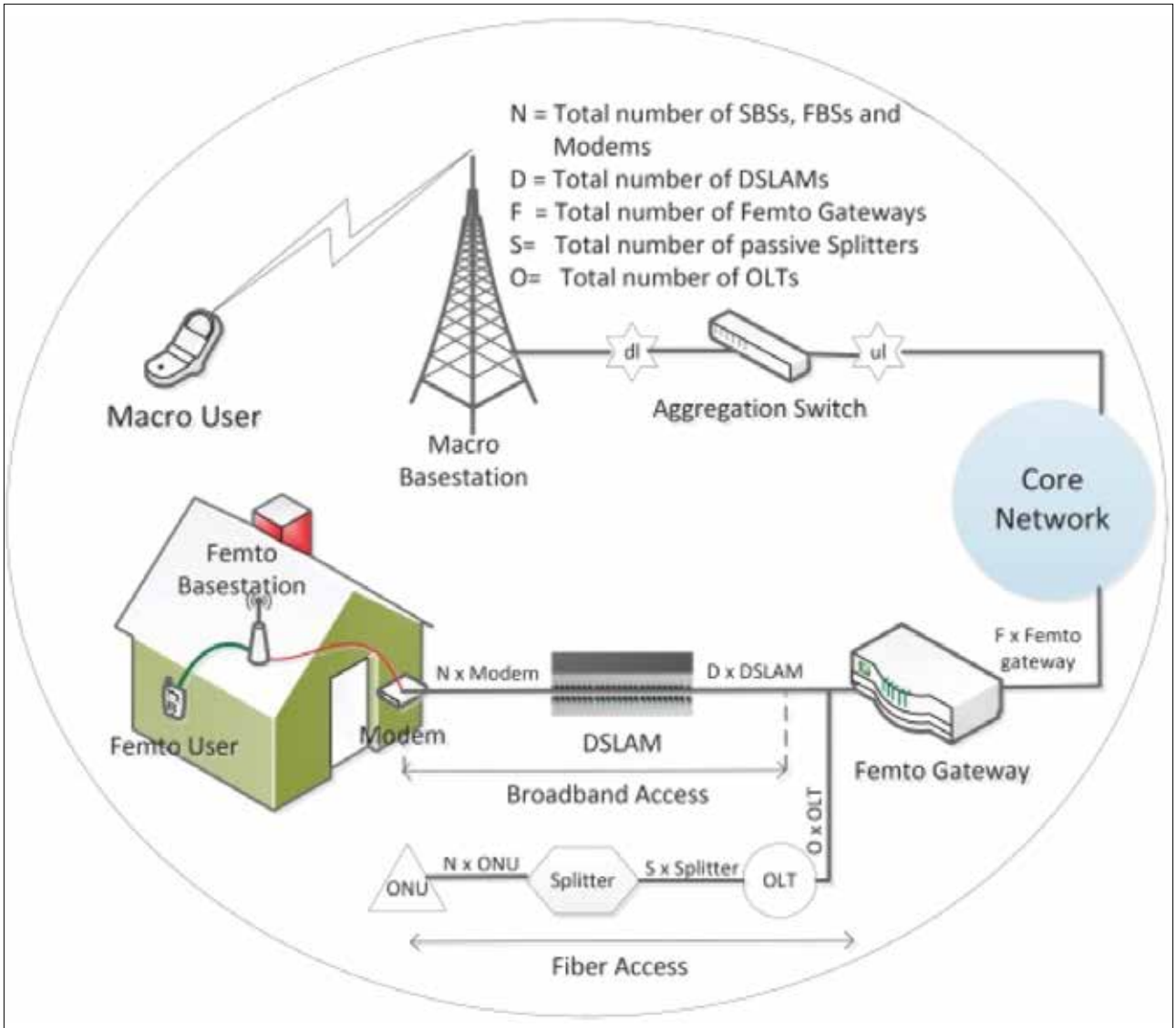

Figure 3. Data transfer and major components in heterogeneous next generation wireless networks

Importance of green communications stems from the fact that oil-based fuels have been at the forefront of the main energy sources. Therefore, carbon emission rates escalate and become an environmental issue affecting the entire globe. Monitoring the spectrum plays a very important role at this point. Studying the high-resolution data obtained by spectral monitoring enables authorities to detect unnecessary stations operating and to find transmitters that employ higher power levels than necessary. Thus, spectrum monitoring directly protects the national wealth and paves the way of realizing more environment-friendly communication systems.

Proposed Spectrum Sensing Strategies for Next Generation Spectrum Monitoring

As discussed above, next generation spectrum monitoring should be comprehensive in terms of both geographical diversity and electromagnetic hyperspace including time, frequency, code, polarization, and so on. This forces one to contemplate a hybrid strategy for future spectrum monitoring infrastructures, services, and applications.

Another important building block for the next generation spectrum monitoring is to deploy a dynamic, adaptive, reconfigurable measurement setup. It is clear that easy-to-deploy campaigns inherently points out mobility. Therefore, it is certain that regulatory bodies should be able to make use of certain technologies such as software-defined radios and/or reconfigurable platforms. Combined with over-the-air update capabilities, such settings could be established once and reused everywhere with their high mobility support. Having said that, one should also consider very cheap, disposable spectrum sensors, which are believed to take their places in the market soon. Note that this idea should be extended in such a

way that all idle, available, no-battery-problem devices could be used to contribute spectrum monitoring efforts as in Search for Extraterrestrial Intelligence (SETI) project.

Such a system should encompass superior modeling, estimating, and predicting capabilities with the historical data at hand along with the contemporary measurements. In conjunction with the adaptation and reconfigurability characteristics, the system needs to take advantage of linear, nonlinear, and heuristic tools depending on the scenario. It is obvious that this enforces the system to have some sort of awareness capability as well, which enables it to choose the appropriate tool.

Decision fusion mechanisms are also integral parts of next generation spectrum monitoring systems. Considering the geographical spread of the possible spectrum sensors, linear, nonlinear, and binary fusion techniques should be employed by such systems too.

Conclusions and Future Directions

The EMS is a never-ending, unlimited, reusable natural resource. Efficient use of the EMS facilitates countries to benefit both economically and technically (non-civilian usage, security intelligence, communication, remote sensing, meteorological observation, etc.) from this source through its commercialization. Countries should monitor, control, and manage the EMS in light of the state-of-the-art techniques, concepts, and paradigms.

The EMS should be monitored in a highly detailed, on a very large-scale, and with high-resolution on each and every possible domain such as space, time, frequency, and code. The monitoring data should be analyzed statistically in such a way that both concurrent and the past observations are exploited to develop accurate planning and smart allocation strategies. Otherwise, the EMS will not be utilized and will become unmanageable rapidly as new technological developments emerge and penetrate the wireless communications ecosystem. Leading countries and multinational organizations in the field of wireless communications technologies have already started experiencing the aforementioned problems. Hence, new concepts and paradigms such as spectrum refarming and flexible licensing are proposed. This implies that countries that follow the leading countries will have a similar roadmap and face almost the same set of issues and problems in the near future.

It should be mentioned that EMS is important from various other perspectives apart from technological and economic aspects. Disaster communications, health, and environment-friendly communications are the most prominent ones. It should be noted that all of the aforementioned topics place serious responsibilities and agendas on the institutions and/or organizations that have the authority to monitor the spectrum.

Finally, one could foresee that next generation spectrum monitoring strategies imply, by definition, massive information flow in various formats and in both structured and unstructured way. Big data and relevant issues inherently take their places. Infrastructure, data processing algorithms and techniques, and effective storage and database designs are important aspects from these perspectives.

Acknowledgments

The work of Serhan Yarkan, in part, was carried out during his PhD study entitled "A Software-Defined Radio Design and Implementation for Next Generation Wireless Networks" at İstanbul University, Institute of Science. Also, this work is supported by İstanbul Commerce University Publishing, Research, and Project Coordination Commission grant YAPKO 2015-02-001.

References

1. W. W. R. Forum, "Visions and research directions for the wireless world," Wireless World Research Forum, Pfingstweidstrasse 102b CH-8005 Zurich, White Paper November 2013, v2.0, November 2013.
2. J. A. Stankovic, "Research directions for the internet of things," *IEEE Internet of Things Journal*, vol. 1, , pp. 3-9, 2014. [CrossRef]
3. A. W. Watt and J. Herd, "An instantaneous direct-reading radiogoniometer," *Electrical Engineers, Journal of the Institution of,* vol. 64, pp. 611-617, 1926.
4. D. Peavey and T. Ogumfunmi, "The single channel interferometer using a pseudo-doppler direction finding system," in Proc. *IEEE International Conference on Acoustics, Speech, and Signal Processing ICASSP-97,* vol. 5, Apr 1997, pp. 4129-4132. [CrossRef]
5. H. W. Wei and Y.-G. Shi, "Performance analysis and comparison of correlative interferometers for direction finding," in Proc. *IEEE 10th International Conference on Signal Processing (ICSP),* 2010, pp. 393-396. [CrossRef]
6. R. O. Schmidt, "Multiple emitter location and signal parameter estimation," I*EEE Transactions on Antennas and Propagation,* vol. 34, pp. 276-280, 1986. [CrossRef]
7. R. Roy and T. Kailath, "Esprit-estimation of signal parameters via rotational invariance techniques," *IEEE Transactions on Acoustics, Speech and Signal Processing,* vol. 37, pp. 984-995, 1989. [CrossRef]
8. H. Hung and M. Kaveh, "Focussing matrices for coherent signal-subspace processing," *IEEE Transactions on Acoustics, Speech and Signal Processing,* vol. 36, pp. 1272-1281, 1988. [CrossRef]
9. I. L. Arteaga, R. Scholte, and H. Nijmeijer, "Improved source reconstruction in Fourier-based near-field acoustic holography applied to small apertures," *Mechanical Systems and Signal Processing,* vol. 32, pp. 359-373, 2012. [CrossRef]
10. N. Harter, J. J. Keaveny, S. Venkatesh, and R. M. Buehrer, "Development of a novel single-channel direction-finding method," in Proc. *IEEE Military Communications Conference, MILCOM* 2005, pp. 2720-2725. [CrossRef]
11. X. Cui, K. Yu, S. Lu, "Evolutionary tdoa-based direction finding methods with 3-d acoustic array," *IEEE Transactions on Instrumentation and Measurement,* vol. 64, pp. 2347-2359, 2015. [CrossRef]
12. E. D. Di Claudio and R. Parisi, "Waves: Weighted average of signal subspaces for robust wideband direction finding," *IEEE Transactions on Signal Processing,* vol. 49, pp. 2179-2191, 2001. [CrossRef]
13. A. Nika, Z. Zhang, X. Zhou, B. Y. Zhao, H. Zheng, "Towards commoditized real-time spectrum monitoring," in Proc. of the 1st ACM Workshop on Hot Topics in Wireless. ACM, 2014, pp. 25-30. [CrossRef]

14. D. Pfammatter, D. Giustiniano, V. Lenders, "A software-defined sensor architecture for large-scale wideband spectrum monitoring," in Proc. of the 14th International Conference on Information Processing in Sensor Networks. ACM, 2015, pp. 71-82. [CrossRef]
15. B. Van Der Bergh, A. Chiumento, and S. Pollin, "Lte in the sky: trading off propagation benefits with interference costs for aerial nodes," IEEE Communications Magazine, vol. 54, no. 5, pp. 44-50, 2016. [CrossRef]
16. EU Commission, "Promoting the shared use of radio spectrum resources in the internal market," EU Commission, Brussel, Belgium, Tech Rep, Sept. 2012.
17. "C-ITS Platform," EU Commission, Brussel, Belgium, Tech Rep, 2016.
18. A. Napp, D. Stunder, M. Maytin, T. Kraus, N. Marx, and S. Driessen, "Are patients with cardiac implants protected against electromagnetic interference in daily life and occupational environment?" *European Heart Journal,* vol. 36, pp. 1798-1804, 2015. [CrossRef]
19. P. M. Mariappan, D. R. Raghavan, S. H. A. Aleem, and A. F. Zobaa, "Effects of electromagnetic interference on the functional usage of medical equipment by 2g/3g/4g cellular phones: A review," Journal of Advanced Research, 2016. [CrossRef]
20. Z. Hasan, H. Boostanimehr, V. K. Bhargava, "Green cellular networks: A survey, some research issues and challenges," *IEEE Communications Surveys & Tutorials,* vol. 13, pp. 524-540, 2011. [CrossRef]
21. J. Xu, L. Duan, R. Zhang, "Cost-aware green cellular networks with energy and communication cooperation," *IEEE Communications Magazine,* vol. 53, pp. 257-263, 2015. [CrossRef]

Ali Boyacı received the B.S. and M.Sc. degrees in computer science from İstanbul University, İstanbul, Turkey, in 2007 and 2010, respectively, and the Ph.D. degree from the Yıldız Technical University, İstanbul, Turkey, in 2015. He worked as a software engineer at Nortel Networks and project leader at Huawei from 2007 to 2012. Currently, he is an Assistant Professor with the Department of Computer Engineering, İstanbul Commerce University, İstanbul. Ali Boyaci's current research interests include computer networks, vehicular networks, operating system, programming languages, software development and embedded systems.

Ali Riza Ekti is from Tarsus, Turkey. He received B.Sc. degree in Electrical and Electronics Engineering from Mersin University, Mersin, Turkey, (September 2002-June 2006), also studied at Universidad Politechnica de Valencia, Valencia, Spain in 2004-2005, received M.Sc. degree in Electrical Engineering from the University of South Florida, Tampa, Florida (August 2008-December 2009) and received Ph.D. degree in Electrical Engineering from Department of Electrical Engineering and Computer Science at Texas A&M University (August 2010-August 2015). He is currently a faculty member at Balıkesir University Electrical and Electronics Engineering Department and also senior researcher at TUBITAK BILGEM. He served as a TPC member for the "LTE/LTE-A, 5G, and Wireless Heterogeneous Networks" track in the IEEE VTC 2016-Spring, "Radio Access Technology, LTE, 5G, and Wireless Heterogeneous Networks" track in the IEEE VTC 2016- Fall, and "Wireless Communications Symposium" track in the IEEE ICC 2016 and ICC 2017. He has been a Technical Reviewer for IEEE conferences and journals. He is an active member of IEEE. His current research interests include statistical signal processing, convex optimization, resource allocation and traffic offloading in wireless communications in 4G and 5G systems and smart grid design and optimization.

Serhan Yarkan received the B.S. and M.Sc. degrees in computer science from İstanbul University, İstanbul, Turkey, in 2001 and 2003, respectively, and the Ph.D. degree from the University of South Florida, Tampa, FL, USA, in 2009. He was a Postdoctoral Research Associate with the Department of Computer and Electrical Engineering, Texas AM University, College Station, TX, USA, from 2010 to 2012. Currently, he is an Associate Professor with the Department of Electrical-Electronics Engineering, İstanbul Commerce University, İstanbul. Serhan Yarkan's current research interests include statistical signal processing, cognitive radio, wireless propagation channel measurement and modeling, cross-layer adaptation and optimisation, and interference management in next generation wireless networks and underground mine channels and disaster communications.

Muhammed Ali Aydın obtained his B.S. degree in computer engineering from İstanbul University in İstanbul, Turkey in 2001. He completed his MSc degree in computer engineering from İstanbul Technical University, İstanbul, Turkey in 2005. He received his Ph.D. degree in computer engineering from İstanbul University, İstanbul, Turkey in 2009. He was a Postdoctoral Research Associate with the Department of RST, Telecom SudParis, Paris, France, from 2010 to 2011. He has been working as an Assistant Professor in İstanbul University Department of Computer Engineering since 2009. He is the Vice Dean of Engineering Faculty and Head of Cyber Security Department since 2016. He received 9 research projects consisting of over Turkey from local industries in Turkey and the İstanbul University Research Foundation. He has authored 18 journal papers, and published and presented 60 papers at international conferences. His research interests include optical networks, network security, information security and cryptography. Specific skills related to the call topic is network security, cyber security, design and analysis trusted software and cyber identity issues, security of both Internet of things and cyber physical systems, and design of intrusion detection systems against cyber-attacks.

İSTANBUL UNIVERSITY PRESS

REVIEW

Electrica 2018; 18(1): 109-120

Review and Performance Comparison of Pansharpening Algorithms for RASAT Images

Sevcan Kahraman, Alp Ertürk

Kocaeli University Laboratory of Image and Signal Processing (KULIS), Kocaeli, Turkey

Cite this article as: S. Kahraman, A. Ertürk. "Review and Performance Comparison of Pansharpening Algorithms for RASAT Images". *Electrica*, vol. 18, no. 1, pp. 109-120, 2018.

ABSTRACT

This study presents the most extensive performance comparison of pansharpening methodologies by considering 17 pansharpening algorithms that are applied to the satellite images obtained from RASAT, which is the first earth observation satellite designed and manufactured in Turkey. Standard and state-of-the-art pansharpening approaches from various categories, such as component substitution (CS), modulation based (MB), multiresolution analysis (MRA), and hybrid and variational methods, are included in order to gain a better insight and perform a thorough analysis of the performance of various pansharpening methods. The experimental validation procedure was designed according to Wald's protocol, and the performance evaluations were conducted both qualitatively and quantitatively on the basis of seven quantitative evaluation criteria.

Keywords: RASAT, pansharpening, performance, review

Introduction

Image fusion is the process of combining relevant information from multitude images, often acquired by different sensors and imaging technologies. The most common approach is the fusion of a high spatial resolution image with a high spectral resolution image. If the high spatial resolution image is a panchromatic image, then the fusion process is called pansharpening.

Pansharpening, in its original form, is the process which combines multispectral (MS) images with high spatial resolution panchromatic (PAN) images in order to construct high spatial resolution MS images. Pansharpening has long been an important field of research because it enables the construction of images with high spatial and high spectral resolution, which is not directly obtainable from imaging sensors due to various technical limitations. Pansharpening was originally applied to PAN an MS images, but have evolved to include fusion of PAN and hyperspectral (HS) images, and MS and HS images, among others. At its basis, pansharpening is the process of extracting spatial information from one image and injecting this information to the other image in order to enhance spatial resolution.

There are various pansharpening reviews in the literature. In [1], the pansharpening performance of four pan-sharpening approaches have been compared and it is stated that context-based decision approach gives the best result. In [2], it has been demonstrated that methods in accordance with the *Amélioration de la Résolution Spatiale par Injection de Structures* (Improving Spatial Resolution by Structure Injection-ARSIS) concept prevent spectral distortion for pansharpened images. In [3], performances of the pansharpening algorithms in commercial software packages have been compared for images acquired from IKONOS, QuickBird, GeoEye-1, and WorldView-2 satellites, and the best fusion quality is reported by principal component analysis (PCA). In [4], eight pansharpening approaches are compared for performance with several spatial and spectral quality indexes, and it has been stated that approaches combining A Tróus wavelet transform with Intensity-Hue-Saturation (IHS) trans-

Address for Correspondence:
Sevcan Kahraman

E-mail:
sevcan.kahraman@kocaeli.edu.tr

Received: 05.06.2017

Accepted: 21.09.2017

DOI: 10.5152/iujeee.2018.1817

form and PCA provide the best spatial–spectral tradeoff. In [5], advanced pansharpening approaches such as Generalized Laplacian Pyramid with Modulation Transfer Function (MTF-matched filter) and Context-Based Decision injection scheme (MTF-GLP-CBD) have been applied to datasets acquired by IKONOS-2 and WorldView-2 satellites, and best pansharpening results are obtained from Gaussian MTF-matched filter with High Pass Modulation injection model (MTF-GLP-HPM) method. In a recent review, eleven different state-of-the-art pansharpening methods are adapted to the HS images, and Bayesian Sparse approach has provided the best performance for hyperspectral pansharpening [6]. In [7], pansharpening approaches in the literature are classified into different categories according to the main technique they use by Amro and et al. In study [8], twenty one pansharpening techniques are presented and evaluated for the VNIR and SWIR bands of Sentinel-2 and MTF-GLP-CBD provides the best consistency pansharpened result.

This paper is concerned with pansharpening performances for RASAT images. RASAT is the first earth observation satellite designed and produced in Turkey by TÜBİTAK-UZAY (TÜBİTAK Space Technologies Research Institute). RASAT has been in operation since 2011, and is the second remote sensing imaging satellite of Turkey after BİLSAT. RASAT provides 7.5 meter spatial resolution PAN and 15 meter spatial resolution RGB images. There are some works on the literature on pansharpening for RASAT images. In [9], nine different pansharpening approaches are evaluated for RASAT images by utilizing six assessment quality metrics, and Hyperspherical Color Space (HCS) and High Pass Filter (HPF) methods are shown to provide the best performances. In [10], GPU speed-up is assessed for pansharpening on RASAT images. In [11], automatic image processing workflow is drawn for RASAT and GÖKTÜRK-2 satellite images. In [12], the performance evaluation of IHS, Brovey and PCA pansharpening methods are evaluated for RASAT and GÖKTÜRK-2 images.

In this paper, a wide range of pansharpening methods, both benchmark and state-of-the-art, are evaluated and compared for performance on RASAT images. The evaluation is performed over several images, both visually and quantitatively, by utilizing a wide array of metrics, i.e. root mean squared error (RMSE), correlation coefficient (CC), spectral angular mapper (SAM), *Erreur Relative Globale Adimensionnelle de Synthese* (ERGAS), peak signal-to-noise ratio (PSNR), structural similarity index (SSIM), and universal image quality index (UIQI). This work's main contribution is the utilization of the largest number of pansharpening approaches and performance metrics used up-to-date in any pansharpening review work in the literature.

The paper is organized as follows. Section 2 summarizes and explains the pansharpening approaches. The experimental results obtained on various RASAT images are provided in Section 3. The paper is concluded in Section 4 with some possible future study lines.

Review of Pansharpening Approaches

The aim of the pansharpening process is the integration of high frequency information, which is extracted from the PAN image, with the lower level spatial information from the MS image in order to obtain high spatial resolution MS image.

Although there is no universal classification, pansharpening approaches can be basically grouped into five categories according to fusion mechanism. These are component substitution (CS), modulation based (MB), multi-resolution analysis (MRA), hybrid methods and variational approaches. These categories and the respective methods in each category that are used in this paper are explained below.

Component Substitution (CS) Methods

CS approach consists of three steps:

1. MS image is upsampled to the resolution of PAN image, and transformed to a new space. This new space aims to separate the spectral and spatial information, which will be kept and changed with the spatial information from the PAN image, respectively.
2. The component of the MS image in the new space that is related or is of similar characteristics with the PAN image is substituted by the high spatial resolution PAN image. In this step, often a histogram matching process is also utilized in an effort to equalization mean and standard deviation for reducing the spectral distortion for both images.
3. The MS image with the substituted PAN image information is transformed back into its original space, resulting in a pan-sharpened image.

CS approach is commonly simplified into the equations below, which basically mean that the PAN image is added to the MS image while the intensity or spatial information derived from the MS image is removed. This addition and removal is multiplied by a coefficient that is determined by the transformation utilized in the process [13].

$$\widehat{MS}_k = \widetilde{MS}_k + g_k(P - I_L) \quad , \quad k = 1, \dots, N \qquad (1)$$

$$I_L = \sum_{k=1}^{N} \omega_k \widetilde{MS}_k \qquad (2)$$

where $\widehat{MS}_k$ denotes the pan-sharpened image, N is the number of bands, $\widetilde{MS}_k$ denotes the MS image upsampled to the resolution of PAN image, P is the PAN image and I_L is the image synthesized from the MS image bands with weight factors, and g_k is a gain factor determined by the utilized transformation in the method [13].

Easy implementation and fast computational time are the major advantages in CS based approaches. In these techniques, if the correlation is very high between PAN and MS images, then the pansharpened MS image has better spatial resolution. The main shortcoming of CS based techniques is the spectral distortion which is also called color or radiometric distortion [14].

IHS is one of the standard pansharpening algorithms in the CS category. Pan-sharpening by IHS involves utilizing the IHS transformation to derive the intensity component of the MS image. This intensity component is substituted by the PAN image that is histogram matched to the intensity component. An inverse IHS transformation is used to obtain the pan-sharpened MS image [15].

PCA based pan-sharpening involves utilizing the PCA transformation on the MS image. The first principal component is assumed to be the component with the most spatial information. The PAN image is histogram matched to the first principal component and substituted prior to inverse PCA transformation [16]. The spatial information from the PAN image substituted to the principal component leads to a pan-sharpened MS image after the inverse PCA transformation.

Gram-Schmidt (GS) based pan-sharpening is another standard pan-sharpening approach with utilizes CS. GS transformation results in vectors which are orthogonal with respect to each other. However, the selection of the initial vector, i.e. image, is crucial, and GS based pan-sharpening has several modes to address this issue. In Mode-1, this initial image is formed by taking the average of the MS bands, whereas in Mode-2 the image is formed by the low-pass filtering of the PAN image and in Mode-3 the minimum least square approach is used [17]. GS based pan-sharpening involves applying GS transformation on the MS image in order to obtain the orthogonal vectors, substituting the histogram matched PAN image in place of the initial vector and using inverse GS process to obtain the pan-sharpened image. GS fusion process can also expressed in the form of equation (1) using the injection gain factor calculated as follows [5]:

$$g_k = \frac{cov(\widetilde{MS}_k, I_L)}{var(I_L)} \quad , \quad k = 1, \dots, N \tag{3}$$

where *cov(.)* emphasize the covariance matrix and *var(.)* denotes the variance value.

In HCS pansharpening approach, MS image is transformed into n-dimensional color space. The squares of the intensity component of the MS image in the color space and the PAN image evaluated. P^2 is then histogram matched to I^2 using the means and standard deviations of P^2 and I^2. The square root of the histogram matched P^2 is used in reverse HCS transformation in order to obtain the pan-sharpened image [18].

The main idea in HPF based pan-sharpening is to extract the high frequency details from the PAN image and then inject these details to the MS bands. In the CS based HPF pansharpening, the high frequency details obtained from the PAN image by high-pass filtering are added to each of the MS bands in order to obtain the pan-sharpened image [19].

Modulation-Based (MB) Methods

In modulation-based pan-sharpening approaches, the ratio of the PAN image and the synthetic PAN image obtained from the MS image is utilized. This normalized term is multiplied by the MS image bands in order to obtain the pan-sharpened image, as seen in the following equation [20]:

$$\widehat{MS}_k = \left(\frac{\widetilde{MS}_k}{Syn}\right) \times P \quad , \quad k = 1, \dots, N \tag{4}$$

where $\widehat{MS}_k$ emphasizes the pan-sharpened image, $\widetilde{MS}_k$ denotes the MS image upsampled to the resolution of PAN image, P denotes the PAN image and the synthetic image (*Syn*) is obtained from the MS bands, often by a weighted summation such as:

$$Syn = \sum_{k=1}^{N} \varphi_k \widetilde{MS}_k \tag{5}$$

where φ_k is a weight factor, determined according to the utilized pansharpening method.

It should be noted that some reviews opt out the use of MB group, and instead include the methods presented here in CS or MRA groups, based on some transformations. If such as classification is preferred, BT and UNB methods may be included in the CS group, whereas SFIM and SSCN methods may be included in the MRA group.

Brovey Transformation (BT) is one of the basic pan-sharpening approaches in the modulation-based category. In BT pan-sharpening, the average of the MS bands is taken as the synthetic PAN image in equation (5). This synthetic image is used to normalize the PAN image, and the resulting term is multiplied by each MS band in order to obtain the pan-sharpened image [21].

Smoothing Filter based Intensity Modulation (SFIM) is a modulation based pansharpening technique which assumes that the radiance ratio between high spatial resolution MS band and original PAN image is equal to the resolution ratio between original MS band and low-pass filtered PAN image. The synthetic image is derived by using a kernel whose size is based on this resolution ratio. The high resolution details, obtained by the normalization of the PAN image with its low-pass synthetic version, is multiplied with the original MS bands in order to create the pansharpened image [22].

University of New Brunswick (UNB) approach utilizes least squares regression between the MS and PAN images in order to find the weight factors. These weights are multiplied by each MS band to obtain the synthetic PAN image. In order to create the pansharpened image, each MS band is multiplied by the ratio between the original PAN and the obtained synthetic PAN image [23]. In this work, Fully Constraint Least Squares (FCLS) algorithm is utilized for the regression analysis.

Spectral Simulation Color Normalization (SSCN) based pansharpening utilizes the concept of sensor spectral response functions (SRF). By using the FCLS regression analysis, the

weights to approximate the PAN SRF from the MS SRFs are calculated, and then the simulated PAN image is obtained by using these weights. Each MS band is then multiplied by the ratio between the PAN image and the simulated PAN image which is histogram matched with PAN, in order to obtain the pan-sharpened image [24].

Multi-Resolution Analysis (MRA)

In order to overcome the spectral distortion shortcoming of the CS approach, MRA methods have been developed. In MRA methods, MS and PAN images are first decomposed into frequency bands. Then, the details coming from high frequency component of the PAN image are injected into the frequency bands of the MS image which have been interpolated to the PAN resolution. In this way, MRA based approaches preserve spectral information better than CS methods. MRA approach is obtained as follows [5]:

$$\widehat{MS}_k = \widetilde{MS}_k + G_k \otimes (P - P_L) \quad , \quad k = 1, \dots, N \tag{6}$$

where $\widehat{MS}_k$ means the pan-sharpened image, $\widetilde{MS}_k$ denotes the MS image upsampled to the resolution of PAN image, $\otimes$ denotes element-wise multiplication, *P* is the PAN image and P_L denotes that low pass version of the PAN image *P*.

The most popular MRA approaches are the wavelet transformation and Laplacian pyramids based approaches. Both of those groups can be represented in a pyramidal scheme as in [2], and are often commonly termed as the ARSIS concept. ARSIS concept is motivated by obtaining the missing spatial information of the MS image from the high frequencies of PAN image between level-0 and level-1 on the pyramid.

MRA based pansharpening techniques have the advantages of temporal cohorence, spectral consistency and robustness to aliasing, whereas the complexity and higher computation time with respect to CS methods can be counted as the disadvantages of MRA [25].

Wavelet Transformation (WT) is the name of a family of methods used to decompose an image into its frequency components based on the utilized basis function. This decomposition is commonly conducted into four components, the first of which is the approximation component, the second and third components are the horizontal and vertical details and the fourth includes the frequency components that are both horizontal and vertical.

Wavelet Transformation based pan-sharpening starts with the histogram matching of the PAN image with each of the MS bands. For each MS band, WT is applied to the histogram matched PAN image, and the second, third and fourth components are set to zero, resulting in only the approximation component remaining. Inverse WT is applied to this component, and the result is subtracted from the original PAN image in order to obtain the high frequency details. These details are added to the respective MS bands, and the pan-sharpened image is obtained [26].

In the literature, instead of the regular discrete WT, stationary WT, more commonly named as A Tróus WT (ATWT) is preferred because of the enhanced pansharpening performance it provides. In this work, for ATWT, the following cubic-spline kernel developed by Starck and Murtagh is utilized [27].

$$h = \frac{1}{256}\begin{bmatrix} 1 & 4 & 6 & 4 & 1 \\ 4 & 16 & 24 & 16 & 4 \\ 6 & 24 & 36 & 24 & 6 \\ 4 & 16 & 24 & 16 & 4 \\ 1 & 4 & 6 & 4 & 1 \end{bmatrix} \tag{7}$$

Laplacian Pyramids (LP), which was first introduced by Burt and Adelson, is derived from Gaussian Pyramid (GP) which utilizes low-pass filter recursively by using reduction and decimation [28]. In GP, the first level is taken as original image, and each upper level image is obtained by low pass filtered lower level image, sequentially. In LP, each level includes a detail image which is obtained by the subtraction of the interpolated lower level image from the same level image. Hence, while GP can be considered as a set of images which constitutes the low-pass filtered versions of an original image, LP can be seen as a set of image details obtained as the difference between the lower level images and their band-pass filtered versions. LP based pansharpening is motivated by extracting high spatial details from the PAN image by the use of LPs, and adding these details to the MS bands.

Enhanced Laplacian Pyramid (ELP) is an MRA technique in which the successive levels of the pyramid should have the lower correlation and zeroth level entropy properties [29]. In ELP, unlike in LP, it is possible to construct different types of kernels for the expansion and reduction operations. Generalized Laplacian Pyramid (GLP) is generalized from ELP by enabling the use fractional numbers as scale ratios. GLP approach is reported to be more advantageous than A Tróus Wavelet transform [30]. In the literature, GLP has also been recently adopted as the name of all LP based pan-sharpening approaches.

Taking into consideration the frequency response functions of different kernels, 23tap filter is suggested in the literature for constructing the LP, i.e. for the expansion of the lower level images, for the higher performances it provides [31], and is also adopted in this work.

Modulation transfer function (MTF) is the amplitude spectrum of the system point spread function. MTFs of the imaging system are different from each other for both MS and PAN images. Generalized Laplacian Pyramid with MTF-matched filter (MTF-GLP) is another MRA based technique. In MTF-GLP pan-sharpening approach, MTFs of the imaging sensor are exploited to design the GLP reduction filter. After the PAN image is reduced by using the MTF filter, interpolation is performed on the histogram matched PAN image by utilizing a 23-tap kernel. Then, the detail image is calculated by subtracting the obtained low resolution PAN image from the original PAN image. Finally, these details are added into the original MS bands to obtain the pan-sharpened image [32].

MTF-GLP-HPM pan-sharpening approach follows the steps of MTF-GLP pan-sharpening, but in the last step high pass modulation injection method is employed in order to obtain the pan-sharpened image [33].

Hybrid Methods

Hybrid pansharpening approaches are a cross between the different pansharpening approach groups and do not belong to a single one. Among such methods, Ehlers fusion, guided filter PCA (GFPCA), and IHS based wavelet transform may be counted among others [34]. In this work, Ehlers fusion is included as a hybrid pansharpening method. Ehlers fusion uses IHS transformation and filtering in the Fourier domain. For the first step, MS bands are transformed to IHS domain. The intensity component and the PAN image is transformed into Fourier domain for filtering. After the low-pass filtering of the intensity component and the high pass filtering of the PAN image, inverse Fourier transform is applied to the filter outputs. Filtered PAN image is added to the filtered intensity component in the IHS domain and inverse IHS transformation is applied in order to obtain the pansharpened image [35].

Variational Approaches

P+XS is a variational pansharpening technique which aims to minimize an energy function by using the Gradient Descent algorithm. The energy function utilized in P+XS is motivated by the assumption that the geometry of the spectral bands are contained in the topographic map of the PAN image and the relationship between the MS bands and the PAN image. P+XS also assumes a low-pass filtering and subsampling approximation relationship between the MS bands and the PAN image in order to construct the energy function [36]. The energy function involves three terms to enforce and utilize these assumptions and is optimized by gradient descent in order to obtain the pan-sharpened image. The derivation of the energy function and its terms are explained in detail in [36].

Experimental Results

Datasets

The datasets used in this study are captured by RASAT remote sensing satellite from different regions of Turkey. The datasets are downloaded from the GEZGİN geoportal, and subsets of the downloaded images are used for computational purposes. MS images are taken as 150×150 pixels, and have three bands, whereas the PAN images have 300×300 pixels coinciding with the same region as in the MS images. The pixel size difference is caused by the resolution ratio as the spatial resolution of the MS images are 15m, whereas the spatial resolution of the PAN images are 7.5m.

Experimental results are provided in this work for three pairs of datasets. The datasets were carefully selected based on the properties of their captured scenes. The first image pair are captured on 15.06.2015 from Mersin region, and contain extensive farm fields, which results in homogeneous patches and unpronounced edges. The second image pair are captured on 12.01.2014 from İstanbul region, and comprise of high spatial frequency containing urban areas, and coast-to-land transitions. The third image pair are captured on 31.08.2015 from Sin- region, and contain roads, land-cover and sea surfaces. The color and grayscale visuals for the MS and PAN images, respectively, are provided below in Figure 1-3.

Wald's protocol

In order to evaluate the performance of pan-sharpening methods quantitatively, a reference image is required to compare with the resulting pan-sharpened images. To overcome this shortcoming, various approaches have been proposed in the literature for performance comparison purposes. The most widely accepted and utilized of these approaches is the Wald's protocol [37]. In Wald's

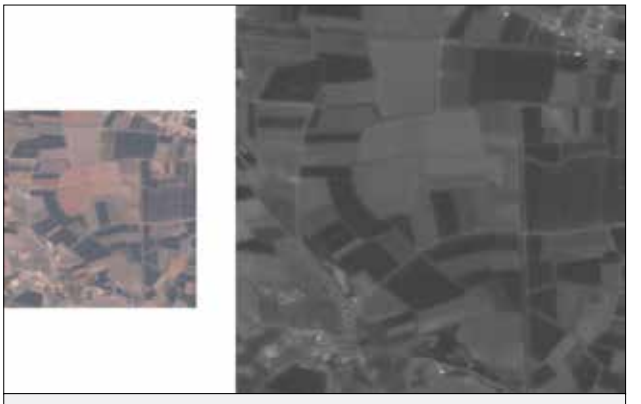

Figure 1. RGB and PAN images for the Mersin dataset

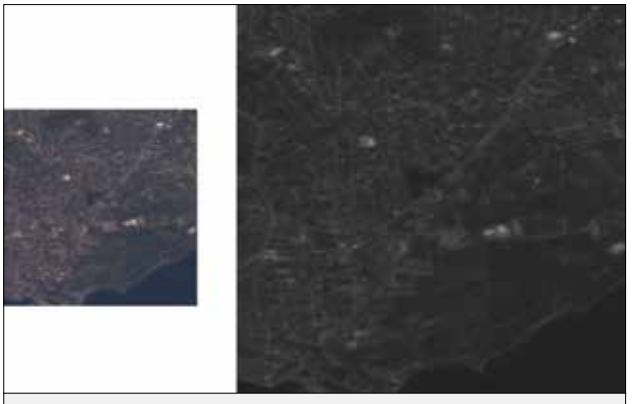

Figure 2. RGB and PAN images for the İstanbul dataset

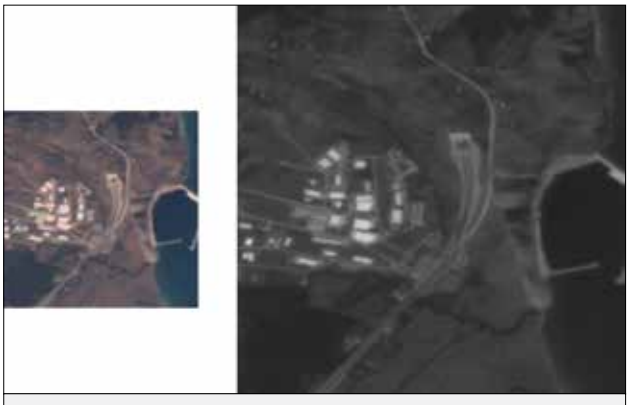

Figure 3. RGB and PAN images for the Sinop dataset

protocol, which is also adopted in this work, the spatial resolution of the MS and PAN images are first reduced, and pan-sharpening methods are applied on these reduced resolution images. The resulting pan-sharpened image is compared with the original MS image to evaluate the pan-sharpening performance.

Results and Discussion

Experimental results obtained in accordance with Wald's protocol are provided in this section. Three datasets have been utilized and the results are provided both visually and quantitatively. For the quantitative results, the performance metrics of RMSE, CC, SAM, ERGAS, PSNR SSIM and UIQI are used. The quantitative results for the three datasets with seven quality assessment metrics and using seventeen pan-sharpening methods are provided in Table 1-3, for the Mersin, İstanbul and Sinop datasets, respectively. The visual results are provided in Figure 4-6, for the Mersin, İstanbul and Sinop datasets, respectively.

It can be observed from the Tables that the state-of-the-art MTF-GLP-HPM method provides the best results overall, followed closely by MTF-GLP, which is in turn followed by ATWT. This is to be expected as utilizing sensor MTFs in the pan-sharpening process enables to obtain better performances than classical approaches [31]. Because of this, whereas ATWT outperforms the basic form of GLP, the inclusion of MTFs to GLP results is significantly better performances.

As can be seen from Figure 4-6, the visual results are also in accord with the quantitative evaluations in that the MTF-GLP-HPM provides the sharpest pan-sharpened images without any color distortion, followed closely in performance with MTF-GLP, ATWT and SFIM. Among the more classical approaches in the CS and MB categories which do not utilize sensor specifications, often blur effects or slight color distortions can be observed in the pan-sharpened visuals. The spatial degradation, i.e. the blurry appearance, is easier to observe on the farm borders in Figure 4, sea-coast border and the small structures in Figure 5, and the main road and the buildings in Figure 6. This afore mentioned effect is more prevalent in the visual outputs of Ehlers, GLP (without the utilization of MTFs), and GS2 methods.

An important point to note is that all methods performed better in Mersin image than in Sinop image. This is also expected, as the high number of high frequency components in the Sinop image makes it a more challenging dataset with respect to Mersin image.

Table 1. Quantitative pan-sharpening results for Mersin dataset

	RMSE	CC	SAM	ERGAS	PSNR	SSIM	UIQI
IHS	4.10	0.98	<0.01	1.51	35.0	0.97	0.97
PCA	4.07	0.98	<0.01	1.50	35.2	0.98	0.97
GS1	4.06	0.98	<0.01	1.50	35.1	0.97	0.97
GS2	4.76	0.97	<0.01	1.76	33.8	0.97	0.96
GS3	4.07	0.98	<0.01	1.50	35.1	0.97	0.97
HCS	4.08	0.98	<0.01	1.51	35.1	0.97	0.97
HPF	4.60	0.97	<0.01	1.70	34.0	0.97	0.96
BT	3.86	0.98	<0.01	1.43	35.5	0.98	0.98
SFIM	3.62	0.98	<0.01	1.33	36.4	0.98	0.98
UNB	4.02	0.98	<0.01	1.49	35.1	0.97	0.97
SSCN	4.13	0.98	<0.01	1.53	34.9	0.97	0.97
ATWT	3.24	**0.99**	<0.01	1.20	37.1	**0.99**	0.98
GLP	4.28	0.98	<0.01	1.58	34.8	0.97	0.97
MTF-GLP	2.73	**0.99**	<0.01	**1.01**	38.4	**0.99**	**0.99**
MTF-GLP-HPM	**2.71**	**0.99**	<0.01	**1.01**	**38.5**	**0.99**	**0.99**
Ehlers	4.91	0.97	<0.01	1.81	33.6	0.96	0.96
PXS	3.59	0.98	<0.01	1.33	36.2	0.98	0.98

RMSE: root mean squared error; CC: correlation coefficient; SAM: spectral angular mapper; ERGAS: Erreur Relative Globale Adimensionnelle de Synthese; PSNR: peak signal-to-noise ratio; SSIM: structural similarity index; UIQI: universal image quality index

Table 2. Quantitative pan-sharpening results for İstanbul dataset

	RMSE	CC	SAM	ERGAS	PSNR	SSIM	UIQI
IHS	4.10	0.96	<0.02	2.77	34.5	0.95	0.93
PCA	4.06	0.96	<0.02	2.74	34.5	0.95	0.93
GS1	4.08	0.96	<0.02	2.75	34.5	0.95	0.93
GS2	4.57	0.95	<0.02	3.08	33.5	0.93	0.91
GS3	4.07	0.96	<0.02	2.75	34.5	0.95	0.93
HCS	4.21	0.96	<0.02	2.84	34.3	0.95	0.93
HPF	4.31	0.95	<0.02	2.91	34.1	0.95	0.93
BT	3.89	0.96	<0.02	2.62	34.9	0.96	0.95
SFIM	3.69	0.97	<0.02	2.50	35.6	0.96	0.95
UNB	4.07	0.96	<0.02	2.74	34.5	0.95	0.93
SSCN	4.12	0.96	<0.02	2.77	34.4	0.95	0.93
ATWT	3.41	0.97	<0.02	2.30	36.1	**0.97**	**0.96**
GLP	4.48	0.95	<0.02	3.02	33.7	0.94	0.92
MTF-GLP	3.12	0.97	<0.01	2.10	**36.8**	**0.97**	**0.96**
MTF-GLP-HPM	**3.10**	**0.98**	<0.01	**2.08**	**36.8**	**0.97**	**0.96**
Ehlers	5.02	0.94	<0.02	3.39	32.7	0.92	0.90
PXS	3.74	0.96	<0.02	2.52	35.3	0.96	0.95

RMSE: root mean squared error; CC: correlation coefficient; SAM: spectral angular mapper; ERGAS: Erreur Relative Globale Adimensionnelle de Synthese; PSNR: peak signal-to-noise ratio; SSIM: structural similarity index; UIQI: universal image quality index

Table 3. Quantitative pan-sharpening results for Sinop dataset

	RMSE	CC	SAM	ERGAS	PSNR	SSIM	UIQI
IHS	5.92	0.98	<0.01	3.18	32.4	0.97	0.97
PCA	6.13	0.98	<0.02	3.29	32.2	0.97	0.97
GS1	5.97	0.98	<0.01	3.20	32.4	0.97	0.97
GS2	6.14	0.98	<0.01	3.29	32.1	0.97	0.97
GS3	6.22	0.98	<0.02	3.33	32.1	0.97	0.97
HCS	7.05	0.98	<0.01	3.77	30.8	0.96	0.95
HPF	5.27	0.98	<0.01	2.82	33.5	0.98	0.98
BT	5.67	0.98	<0.01	3.04	32.8	0.98	0.98
SFIM	4.56	0.99	<0.01	2.44	34.9	0.99	0.98
UNB	5.81	0.98	<0.01	3.11	32.5	0.97	0.97
SSCN	6.51	0.97	<0.01	3.48	31.5	0.97	0.96
ATWT	4.37	**0.99**	<0.01	2.34	35.3	**0.99**	**0.99**
GLP	6.09	0.98	<0.01	3.26	32.2	0.97	0.97
MTF-GLP	3.98	**0.99**	<0.01	2.14	36.0	**0.99**	**0.99**
MTF-GLP-HPM	**3.91**	**0.99**	<0.01	**2.10**	**36.2**	**0.99**	**0.99**
Ehlers	6.77	0.97	<0.01	3.63	31.3	0.96	0.96
PXS	5.02	0.98	<0.01	2.69	33.9	0.98	0.98

RMSE: root mean squared error; CC: correlation coefficient; SAM: spectral angular mapper; ERGAS: Erreur Relative Globale Adimensionnelle de Synthese; PSNR: peak signal-to-noise ratio; SSIM: structural similarity index; UIQI: universal image quality index

Figure 4. Pan-sharpening visual results for Mersin dataset

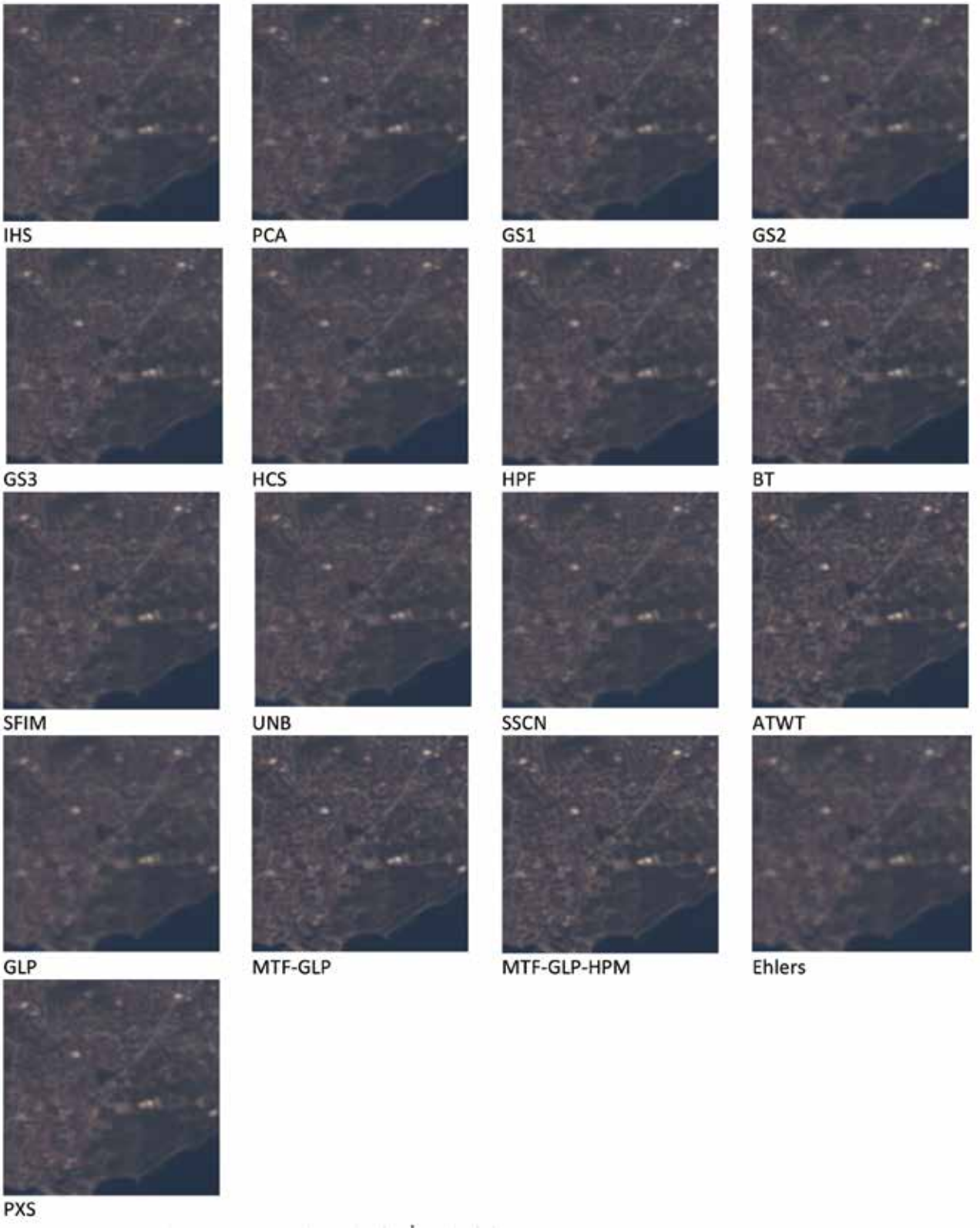

Figure 5. Pan-sharpening visual results for İstanbul dataset

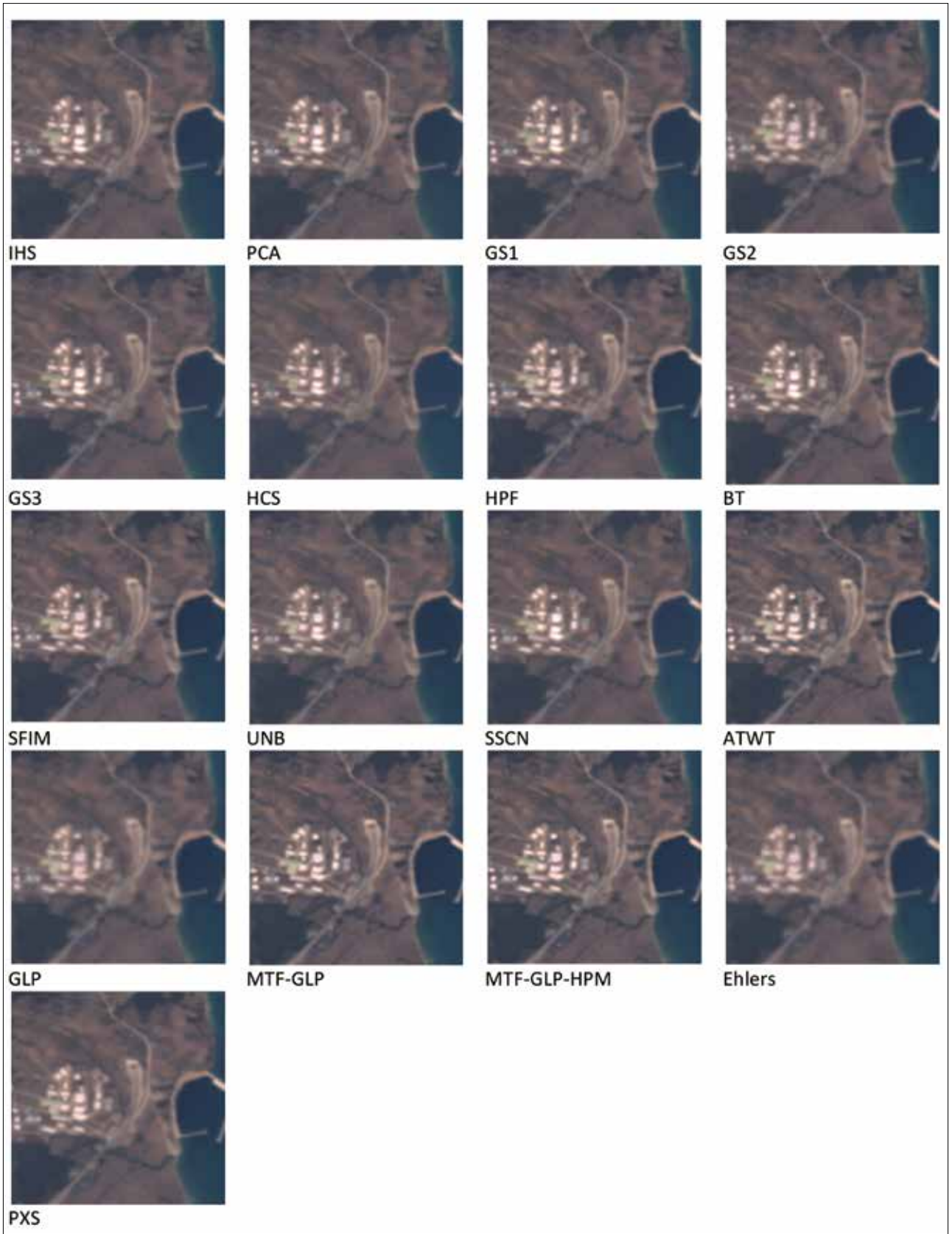

Figure 6. Pan-sharpening visual results for Sinop dataset

In [7], it is mentioned that HPF and HCS approaches give the best pansharpening performance results among the other utilized methods in [7], which is also in accordance with the results of this work. In [10], it is stated that PCA provides the best performance quantitatively, but BT provides the best visual result for RASAT satellite images. However, in our experiments BT showed better performance with respect to IHS and PCA approaches both qualitatively and quantitatively. In [5], state-of-the-art pansharpening approaches were studied and applied to IKONOS-2 and WorldView-2 satellites, and the MTF-GLP-HPM approach provided the best performance, as it also did in this study.

Conclusions

The aim of this paper was to provide the most comprehensive review and performance comparison of pansharpening methods for RASAT images up-to-date. The experimental validation procedure followed Wald's protocol in accordance with current literature. Experimental results were provided for three datasets of different properties due to their scenes.

It was determined through both qualitative and quantitative analysis that MTF-GLP-HPM provides the best performance overall among all groups of pan-sharpening approach, whether CS, MB, MRA, hybrid or variational. This points out that utilizing the MTFs of the sensor provides a significant boost in the pan-sharpening performance.

It was also observed that overall, the MRA based pansharpening methods provide enhanced performance with respect to CS or MB based methods. Whereas there was no clear best performing method in the CS group, SFIM outperformed the other methods in the MB group. The variational P+XS method is seen to be competing with SFIM in terms of performance, whereas the hybrid Ehlers method is outperformed by many of the utilized methods.

Future studies may include a similar review of pan-sharpening methods' performance for GÖKTÜRK-2 images, which also contain the near infrared spectral band, or adapting the various methodologies for the fusion of different sensor images, such as hyperspectral – multispectral fusion.

Acknowledgments

This work is supported by TÜBİTAK under project no 115E883. The authors would like to thank TÜBİTAK Uzay for making the RASAT images publicly available, and for providing the SRFs and MTFs for the RASAT sensor.

References

1. A. Garzelli, F. Nencini, L. Alparone, B. Aiazzi, and S. Baronti, "Pan-sharpening of multispectral images: a critical review and comparison," *IGARSS IEEE International Geoscience and Remote Sensing Symposium,* vol.1, pp.81-84, 2004. [CrossRef]
2. C. Thomas, T. Ranchin, L Wald and J. Chanussot, "Synthesis of multispectral images to high spatial resolution: A critical review of fusion methods based on bemote sensing physics," *IEEE Transactions on Geoscience and Remote Sensing,* vol. 46, pp. 1301 - 1312, 2008. [CrossRef]
3. Y. Zhang and. R. K. Mishra, "A review and comparison of commercially available pan-sharpening techniques for high resolution satellite image fusion," *IEEE International Geoscience and Remote Sensing Symposium,* pp. 182-185, 2012.
4. J. Marcello, A. Medina F. Eugenio, "Evaluation of spatial and spectral effectiveness of pixel-level fusion techniques," *IEEE Geoscience and Remote Sensing Letters*, vol. 10, no. 3, pp. 432–436, 2013. [CrossRef]
5. G. Vivone, L. Alparone, J. Chanussot, M. D. Mura, A. Garzelli, L. G. A. Licciardi, R. Restaino, L. Wald, "A critical comparison among pansharpening algorithms," *IEEE Transactions on Geoscience and Remote Sensing,* vol. 53, no.5, pp. 2565-2586, 2015. [CrossRef]
6. L. Loncan, L. B. de Almeida, J. M. Bioucas-Dias, X. Briottet, J. Chanussot, N. Dobigeon, S. Fabre, L. W. Liao, G. A. Licciardi, M. Simoes, T. J.Y. Tourneret, M. A. Veganzones, G. Vivone, Q. Wei and N. Yokoya, "Hyperspectral pansharpening: A review," *IEEE Geoscience and Remote Sensing Magazine,* vol. 3, no. 3, pp. 27-46, 2015. [CrossRef]
7. I. Amro, J. Mateos, M. Vega, R. Molina, A. K. Katsaggelos, "A survey of classical methods and new trends in pansharpening of multispectral images," *Journal on Advances in Signal Processing EURASIP*, vol. 79, 2011.
8. A. D. Vaiopoulos, K. Karantzalos, "Pansharpening on the narrow VNIR and SWIR spectral bands of Sentinel-2", *The International Archives of the Photogrammetry, Remote Sensing and Spatial Information Sciences, XLI-B7, XXIII ISPRS Congress*, 2016. [CrossRef]
9. M. Teke, M. S. Seyfioğlu, A. Ağçal, S. Z. Gürbüz, "RASAT Uydu görüntülerinin optimal pankeskinleştirilmesi", *IEEE 22. Sinyal İşleme ve İletişim Uygulamaları Kurultayı (SIU)*, pp. 1967-1970, 2014.
10. İ. S. Açıkgöz, S., T. M. Teke, K. U. Kutbay, F. Hardalaç, "Performance evaluation of pansharpening methods on GPU for RASAT images", *7th International Conference on Recent Advances in Space Technologies* (RAST), pp. 283-288, 2015.
11. M. Teke, "Satellite image processing workflow for RASAT and Göktürk-2," *Journal of Aeronautics and Space Technologies,* vol. 9 no. 1 pp. 1-13, 2016.
12. M. Özendi, H. Topan, A. Cam and Ç. Bayık, "RASAT ve GÖKTÜRK-2 görüntülerinin pankeskinleştirilmiş görüntü üretimi ve kalite değerlendirilmesi," *6. Uzaktan Algılama-CBS Sempozyumu* (UZAL-CBS 2016), pp. 447-453, 2016.
13. W. Dou, Y. Chen, X. Li, D. Z. Sui, "A general framework for component substitution image fusion: An implementation using the fast image fusion method", *Computational Geoscience*, vol. 33 no.2, pp. 219–228, 2007. [CrossRef]
14. B. Aiazzi, S. Baronti, M. Selva, "Improving Component Substitution Pansharpening through multivariate regression of MS+Pan data," *IEEE Transactions on Geoscience and Remote Sensing*, vol. 45, no. 10, pp. 3230-3239, 2007. [CrossRef]
15. T. M. Tu, S. C. Su, S. H. C. Shyu, P. S. Huang, "A new look at IHS-like image fusion methods," *Information Fusion,* vol. 2, no. 3, pp. 177-186, 2001. [CrossRef]
16. P. S. Chavez, Jr. S. C. Sides, J. A. Anderson, "Comparison of three different methods to merge multiresolution and multispectral data: Landsat TM and SPOT panchromatic," *Photogramm. Eng. Remote Sens.*, vol. 57, no. 3, pp. 295–303, 1991.

17. C. A. Laben and B. V. Brower, "Process for enhancing the spatial resolution of multispectral imagery using pan-sharpening," *U.S. Patent* 6 011 875, 2000.
18. C. Padwick, M. Deskevich, F. Pacifici, S. Smallwood, "WorldView-2 pan-sharpening", *ASPRS Annual Conference,* 2010.
19. G. U. G. Gangkofner, P. S. Pradhan, D. W. Holcomb, "Optimizing the high-pass filter addition technique for image fusion," *Photogramm. Eng. Remote Sens.*, vol. 74, no. 9, pp.1107-1118, 2008. [CrossRef]
20. Y. Junghui, Z. Jixian, L. Haitao, S. Yushan, P. Pengxian, "Pixel level fusion methods for remote sensing images: A current review", *ISPRS TC VII Symposium*, vol. 38, pp. 680-686, Vienna, Austria, 2010.
21. A. R. Gillespie, A. B. Kahle, R. E. Walker, "Color enhancement of highly correlated images—II. Channel ratio and "chromaticity" transform techniques," *Remote Sensing Env.,* vol. 22, no. 3, pp. 343-365, 1987. [CrossRef]
22. J. G. Liu, "Smoothing filter-based intensity modulation: A spectral preserve image fusion technique for improving spatial details," *International Journal of Remote Sensing*, vol. 21, no.18, pp. 3461–3472, 2000. [CrossRef]
23. Y. Zhang, "A new merging method and its spectral and spatial effects," *International Journal of Remote Sensing,* vol. 20, no. 10, pp. 2003–2014, 1999. [CrossRef]
24. N. Yokoya, N. Mayumi, A. Iwasaki, "Cross-calibration for data fusion of EO-1 / Hyperion and Terra / ASTER," *IEEE Journal of Selected Topics in Applied Earth Observations and Remote Sensing,* vol. 6, no. 2, pp. 419-426, 2013. [CrossRef]
25. S. Baronti, B. Aiazzi, M. Selva, A. Garzelli, L. Alparone, "A theoretical analysis of the effects of aliasing and misregistration on pansharpened imagery," *IEEE Journal of Selected Topics in Signal Processing,* vol. 5, no. 3, pp. 446-453, 2011. [CrossRef]
26. F. Murtagh, S. J.L. Starck, A. Bijaoui, "Image restoration with noise suppression using a multiresolution support," *Astronomy and Astrophysics supplement series*, vol. 112, pp.179-189, 1995.
27. J. Nunez, X. Otazu, O. Fors, A. Prades, V. Pala, R. Arbiol, "Multiresolution-based image fusion with additive wavelet decomposition," *IEEE Transactions on Geoscience and Remote Sensing,* vol. 37, no. 3, pp. 1204-1211, 1999. [CrossRef]
28. P. Burt and E. Adelson, "The Laplacian Pyramid as compact image code," *IEEE Transactions on Communications*, vol. 31, no. 4, pp. 532 - 540, 1983. [CrossRef]
29. S. Baronti, A. Casini, F. Lotti, L. Alparone, "Context-driven differential encoding of an enhanced image pyramid," *Signal Processing Image Communication*, vol. 6, pp. 463-469, 1994. [CrossRef]
30. B. Aiazzi, S. Baronti, L. Alparone, A. Garzelli, M. Selva, "Advantages of Laplacian pyramids over "à trous" wavelet transforms for pansharpening of multispectral images," *Proceedings of SPIE-The International Society for Optical Engineering,* 2012. [CrossRef]
31. B. Aiazzi, A. L. Alparone, S. Baronti, A. Garzelli, "Context-driven fusion of high spatial and spectral resolution images based on oversampled multiresolution analysis," *IEEE Transactions on Geoscience and Remote Sensing*, vol. 40, no. 10, pp. 2300-2312, 2002. [CrossRef]
32. B. Aiazzi, L. Alparone, S. Baronti, A. Garzelli, M. Selva, "MTF-tailored multiscale fusion of high resolution MS and Pan imagery," *Photogramm. Eng. Remote Sens.,* vol. 72, no. 5, pp. 591–596, 2006. [CrossRef]
33. J. Lee and C. Lee, "Fast and efficient panchromatic sharpening," *IEEE Trans. Geosci. Remote Sens*., vol. 48, no. 1, pp. 155–163, Jan. 2010. [CrossRef]
34. Y. Chibani and A. Houacine, "The joint use of IHS transform and redundant wavelet decomposition for fusing multispectral and panchromatic images," *International Journal of Remote Sensing,* vol. 23, no. 18, pp. 3821–3833, 2002. [CrossRef]
35. S. Klonus and M. Ehlers, "Image fusion using the Ehlers spectral characteristics preservation algorithm," *GIScience & Remote Sensing,* vol. 44, no.2, pp. 93-116, 2007. [CrossRef]
36. C. Ballester, V. Caselles, L. Igual, J. Verdera, B. Rougé, "A variational model for P+XS image fusion", *International Journal of Computer Vision*, vol. 69, no. 1, pp. 43–58, 2006. [CrossRef]
37. L. Alparone, B. Aiazzi, S. Baronti, A. Garzelli, F. Nencini and M. Selva, "Multispectral and panchromatic data fusion assessment without reference," *Photogrammetric Engineering & Remote Sensing,* vol. 74, no. 2, pp. 193-200, Feb. 2008. [CrossRef]

Sevcan Kahraman received the B.Sc. degree in Mathematics department at Dokuz Eylül University in 2005, and the M.Sc. degree in Mathematics at İzmir Institute of Technology in 2008. She is currently a Ph.D student and working at the Kocaeli University Laboratory of Image and Signal Processing (KULIS) at Kocaeli University. Her research interests focus on image processing, data fusion on remotely sensed data and hyperspectral imaging.

Alp Ertürk received his B.Sc. and M.Sc. degrees in Electrical and Electronics Engineering from Middle East Technical University, Ankara, Turkey, in 2007 and 2010, respectively. He received his Ph.D. degree in Electronics and Telecom. Engineering from Kocaeli University, Kocaeli, Turkey, in 2013. He was a postdoctoral researcher with the Hyperspectral Computing Laboratory (HyperComp) in University of Extremadura, Cáceres, Spain. He is currently an Assistant Professor with the Electronics & Telecom. Eng. Department, Kocaeli University, Turkey. His research interests are in the areas of digital image processing, remote sensing and hyperspectral imaging. He is a reviewer for several journals including IEEE Geoscience and Remote Sensing (GRSL), IEEE Journal of Selected Topics in Applied Earth Observations and Remote Sensing (JSTARS) and IEEE Transactions of Geoscience and Renote Sensing (TGRS). He is also currently serving as the Secretary and Treasurer of the IEEE GRSS Turkey Chapter.